6. Electrical Conductivity Structure beneath the Northeastern Part of Japan

Rikitake (1969) compiled the distribution of the ratio of the vertical to the horizontal component (Z/H) of the geomagnetic variation at short periods in Japan. He pointed out that the anomalous value of Z/H can be recognized not only in the central part of Japan but also in Tohoku district, northeast Japan. On the basis of the intense measurements by induction magnetometers, Kato et al.(1970) obtained a model of the electrical conductivity structure beneath this region. They concluded that the mantle conductor rises up to the depth of 30 km or so just below the volcanic front, and the top of the conductor is suddenly depressed in the Pacific side. Hence, the anomalous behavior of the geomagnetic variation in this district was attributed to the anomalous distribution of the subsurface conductivity.

Honkura (1974) applied a numerical modeling technique developed by Jones and Pascoe (1971) to investigate the conductivity structure beneath this region. He suggested that the spatial distribution of the transfer functions could be explained by taking into account the effects of the Pacific Ocean and the Japan Sea. Thus, the necessity of seafloor observations was realized in order to evaluate the effect of ocean and to extract the information on the conductivity distribution below the Japanese Islands.

In 1981, Research Group for Crustal Resistivity Structure, Japan, carried out magnetometer array observation at 10 sites in northeastern Japan (Research Group for Crustal Resistivity Structure, Japan , 1983), including electric field measurements. Magnetotelluric survey at ELF and VLF frequency ranges was also conducted along a

traverse across the area to obtain the surface conductivity distribution. In addition to these land measurements, geomagnetic and electric field variations were observed on the seafloor across the Japan Trench (Yukutake et al., 1983).

Based on these observations, Ogawa et al.(1985) pointed out the existence of conductive layer in the western half of lower crust beneath the northeastern Japan Arc in order to explain the distribution of transfer functions. The eastern boundary of the conductor coincides with the volcanic front. Their conclusion is quite important since this was the first that revealed existence conductive layer in the lower crust in Japan.

In this chapter, the present direct inversion method is applied to the investigation of the electrical conductivity structure beneath the northeastern part of Japan to obtain a reliable structure. The new data set of electromagnetic variations were used to derive an optimum model by the least squares method.

6.1 Spatial and period dependence of the response functions

Observation sites for the present investigation are given in Table 6.1, where MZS and ESS are the permanent geomagnetic observatories belonging to the Geographical Survey Institute. Other land sites are the temporary ones during the 1981 project by Research Group for Crustal Resistivity Structure, Japan. The seafloor measurements were made in 1981 (Yukutake, et al., 1983). At the two seafloor sites, J1 and J2, the variation of of the geomagnetic fields were measured by Japanese made ocean bottom magnetometer (OBM), which was developed by the joint project between Ocean Research Institute and Earthquake Research Institute, the University of Tokyo. The OBM, installed at J1, was recovered with a fine record of 3-components of geomagnetic storm, which is the first seafloor data measured by Japanese instrument (Segawa, et al.1982). However, the measurement by another OBM was unsuccessful at J2.

The Scripps Institution of Oceanography conducted seafloor measurements at 4 sites: S1, S2, S3 and S4. Three component geomagnetic field variations were obtained at S1, S2 and S4, while electric field measurements were successful at S1, S2 and S3. The electric field data at S3 will be analyzed by combining the magnetic field data at S4 as had already been done by Yukutake et al.(1983).

6.1.1 Geomagnetic transfer functions

At most of the land sites, 3 components of the geomagnetic variations were simultaneously recorded in every minute by flux-gate magnetometers with a resolution of 0.1 nT. Data at KKD, KZK, TON and MYK, which was originally recorded on recording charts, were digitized also at every 1 minutes and with 0.1 nT resolution. Data from OBM sites were acquired in digital form. The OBM at J1 recorded the geomagnetic field at a sampling interval of three minutes and with a resolution of about 0.7 nT (Segawa et al.,1984). By Scripps instruments, geomagnetic and electric field variations were recorded with a sampling rate of 64 or 128 cycles per hour with resolutions of 0.01 nT and 0.01 μ V/m, respectively. Fig.6.1 gives an example of the simultaneous records of the geomagnetic storm which took place on Jul.25, 1981.

From the compiled geomagnetic variation data, complex geomagnetic transfer functions A(f) and B(f) were calculated at each station for several geomagnetic disturbances by using the spectral analysis method, as well as 95% confidence intervals (see Chapter 5).

Durations of magnetic disturbances which were analyzed here were about two days for the longest and twenty four hours for most of the stations, which enables us to obtain reliable estimates of the spectra at periods up to about 120 minutes. On the other hand, the shortest observable period is 6 minutes. Spectra of geomagnetic variations at several stations were found to be disturbed by artificial noises at shorter periods of less than 10 minutes. Therefore, we had to eliminate these noises by using numerical high-cut filter beforehand. Finally, We selected period range between 120 and 15 minutes for the

analysis.

Figs.6.2 (a)-(d) show overall distributions of the induction vectors in this area for the periods, 15, 30, 60 and 120 minutes, respectively, which were obtained from the calculated complex transfer functions A(f) and B(f). As a general feature, the vectors point to the east at seafloor sites and land sites in the vicinity of the Pacific coast, which is almost normal to the mean trend of the northeastern Japan Arc. At the OBM site far off the coast, S4, the induction vector become very small particularly at the shorter periods.

Going inland toward the back arc side, north component of the induction vector becomes conspicuous, except the two southern sites, NRG and TZW. The north pointing induction vector indicates the existence of strong induced current in the north of the site. This situation may imply the two-dimensional approximation beneath this area to be inappropriate.

Yamashita and Yokoyama (1977) revealed that the main characteristic of the geomagnetic variation in both side of the Tsugaru Strait can be explained by the strong electric current induced in the strait. On the other hand, Nishida (1982) suggested the existence of a shallow conductor beneath the Oshima Peninsula to account for the geomagnetic variation in southwest Hokkaido region. He also pointed out that the area of shallow conductor coincides with that of high heat flow which extends from the border of Aomori-Akita prefecture (Watanabe,1973) to the north along the Japan Arc. Therefore, the shallow conductor may exist to the north to cause north component of the transfer function in this area.

Ogawa et al.(1986) discussed this feature in detail and concluded as follows. Along the north-south cross section, the amplitude

of the transfer function, A(f), sharply attenuates toward south, while that of B(f) is almost constant and no local dependence can be seen in its distribution (Fig.6.3). Large value of A(f) means that a conductor does exist north of the present array, which causes a strong induction effect in this area, either by the strait effect or the possible shallow conductor, or by combination of both. However, this induced current affects little on the distribution of B(f) but only on that of A(f). Thus, so long as we consider the east-west cross section, B(f) works as a response function independent of the induction effect on A(f).

The direct inversion will be carried out with a set of transfer function, B(f), given in Tables 6.2(a)-(d) in the east-west cross section of northeast Japan. Figs. 6.4(a)-(d) show E-W profiles of the observed response functions, including the magnetotelluric responses described in the next section, for respective periods. In these figures, the Pacific coast is taken as the origin of horizontal coordinate.

At seafloor sites on the continental slope between the Pacific coast and the Japan Trench, J1 and S1, the amplitude of the transfer function becomes remarkably large, at 30 minutes period in particular, exceeding unity. This should be caused by the strong induced electrical current in the deep sea. The phase of transfer functions at these two sites has nature of out-of phase for each period, indicating that the induction vector points eastward. At S2, beyond the Japan Trench, the transfer function becomes in phase (between -90 and 90 degrees). These behavior of transfer function suggests that the center of the induced current concentration possibly coincides to the trench. The transfer function at the farthest site from the coast, S4, can be

regarded as null, so that we can reasonably assume the one-dimensinality of the conductivity structure below the station.

Main features of the transfer function B(f) are as follows.

1) On the Pacific side, the vertical component of the magnetic field varies almost out-of phase to the eastward component, while it becomes in phase on the Japan Sea side. In other word, the induction vector points the adjacent sea. Roughly speaking, therefore, the effect of Sea water in the Pacific Ocean and the Japan Sea is most dominant in determining the characteristics of the geomagnetic variation in this region (Honkura, 1974; Ogawa et al., 1986)

2) The amplitude of transfer function on the Japan Sea coast, at OGA for example, is much smaller than that on the Pacific coast, at MYK. Although one of the most plausible cause of this difference should be referred to the difference in the water depth, it may be partly caused by heterogeneity of subterranean conductivity distribution.

3) The argument, or phase, of the transfer function turns its sense from out-of to in phase between KZK and SZI, between -49 km and -126 km in the present coordinate system; i.e. the argument decreases from about 150-170 degrees to 50-80 degrees toward Japan Sea side. The rate of change becomes moderate with increasing period as can be seen in Figs.6.4(a)-(d). This also reflects the possible induction effect by the subterranean inhomogeneity. Ogawa et al.,(1986) concluded that this anomalous behavior can be attributed to the large conductivity contrast in the lower crust at the volcanic front (VF).

In the present study, the regional two-dimensional conductivity structure beneath this region is investigated as one of the application of the direct inversion method, using thus evaluated transfer functions together with the magnetotelluric impedances shown in the

followings.

6.2 Magnetotelluric Results

As previously discussed, even a shallow conductivity structure sometimes causes a significant geomagnetic induction effect at fairly longer periods. Therefore, the information on the shallow structure is indispensable in order to investigates the deep conductivity structure. In this study, a newly developed technique of ELF·VLF magnetotelluric method was used to provide the information on the near-surface conductivity distribution down to several kilometers or so.

In 1981, an ELF·VLF magnetotelluric survey has been conducted along the traverse across the northeastern part of Japan as shown in Fig.6.5 (Utada, et al.,1982). Measurements were made at 27 sites denoted by small circles in the figure, including two of the ULF sites, NRG and TZW. For the ELF range, electric and magnetic fields were recorded simultaneously, and then complex tensor impedances were determined at the frequencies of three fundamental modes of the Schumann resonance following the procedure described in Chapter 4. Apparent resistivity and phase difference between electric and magnetic field variations were also measured for the VLF range by use of an EM16-16R system of Geonics (see Chapter 4).

Figs.6.6 shows the profiles of the apparent resistivity and the phase difference at the frequencies 17.4 (top) kHz and 8 Hz (middle), respectively. It is quite noticeable that the distribution of magnetotelluric responses correlates well to the surface topography shown

in this figure (bottom). The highest apparent resistivity of about 1 k Ω ·m was obtained in the midst of the Kitakami Mountains at 8Hz. Going down to the Sendai Plain, it steeply decreases down to less than 10 Ω ·m. These features are in harmony with the surface geology; i.e. the former corresponds to the outcrop of Paleozoic sedimentary rocks, while the latter to Quaternary sedimentary layer formed along the Kitakami River. A couple of similar depressions of apparent resistivity can be seen on the western half of this traverse. One on the Japan Sea side corresponds to the Shonai Plain, and the inner one to the Shinjo Basin, respectively.

Relatively high apparent resistivities of an order of 100 Ω ·m have been obtained in the mountains. A sharp decrease of the apparent resistivity is found at the sites close to the volcanic front in the vicinity of the Onikobe and Narugo Hotsprings in the Oou Mountains area. This low resistivity is presumably related to the geothermal activity in this area.

From above considerations, we can conclude that the distributions of ELF and VLF magnetotelluric impedances correspond well to the regional structure of surface geology. Moreover, most of the sites are situated far enough from the coast to be free from the induction effect by ocean at these higher frequencies. Hence, we construct a model of surface conductivity distribution across the northeast Japan Arc by means of one dimensional inversion at each site, using the impedances at ELF and VLF ranges. The farther two-dimensional analysis is carried out by use of the surface conductivity distribution thus obtained.

For the shorter period band of ULF, such as about 30 seconds, electric field records were severely affected by noises mostly of ar-

tificial origin. However, since the noise level is much lower in this region than in central Japan, reliable estimates of magnetotelluric impedance for this band have been obtained at 3 sites, TZW, NRG and ESS (Utada et al., 1982; Research Group for crustal Resistivity Structure, Japan, 1984).

On the other hand, we have records of the electric field variations at 5 sites, TZW, NRG, ESS, KZK and TON, on land and at 3 seafloor sites, S1, S2 and S3, observed simultaneously with the geomagnetic field variation for the longer period band of ULF. By use of data from 8 sites, the impedance tensors have been evaluated at 15, 30, 60 and 120 minutes of period. For S3, the geomagnetic data at S4 has been used for the evaluation, as mentioned previously.

At each seafloor site, the impedance tensor has been obtained with sufficiently small skewness (<0.2) of Eq.(4-4-2), suggesting the one or two-dimensional structure below the site. The off-diagonal elements of the impedance tensor, Z_{xy} and Z_{yx}, have been used as data in E- and H-polarization cases, respectively, in the following two dimensional investigations (Tables 6.3(a)-(d) and 6.4(a)-(d); Figs.6.4(a)-(d)). Impedance tensor at TZW has also shown relatively small skewness ranging 0.2 to 0.4. Taking into account the fact that the noise level is higher on land than that on seafloor, the impedance at TZW can be regarded as a response function reflecting the mean two-dimensional structure in the earth. However, impedances at other land sites have shown anomalously large anisotropy , as well as with large skewness sometimes exceeding unity.

Asakawa (1986) applied the newly developed Sompi method to time series analysis, and re-calculated the impedance tensors from the same data set. He pointed out some impedance indicates only a little smal-

ler skewness than those obtained by the FFT method. He has also demonstrated the complexity of the structure beneath these sites, referring to the result of one dimensional modelings. Therefore, we have to omit the impedances at land sites, except those at TZW, from the following analysis of two-dimensional structure.

Once the impedance tensor, Z(f), is evaluated, we can obtain a polar orbit of expected electric field variation from a magnetic field variation with unit intensity. Letting the unit vector of horizontal magnetic field variation with polarization azimuth θ be $h(\theta)$

where

$$h(\theta) = \begin{bmatrix} \cos\theta \\ \sin\theta \end{bmatrix} \qquad (6\text{-}2\text{-}1)$$

the expected orbit of the induced electric field, $e(f,\theta)$, will be given as:

$$e(f,\theta) = Z(f)\, h(\theta) \qquad (6\text{-}2\text{-}2)$$

or written explicitly with each component,

$$\begin{aligned} e_x(f,\theta) &= Z_{xx}(f)\cos\theta + Z_{xy}(f)\sin\theta \\ e_y(f,\theta) &= Z_{yx}(f)\sin\theta + Z_{yy}(f)\sin\theta \end{aligned} \qquad (6\text{-}2\text{-}3)$$

By use of these expressions, polarization diagrams have been obtained

as shown in Figs.6.7(a)-(d) from respective impedance tensor estimates at TZW, S1, S2 and S3.

Polar diagrams of the expected electric field at the OBE sites represent apparent anisotropy similar to each other in N-S direction (Figs.6.7(b)-(d)) for each frequency, which is almost parallel to the mean direction of the coast line and of the axis of the Japan Trench, decreasing the degree of anisotropy with going offshore. In fact, the polar diagram at S3 (Fig.6.7(d)) can be regarded as almost isotropic. The direction of anisotropy is almost perpendicular to the mean direction of the induction vector at OBM sites: i.e. the E-W direction. These features indicate the existence of the strong electric current induced along the Japan Trench.

At the inland site TZW, polar diagram shows almost isotropic feature as shown in Fig.6.7(a). In such a geological situation, any land site cannot be free from the induction effect of the ocean for these period range, where the skin depth becomes longer than the width of the Japanese Island. Therefore, we can not directly assume the one dimensionality of the conductivity structure beneath TZW. What we have to aim at is to establish a conductivity model which explain the apparent isotropy of the impedance.

The magnetotelluric impedance obtained at TZW covers the whole frequency range from VLF to ULF. Referring the frequency characteristics of Z_{yx}, one-dimensional structure was inferred inversely using a five-layer model (Yukutake,1984), as shown in Fig.6.8. Since TZW is situated in the midst of the Shinjo Basin, the surface is covered with conductive layer of several kilometers thickness. Besides shallow conductor, highly resistive layer is predominant in the upper part of

crust down to the depth of about 15-20 km. This depth is approximately coincides with that of the Conrad Plane in this area revealed by explosion seismology (Asada and Asano, 1973; Yoshii, 1979). The five layer model shows that the resistivity below the resistive layer decreases by nearly 3 orders of magnitude. Since the MOHO depth is about 30 km in this area, above result implies that the lower crust is conductive. Present data set, however, could not resolve the deeper structure, whether the mantle is also conductive or not.

By using the results on the seafloor, one-dimensional inversions have been also carried out. By applying various layered models (see Fig.3.7 in Section 3.3), optimum models have been derived at each site for each polarization. Optimum models at S1, S2 and S3, inferred by Z_{xy} are given in Fig.6.9(a)-(c), while Fig.6.10(a)-(c). shows those by Z_{yx}. The resulting models on seafloor beyond the trench, S2 and S3, show similar features as can be seen in these figures; i.e. highly conductive layer beneath a thick resistive layer whose conductivity ranges from 10^{-2} to 10^{-3}. At S1, on the other hand, different features are inferred for different polarizations. This can be ascribed to the lateral heterogeneity of the conductivity structure, and partly to the coast effect on the continental slope.

Such feature with a conductor beneath a resistive layer has been commonly implied by previous magnetotelluric results in the open ocean (e.g. Filloux, 1967,1978,1981). The deep conductor is usually regarded as corresponding to the oceanic asthenosphere (Oldenburg, 1983). Filloux (1981) suggested a possible relation between the age of the ocean floor and the depth to the highly conductive layer of about 0.1 S/m beneath the Pacific Plate. Yukutake et al.(1983) demonstrated that the results at S2 and S3 are in harmony with the previous works by Fil-

loux. In the present study, the depth to the conductor has been estimated as shown in Fig.6.11 for E-(above) and H-polarization (below) cases against the distance from the trench axis. All results, except for H-polarization at S1, indicate a possible tendency of increasing depth towards the Japanese Island Arc. This tendency may reflect the subduction of the Pacific Plate.

These results are used in the further two-dimensional modeling as a initial constraints of the structure as following.

6.3 Two-dimensional Conductivity Model across northeastern Japan

6.3.1 Construction of the finite element network and inhomogeneous block division

In this section, the direct inversion method has been applied to investigate the subterranean structure beneath this region. The data set used for the analyses consists of geomagnetic transfer functions and the magnetotelluric impedances for E-polarization case as tabulated in Tables 6.2(a)-(d) and 6.3(a)-(d), at respective period 15, 30, 60 and 120 minutes.

A basic mesh network has been constructed for the finite element calculation to evaluate the response functions and the partial derivatives, which covers the area between 2,000 km away from the Pacific coast and about 1,500 km from the Japan Sea coast horizontally, from 150 km above sea level down to 2,000 km depth in the earth, with the total area being 3,700 km x 2,150 km (Table 6.5). In this way boundaries have been taken far enough so that boundary conditions are unlikely to affect the calculated responses for the areas under consideration (Ogawa, et al.,1985; Utada, et al.,1986).

The whole space was divided into 6314 triangular elements, whose sizes were carefully chosen to be sufficiently small compared with the spatial scale length of the electromagnetic field variation in each element. For example, vertical sizes of the near surface elements were taken as 100 m for the smallest ones because the skin depth for the electromagnetic field variation of 15 minutes period is as shallow as about 7.5 km in sea water whose conductivity is 4 S/m or so. On the coast and continental shelf, the amplitude of electromagnetic varia-

tion changes sharply also in the horizontal direction because of the large conductivity contrast between the land and the sea. Hence, we adopted 5 km as the horizontal scale of the elements in this area.

We began modeling with incorporation of the surface structures so far known along the profile into the model, particularly the following features which were obtained from geology and magnetotelluric results (Fig.6.6);

1) Conductive sea water of the Pacific Ocean and the Japan Sea. Seafloor topographies were carefully read along the profile from the bathymetric chart.

2) Thick sedimentary layer on the seafloor and continental shelf. Conductivity of 1-0.5 S/m was adopted to sediment. Sedimentary layers have been modeled with reference to the results of seismic profiler (e.g. Shipboard Scientific Party of DSDP leg 57, 1980).

3) Tertiary or Quaternary sediments or sedimentary rocks in the coastal areas and inland basin. Shallow conductivity distribution on land has been modeled on the basis of the ELF·VLF magnetotelluric results as mentioned above.

4) Outcrops of resistive rocks, as resistive as 10^{-3} S/m, in the Kitakami Mountains.

5) Result of magnetotelluric sounding at TZW suggests the conductivity of the upper crust beneath northeastern Japan to be 10^{-3}-10^{-4} S/m. This value has been also confirmed by preliminary magnetotelluric result by Yukutake et al.(1984).

6) Seafloor magnetotelluric result reveals the resistive lithosphere and the highly conductive asthenosphere. The depth of the boundary is determined as about 140 km beneath the seafloor.

Taking into account the above information, block division has been made to model the near-surface inhomogeneous structure as shown in Fig.6.12. A proper value has been given to the conductivity of each block, assigned by A-L (Table 6.6). The block division of the deeper structure was made on the basis of various kinds of geophysical and geological evidences. A conductive region was inferred in the lower crust between the volcanic front (VF) and the Japan Sea coast beneath northeastern Japan by the distribution of geomagnetic transfer function (Ogawa, et al.,1986). The result of one-dimensional magnetotelluric inversion at TZW also suggests the existence of conductive layer 15-20 km deep below. It is well-known that the distribution of surface heat flow in northeastern Japan Arc is characterized by a remarkable contrast across VF; i.e. high value in the west and low in the east. Distribution of the micro earthquake foci also investigated in detail in this area (e.g. Takagi, et al., 1981). The aseismic front (AF) is the boundary of the occurrence of earthquakes in the crust (Yoshii, 1974). Thus, taking into account these evidences, the lower crust of northeastern Japan has been divided into three blocks, No.1, 2 and 3, as shown in Fig.6.13.

The trace of upper surface of down-going Pacific Plate beneath the northeast Japan Arc was determined with reference to the distribution of earthquakes (Takagi, et al., 1981). A thin layer of about 10 km of thickness was added to the plate boundary assigned by No.8 (Fig.6.13). As has been discussed previously, the oceanic lithosphere is usually detected as a resistive layer. However, several in-situ measurements indicate the upper part of the oceanic crust is fairly conductive, as well as the sedimentary layer. Numerical models of

oceanic crust by Drury (1979) also suggests the possible formation of conductive layer down to Layer 2B. The thin block has been divided in order to examine whether the conductive surface layer of the oceanic crust goes down into the mantle beneath the northeastern Japan Arc or not.

The upper most part of the mantle beneath the Japan Arc, or the mantle wedge, has been divided into three blocks; No.4, 5 and 6, corresponding to the parts between the Japan Trench and AF, beneath the Japan Arc and beneath the Japan Sea, respectively. This block division of the mantle wedge has been made on the basis of the geothermal model by Honda (1985), the petrological model by Tatsumi, et al. (1983), and so on.

Block No.7 simulates the oceanic asthenosphere (Fig.6.14). The depth to its surface is 140 km below the open ocean, which was determined by the prescribed one-dimensional magnetotelluric inversion at S3. The wedge shape of the asthenosphere beneath the Japan Arc is made on the assumption of the constant thickness of the subducting lithosphere.

The structure deeper than 100 km is assumed simply to consist of three blocks (Fig.14), i.e. the deeper mantle beneath the Japan arc, the deeper extension of the slab and the middle mantle below 400km. The last block has been fixed as having the conductivity of 1 S/m, which is a representative value of the conductivity of the middle mantle (Rikitake,1975). The conductivities of the formers, on the other hand, have been first assumed, and then the validity of the values has been examined, as shown in the following section.

6.2.2 Result

In general, it is natural that the least squares process will be more stable and be able to give more convincing solutions with the lower degree of freedom. Consequently, we adopted some restrictions on the model to reduce the number of unknowns as shown above. One is the near-surface conductivity distribution including sea water, and the other is the conductivity distribution of the deeper structure. As a result, final number of unknown parameters became to be 8.

Then, several calculations were made in order to obtain initial parameters for the direct inversion. We first calculated the theoretical responses for the model in which uniform conductivity of 10^{-3} S/m was assumed except for the fixed blocks. Several discrepancies were found between the observed responses and the calculated ones, as shown in Fig.6.15, which shows one of the results for the period of 15 minutes. For example, the calculated amplitudes of both the impedance and the transfer function are much larger than the observed one just in the vicinity of the Japan Trench; the calculated phase of the transfer function behaves quite differently in the midst of the Japan arc; the calculated amplitude of the transfer function becomes twice as large as the observed one in the Japan Sea coast. It is obvious that additional conductivity inhomogeneities are required in order to explain these features.

Ogawa et al.(1986) showed that the spatial distribution of the transfer function can be explained by the existence of a highly conductive layer beneath the volcanic region of the Japan Arc; i.e. between the volcanic front (VF) and the Japan Sea coast. They also suggested the mantle wedge as moderately conductive as 10^{-2} S/m. Utada et

al.(1985) indicated that the lower crust between the aseismic front (AF) and VF, as well as the conductor beneath the volcanic region, is likely to be conductive to provide a better fitness between the calculation and the observation. The highly confident result of one-dimensional inversion at TZW has also been referred in adopting the initial parameters.

The initial value of the asthenosphere below the Pacific plate was given as shown in Table 6.6 on the basis of the seafloor magnetotelluric results shown in the previous section. The surface thin layer of the plate was assigned initially as 2×10^{-2} S/m by referring the numerical model by Drury (1983) and the large scale resistivity measurement by DSDP (e.g. Shipboard Scientific Party of DSDP leg 57, 1980).

The direct inversion by the iterative process has been carried out with the set of 8 unknown parameters tabulated in Table 6.7. After 48 cycles iteration of parameter refinement, the process has converged. It took totally about 270 minutes of CPU time on HITAC M280H computer at the Earthquake Prediction Data Center of the Earthquake Research Institute, the University of Tokyo. The actual procedure of the computation is explained as follows.

In order to give proper value of a priori covariance to each unknown parameter, we first calculate the partial derivatives of the response functions with respect to the initial value of each unknown parameter. The spatial variations of the partial derivatives are given in Appendix B. The diagonal elements of the initial covariance can be obtained by the procedure shown in Section 3.6. Then the total inversion is performed by use of the initial information.

Because of the restriction of CPU time of the system, the com-

putation has to be suspended at every 8'th cycle. Then the variations of each parameter and χ^2 throughout the 8 cycles are plotted to examine the convergence. If some parameters or χ^2 are still changing their values, the process is continued with the final values in the previous cycle as the starting points. When the process converged, whole computation is stopped.

Fig.6.16 shows the behavior of parameters and χ^2's of the transfer function and the impedance at the last 8 cycles of the iterative process. As shown in Table 6.7, both χ^2's were reduced by 30 % from those of the initial stage. Fig.6.17(a)-(d) show the comparison of the observed and the calculated responses from the final set of parameters for the period of 15, 30, 60 and 120 minutes. Though the final parameters are determined by use of E-polarization responses, these figures show that they well account for the observed H-polarization ones, too.

Since the initial to final covariance ratio, C_{popo}/C_{pp}, is greater than 2 except for the blocks No.1 and No.5, each parameter can be regarded as well resolved. The spatial distribution of the partial derivative given in Appendix B also provides an information on the resolution of each structure. For example, the partial derivative with respect to the block No.8 becomes large in the vicinity of the Japan Trench, where we have several observation sites. Without data points with large partial derivative, the solution of the iterative process is inevitably less confident and may be unstable.

The existence of the lower crustal conductors, blocks No.2 and No.3 corresponding to those between AF and VF and between VF and the Japan Sea coast, respectively, have been confirmed by the present method. Moreover, the result also indicates the possible conductivity

contrast between them; i.e. the structure in the west of VF is more conductive than that between AF and VF.

On the other hand, the result shows the tendency of the decreasing conductivity of the arc mantle toward the back arc side. The final conductivity of the block No.4, corresponding to the tip of the mantle wedge, is the highest in these three blocks, although the block No.6, corresponding to the mantle beneath the Japan Sea, has not been well resolved with such a small covariance ratio as 1.07. The block No.6 has been almost utterly unresolved, because we have no data point on the Japan Sea floor and the continental shelf at present, where large partial derivatives can be expected (see Appendix B).

The Pacific asthenosphere has finally been assigned as having the high conductivity of 7.3×10^{-2} S/m. This value is in good agreement with that determined by the prescribed one dimensional inversion of the magnetotelluric data.

The direct inversion inferred a highly conductive layer on the surface of the subducting Pacific plate. The conductivity of the layer was determined as 8.5×10^{-2} S/m, though its initial value was 2.0×10^{-2}. Since the model contains a highly conductive layer corresponding to the seafloor sedimentary layer as given in Table 6.6 with 1 km thickness, this layer is likely to correspond to the oceanic crust. This result indicates that the oceanic crust is possibly conductive down to about 10 km, and that the conductive layer extends deep in the earth as shown in Fig.6.14.

In the following, farther investigations will be made to make clear of the implications of the structure beneath northeast Japan determined by the present method.

The lower crustal conductor beneath the northeastern Japan Arc is of great geophysical implication, because no earthquake occurrence means that the lower crust is ductile in the west of the aseismic front. In the present investigation, it has been confirmed that a highly conductive layer exists not only beneath the volcanic region but also in the lower crust between the aseismic front and volcanic front. Here it will be demonstrated how the model response can be improved by introducing the lower crustal conductors and how convincing is their existence.

Fig.6.18 shows a part of the present traverse across northeast Japan. Each closed circle with thick error bar denotes the amplitude(above) and the phase(below) of the observed transfer function for the period 15 minutes. When conductivity as low as $1x10^{-3}$ S/m is assigned equally to both of the structure, the resultant response, especially the phase of the transfer function, behaves quite differently from the observation as shown by dashed line in the figure. In this case, the vertical component of geomagnetic variation is purely generated by the electromagnetic induction in the Pacific ocean and the Japan Sea. In the absence of the conductive layer, the vertical component vanishes at an inductive neutral point of both seas where the phase varies quite sharply. Ogawa et al.(1986) pointed out, though they did not use the expression by amplitude and phase but by real and imaginary parts, that the gradual change of the observed transfer function could be well represented by introducing a conductive layer in the lower crust beneath the volcanic region. In fact, the conductor makes the phase variation gradual as shown by thin line in Fig.6.18. However, one can notice that there still remains some discrepancy or bias between the observation and the calculation. This

bias can be canceled by introducing additional conductor to the east. The final model represents most of the features of the observed transfer function as denoted by thick line in Fig.6.18. Thus, we can conclude that the eastern boundary of the lower crustal conductor lies at the aseismic front.

Next, we check how definitely these parameters have been determined. For that purpose, the direct inversion was carried out against the same data set by letting these two parameters, conductivities of the two blocks in the lower crust, unknown. Since the final conductivity values were large, small values have been assigned as their initial values as given in Table 6.8. Each parameter has converged to the similar value to the previous case after 12 cycles iteration (Fig.6.19, Table 6.8). This example clearly shows the unambiguous existence of the lower crustal conductor beneath the northeastern Japan arc.

Fig.6.20 illustrates the induction effect caused by the thin conductive layer on the subducting Pacific plate. Here, the observed impedances as well as the transfer functions are compared with the model responses for the period of 15 minutes. In the absence of this thin layer, a large concentration of the induced current occurs in the vicinity of the continental slope, about 150 km off the east coast of northeast Japan. The current concentration causes a large amplitude of the electric field, and thus a large value of apparent resistivity as shown by thin line in the top of the figure. The concentration also causes the discontinuous phase variation as illustrated below. These features of the impedance are not observable. Similarly, the model response does not account for the spatial distribution of the observed transfer function without the thin conductor. The induced current

causes a large amplitude of vertical component of geomagnetic variation, so that the calculated amplitude becomes several times greater than the observed one.

Since the current concentration is due to the large conductivity contrast between sea water and seafloor, the model should be improved by reducing the contrast in order to account for the observed responses. In this case, a conductive layer of about 1 km thickness, corresponding to the sedimentary layer, has such an effect to some extent. The model also includes a thick conductor which represents an accretionary prism. However, the reducing effects by these conductors are not enough to represent the feature of the observation as shown above. Therefore, we have to consider an additional conductive layer below. This additional layer does not necessarily extend throughout the ocean. One possible solution is a conductive layer extending just from below the position of the current concentration to deeper part along the subducting slab. Thus, a possible existence of the top conductive layer on the subducting lithosphere has been considered. The resulting responses have been found to be much improved to explain the observed ones as illustrated by thick lines in Fig.6.20.

Finally, we examine the validity of the assumptions on the conductivity of the deeper structure than 100 km. Since the deep structure of the Pacific asthenosphere has been determined independently from the direct inversion, our effort has been concentrated on determination of the conductivity distribution in the back arc mantle and the deeper portion of the subducting lithosphere assigned by M and N, respectively, in Fig.6.14. The direct inversion was applied to the two unknown parameters with the other parameters fixed equal to the final ones. The partial derivatives with respect to each parameter are quite

small at any observation sites. Hence, the convergence was not a definite one as shown in Fig.6.21 after 8 cycles iteration. It was found that, as given in Table 6.9, the iterative process required small constraints on the initial parameter (C_{popo}), otherwise it became unstable. Consequently, no significant refinements have been made on the parameters by the iteration. In other word, these parameters have not well been resolved by the present data set. This is undoubtedly due to lack of information at longer periods, as well as observations in Japan Sea.

The result of the present investigation on the electrical structure beneath the northeastern Japan Arc system can be summarized as follows:

1) A highly conductive layer exists within the lower crust beneath northeast Japan. The conductivity is about 5×10^{-2} in the western part beneath the volcanic region. The eastern part is likely to be a little more resistive as 3×10^{-2} S/m.

2) A conductive layer exists beneath the northwest Pacific Ocean at the depth of about 140 km beneath the ocean bottom. The conductivity of this layer has been estimated as 7×10^{-2} S/m. This layer corresponds to the electrically recognizable asthenosphere.

3) The mantle wedge is moderately conductive as about 5×10^{-3} S/m, which is more conductive than the Pacific lithosphere but is less conductive than the asthenosphere. The conductivity of the mantle wedge may tend to decrease toward backarc side.

4) A highly conductive thin layer, with conductivity of about 8×10^{-2} S/m and thickness of 10 km, exists on the surface of the subducting

Pacific plate. The present investigation has indicated that the conductive layer should extend deep into the earth in order to provide a significant induction effect due to concentrated current in the vicinity of the Japan Trench.

The geophysical implications of these features, revealed by the present investigation, will be discussed in detail with reference to the other geophysical, geological and geothermal evidences in Chapter 8. Before that, in the next chapter, the electrical conductivity structure beneath the central part of Japan will be investigated by use of the present interpretation method. Comparison of the results from two different regions in the island arc of Japan will also be made later.

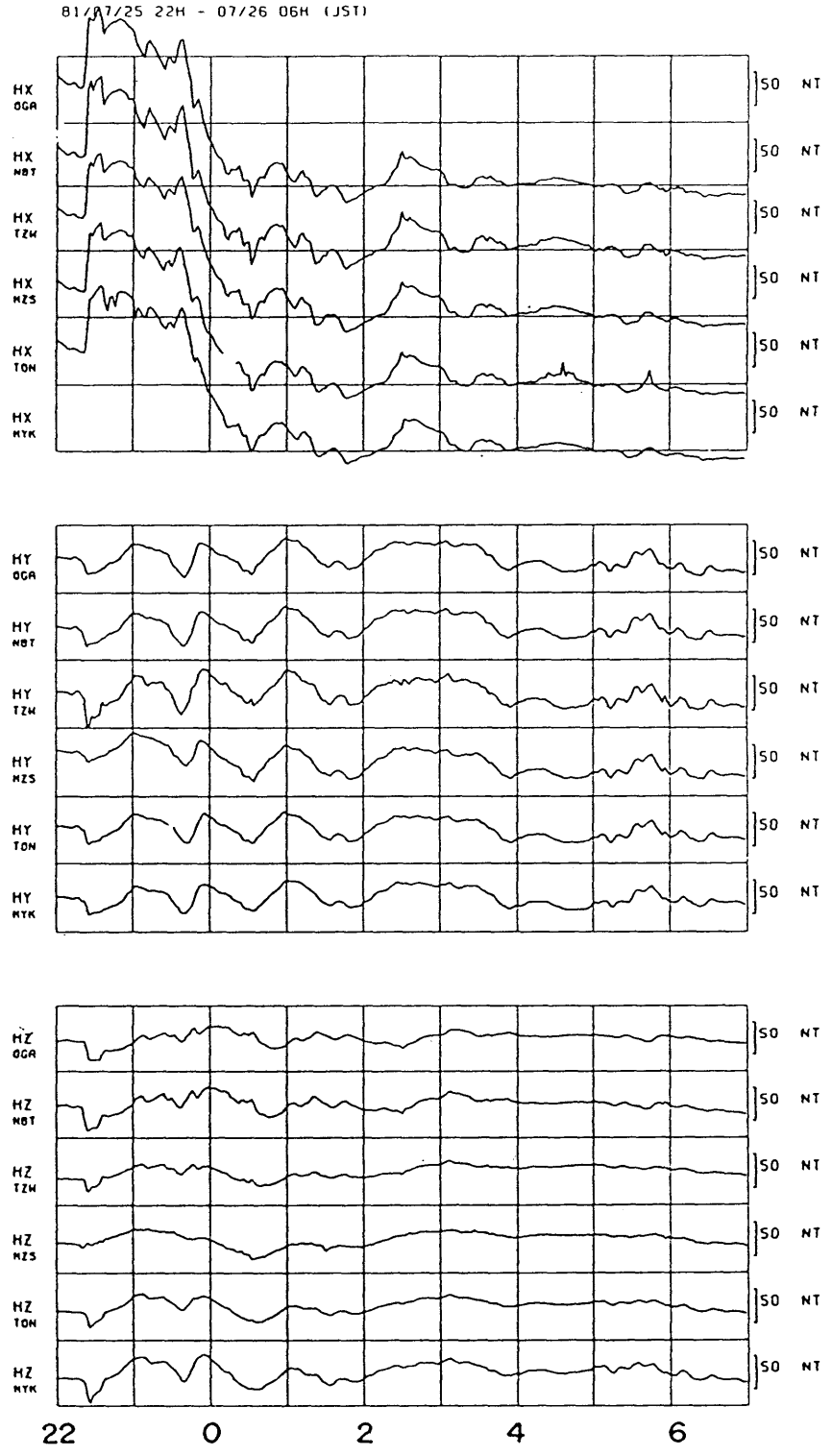

Fig.6.1 An example of simultaneous record of a geomagnetic storm on Jul.25, 1981 observed at OGA, NBT, TZW, MZS, TON and MYK in northeast Japan. Geomagnetic north, east and vertical components are given.

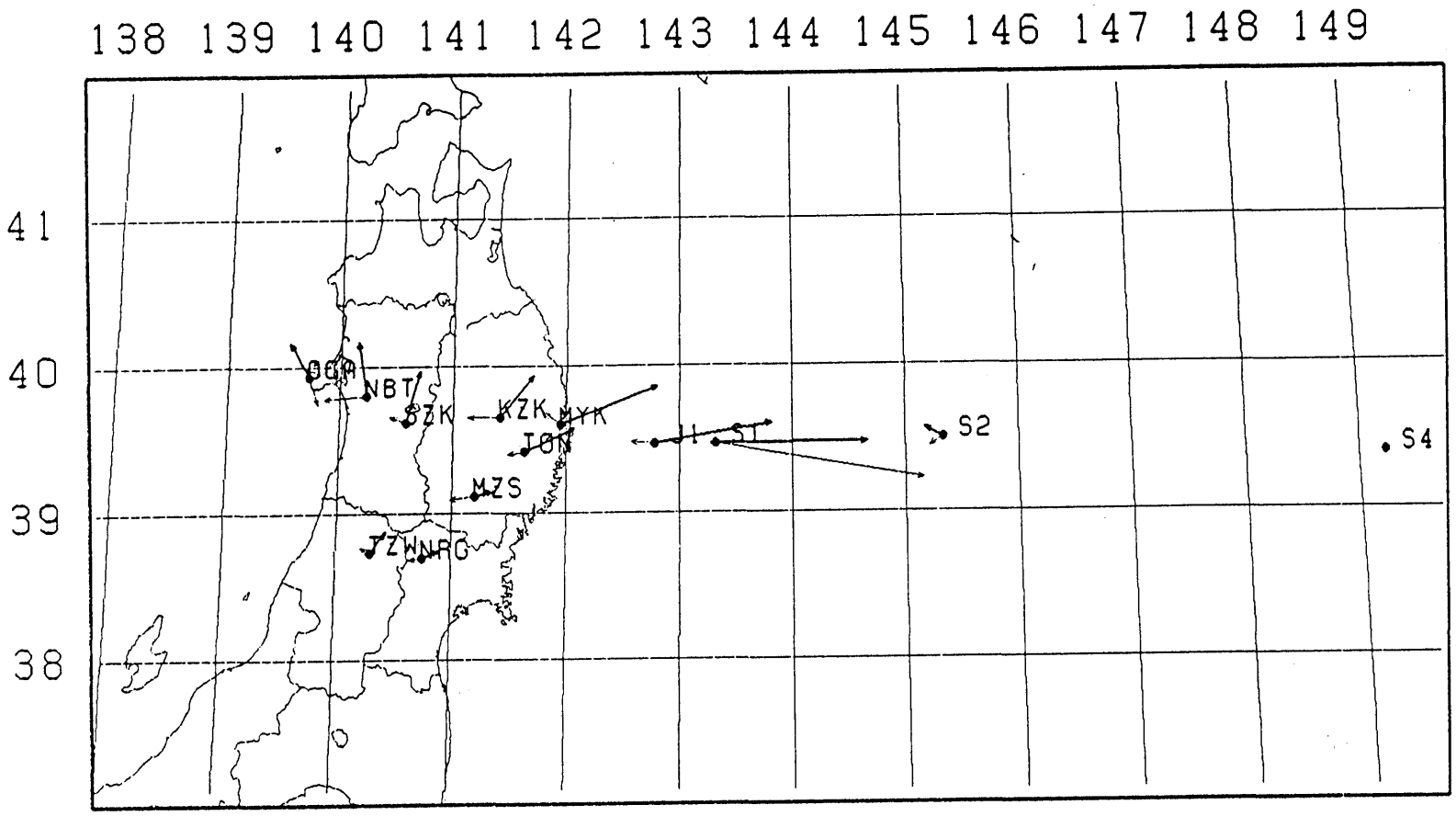

Fig.6.2(a) Distribution of the induction vectors at observation sites in northeast Japan and in the Pacific Ocean for the period 15 minutes.

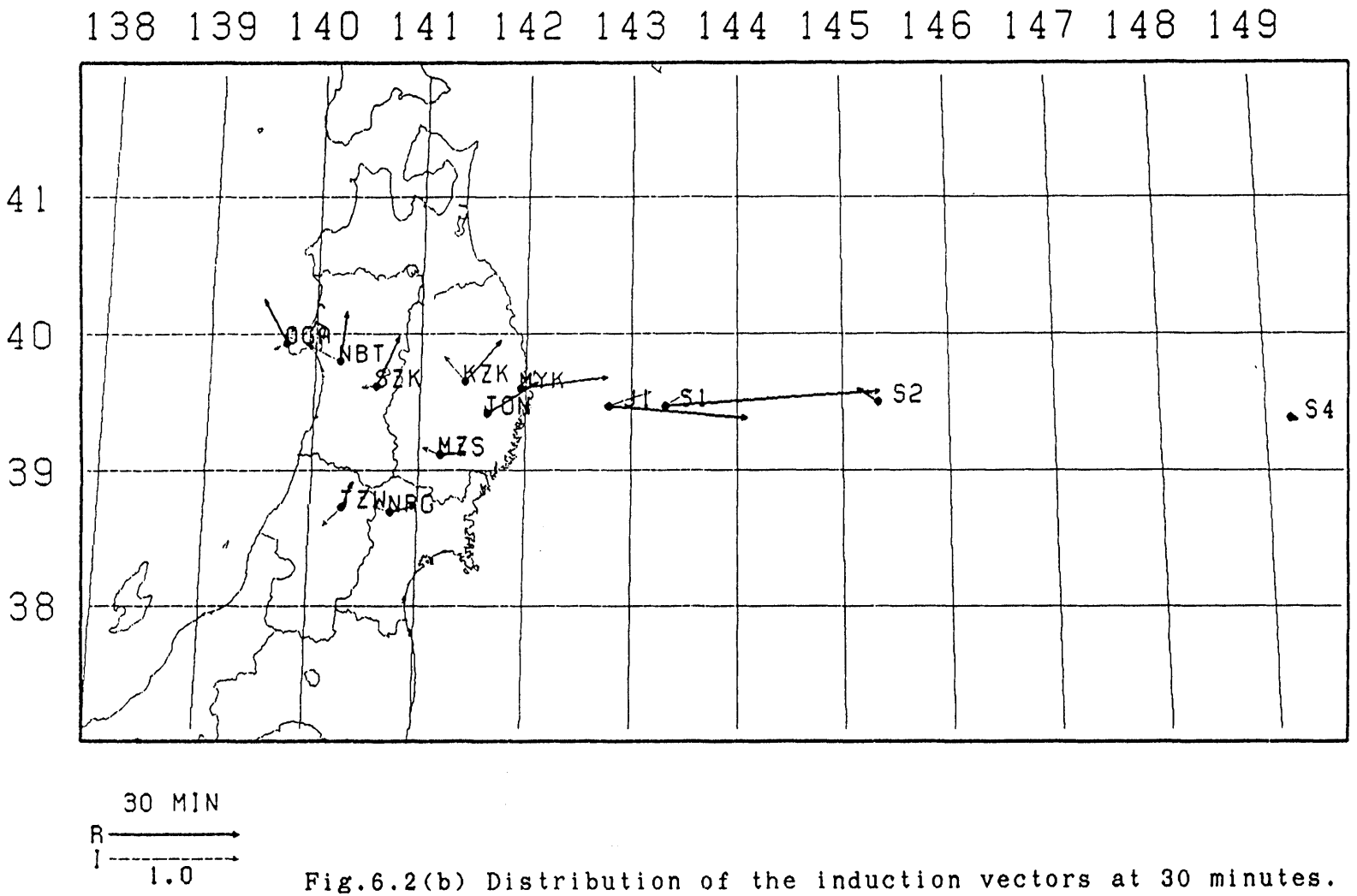

Fig.6.2(b) Distribution of the induction vectors at 30 minutes.

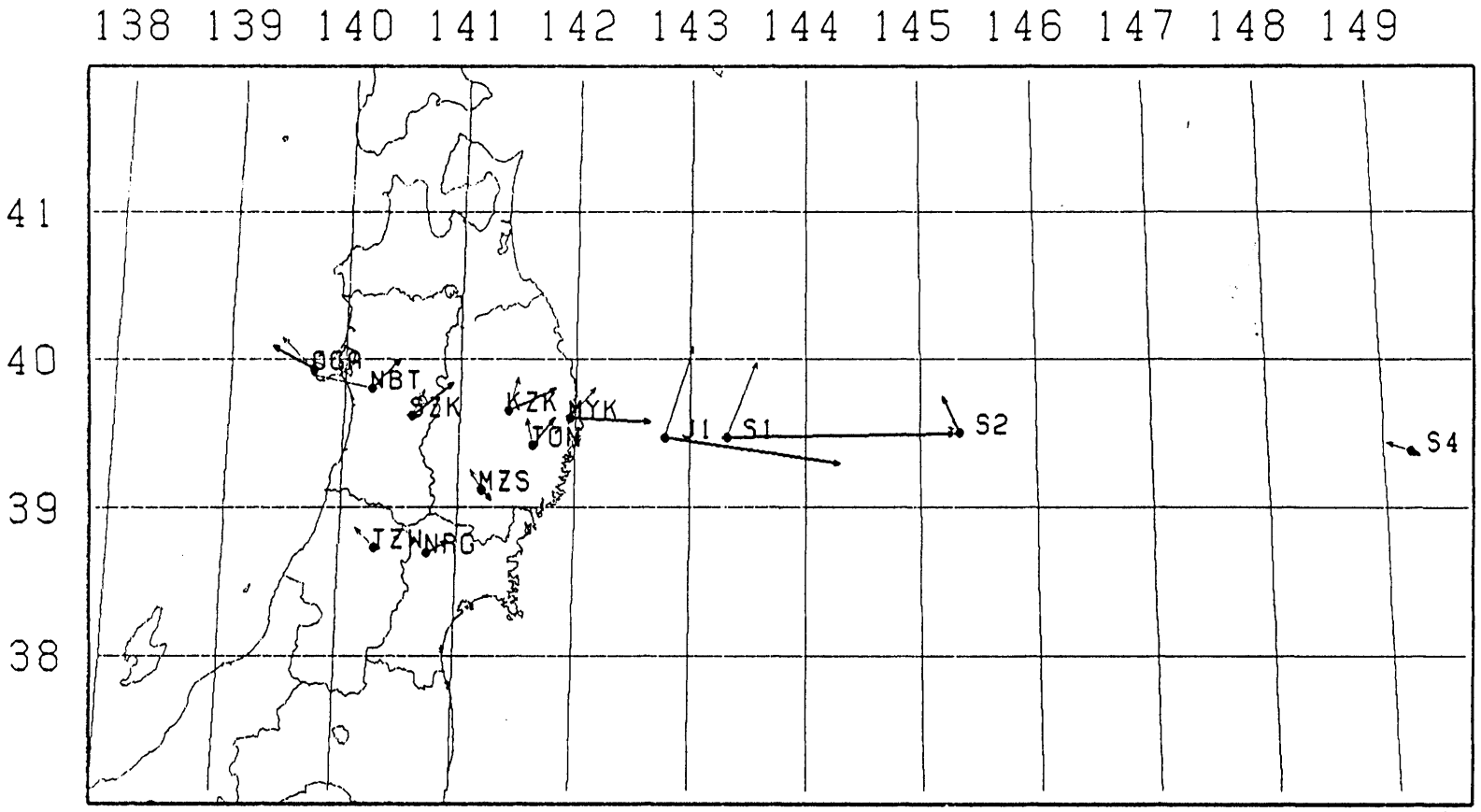

Fig.6.2(c) Distribution of the induction vectors at 60 minutes.

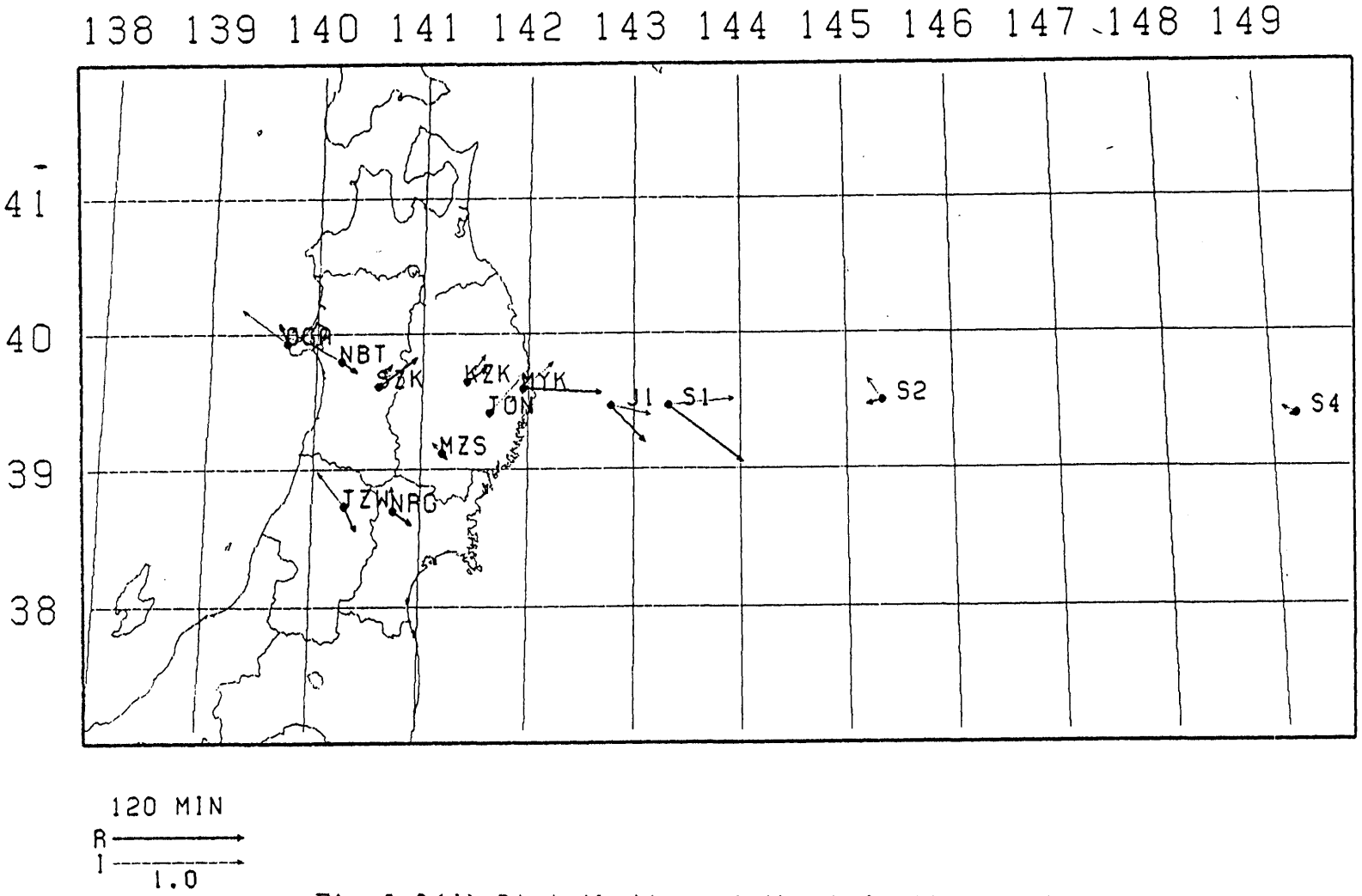

Fig.6.2(d) Distribution of the induction vectors at 120 minutes.

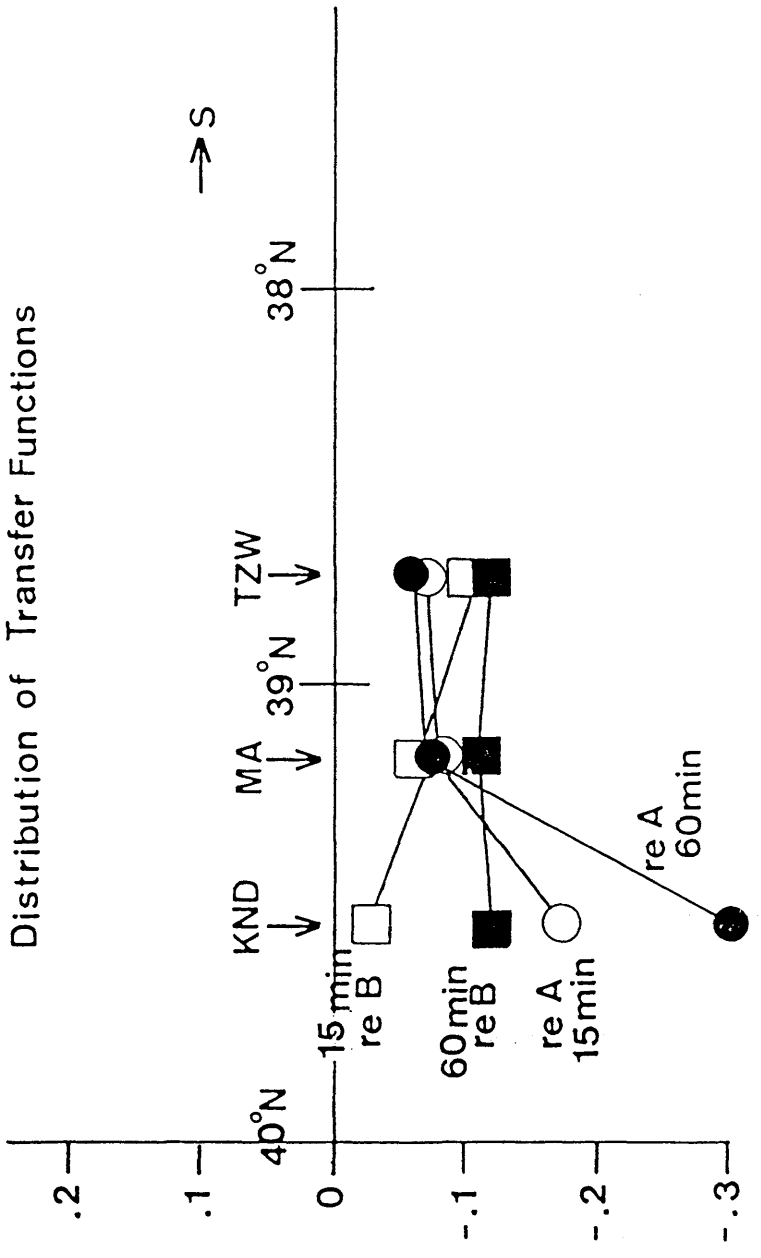

Fig.6.3 North-south cross section of the real parts of the transfer function A (circles) and B (squares) in northeast Japan (Ogawa, et al., 1986).

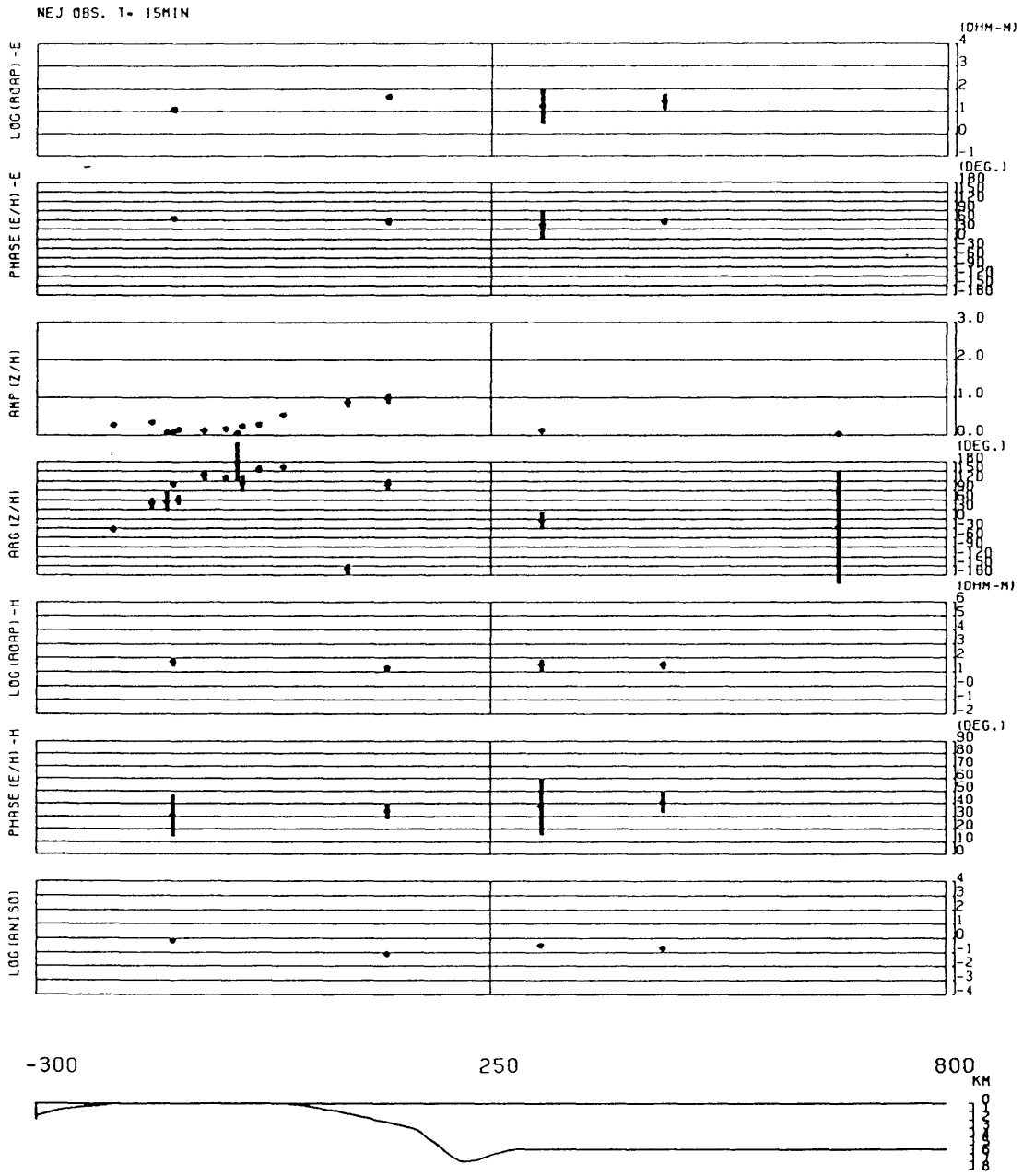

Fig.6.4(a) East-west profile of the response functions for 15 minutes. The E-polarization apparent resistivity and phase, the transfer function B and its phase, H-polarization apparent resistivity and Phase, and ratio E- to H-polarization apparent resistivity (denoted as ANISO) are illustrated from top to bottom. Error bar denotes the 67% confidence interval.

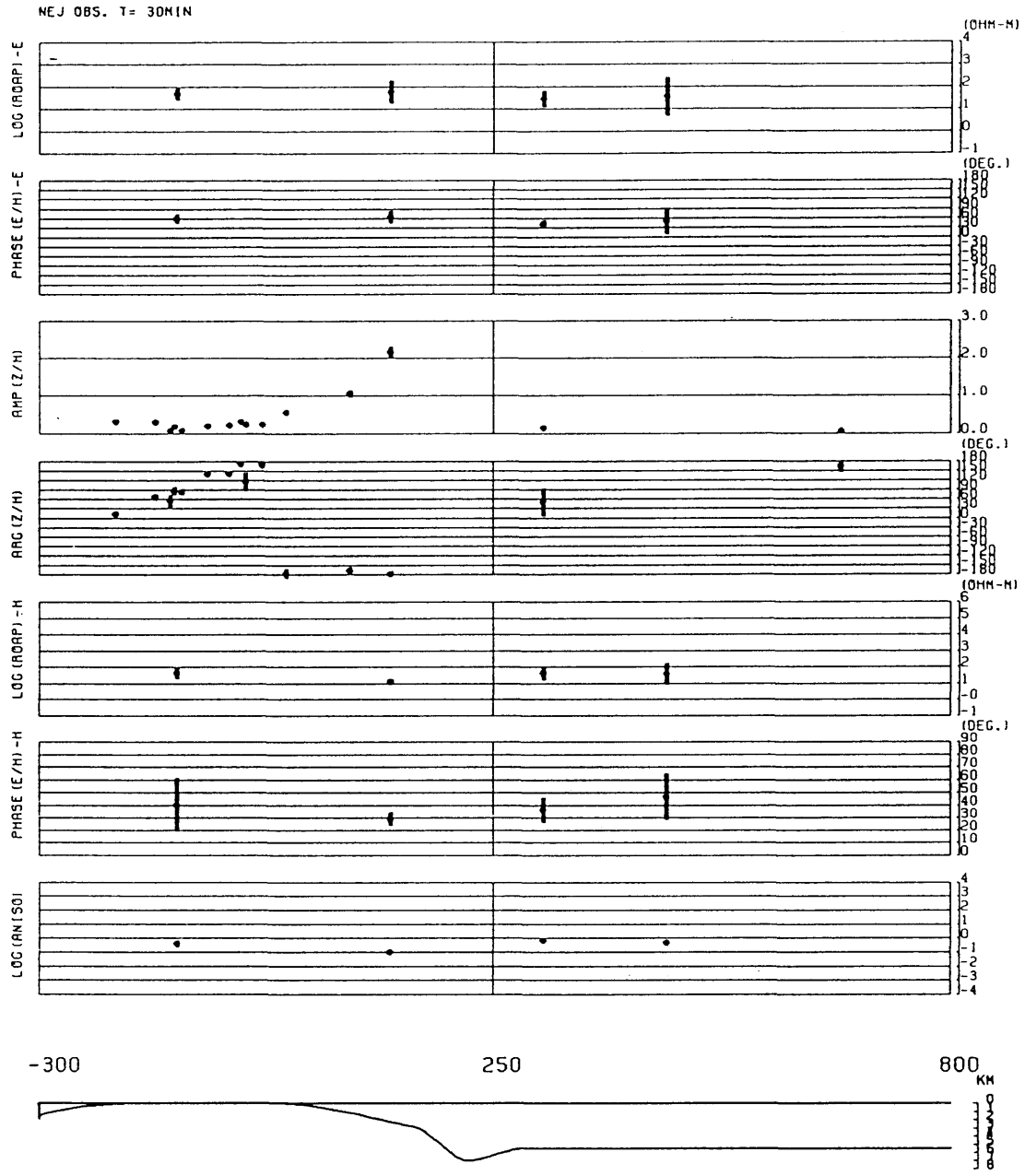

Fig.6.4(b) East-west profile of the response functions for 30 minutes.

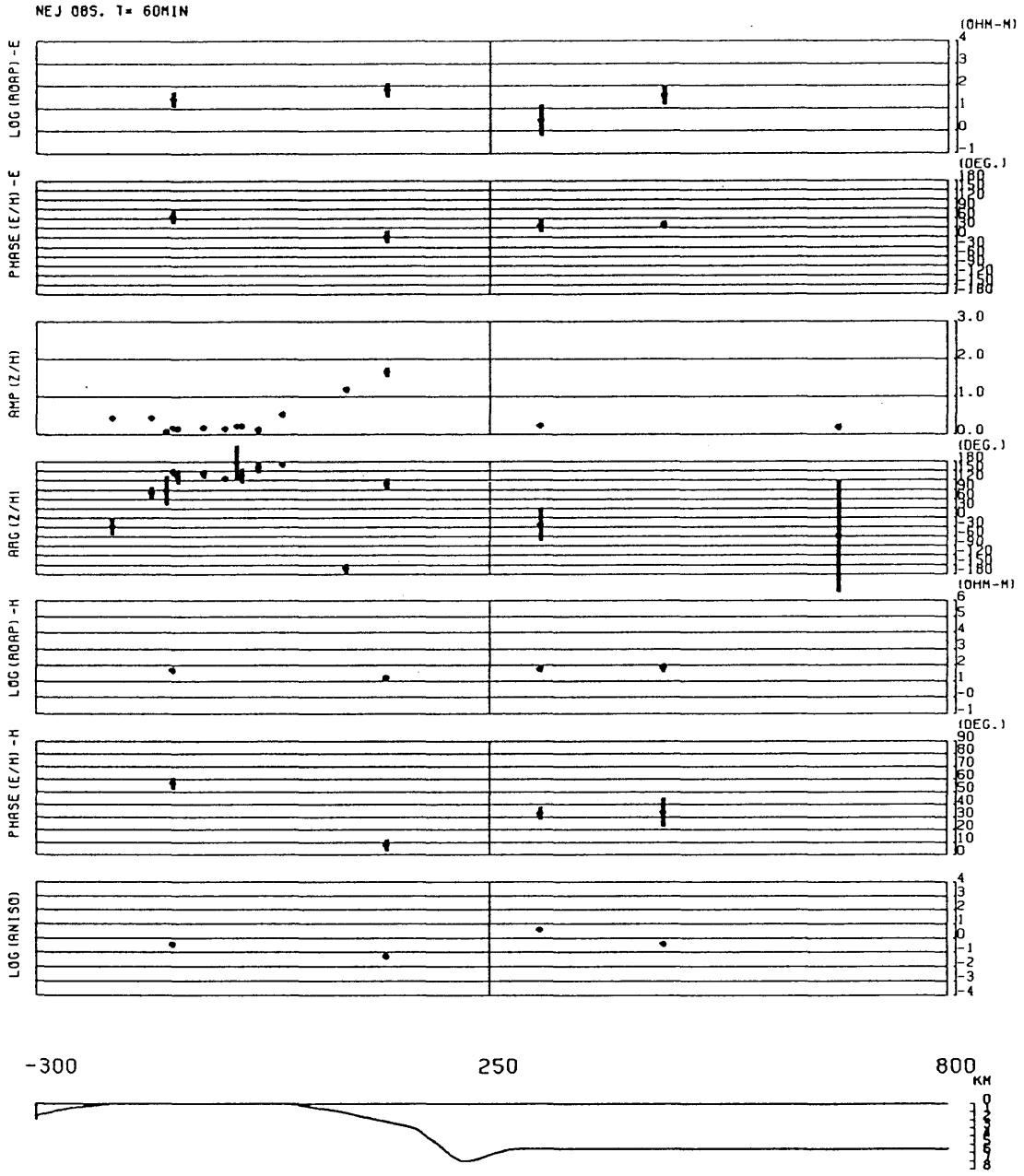

Fig.6.4(c) East-west profile of the response functions for 60 minutes.

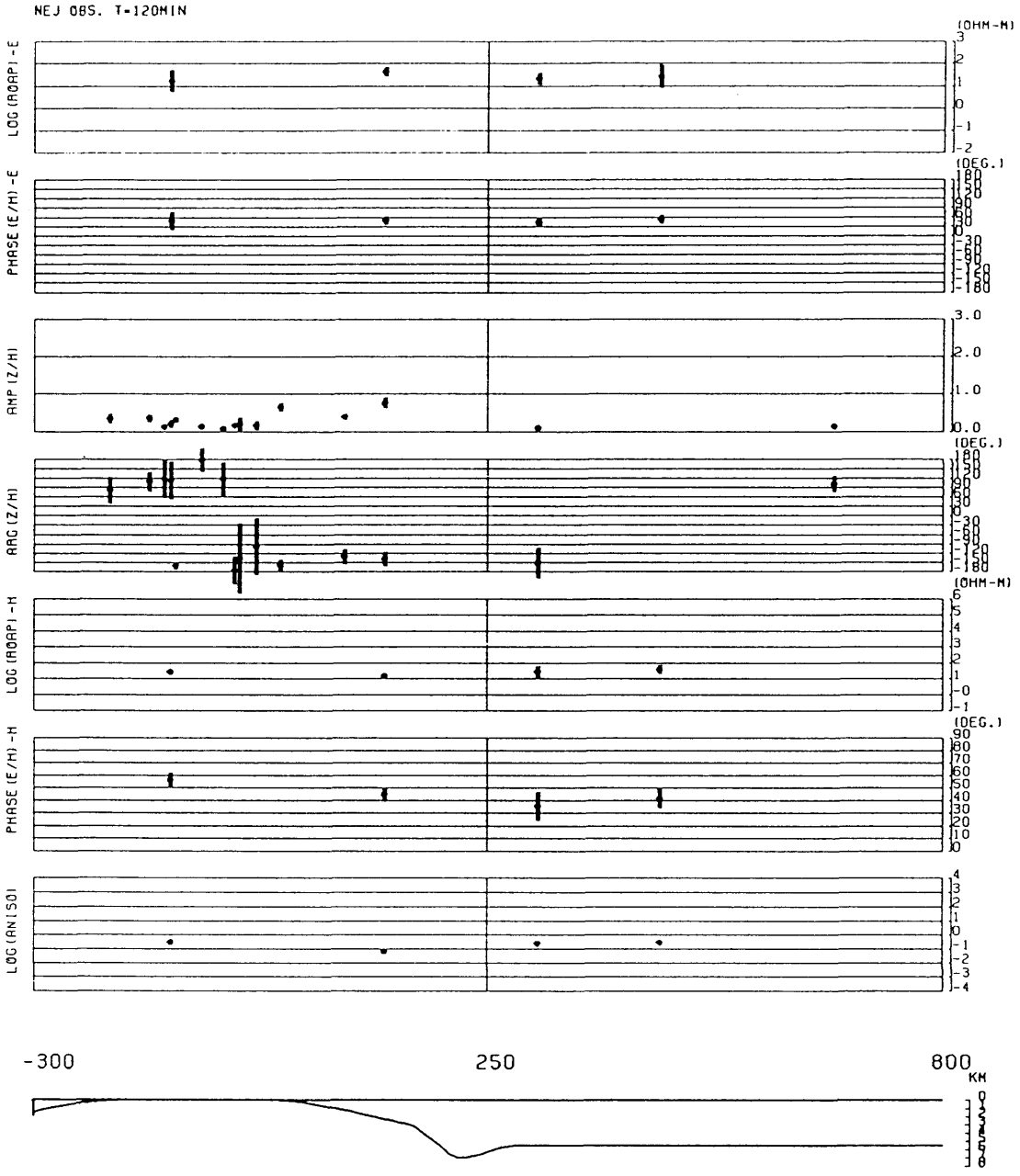

Fig.6.4(d) East-west profile of the response functions for 120 minutes.

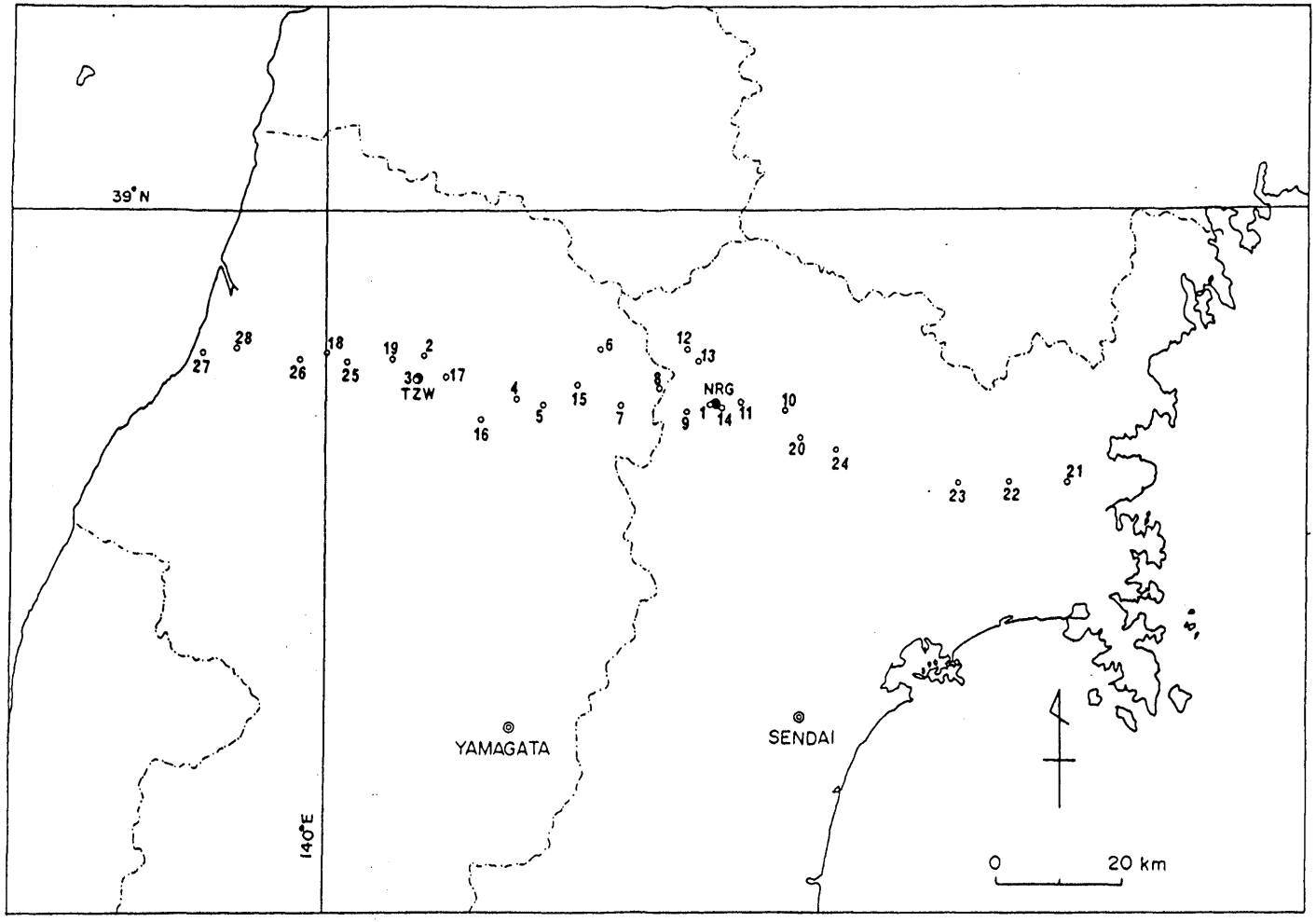

Fig.6.5 Distribution of observation sites for ELF·VLF magnetotelluric survey (open circles) across northeast Japan. Closed circles denote the temporal station for electromagnetic field measurement at ULF range, TZW and NRG.

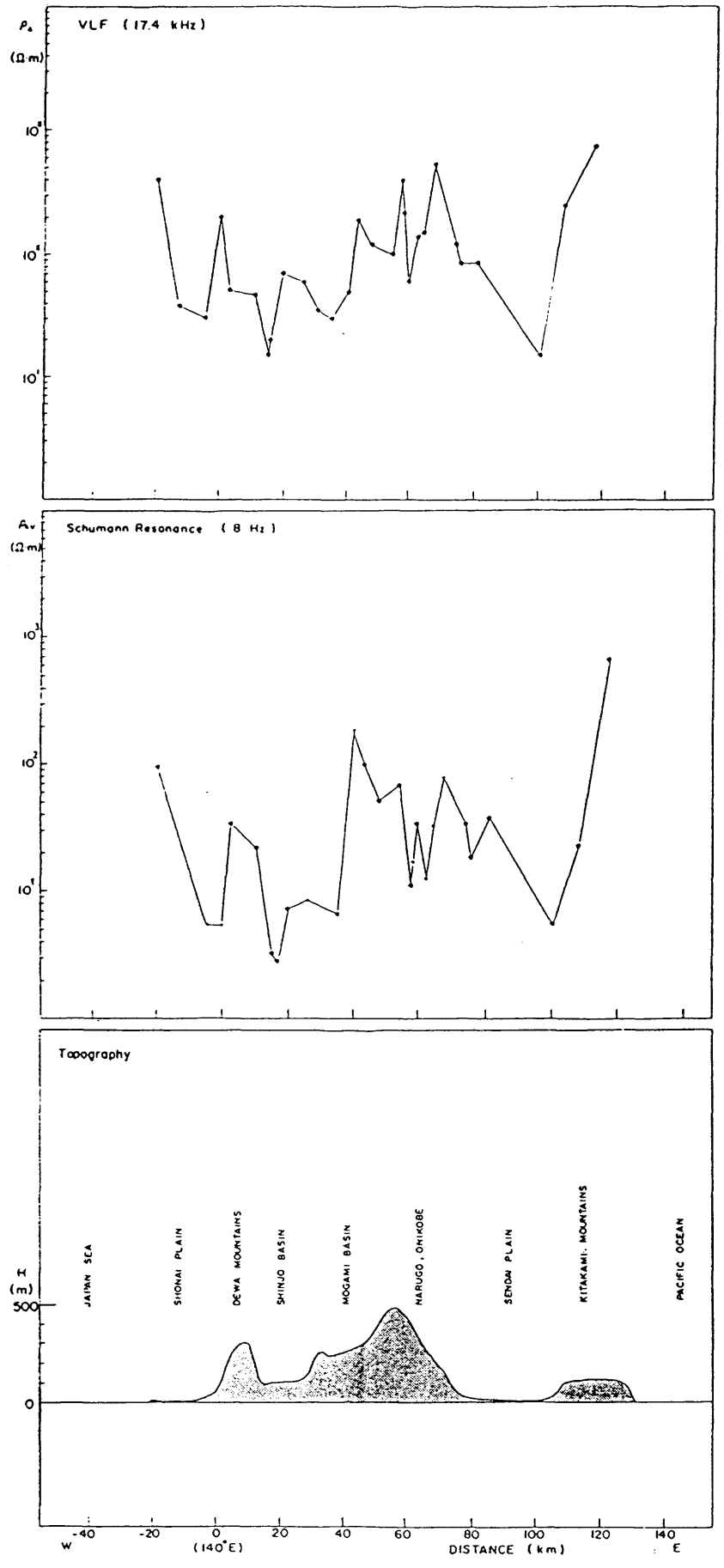

Fig.6.6 East-west profiles of apparent resistivity at 17.4kHz(top) and 8 Hz(middle). Cross section of surface topography is given at the bottom.

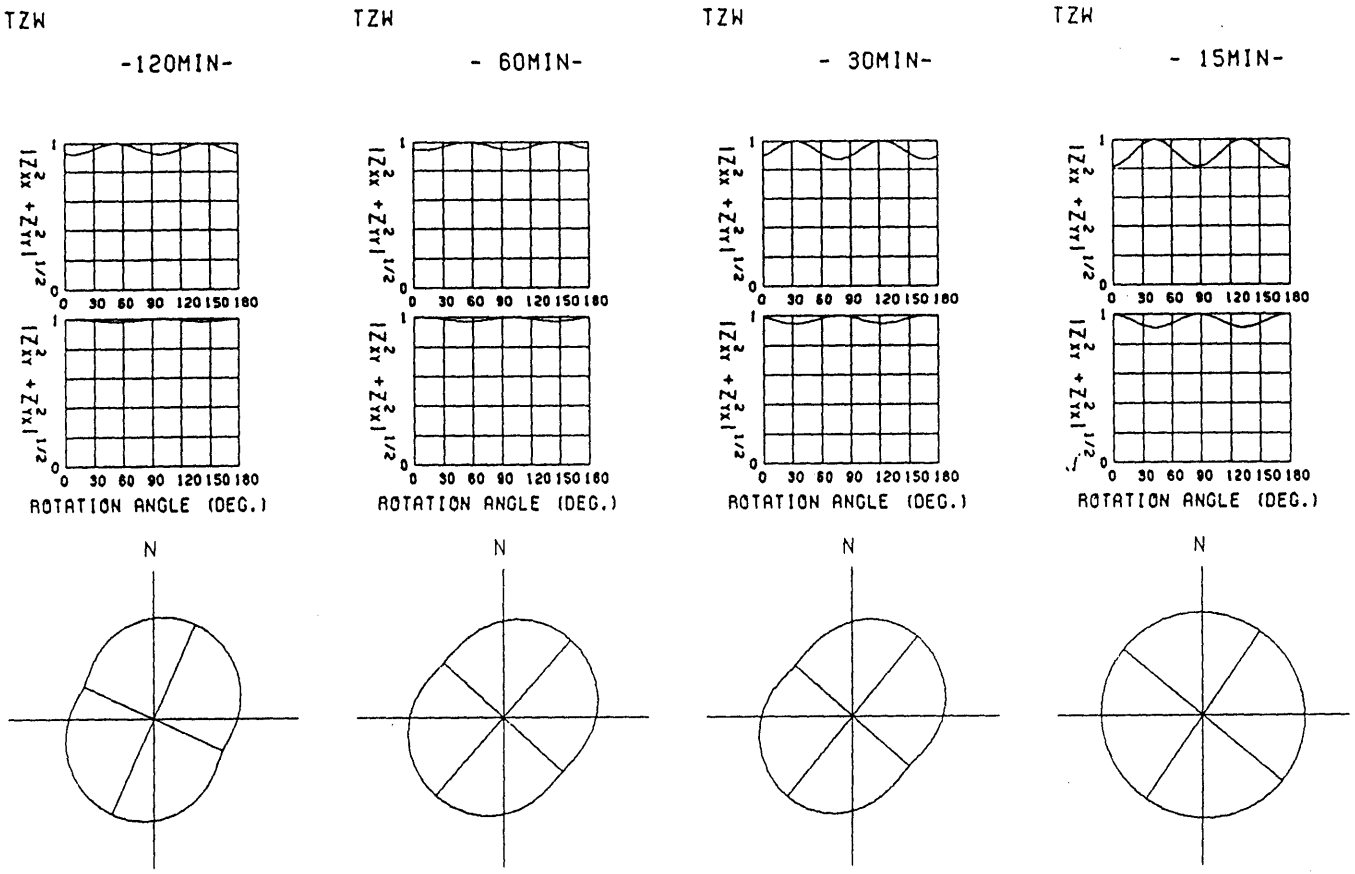

Fig.6.7(a) Polarization diagrams obtained from impedance tensor at TZW for the periods of 15, 30, 60 and 120 minutes.

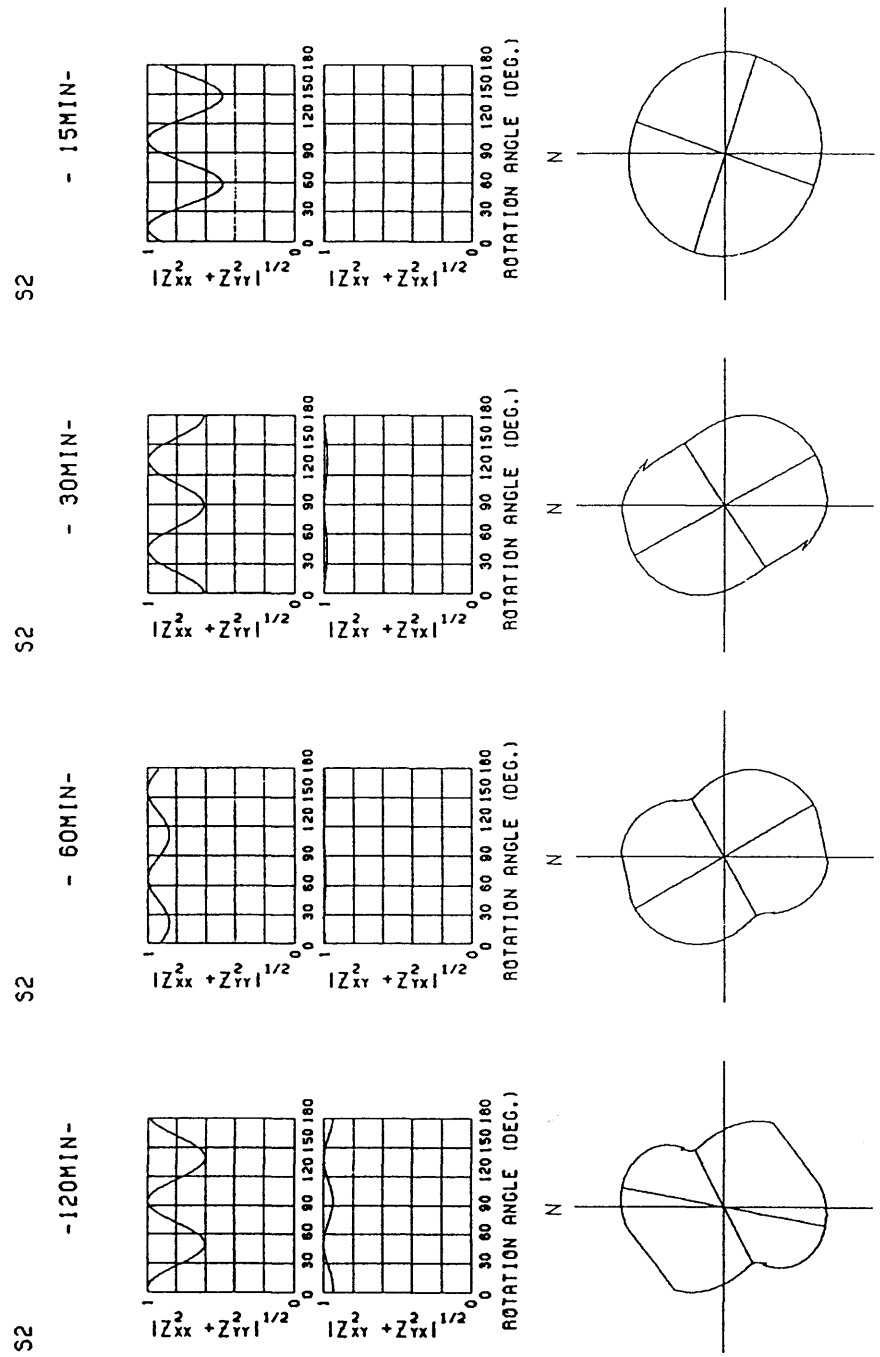

Fig.6.7(c) Polarization diagrams at S2 for the periods of 15, 30, 60 and 120 minutes.

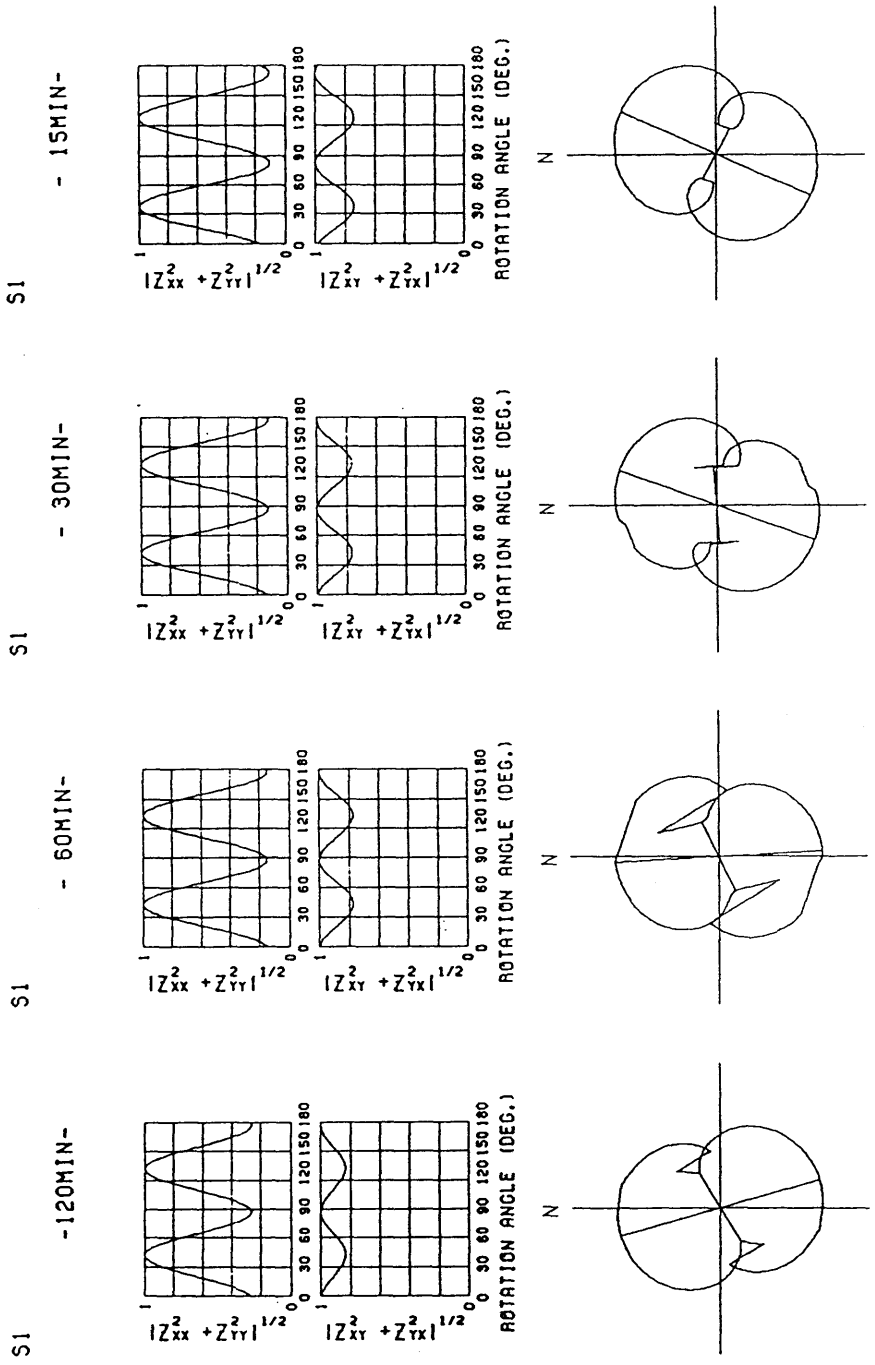

Fig.6.7(b) Polarization diagrams at S1 for the periods of 15, 30, 60 and 120 minutes.

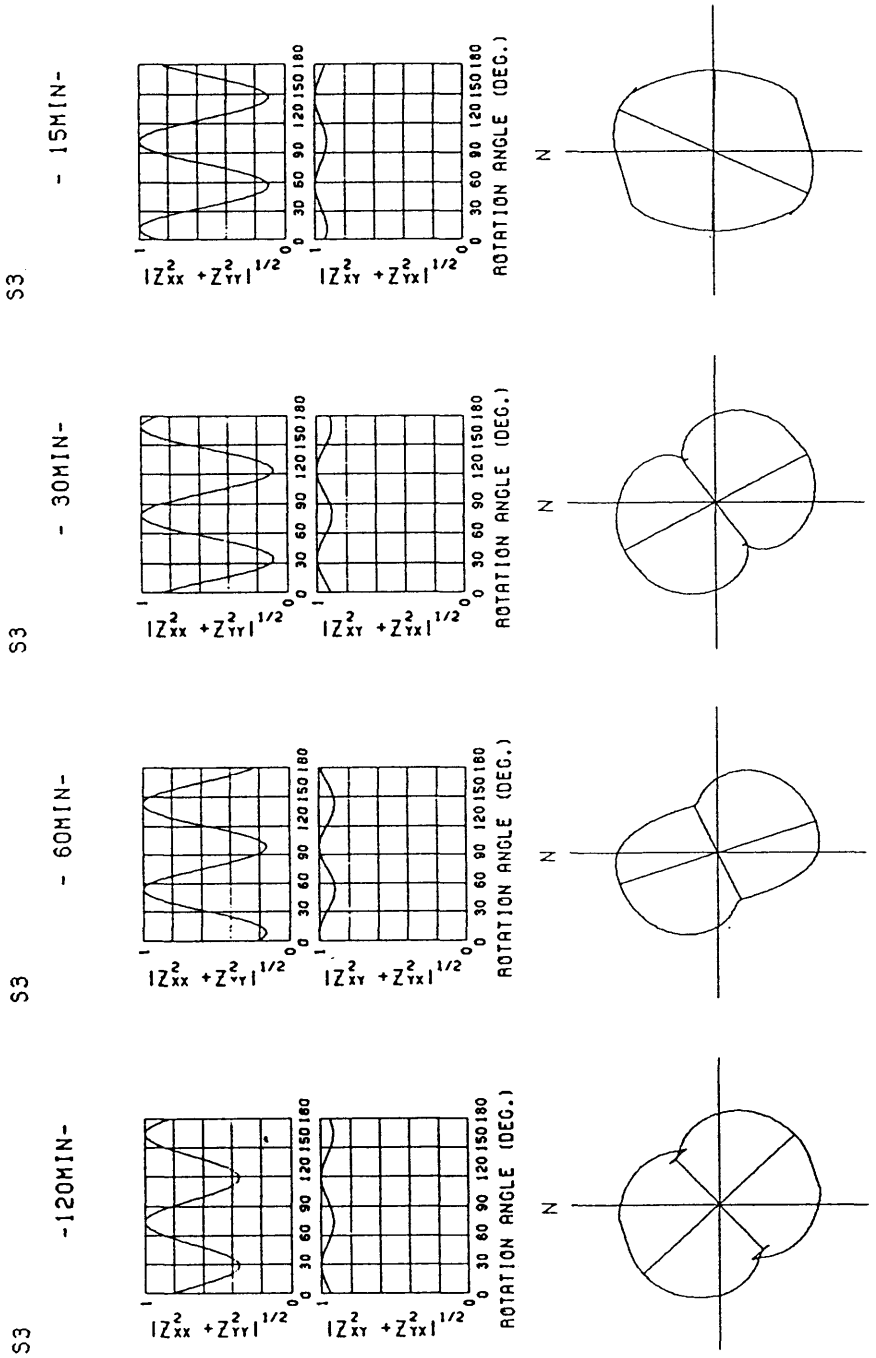

Fig.6.7(d) Polarization diagrams at S3 for the periods of 15, 30, 60 and 120 minutes.

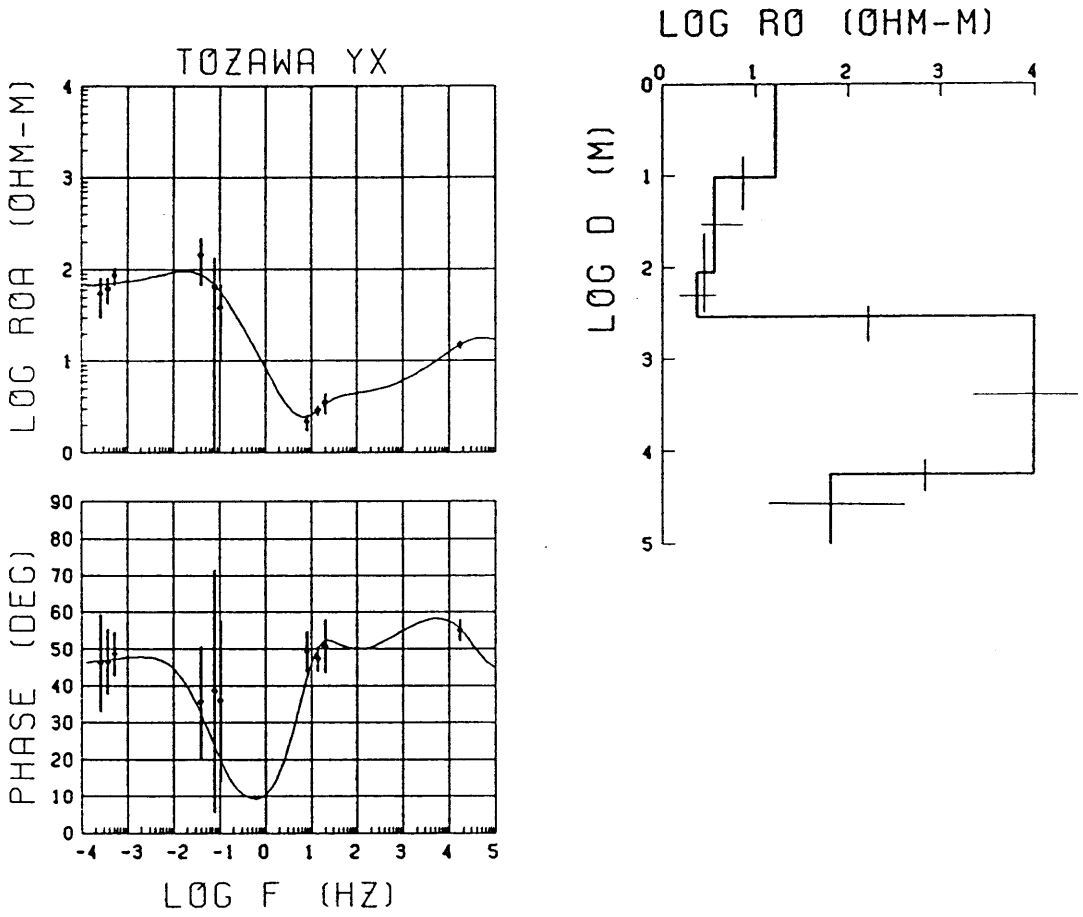

Fig.6.8 Result of one-dimensional inversion of impedance Zyx at Tozawa (TZW). Final 5 layer model (right) and the theoretical response from it (left).

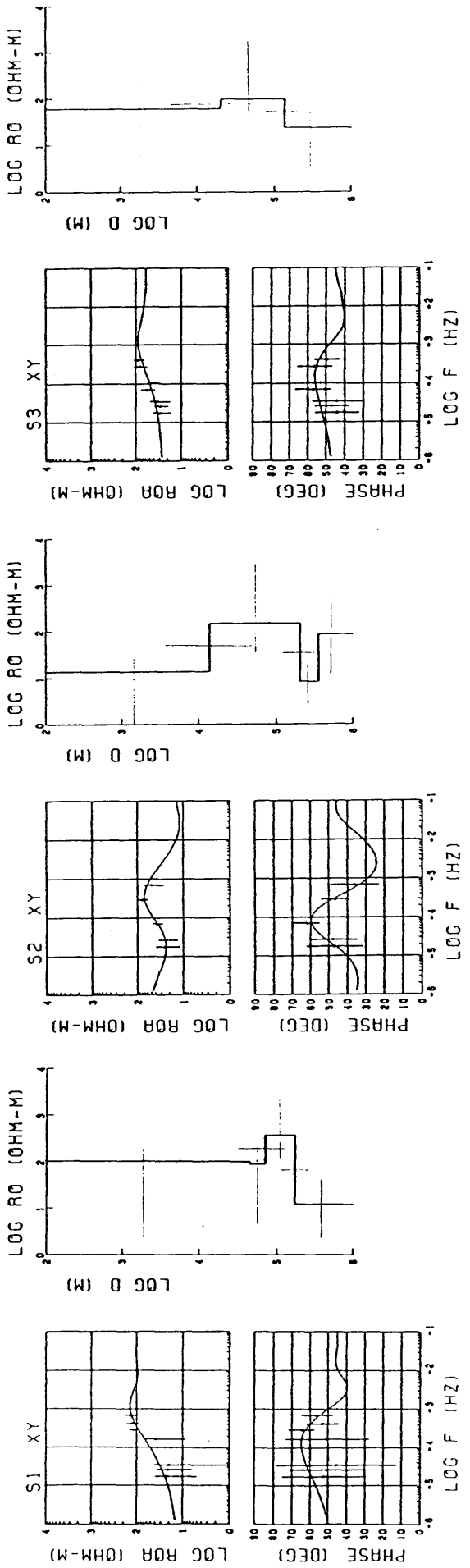

Fig.6.9 Optimum one-dimensional models at S1, S2 and S3, inferred by the impedance Zxy.

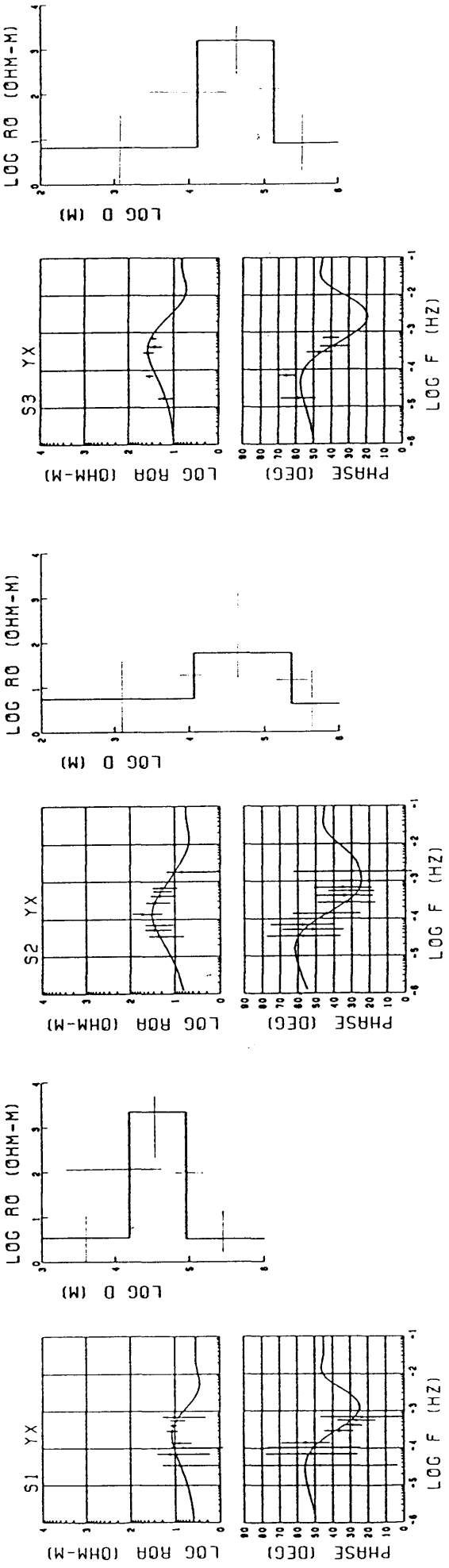

Fig.6.10 Optimum one-dimensional models at S1, S2 and S3, inferred by the impedance Zyx.

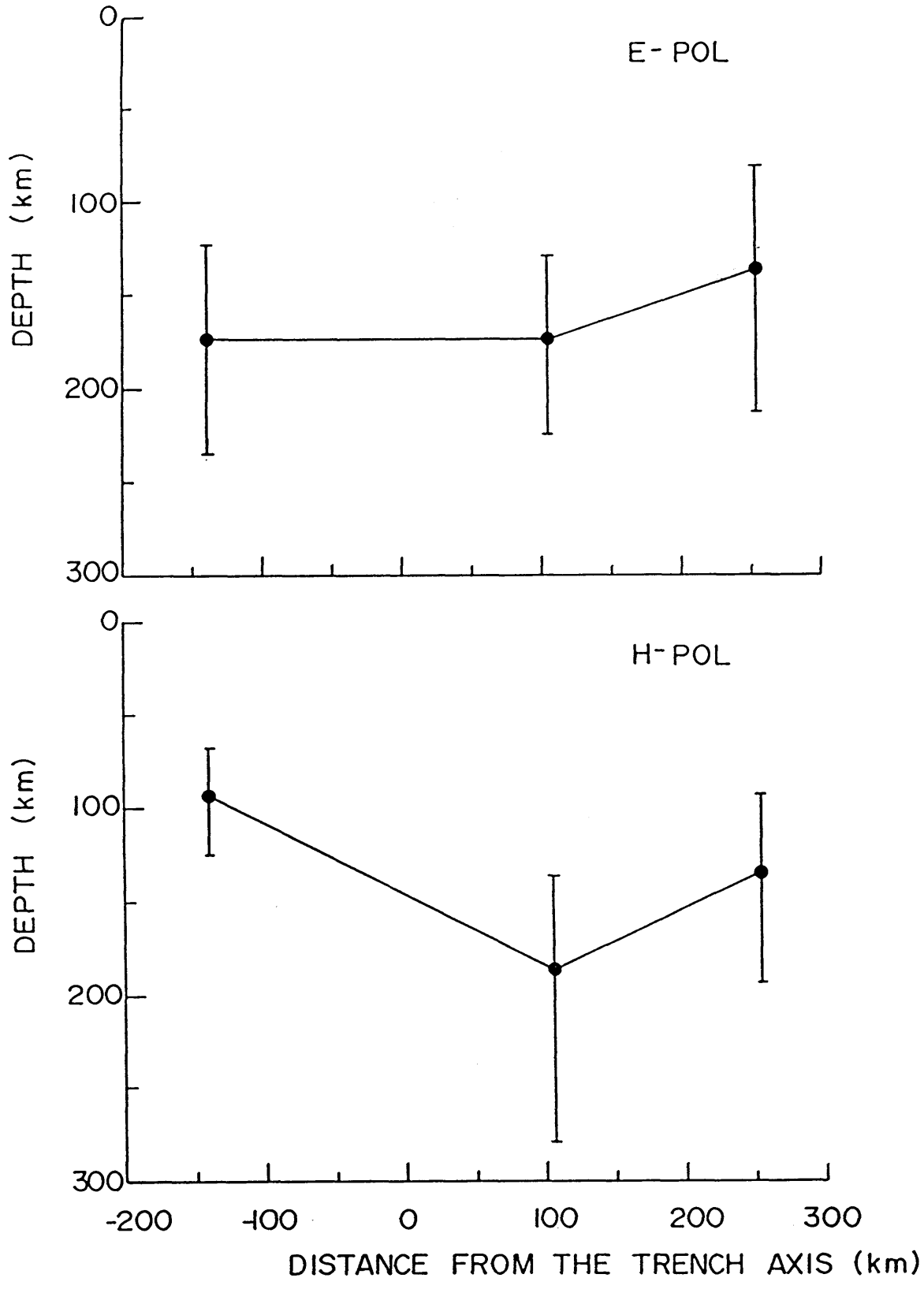

Fig.6.11 The depth to the conductive layer beneath the seafloor sites S1, S2 and S3 for E-polarization (above) and H-polarization (below).

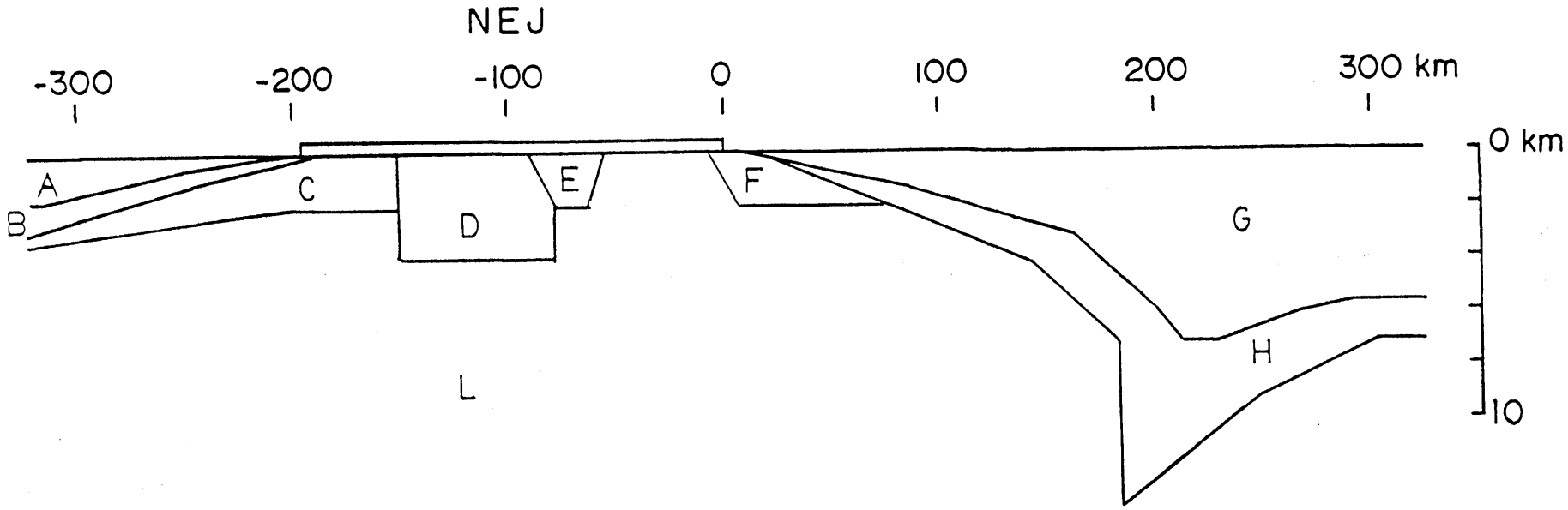

Fig.6.12 Near-surface view of the block division for modeling of Northeast Japan Arc. Blocks with given conductivities are assigned by A-L.

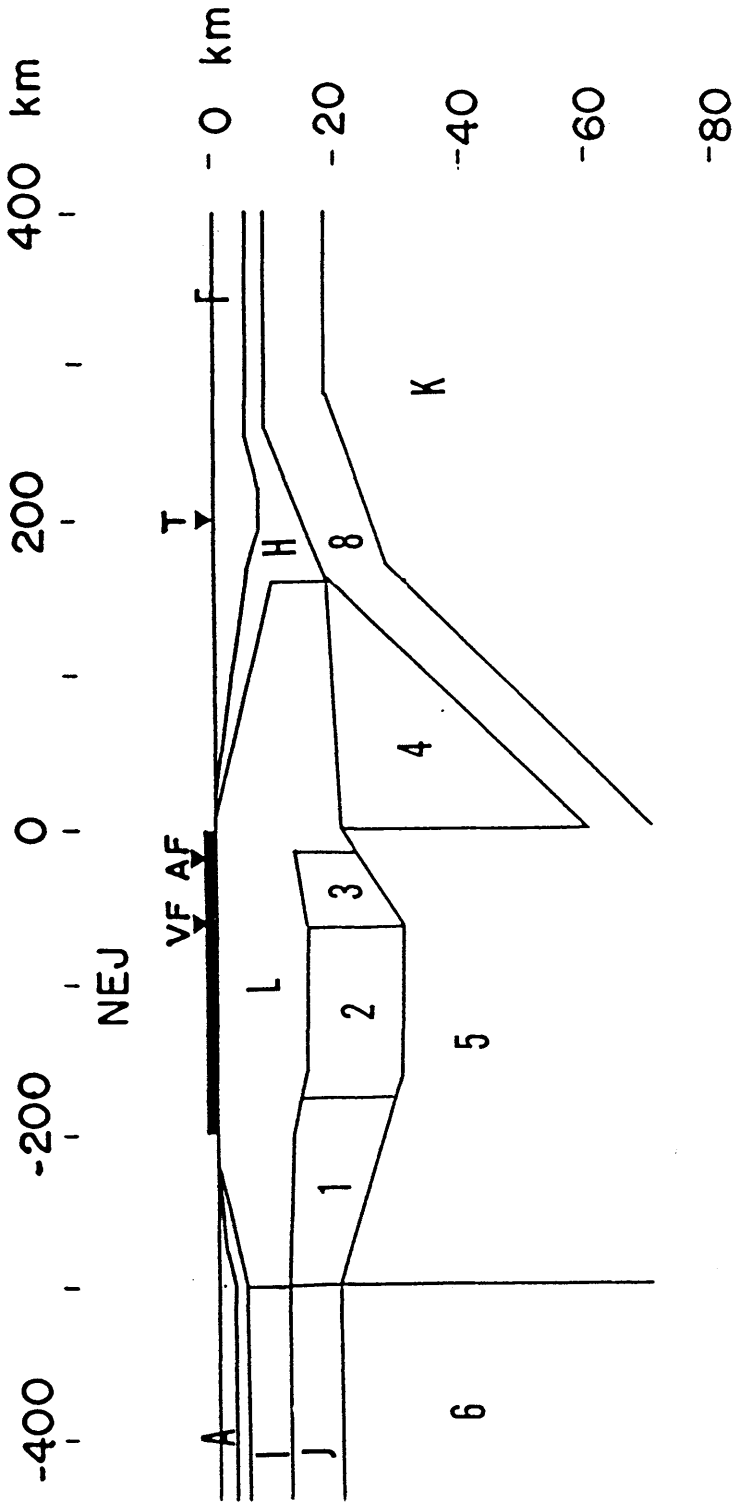

Fig.6.13 Intermediate depth view of the block division.

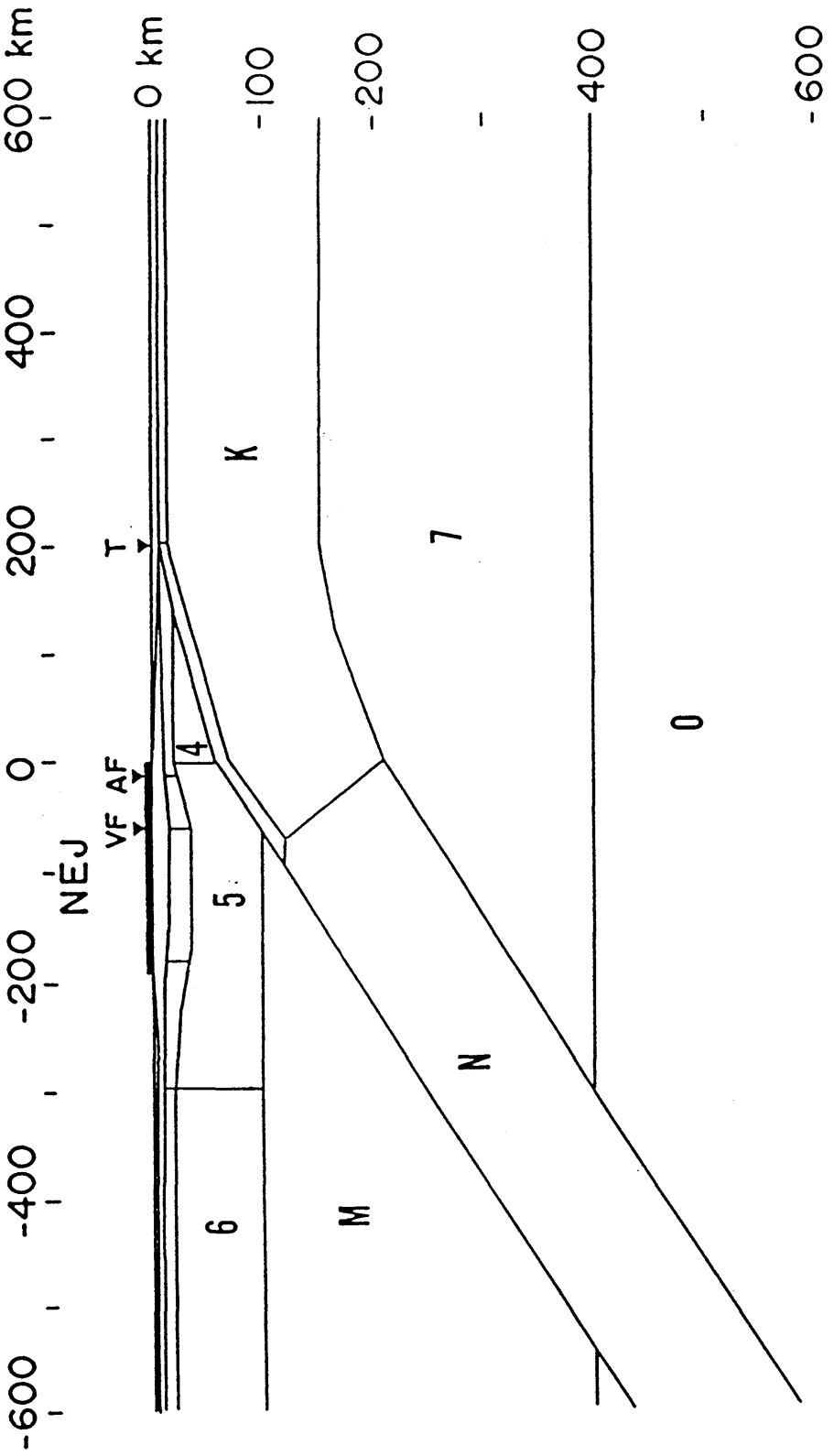

Fig.6.14 Deepest view of block division.

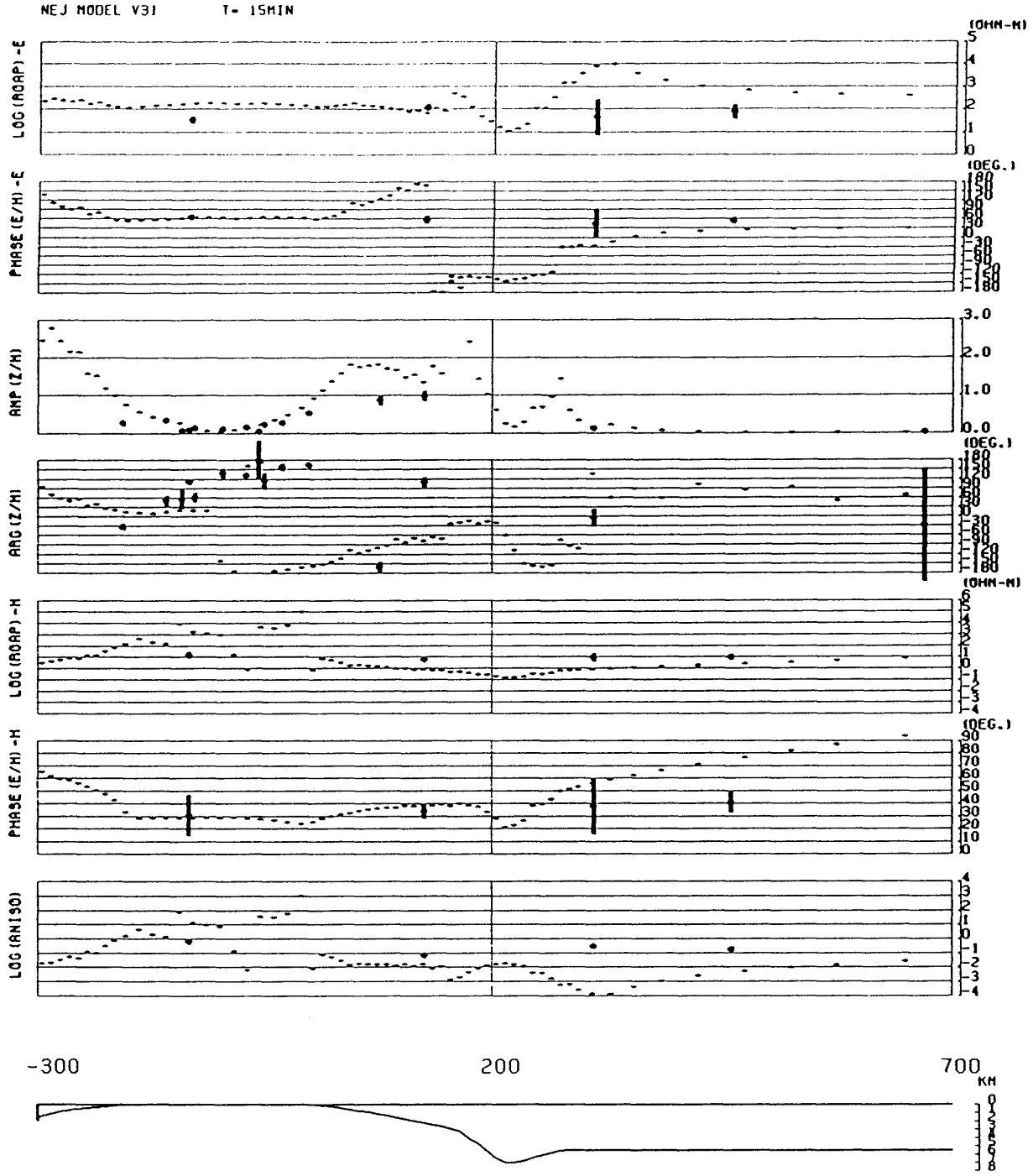

Fig.6.15 Comparison of the observed responses (Dots with error bars) and calculated ones (dotted lines) from the starting model for the period of 15 minutes.

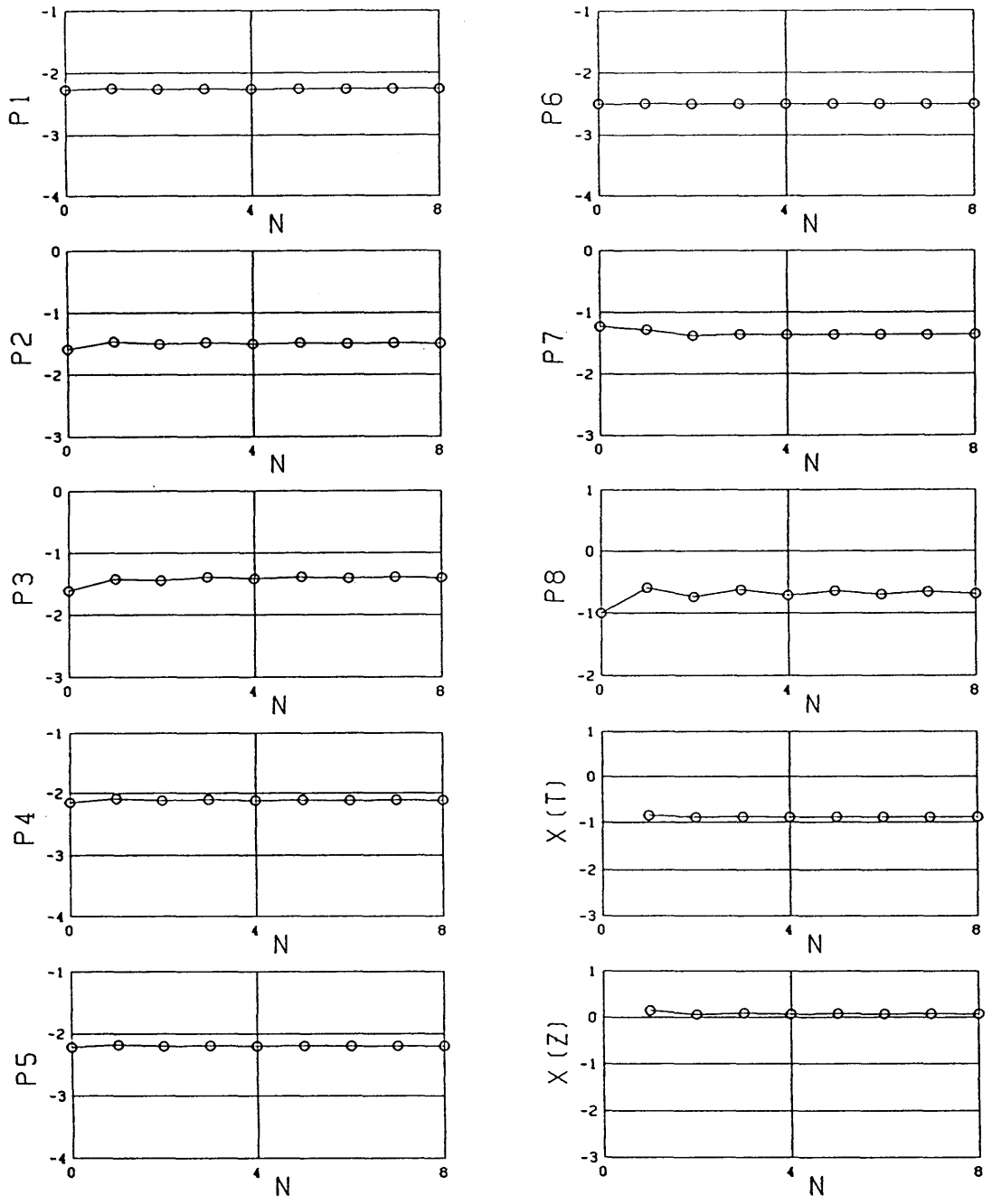

Fig.6.16 Behavior of parameters (log of conductivity), p_1-p_8, and χ^2 of the transfer functions (denoted by T) and of the impedances (denoted by Z) at the last 8 cycles of the iterative process.

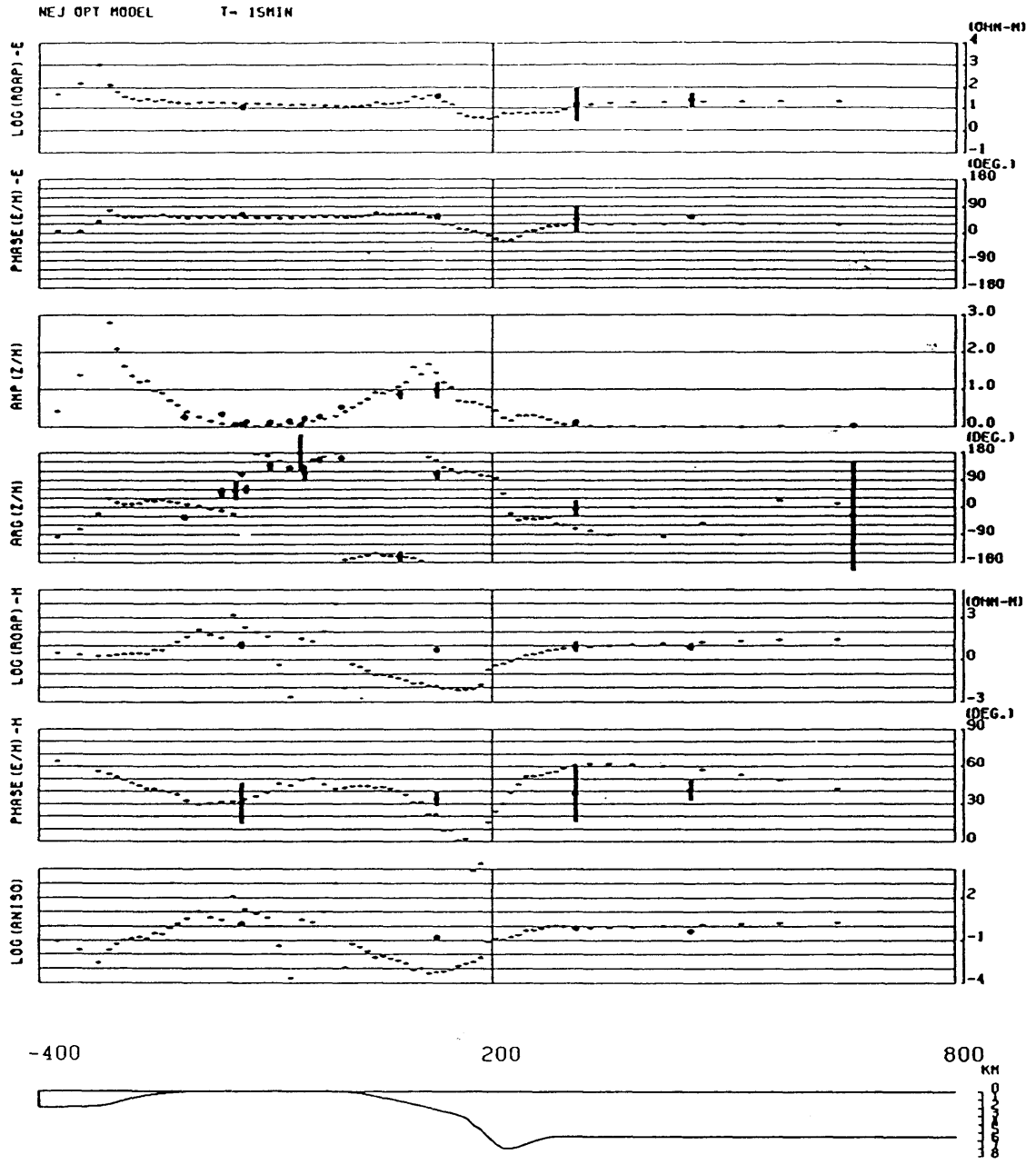

Fig.6.17(a) Comparison of the observed responses (Dots with error bars) and calculated ones (dotted lines) from the final model for the period of 15 minutes.

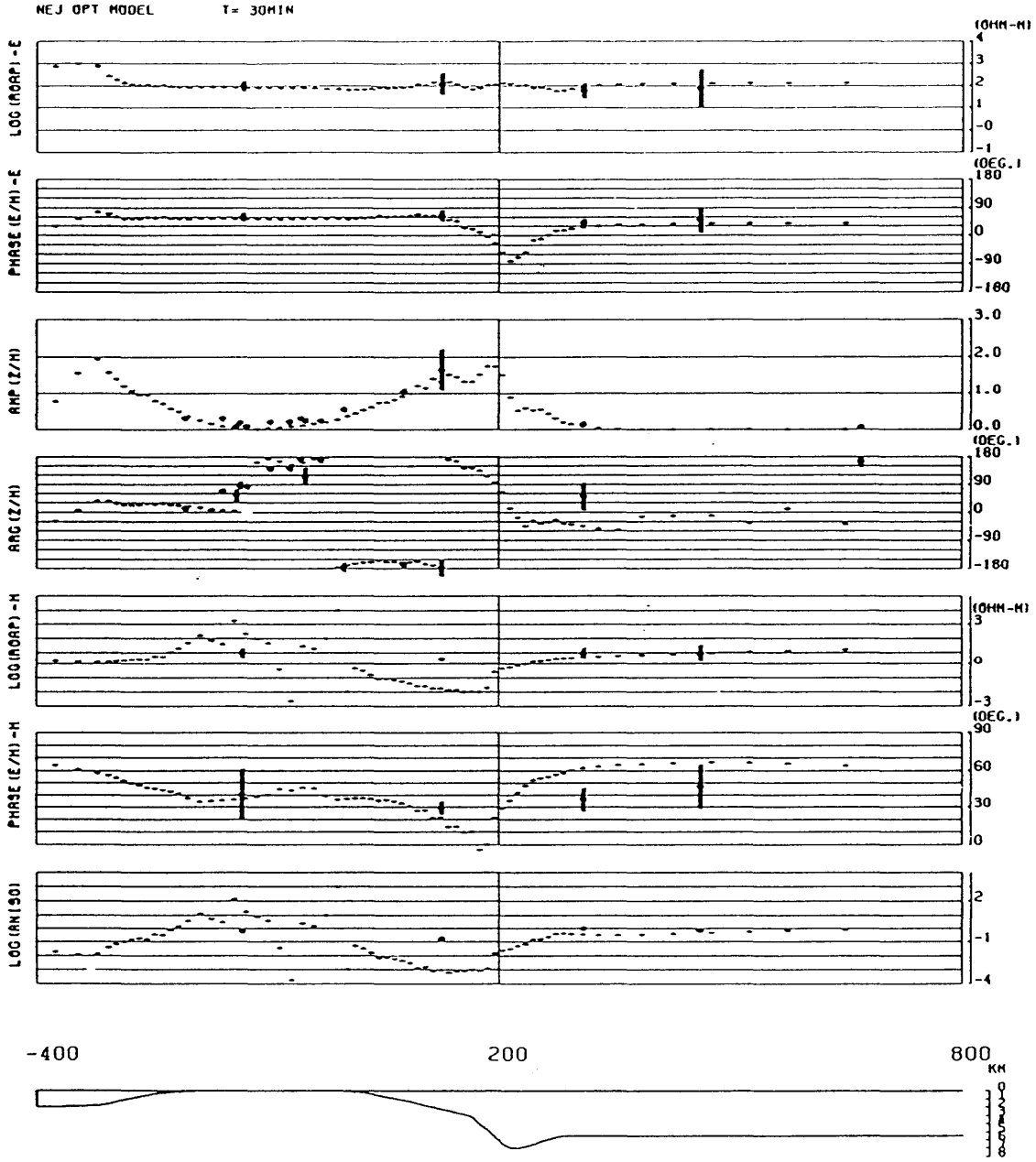

Fig.6.17(b) Comparison of the observed responses and calculated ones from the final model for the period of 30 minutes.

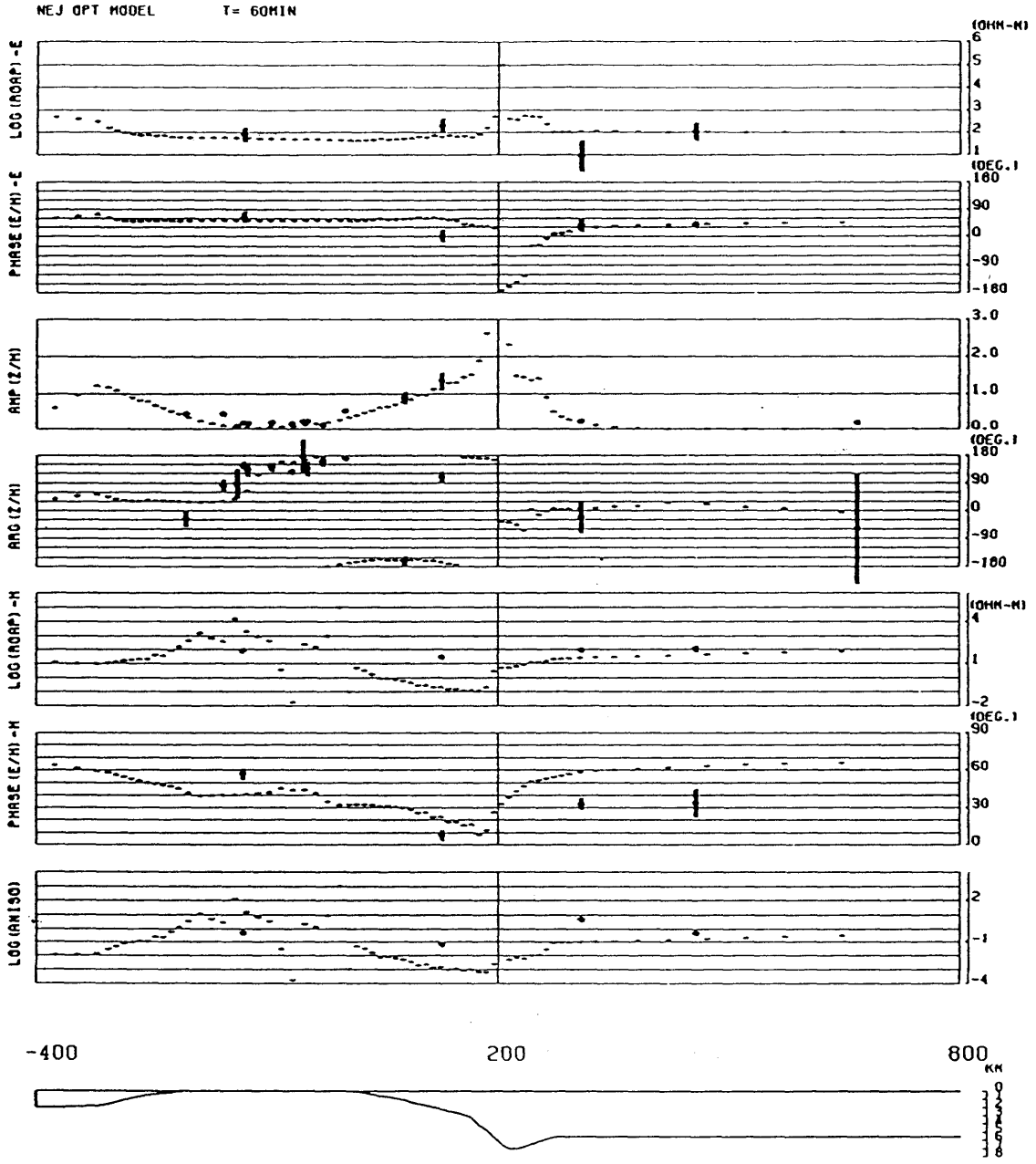

Fig.6.17(c) Comparison of the observed responses and calculated ones from the final model for the period of 60 minutes.

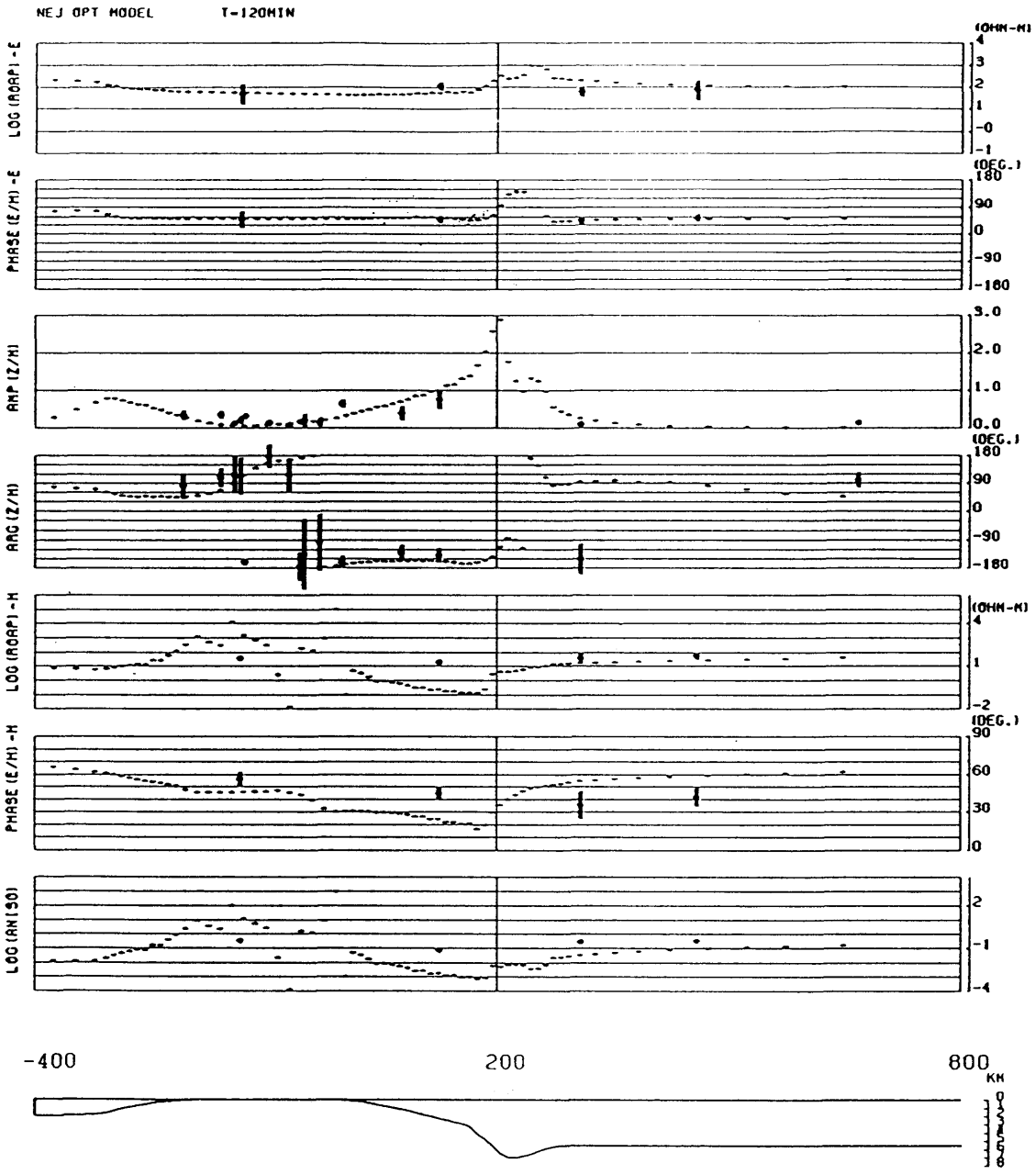

Fig.6.17(d) Comparison of the observed responses and calculated ones from the final model for the period of 120 minutes.

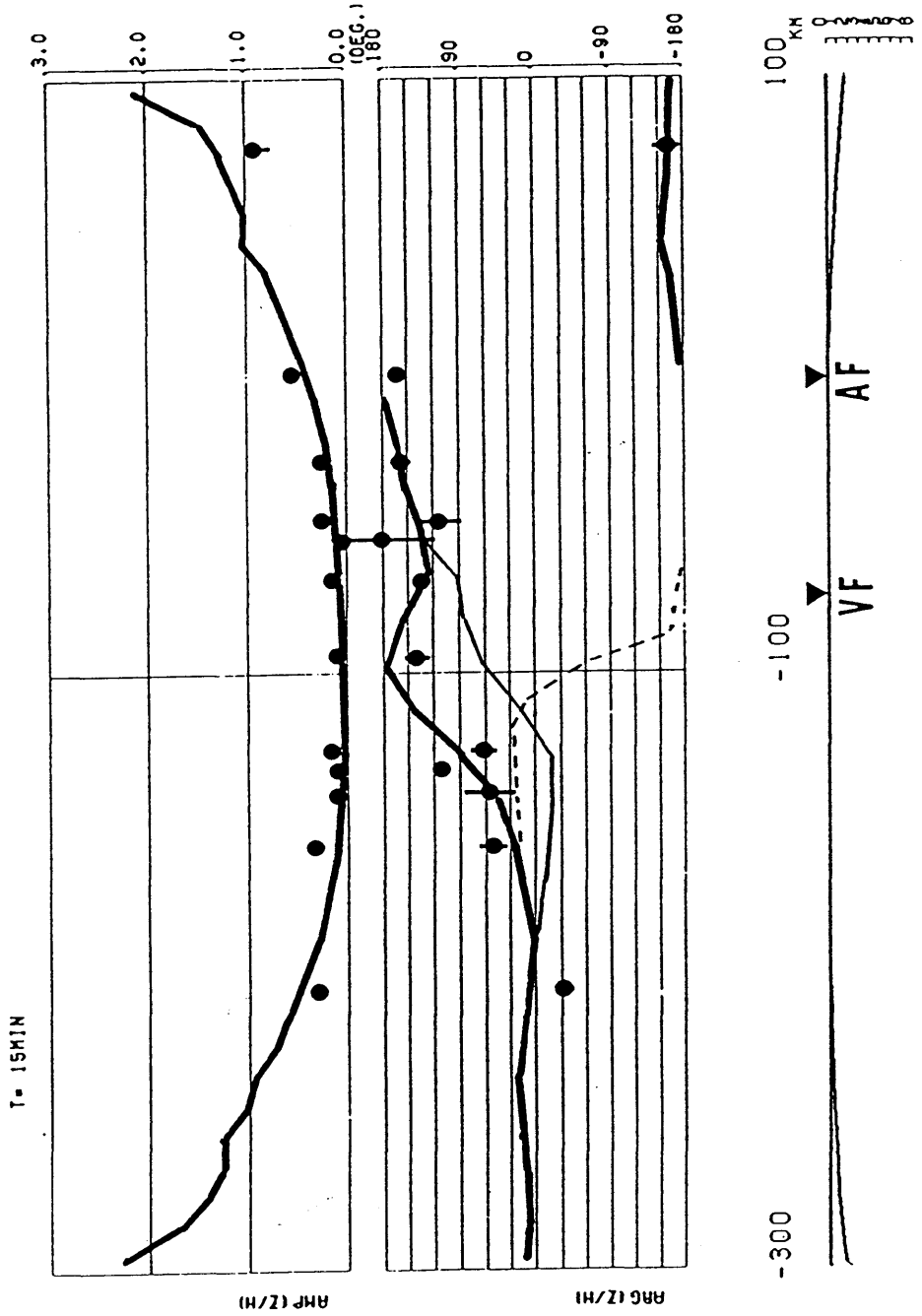

Fig.6.18 Comparison of three models for the period of 15 minutes. Thick line shows a response from the final model with conductive lower crust. Dashed line denotes a response from a model without conductor in the lower crust, while the thin line is a theoretical value from the model by Ogawa et al.(1986) with a conductive lower crust in the western half of northeast Japan.

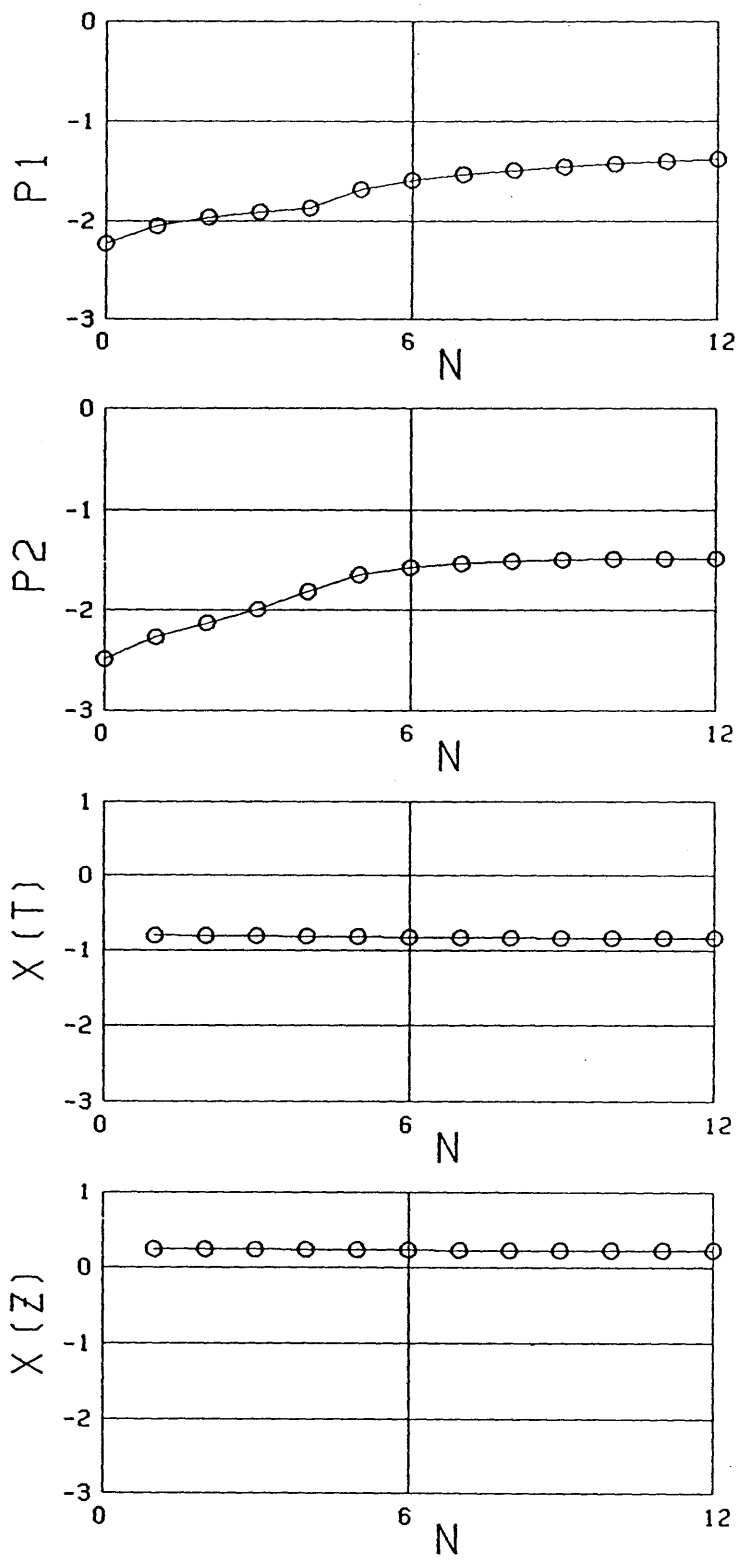

Fig.6.19 Direct inversion against two blocks in lower crust. Initial value of each has been assigned as 1 order of magnitude less than that of the final model. Iteration converged after 12 cycles.

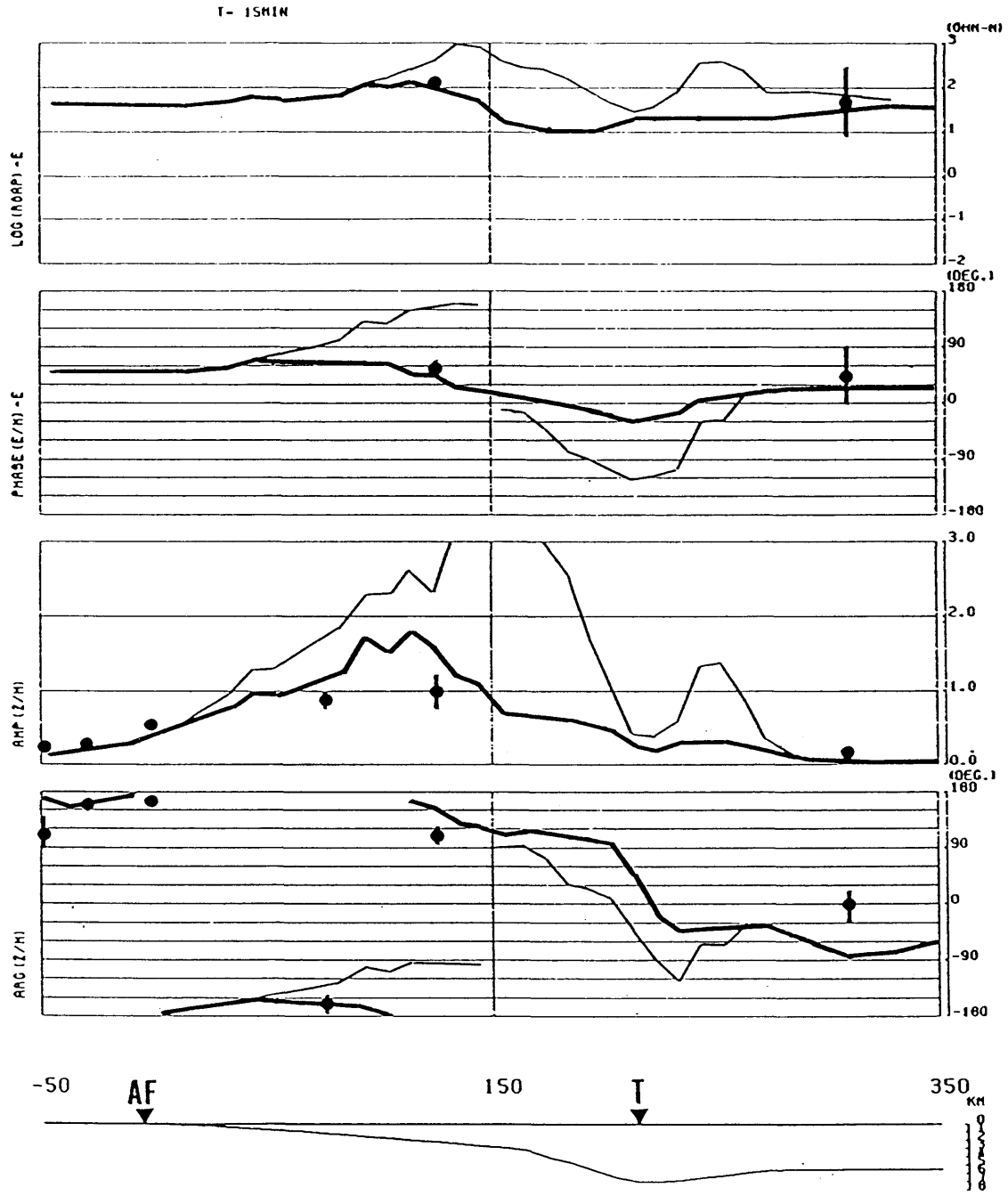

Fig.6.20 Comparison of the observed responses and theoretical ones from the final model (thick line) and from a model without thin conductor on the subducting Pacific Plate (thin line) for the period of 15 minutes.

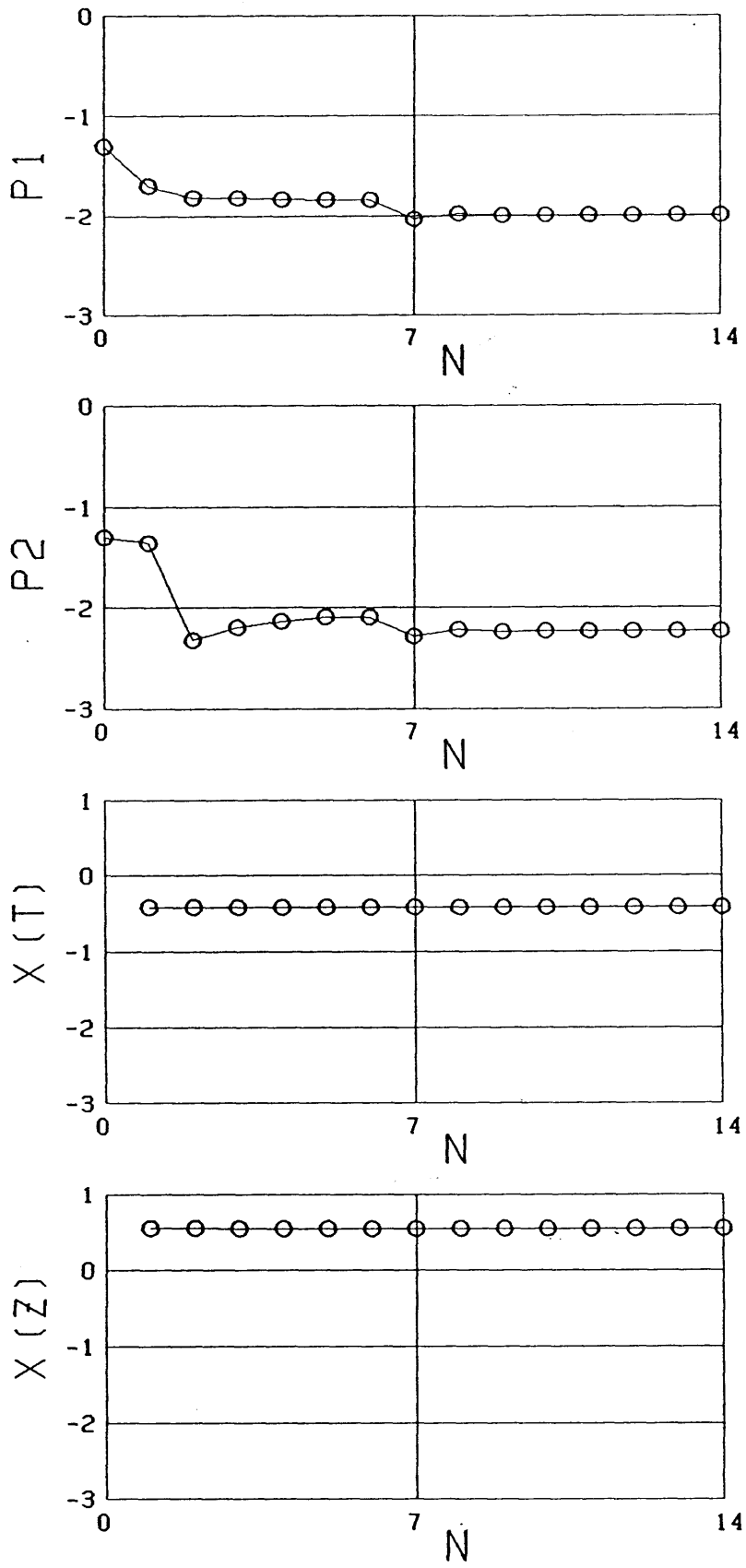

Fig.6.21 Direct Inversion against the conductivity of back arc mantle and the deeper portion of the downgoing slab assigned as M and N in Fig.6.14.

Table 6.1 Observation sites in northeast Japan and in the Pacific Ocean.

Site		Latitude	Londitude	Remark
OGA	Oga	39°56'	139°43'	
NBT	Nibetsu	39°48'	140°14'	
SZI	Shizukuishi	39°37'	140°35'	
KSK	Kusakai	39°39'	141°25'	
TON	Tono	39°25'	141°38'	
MYK	Miyako	39°36'	141°57'	
TZW	Tozawa	38°44'	140°18'	
NRG	Narugo	38°42'	140°45'	
MIZ	Mizusawa	39°07'	141°12'	
ESS	Esashi	39°17'	141°24'	
J1	OBM	39°28'	142°47'	Depth=1540 m
S1	OBM,OBE	39°28'	143°19'	2410 m
S2	OBM,OBE	39°30'	145°20'	5360 m
S3	OBE	39°30'	147°00'	5200 m
S4	OBM	39°23'	149°14'	5620 m

Table 6.2(a) Observed transfer functions at 15 minutes. amp(T), arg(T) and ε_T denote the amplitude and phase of the transfer function and estimation error, respectively.

Site	Y(km)	amp(T)	arg(T)	ε_T
OGA	-206.	0.268	-33.8	0.0235
NBT	-158.	0.342	50.6	0.0468
KND	-140.	0.073	54.4	0.0187
SZI	-126.	0.140	60.4	0.0182
KSK	- 49.	0.229	113.5	0.0528
TON	- 29.	0.276	157.8	0.0271
MYK	0.	0.532	164.4	0.0209
TZW	-132.	0.088	111.1	0.0281
NRG	- 95.	0.120	138.8	0.0149
MIZ	- 69.	0.160	131.8	0.0019
ESS	- 55.	0.045	179.8	0.0231
J1	77.	0.866	-161.0	0.1229
S1	126.	0.980	109.5	0.2350
S2	311.	0.124	-4.6	0.0290
S4	670.	0.025	-27.5	0.0326

Table 6.2(b) Observed transfer functions at 30 minutes.

Site	Y(km)	amp(T)	arg(T)	ε_T
OGA	-206.	0.330	12.9	0.0516
NBT	-158.	0.310	67.8	0.0266
KND	-140.	0.088	55.5	0.0148
SZI	-126.	0.098	83.0	0.0077
KSK	- 49.	0.256	115.6	0.0606
TON	- 29.	0.253	170.1	0.0261
MYK	0.	0.566	-175.9	0.0700
TZW	-132.	0.198	86.1	0.0218
NRG	- 95.	0.212	139.7	0.0118
MIZ	- 69.	0.224	140.1	0.0109
ESS	- 55.	0.317	172.6	0.0228
J1	77.	1.067	-166.1	0.0982
S1	126.	1.652	-176.6	0.5505
S2	311.	0.153	50.4	0.0577
S4	670.	0.070	163.1	0.0109

Table 6.2(c) Observed transfer functions at 60 minutes.

Site	Y(km)	amp(T)	arg(T)	ε_T
OGA	-206.	0.440	-28.2	0.0545
NBT	-158.	0.444	80.9	0.0114
KND	-140.	0.084	87.4	0.0467
SZI	-126.	0.161	132.4	0.0078
KSK	- 49.	0.235	136.5	0.0510
TON	- 29.	0.133	160.9	0.0598
MYK	0.	0.530	170.6	0.0479
TZW	-132.	0.184	147.5	0.0398
NRG	- 95.	0.189	142.3	0.0021
MIZ	- 69.	0.157	126.9	0.0407
ESS	- 55.	0.229	177.8	0.0559
J1	77.	0.893	-162.0	0.1721
S1	126.	1.357	108.5	0.2207
S2	311.	0.236	-21.2	0.0264
S4	670.	0.193	-58.5	0.0741

Table 6.2(d) Observed transfer functions at 120 minutes.

Site	Y(km)	amp(T)	arg(T)	ε_T
OGA	-206.	0.347	81.4	0.1210
NBT	-158.	0.362	108.3	0.0950
KND	-140.	0.136	118.3	0.0668
SZI	-126.	0.317	-160.5	0.0267
KSK	- 49.	0.212	-136.2	0.1751
TON	- 29.	0.169	-98.2	0.1194
MYK	0.	0.652	-158.6	0.1033
TZW	-132.	0.212	112.7	0.1049
NRG	- 95.	0.141	177.2	0.1051
MIZ	- 69.	0.084	117.8	0.0448
ESS	- 55.	0.176	-175.4	0.0372
J1	77.	0.396	-130.8	0.1844
S1	126.	0.765	-138.7	0.2449
S2	311.	0.104	-151.2	0.0440
S4	670.	0.144	100.8	0.0312

Table 6.3(a) E-polarization apparent resistivities, phases and standard errors for the period of 15minutes.

Site	Y(km)	$\rho_E(\Omega \cdot m)$	$\phi_E(deg)$	ε_E
TZW	-132.	34.9	65.9	5.20
S1	126.	124.6	56.7	17.50
S2	311.	47.1	45.1	37.52
S3	460.	77.3	54.7	25.25

Table 6.3(b) E-polarization apparent resistivities, phases and standard errors for the period of 30minutes.

Site	Y(km)	$\rho_E(\Omega \cdot m)$	$\phi_E(deg)$	ε_E
TZW	-132.	51.8	59.2	13.10
S1	126.	64.9	63.7	33.00
S2	311.	30.6	41.3	10.84
S3	460.	39.46	49.6	33.88

Table 6.3(c) E-polarization apparent resistivities, phases and standard errors for the period of 60minutes.

Site	Y(km)	$\rho_E(\Omega \cdot m)$	ϕ_E(deg)	ε_E
TZW	-132.	53.3	65.1	17.53
S1	126.	136.8	1.7	44.70
S2	311.	6.01	37.1	4.06
S3	460.	74.9	39.8	31.31

Table 6.3(d) E-polarization apparent resistivities, phases and standard errors for the period of 120 minutes.

Site	Y(km)	$\rho_E(\Omega \cdot m)$	ϕ_E(deg)	ε_E
TZW	-132.	32.0	48.2	15.44
S1	126.	80.7	50.7	17.70
S2	311.	39.4	44.5	9.98
S3	460.	47.4	53.9	23.16

Table 6.4(a) H-polarization apparent resistivities, phases and standard errors for the period of 15minutes.

Site	Y(km)	$\rho_H(\Omega \cdot m)$	$\phi_H(deg)$	ε_H
TZW	-132.	33.6	30.8	9.33
S1	126.	13.2	33.9	1.31
S2	311.	21.6	37.8	8.19
S3	460.	21.9	40.7	6.18

Table 6.4(b) H-polarization apparent resistivities, phases and standard errors for the period of 30minutes.

Site	Y(km)	$\rho_H(\Omega \cdot m)$	$\phi_H(deg)$	ε_H
TZW	-132.	26.2	40.5	9.45
S1	126.	8.07	29.2	0.800
S2	311.	25.7	36.2	10.47
S3	460.	22.9	46.7	14.83

Table 6.4(c) H-polarization apparent resistivities, phases and standard errors for the period of 60minutes.

Site	Y(km)	$\rho_H(\Omega \cdot m)$	$\phi_H(deg)$	ε_H
TZW	-132.	29.8	56.8	2.45
S1	126.	10.4	7.5	0.86
S2	311.	34.6	32.9	5.90
S3	460.	43.6	33.9	11.43

Table 6.4(d) H-polarization apparent resistivities, phases and standard errors for the period of 120 minutes.

Site	Y(km)	$\rho_H(\Omega \cdot m)$	$\phi_H(deg)$	ε_H
TZW	-132.	18.3	56.4	1.82
S1	126.	10.3	44.7	0.99
S2	311.	19.0	35.4	7.26
S3	460.	25.9	41.6	6.72

Table 6.5 Finite element network for the inversion of northeast and central Japan data.

Number of nodes	3276
Number of elements	6314
Upper boundary	-150 km
Lower boundary	2000 km
Side boundary (left)	-1500 km
Side boundary (right)	-2000 km
size of element matrix	80 x 3276

Table 6.6 Blocked conductivity structure with given conductivity for the direct inversion of northeast Japan data.

Block	conductivity(S/m)	comment
A	4.0×10^{0}	Japan Sea
B	2.0×10^{-1}	sea floor sediment
C	1.0×10^{-1}	sediment on Japan sea coast
D	1.2×10^{-2}	inland sediment (resistive)
E	1.0×10^{-1}	inland sediment (conductive)
F	1.0×10^{-1}	sediment on Pacific coast
G	4.0×10^{0}	Pacific Ocean
H	2.0×10^{-1}	sea floor sediment
I	3.0×10^{-2}	shallower crust of Japan Sea
J	2.0×10^{-3}	crust of Japan Sea floor
K	2.0×10^{-3}	Lithosphere of Pacific Plate
L	5.0×10^{-4}	Upper crust of Japan
M	2.0×10^{-2}	Upper mantle (100-400km)
N	2.0×10^{-2}	deep slab
O	1.0×10^{0}	Mantle (>400km)

Table 6.7 Result of direct inversion of northeast Japan data for 8 inhomogeneities with unknown conductivity.

No.	initial(S/m)	C_{popo}	final(S/m)	C_{pp}	C_{popo}/C_{pp}
1	1.0×10^{-3}	1×10^{-2}	2.5×10^{-3}	9.0×10^{-3}	1.11×10^{0}
2	5.0×10^{-2}	1×10^{-2}	5.2×10^{-2}	4.3×10^{-3}	2.33×10^{0}
3	5.0×10^{-2}	1×10^{-2}	3.6×10^{-2}	4.9×10^{-3}	2.04×10^{0}
4	1.0×10^{-2}	5×10^{-3}	5.9×10^{-3}	9.9×10^{-4}	5.05×10^{0}
5	1.0×10^{-2}	3×10^{-3}	5.1×10^{-3}	1.0×10^{-3}	3.0×10^{0}
6	1.0×10^{-2}	3×10^{-3}	3.2×10^{-3}	2.8×10^{-3}	1.07×10^{0}
7	1.0×10^{-1}	2×10^{-3}	7.3×10^{-2}	9.8×10^{-4}	2.04×10^{0}
8	2.0×10^{-2}	5×10^{-3}	8.5×10^{-2}	1.3×10^{-3}	3.85×10^{0}

Iteration cycles	48
Initial $\chi^2(d_Z)$	1.714×10^{0}
Final $\chi^2(d_Z)$	1.413×10^{0}
Initial $\chi^2(d_T)$	1.737×10^{-1}
Final $\chi^2(d_T)$	1.320×10^{-1}

Table 6.8 Result of direct inversion of northeast Japan data for 2 unknown inhomogeneities in the lower crust.

No.	initial(S/m)	C_{popo}	final(S/m)	C_{pp}	C_{popo}/C_{pp}
1	4.0×10^{-3}	2×10^{-2}	4.2×10^{-2}	1.1×10^{-2}	1.82×10^{0}
2	1.2×10^{-3}	3×10^{-2}	3.3×10^{-2}	1.4×10^{-2}	2.14×10^{0}

Iteration cycles	12
Initial $\chi^2(d_Z)$	1.549×10^{0}
Final $\chi^2(d_Z)$	1.471×10^{0}
Initial $\chi^2(d_T)$	1.564×10^{-1}
Final $\chi^2(d_T)$	1.341×10^{-1}

Table 6.9 Result of direct inversion of northeast Japan data for 2 unknown inhomogeneities (deeper parts of the mantle wedge and the subducting slab).

No.	initial(S/m)	C^{popo}	final(S/m)	C_{pp}	C_{popo}/C_{pp}
1	2.0×10^{-2}	1×10^{-3}	2.8×10^{-2}	8.7×10^{-4}	1.15×10^{0}
2	2.0×10^{-2}	2×10^{-3}	1.8×10^{-2}	1.6×10^{-3}	1.25×10^{0}

Iteration cycles	8
Initial $\chi^2(d_Z)$	1.413×10^{0}
Final $\chi^2(d_Z)$	1.409×10^{0}
Initial $\chi^2(d_T)$	1.320×10^{-1}
Final $\chi^2(d_T)$	1.309×10^{-1}

7. Electrical Conductivity Structure beneath the Central Part of Japan

Since Rikitake and Yokoyama(1953) pointed out the anomalous behavior of the vertical component of the geomagnetic variation at short periods in the central Japan area, many studies have been made to make clear the subsurface electrical conductivity structure in this region (e.g. Rikitake and Honkura, 1973, Rikitake, 1969, 1973, Honkura, 1974). Conductivity models proposed in these studies have a common feature; i.e. there exist highly conductive layers in the upper mantle beneath both the Japan Sea and the Philippine Sea, while the conductor is depressed beneath the central part of Japan. The cause of the highly conductive layer is generally attributed to high temperature or partial melting in the upper mantle (Honkura, 1974, 1975), which is consistent with the distribution of heat flow values around the Japanese islands (Watanabe, 1968; Nagao, 1986). Besides these highly conductive layers beneath the oceanic plates, previous geomagnetic observations, in both spatial and frequency dependences, have been explained by the coast effect due to the conductive sea water.

In 1982, the Research Group for Crustal Resistivity Structure, Japan, carried out magnetometer array observation at 16 sites in central Japan (Yukutake, 1984), including electric field measurements. Magnetotelluric responses at ELF and VLF frequency ranges were also obtained at these sites to reveal the surface conductivity structure. In addition to these land measurements, observations of geomagnetic variations have been conducted every year on the seafloor off the southern coast of central Japan since 1983 by use of newly developed ocean bottom magnetometers (OBM) (Segawa, et al., 1982). Seafloor measurements of the electric field variation have also been carried

out since 1984 by means of electric field measuring apparatus (OBE) newly developed by Hamano et al.(1984).

In this chapter, the electrical conductivity structure beneath this area, including surrounding seas, is examined on the basis of not only newly acquired electromagnetic variation data, but also those previously obtained. The final model will be obtained by the direct inversion method.

7.1 Spatial and period dependence of the response functions

7.1.1 Geomagnetic transfer functions

Observation sites for the present investigation are given in Table 7.1. Sites numbered from 1 to 17 are those of the co-operative project in 1982 by Research Group for Crustal Resistivity Structure, Japan (Yukutake, 1984). Sites with abbreviated names UCU, KMR and SRT are those for temporal measurements previously conducted, results of which were already reported partly by Sasai (1969), while YAT and SIM are permanent observatories belonging to the University of Tokyo and the Maritime Safety Agency, respectively. Seafloor sites, named such as J6, are those for magnetic observation. JE1, JE2 and JE3 are seafloor sites for measurement of electric field variations.

At YAT and most of the 1982 sites, 3-component geomagnetic variations were simultaneously recorded every minute by flux-gate magnetometers with a resolution of 0.1 nT. Data from OBM sites were also acquired in digital form with a sampling interval of two or three

minutes and with resolution of 0.1 or 0.7 nT (Segawa et al.,1984). Data at UCU, KMR, SRT and SIM, which were originally recorded on recording charts, were digitized at every 3 minutes. Fig.7.1 gives an example of simultaneous record of 3-component geomagnetic disturbances observed at HAM(No.14) and the OBM sites J12, J13, and J14, on ,1984.

From the compiled geomagnetic variation data, complex geomagnetic transfer functions A(f) and B(f) were calculated at each station for several geomagnetic disturbances by using the spectral analysis method, as well as 95% confidence intervals (see Chapter 5). Several records of magnetic disturbances were analyzed here with duration of two days for the longest and twenty four hours for most of them. Numerical filter was applied in order to eliminate the high frequency noise mostly from electric railways and industrial areas. We selected period range between 120 and 15 minutes for the analysis.

Figs.7.2 (a)-(d) show overall distributions of the induction vectors in this area for the periods, 15, 30, 60 and 120 minutes, respectively, by using the complex transfer functions A(f) and B(f). As a general feature, most of the vectors point to the south or the southeast, which is almost normal to the mean trend of the southern coastline. At the OBM sites far off the coast, the induction vectors become quite small at the shorter periods, while they become significantly large and point south- to southeastward at the longer periods. At the land sites near the southern coast, they point to almost the same direction, perpendicular to the coastline, and have nearly the same amplitudes. However, the vector at SIM shows quite different feature; i.e. anomalously large amplitude especially at the shorter periods. This particular feature can be attributed to the peninsula effect (Sasai,1969; Honkura, 1983). Similar effect can be

seen in the behavior of the induction vector at UCU situated in the Noto Peninsula. Therefore, these data have not been used for the further modeling study.

Length of induction vector at each frequency becomes shorter for the inland stations far from the Pacific coast. This implies that geomagnetic variations in this area are strongly affected by the induced current in conductive sea water. However, we can not explain all the features by the coast effect. At the midst of Japanese island, the vectors become small or change their directions northward at YAT and KMR for shorter periods. Meanwhile, they still remain large and point southward at No.02 and No.17 which are situated farther north from the Pacific coastline and nearer to the Japan sea coast than YAT and KMR. This feature could not be explained by only the coast effect.

In view of the similar directions of induction vectors, about 30 degrees east from south, we can reasonably assume a two-dimensional conductivity structure beneath this region. In order to determine the subterranean structure by comparing the observed electromagnetic responses to those by theoretical calculations, we obtained two-dimensional profiles of complex transfer functions by projecting the observed induction vectors onto the line parallel to N30W- S30E. The values of the projected transfer functions are given in Tables 7.2(a)-(d) at the periods of 15, 30, 60 and 120 minutes, respectively. Figs.7.3(a)-(d) present the profiles of the projected transfer functions for corresponding periods.

Since all the observed induction vectors do not strictly point to the projected direction, prescribed vector projection yields residual components which are perpendicular to the traverse. Here we call them residual transfer functions. Fig.7.4 shows profiles of the residual

transfer functions at the period of 30 minutes in this area and those in northeast Japan in the previous chapter along the east-west direction. If the subterranean structure is strictly two-dimensional along the projected line, all induction vectors should point to the same direction, that is perpendicular to the structural trend, leaving the residual transfer functions to be null amplitude. The result, Fig.7.4, shows that, in central Japan, amplitudes of the residual transfer functions are sufficiently small compared with those of the projected ones (Fig.7.3(b)), even smaller than those in northeast Japan, where the subterranean structure is considered to be well approximated as two-dimensional. This fact supports the validity of the assumption of two-dimensional structure beneath this region. Of course, these residual transfer functions should contain some information about three-dimensionality of the subsurface structure. However, we will not discuss it any further here, because much denser distribution of observation sites is required for the discussion.

Now we pick up some prominent features of the projected transfer functions shown in these figures. At sites between the Pacific coast and the Nankai trough, the amplitude of transfer function is large, sometimes exceeding 1.0, presumably arising from the large conductivity contrast between the land and sea water. The phase varies on the seafloor differently for different periods, while it is almost zero at the Pacific coast. The rate of phase variation seems to become small for the longer periods. In contrast to the strong coast effect observed in the Pacific coast, the effect seems weaker in the Japan sea side. The phase does not exceed -90 degrees even at the site No.2 which is the nearest to the Japan Sea. This has already been discussed by Honkura (1974) and Ogawa et al.(1985).

In the middle of central Japan, a striking feature is observed in spatial and period dependence of phase: from the south to the north, the phase for the period of 15 minutes once decreases down to about -120 degrees at YAT and KMR, then turns to increase at sites No.02 and No.17. Similar tendency can be seen at longer periods though less remarkable. Since the spatial scale of the anomalous phase variation is as small as about 50-70 km and it is more conspicuous at the shorter periods, this anomaly can be attributed to a rather shallow conductor, possibly in the crust.

7.1.2 Magnetotelluric Results

Sometimes surface sedimentary layers cause significant geomagnetic variation anomalies (Porath and Dziewonski, 1971). Therefore, it is very important and helpful to know conductivity distribution at shallower depth even when one wants to investigate the deep conductivity structure. We conducted magnetotelluric measurements in the ELF and VLF ranges at each of the 1982 sites. For ELF range, electric and magnetic fields were recorded simultaneously, and then complex tensor impedances were determined at the frequencies of three fundamental modes of the Schumann resonance. Apparent resistivity and phase difference between electric and magnetic field variations were also measured for the VLF range by use of an EM16-16R system.

Figs.7.5(a) and (b) show the distributions of the apparent resistivity and the phase difference at the frequencies of 17.4 kHz and 8

Hz, respectively. Striking resistivity contrast is observed between the central mountain and the coastal areas. For example, 2 kΩ·m and 3 kΩ·m were obtained at No.06 for VLF and ELF apparent resistivities, respectively, while both of them were less than 10 Ω·m at No.14 on the Pacific coast. These maps were used in determining the shallow conductivity values for the modelings in the following section.

For the shorter period band of ULF, such as about 30 seconds, electric field records were severely affected by noises mostly due to electric railways. Because of this situation, we could not obtain reliable estimates of the magnetotelluric impedance for this band except for one site, No.03(NGW), which is situated on the southeastern foot of Volcano Norikura in the midst of Hida mountain area.

In 1982, electric field variations were also recorded at many stations for the longer period band of ULF. However, the records were found to be severely contaminated by artificial noises. At present, for this period band, we have impedance estimates at 5 sites. Data from 3 land sites, No.03, No.13(HRN) and No.14(HAM), were used to evaluate the impedance tensors at 15, 30, 60 and 120 minutes of period. On the seafloor off the southern coast of this district, the impedance tensors were obtained at 2 sites, JE2 and JE3, at the corresponding periods. At JE3, because of the break down of one of the amplifiers, we have a record of only one component, nearly east-west, of electric field variation. Data from JE2 was found to be contaminated with high frequency noise, and therefore, the evaluation was made for the periods longer than equal to 30 minutes (Hamano,1985). All the impedances, except those at JE3 and that at JE2 for 15 minutes, have been rotated by 30 degrees and separated into the E- and H-polarization ones. Evaluated impedances are also tabulated in Tables

7.3(a)-(d) and Tables 7.4(a)-(d). The impedances at JE3 are tabulated as E-polarization ones because the measuring direction, east-west, is nearly perpendicular to the present traverse.

Once the impedance tensor is evaluated, we can obtain a polar orbit of the expected electric field variation from a magnetic field variation with a unit intensity, in the same way as described in the previous chapter. By use of the expressions Eqs.(6-2-1)-(6-2-3), polarization diagrams have been obtained as shown in Figs.7.(a)-(c) from respective impedance tensor estimates at JE2, No.14 and No.13.

Polar diagrams of the electric field at the OBE site, JE2, represent apparent anisotropy in NE-SW direction (Fig.7.6(a)) for each frequency, which is almost parallel to the mean direction of the coast line and to the trend of the Nankai Trough. This anisotropy indicates that the strong induced electric current flows along the trend of the seafloor topography. At a land site close to the southern coastline, No.14, an anisotropy is recognized in almost the same direction as that at JE2 (Fig.7.6(b)). This means that the induced current here is also flowing along the mean trend of the coast line. On the other hand, the polar diagram at No.13 shows an anisotropy nearly perpendicular to those of the previous ones (Fig.7.6(c)). The result of numerical calculation on model II in Section 3.6 has shown the expected anisotropy in the electric variation in the region close to the boundary of two-dimensional conductivity heterogeneity such as coastal area as follows: major axis of anisotropy will be parallel to the boundary on the conductive side, while it turns normal to it on resistive side because of the large conductivity contrast. Thus, these polar diagrams suggest that the site No.14 situates in conductive side and the main boundary of conductivity heterogeneity exists between,

not JE2 and No.14, but No.14 and No.13. This implication is consistent with the result of ELF and VLF magnetotelluric measurements, i.e. a contrast as large as nearly two orders of magnitude was seen between the apparent resistivities at these two sites, No.13 and No.14. The apparent resistivity at No.14 of 2-4 Ω·m provides a contrast of only one order of magnitude compared with the resistivity of sea water. The direction of the impedance anisotropy on land also indicates that the inland boundary of the conductivity structure is nearly parallel to the mean trend of coast line. Thus, the polar diagram analysis confirms the validity of the assumption on the mean structural trend as in the direction N60E-S60W.

Using all the results ranging from VLF to ULF, one-dimensional structure was inferred inversely at the site No.03 (Fig.7.7) using a five-layer model (Yukutake,1984). Beneath relatively conductive surface layers, a resistive upper crust exists down to the depth of about 20 km. This depth is well coincide with that of the Conrad Plane in this area revealed by explosion seismology (Asada and Asano, 1973). Then resistivity decreases by more than 3 orders of magnitude. A thin conductive layer is thus suggested at this depth. However, its existence can not be regarded as firmly established when the confidence intervals for the layer thickness is taken into consideration. Nevertheless, the fifth layer underlying this conductive layer is more conductive, with resistivity of about 100 Ω·m, than the third resistive layer. Thus, the conductive layer should be located within the crust, since the MOHO depth is deeper than 30 km in this area, implying that the lower crust is conductive. It remains uncertain from a magnetotelluric result at the single station whether this conductive lower crust

reflects a general feature of the crustal structure beneath this region or only a local one.

One-dimensional inversion was also carried out by using the frequency dependence of the impedance on the seafloor site, calculated from electric field at JE3 and magnetic field at J13, situated a few km apart. A three layer model has been derived as shown in Fig.7.8. A highly conductive layer is inferred at the depth of about 50 km between a relatively resistive layer by the model. However, the depth to the interface between the first and the second layers seems too shallow to be well resolved by the present data set for lack of high frequency data. On the other hand, the interface between the second and the third layer has been determined with the higher confidence. The increasing apparent resistivity with period implies that the deeper layer is more resistive than the shallower one. The result shows that the interface lies at 80-150 km beneath the seafloor. Anyway, the first resistive layer can be considered to correspond to the oceanic lithosphere as has been described in the previous chapter. As for the Pacific Plate, the depth to the corresponding boundary was as deep as about 140 km off the Japan Trench, which is likely to reflect the thickening of the oceanic plate as has been discussed in Section 6.1. Above result of the Philippine Sea Plate is possibly suggesting that the plate thickness is considerably thin compared with that of the Pacific Plate in the West Pacific.

7.2 Two-dimensional Conductivity Model across Central Japan

7.2.1 Construction of the finite element network and inhomogeneous block division

In order to investigate how the observed responses can be explained by a two-dimensional structure, modeling has been carried out by using the direct inversion method. The geomagnetic transfer function and the magnetotelluric impedance have been evaluated at each available site as a response function for E-polarization induction case; the case where the electric field varies in parallel with the trend of structure.

A basic mesh network has been constructed in a similar way to that in the case of northeast Japan described in the previous chapter. Whole network covers the area between 2,000 km away from the Pacific coast and about 1,500 km from the Japan sea coast horizontally, from 150 km above sea level down to 2,000 km depth vertically, with the total area being 3,700 km x 2,150 km. The entire region was modeled by 6,326 triangular elements.

Modeling is started with incorporation of the surface structures so far known along the profile into the model, particularly the following features which were obtained from geology and magnetotelluric results (Fig.7.9);

1) Conductive sea water of the Philippine and Japan Seas. Seafloor topographies were carefully read along the profile from the bathymetric chart.

2) Thick sedimentary layer on the seafloor and continental shelf, whose conductivity was taken to be 1-0.5 S/m.

3) Tertiary or Quaternary sediments or sedimentary rocks in the coas-

tal areas. The conductivity was estimated as 0.5 S/m for the Philippine Sea side, while the conductivity of 0.1 S/m was applied for the Japan sea coast, on the basis of the ELF VLF magnetotelluric results as mentioned above.

4) Outcrops of resistive rocks, as resistive as 10^{-3} S/m, in the areas north of the Median Tectonic Line.

5) Result of magnetotelluric sounding at No.03 site suggests the conductivity of the upper crust beneath the Central Japan to be 10^{-3}-10^{-4} S/m. A similar or a little more conductive value has been assigned to the oceanic plates based on the previous studies (e.g. Filloux, 1980, 1981; Yukutake, et al., 1983) and the preliminary one-dimensional inversion of the seafloor magnetotelluric data.

Fig.7.10(a) shows the near-surface inhomogeneous structure of the model. Each block, with known conductivity as shown above, was assigned by A-L (Table 7.5). Since the resolution for the structure deeper than 100 km is poor compared to that for the shallower structure, the deeper part was divided into a small number of large blocks (M and N in Fig.7.10(b)). Plausible initial values of conductivity are adopted to each block as follows, similarly to the modeling of northeast Japan in the previous chapter. A moderately conductive layer of 10^{-2} S/m was assigned between the depth of 100 and 400 km taking into account the prescribed magnetotelluric result at JE3. High conductivity of 1 S/m was assumed for the substratum below 400 km. Rests of the parameters were left unknown to be determined inversely with a block division as shown in Figs.7.10(a) and (b).

These block division was made on the basis of various kinds of geophysical and geological evidences, though there are not so many

compared with those in northeast Japan. A conductive region was inferred in the lower crustal structure beneath central Japan by the distribution of the geomagnetic transfer function (Utada, et al.,1986). Since this feature is a quite conspicuous one and the one-dimensional magnetotelluric result at No.03 also confirms the existence of conductive layer at 20 km depth below surface, the lower crust has been divided into three blocks.

Ishida (1985) revealed the distribution of micro earthquake foci relating to the subduction of the Philippine Sea Plate in various regions. The shape of the block representing the downgoing plate was determined by referring one of her cross section closest to the present traverse.

The uppermost part of mantle down to 100 km depth has been divided into three blocks, i.e. beneath the Philippine Sea, the Japan Arc and the Japan Sea. The subducting part of the plate was assumed to have constant thickness. As a result, a wedge shape was assigned to the uppermost part of the mantle beneath the Philippine Sea.

The result of the previous chapter around the Japan Trench has suggested the existence of a thin conductive layer on the top surface of the Pacific Plate beneath the northeast Japan arc. Here, with regard to the Philippine Sea Plate, we are going to examine the possible existence of the conductive surface layer, too. For this purpose, a thin block was set up with 6 km thickness, which elongates deep into the mantle beneath the Japan arc with the downgoing slab.

7.2.2 Result

In constructing a reliable model beneath central Japan and surrounding seas, we have given the surface conductivity structure, down to 4 km, and the deeper structure than 100 km, as has been shown above. Then, several calculations were made in order to obtain initial parameters for the direct inversion. We first calculated the theoretical responses for the model in which a uniform conductivity of 10^{-3} S/m was assumed except for the surface structure. The response functions calculated for this starting model shows several discrepancies from the observed responses, as shown in Fig.7. which shows one of the results for the period of 15 minutes. For example, the calculated amplitudes of both impedance and transfer function is much larger than the observed one on the Philippine Seafloor. Besides, the calculated phase of the transfer function behaves quite differently in central Japan area. It is obvious that additional conductivity inhomogeneities are required in order to explain these features. Utada, et al.(1986) pointed out that these typical features of the transfer function can well be represented by introducing conductive bodies, whose conductivities should be both as high as about 0.1 S/m, beneath the Philippine Sea and the central part of Japan. Accordingly, their optimum model has been adopted as an initial model of the least squares method.

By use of thus estimated set of initial parameters, the direct inversion has been carried out. The set of parameters consists of 7 unknowns which are assigned as No.1 - 7 as shown in Figs.7.10(a) and (b). The distribution of partial derivatives with respect to the initial conductivity of each block is given in Appendix C. The iterative

process was converged after 32 cycles of iteration, the result of which is tabulated in Table 7.6. Fig.7.11 shows the behavior of each parameter and χ^2 at the last 8 cycles of the whole process. The resulting responses are found to represent typical features of observed ones, in the spatial characteristics for the whole period range. Figs.7.12 (a)-(d) gives comparison of the observed and calculated responses for the periods of 15, 30, 60 and 120 minutes, respectively.

Large initial to final covariance ratio, C_{poPo}/C_{pp}, of over 10^3 (Table 7.6) shows that the existence of the conductor beneath the Philippine Sea is highly convincing. The conductivity of this layer is determined as 1.4×10^{-1} S/m, whereas the initial value is 1.0×10^{-1}. We can recognize large partial derivatives, as shown in Appendix C-6, on the seafloor around the Nankai Trough, implying that the observed data at the seafloor sites both of OBM and OBE have a large contribution in determining the conductivity of this layer.

As has already been indicated by Utada, et al.(1986), this conductive layer was introduced in order to suppress the large amplitudes of Z/H and the impedance in the starting model and to fit the phase variations on the seafloor sites in the vicinity of the Nankai Trough. Because of the large conductivity contrast between land and seawater, Z/H values would be several times larger at these sites without the deeper conductor (see Fig.7.14). The contrast also causes a concentration of induced electric current around the transition zone between land and ocean. It was found that the existence of the conductive upper mantle reduces the induced current to some extent by electromagnetic coupling (Utada, et al.,1986).

It should be emphasized here that the wedge shape of this block

is essential in the induction effect. Without the conductor beneath the subducted part of the Philippine Sea Plate, but with one extending only below the open ocean, the suppression of current concentration described above cannot be expected in the vicinity of the Nankai Trough (Fig.7.14). Sharp edge of a conductor generally causes a concentration of induced current there. The shape of the boundary here should be gradual since observation shows that the conductor really suppresses the induced current in the ocean.

However, it was found that the observed responses cannot be explained only by introducing the deeper conductor. Without considering the shallower structure, significant discrepancy of the responses has been found to remain in a restricted area just around the trough. The surface conductor of the subducting slab has thus introduced in order to solve this discrepancy. The conductivity of this layer has been well resolved with a large value of C_{popo}/C_{pp} of 3.85 as given in Table 7.6. This thin layer, with conductivity of 1.6×10^{-1} S/m and thickness of 6 km, reduces the contrast between the sea water and the earth effectively, particularly in the vicinity of the trough axis. The partial derivatives with respect to the conductivity of this thin block (Appendix C-7) show that the observation just on the trough axis is particularly sensitive to the determination of the conductivity. In fact, the existence of this layer affects the response at observation sites only very close to the trough axis;i.e. JE3 and J13. Fig.7.15 shows the comparison of theoretical responses for the final model (thick lines) with those for a model with absence of this thin conductive layer (thin lines). Both the transfer function and E-polarization impedance sharply increase in the vicinity of the Nankai trough without this thin conductor. These features can be explained as caused

by the concentration of induced current in this area. The concentrated current with short spatial wavelength cannot be suppressed effectively by the deeper conductor in the mantle. When the thin conductor with a conductance of about 10^3 S (conductivity of 1.6×10^{-1} and thickness of 6 km) is introduced into the model, the intensity of the induced current can be reduced as shown in Fig.7.15. The thin layer in the final model connects the seafloor and the deeper conductive mantle. This connection is the essential configuration in an electrical sense. If this layer is cut at the shallower depth and surrounded only by resistive materials such as upper part of crust and the lithosphere, the suppression effect of current concentration cannot be expected (Fig.7.15) because the current still concentrates in the conductor in this case. The effect of the slabtop conductor is less significant than that in case of the Japan Trench. This difference may be attributed to the differece in the thickness of the seafloor sediments. In the model of northeast Japan, an accretion prism as thick as about 10 km has been assumed in the Japan Trench. Therefore, the more intense concentration of total induced current can be expected around the trench than that in the vicinity of the Nankai Trough. The suppression effect by the slabtop conductor will become more conspicuous with the larger induced current. Thus, the effects of similar slabtop conductors appear to be different in both regions, but the difference can be interpreted as only reflecting the difference in the intensity of total current.

Beneath the Japan Sea and the Japan Arc, numerical calculation prefers moderately resistive upper mantle. The former may tend to be a little more resistive than the latter. On the other hand, previous works (Rikitake, 1975; Honkura, 1975) had given highly conductive one

beneath the Japan Sea and a large depression of conductor beneath the central part of the Japan Arc. Meanwhile, recent studies (Ogawa, et al, 1985; Utada, et al.,1986) have put forward conductivity models negative to the existence of a shallow conductor beneath the Japan Sea. The conductivity of the Japan sea mantle has been estimated by the present direct inversion as about $4x10^{-3}$, which almost coincides with the result of the northeastern Japan modeling. However, as was the case in the previous chapter, the parameter has been resolved quite weakly with the covariance ratio of as low as 1.08 (Table 7.6). Seafloor measurements in the Japan Sea is necessary to make clear of the problem.

The lower crustal structure beneath central Japan inferred by Utada et al.(1986) has also been confirmed by the direct inversion. The conductor in the lower crust beneath central Japan has never been seen in any of the previous investigations. It is probably because no geomagnetic variation data had been obtained except at KMR ,YAT and UCU before the 1982 project. The geomagnetic variation at UCU is, as previously described, inappropriate for investigation of subsurface structure since it is contaminated by a peninsula effect. Besides, at both former sites, the phase of Z/H decreases down to about -120 degrees at shorter periods. This behavior of phase variation may be taken as the beginning of the coast effect by the Japan Sea. In fact, In the absence of the lower crustal conductor, the phase of the calculated transfer function decreases towards the Japan Sea and never come back as shown by thin lines in Fig.7.16. However, detailed Observations in 1982 have revealed that the phase increases again to nearly 0 degree towards the coast at sites No.3 and No.17. This requires an additional conductor in the lower crust beneath the central part of

Japan (Fig.7.16; Utada et al.,1986).

Horizontal extension of this conductor can be determined very strictly because of the relatively short site spacings; between 120 km from the Pacific coast and 60 km from the Japan Sea coast. The depth to its surface was also estimated as about 20 km by one-dimensional inversion of magnetotelluric data at No.03. Spatial and period dependences of the transfer function also infers the depth as shallower than 20 km (Utada et al., 1986). We are now conscious of the role of the crustal conductor beneath central Japan in the geomagnetic induction process; i.e. the southeastern edge of the conductor causes a decrease in the phase of Z/H at those sites situated 50-100 km away from the Pacific coast at shorter periods, while the northwestern one makes an increase in the phase, in other word, suppresses the coast effect by the Japan Sea, at those sites situated 30-60 km away from the Japan Sea coast. The presence of upper mantle conductor beneath the Japan Sea modifies this induction effect by mutual coupling, resulting in poorer fit to the observed responses as shown by dashed line in Fig.7.16.

Finally, two case of direct inversion have been carried out in order to examine the reliability in several parameters, limiting the the degree of freedom with two unknowns for each. One has been performed for the conductivities of the lower crustal conductor and the Philippine Sea asthenosphere. The other has been performed for rather weakly resolved parameters by the total inversion described above;i.e. the conductivities of the mantle beneath Japan Sea and Japan Arc. Results are summarized in Tables 7.7 and 7.8, respectively.

For the former case, each parameter has converged to similar value to one in the final model, though the initial value of each has

been made one order of magnitude lower than the final model parameter (Fig.7.17). The large values of initial to final covariance ratio (Table 7.8) also confirms the reliability of the solution. On the other hand, the latter parameters have shown a rather unstable nature in the iterative process. In this test, a relatively high conductivity has been assigned to each initial parameter for the purpose of examining the possible presence of high conductor beneath the Japan Sea and Japanese Islands. However, the result, although it is less convincing, seems to imply a resistive structure in this region (Fig.7.18). Utada et al.(1986) demonstrated that a conductive layer does not exist in the upper mantle beneath the Japan Sea, within at least about 200 km from the coast. Anyway, measurements in the Japan Sea are indispensable to reveal the electrical state in the upper mantle below, as has been mentioned previously. The large amplitude of the partial derivatives in the Japan Sea (Appendix C-4) also indicates the importance of the experiment there.

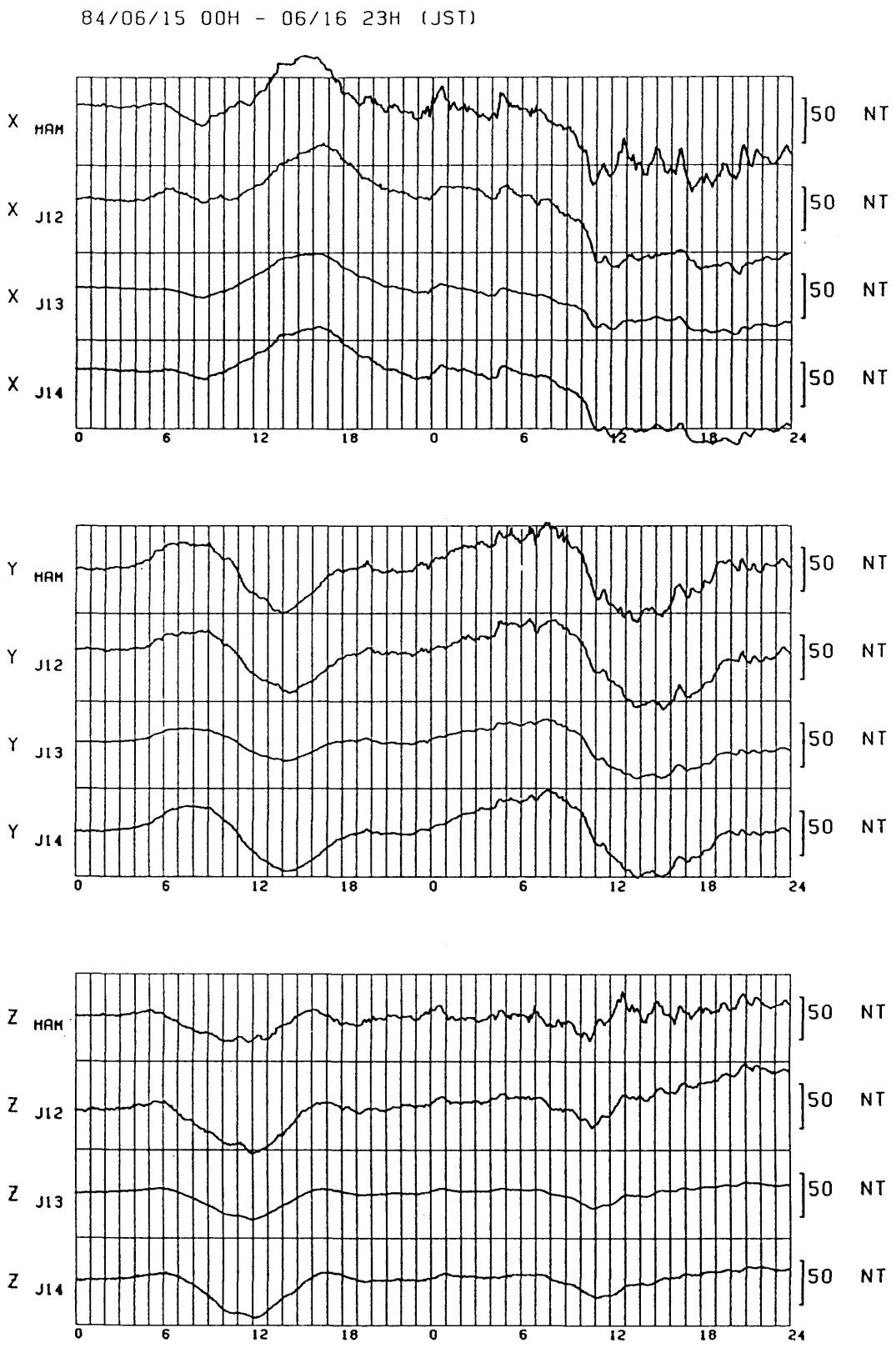

Fig.7.1 An example of simultaneous record of 3-component geomagnetic disturbances observed at Hamaoka (HAM) and seafloor sites, J12, J13, and J14.

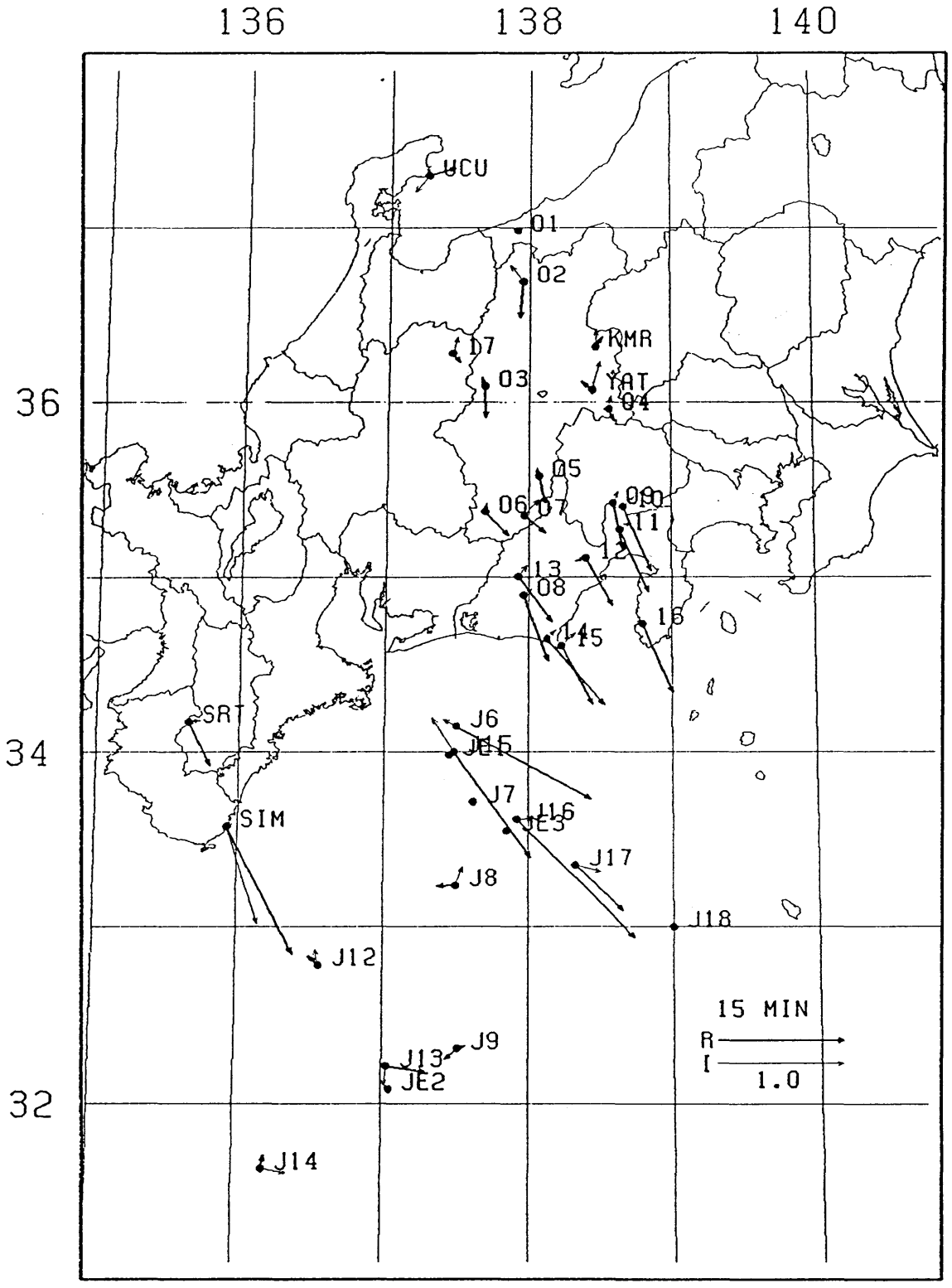

Fig.7.2(a) Distribution of the induction vectors for the period of 15 minutes. Real and imaginary vectors are denoted by thick and thin arrows, respectively.

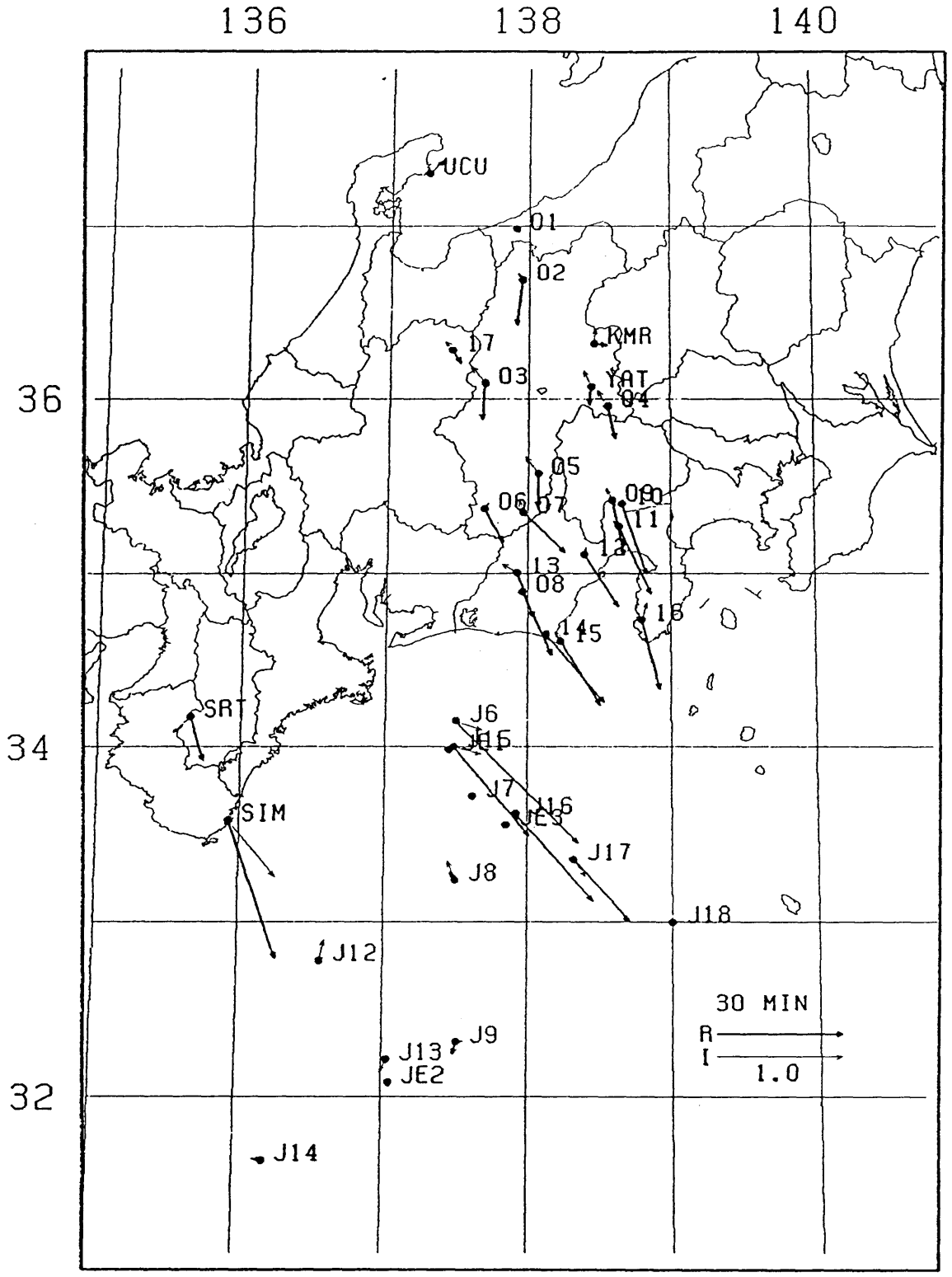

Fig.7.2(b) Distribution of the induction vectors for the period of 30 minutes.

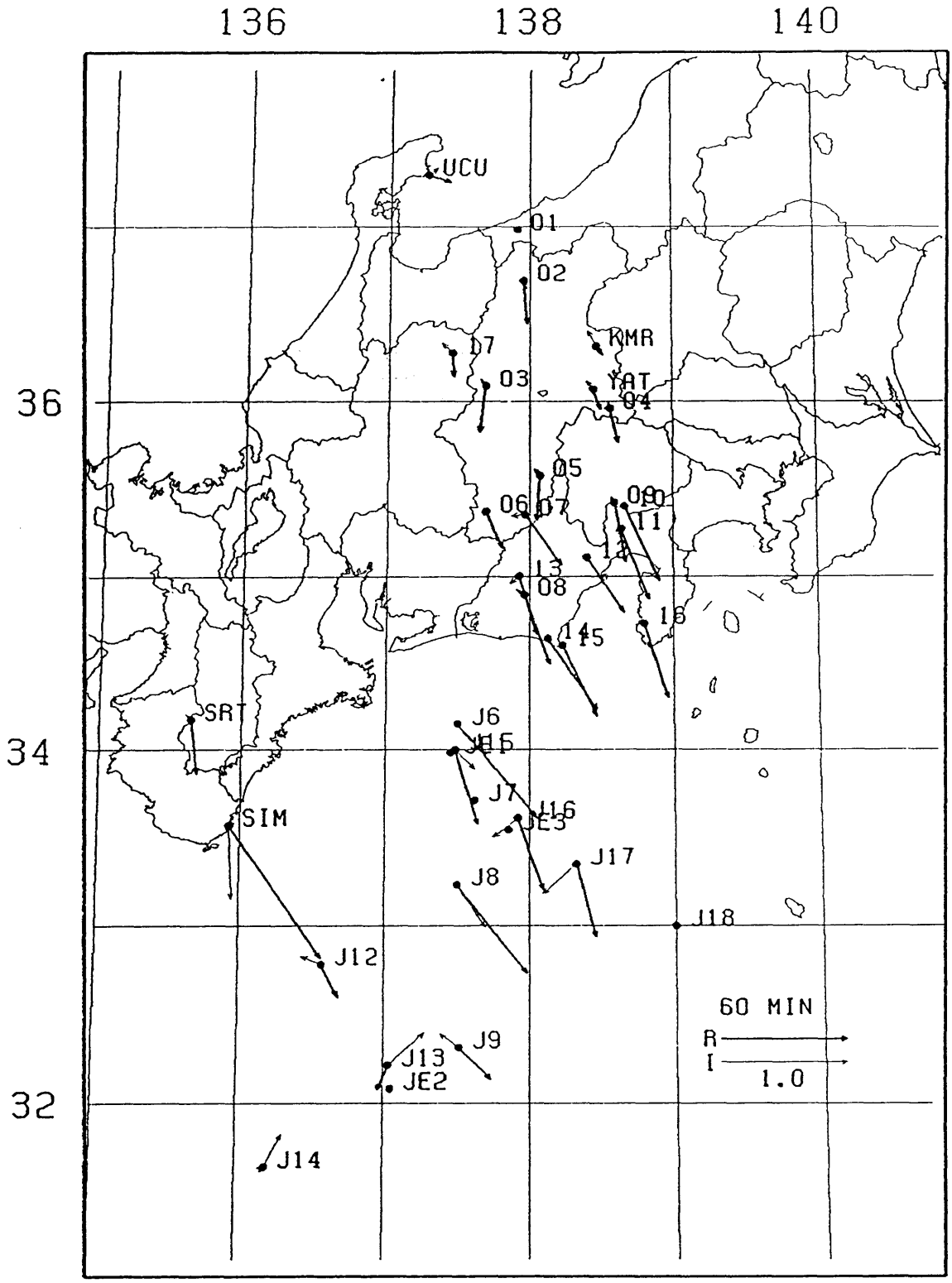

Fig.7.2(c) Distribution of the induction vectors for the period of 60 minutes.

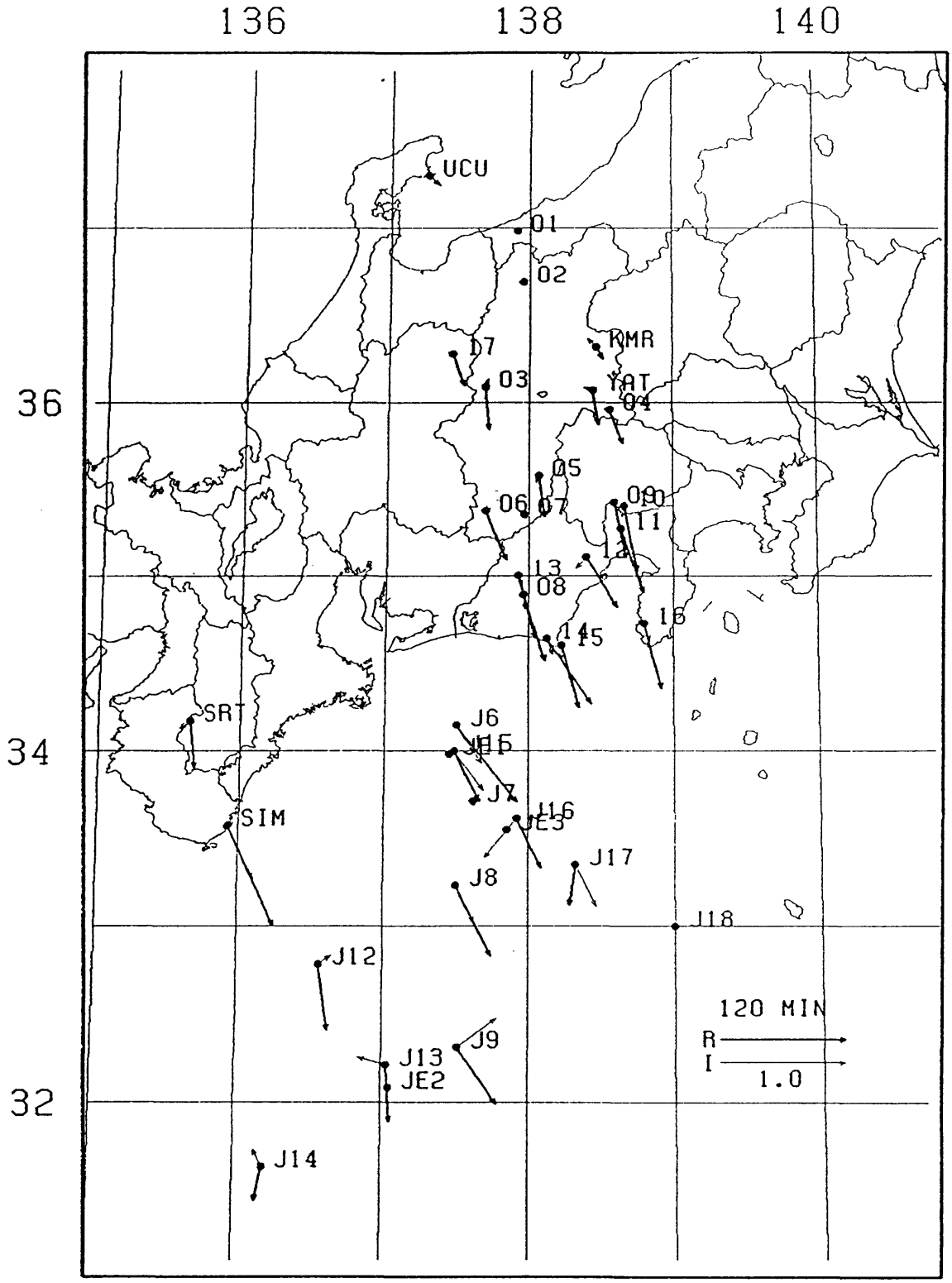

Fig.7.2(d) Distribution of the induction vectors for the period of 120 minutes.

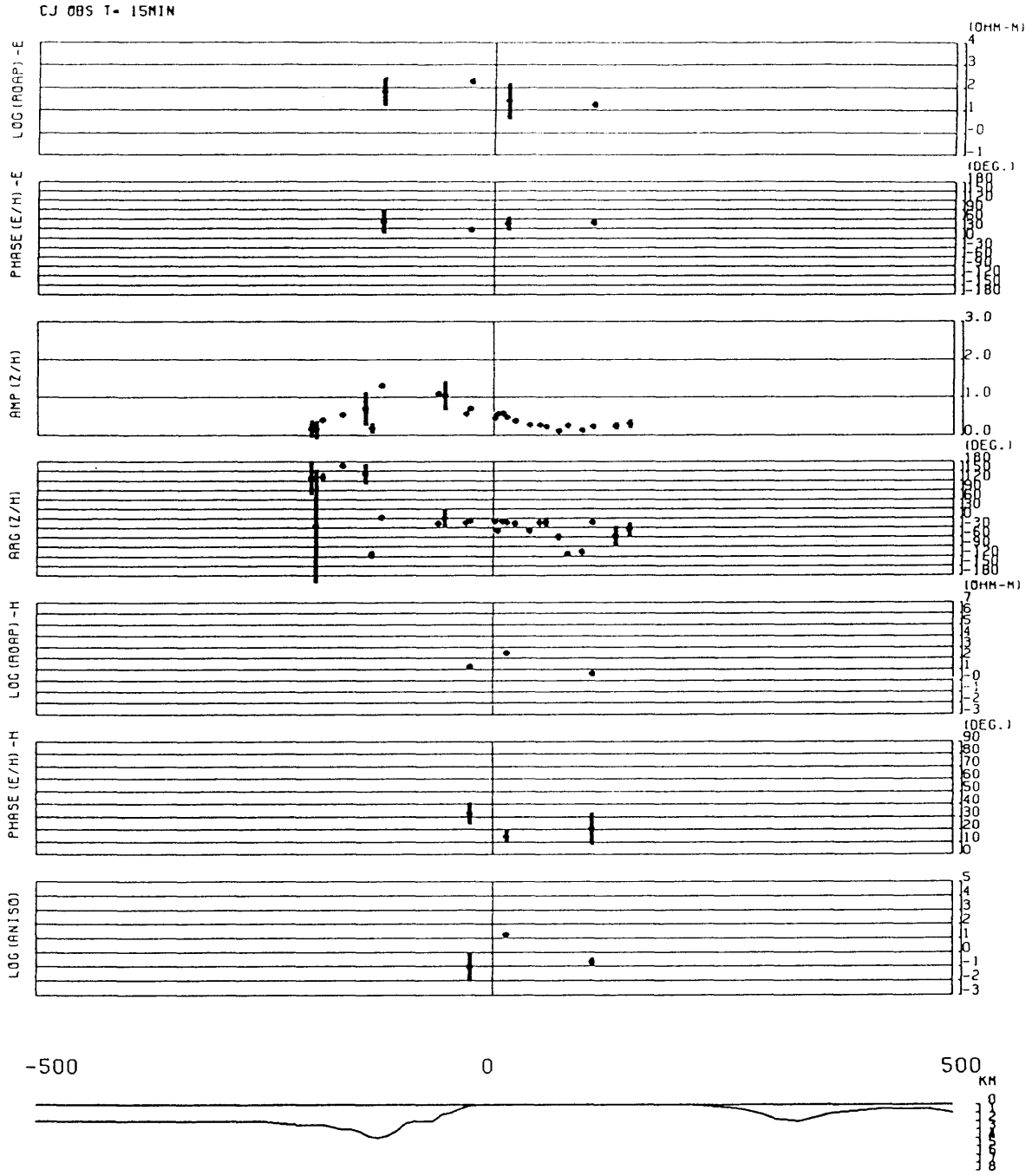

Fig.7.3 (a) Profiles of the observed response functions along the traverse. Presented are the E-polarization apparent resistivity and phase, amplitude and phase of the transfer function, the H-polarization apparent resistivity and phase, and the ratio E- to H-polarization apparent resistivity along the line parallel to N30W-S30E for the period of 15 minutes.

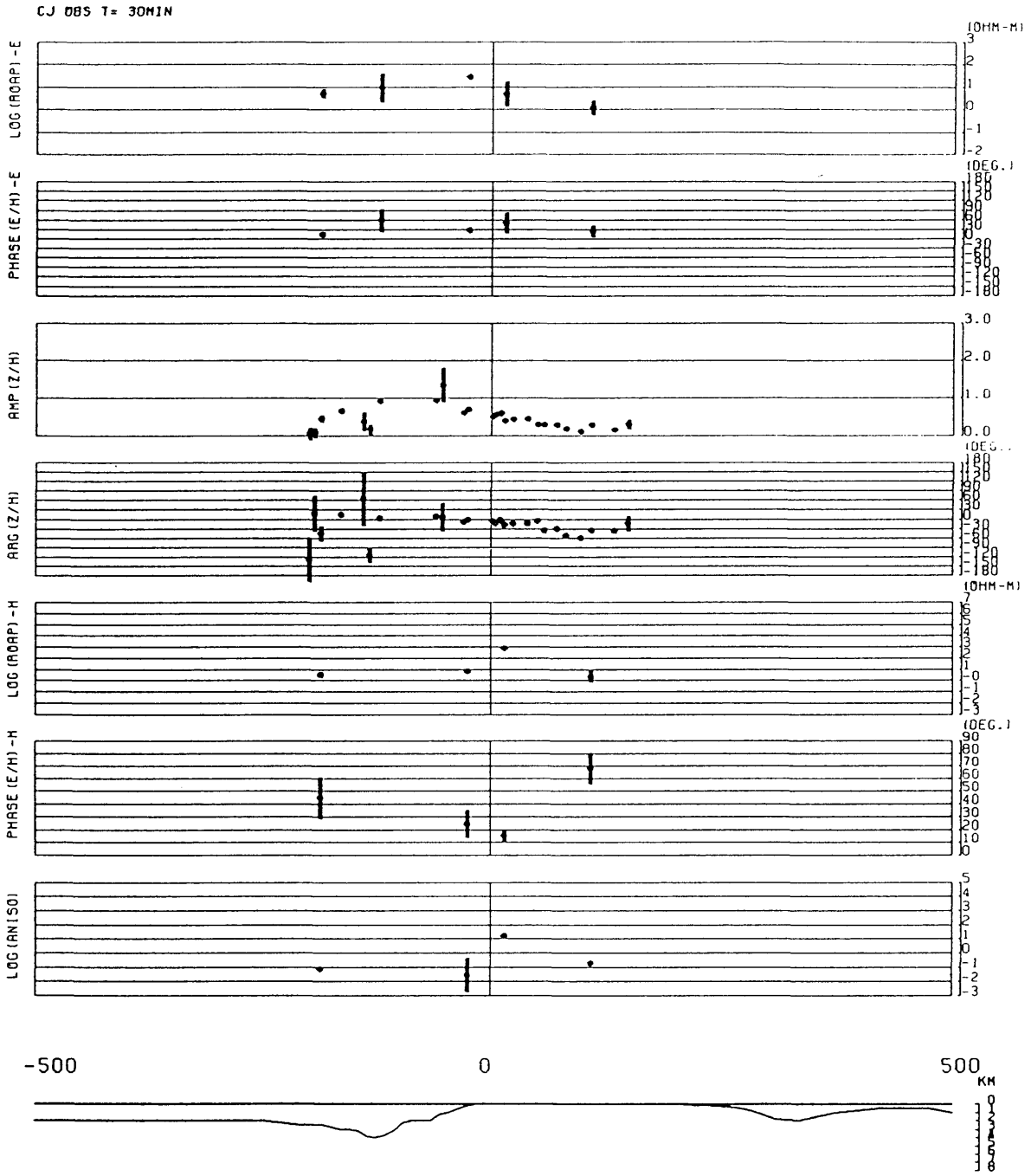

Fig.7.3 (b) Profiles of the observed response functions for the period of 30 minutes.

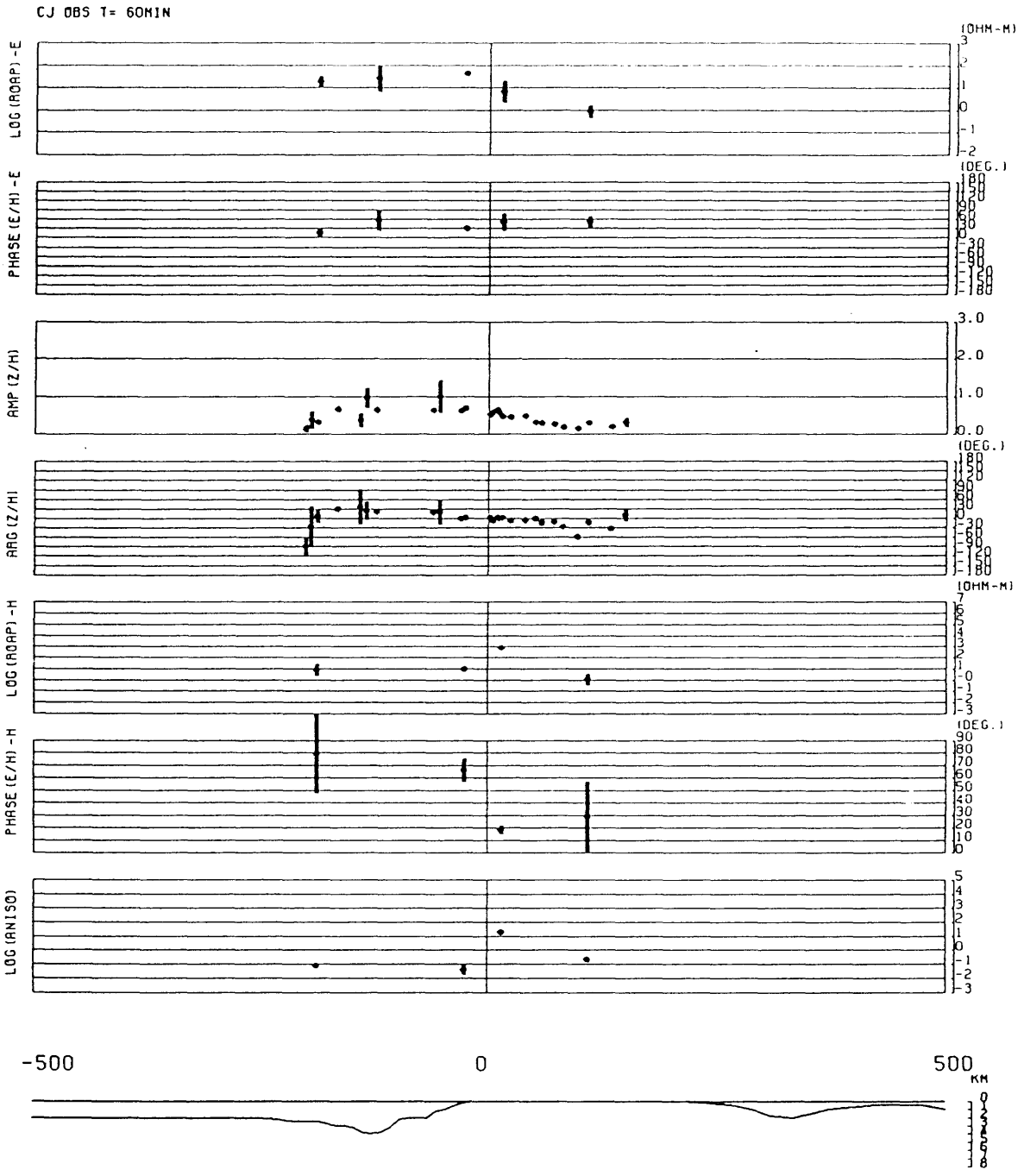

Fig.7.3 (c) Profiles of the observed response functions for the period of 60 minutes.

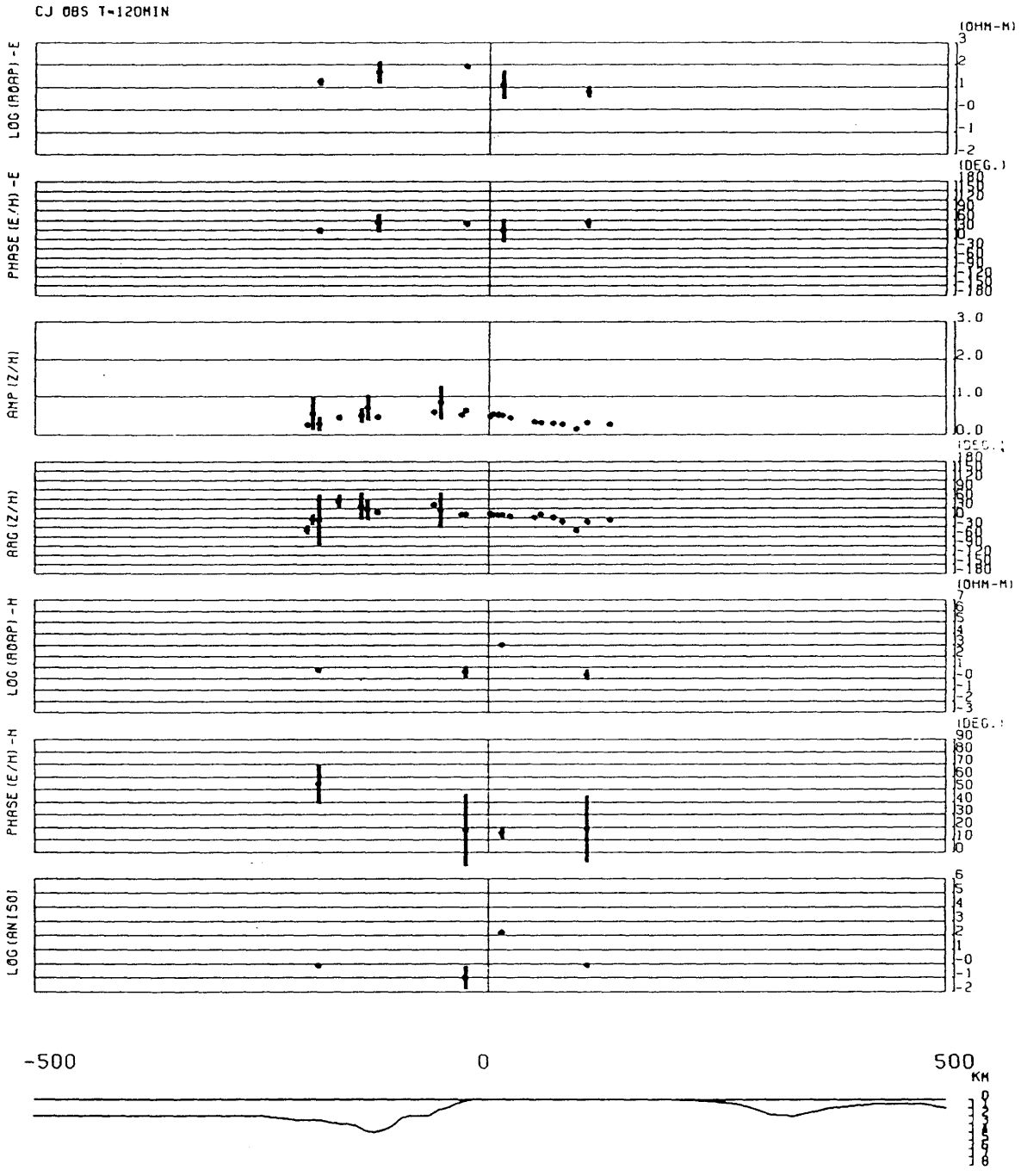

Fig.7.3 (d) Profiles of the observed response functions for the period of 120 minutes.

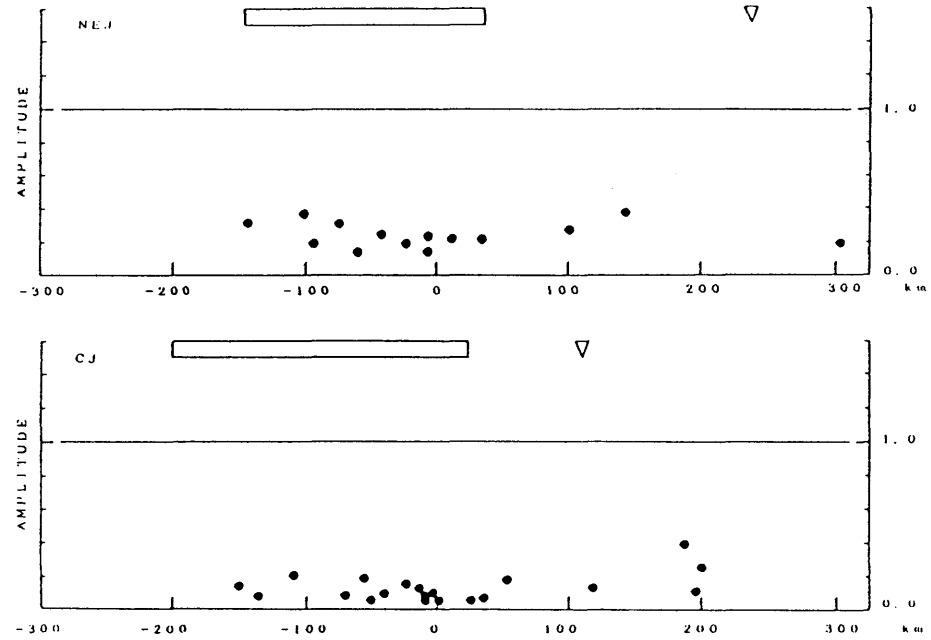

Fig.7.4 Profiles of amplitude of the residual transfer functions for the period of 30 minutes for northeastern Japan (above) and central Japan (below). Triangles denote the Japan Trench for NEJ and the Nankai Trough for CJ, respectively (after Utada et al.,1986).

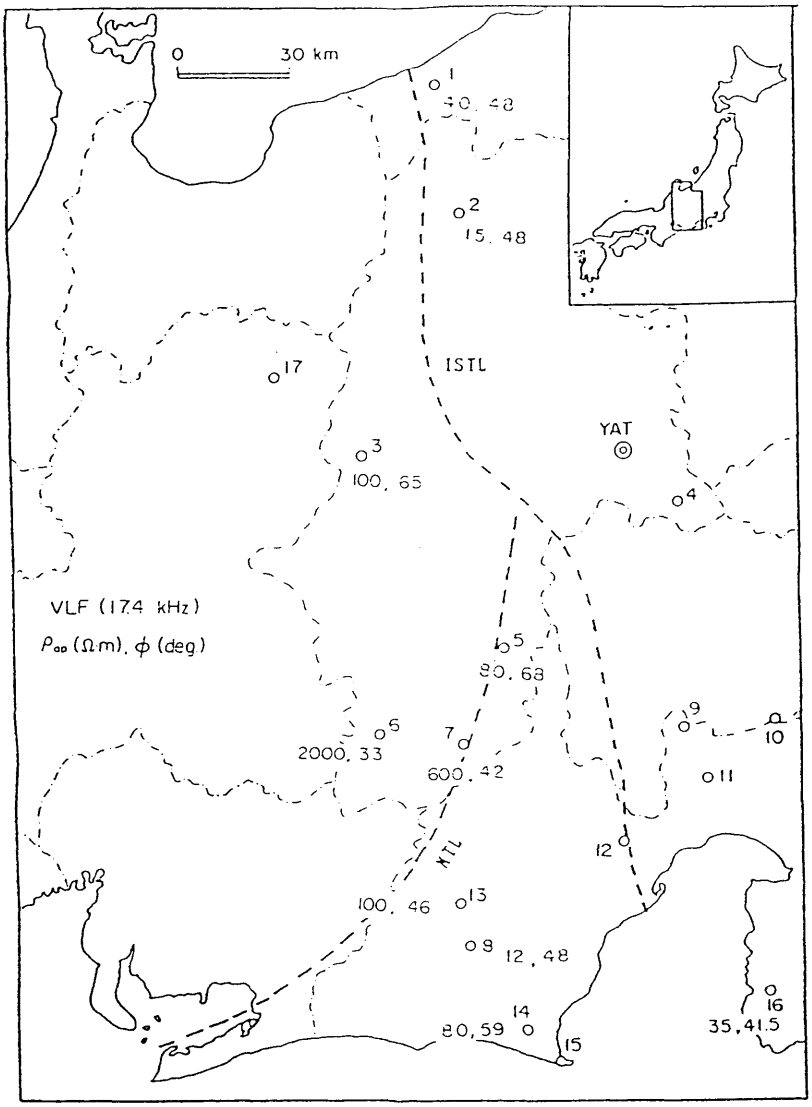

Fig.7.5(a) Distribution of VLF apparent resistivity and phase at 1982 observation sites at the frequency of 17.4 kHz. MTL and ISTL denote the Median Tectonic Line and the Itoigawa-Shizuoka Tectonic Line, respectively.

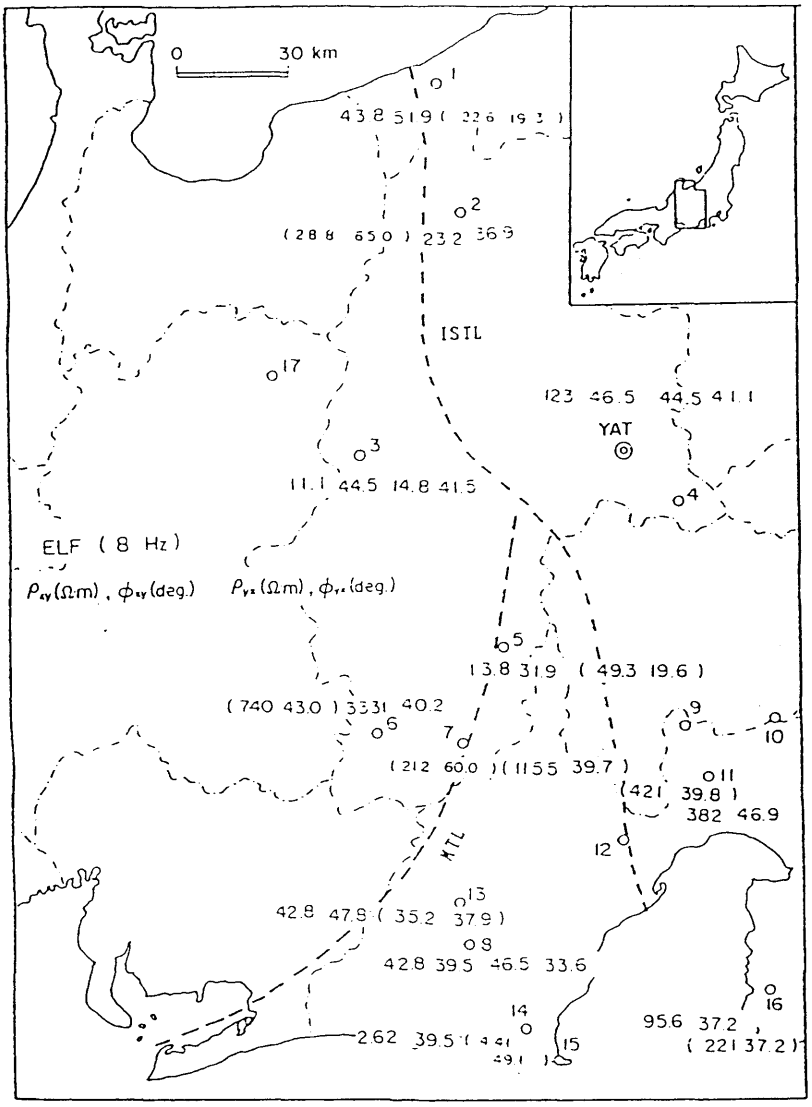

Fig.7.5(b) Distribution of ELF apparent resistivity and phase calculated from the off-diagonal elements of impedance tensor at 1982 observation sites at the frequency of 8 Hz.

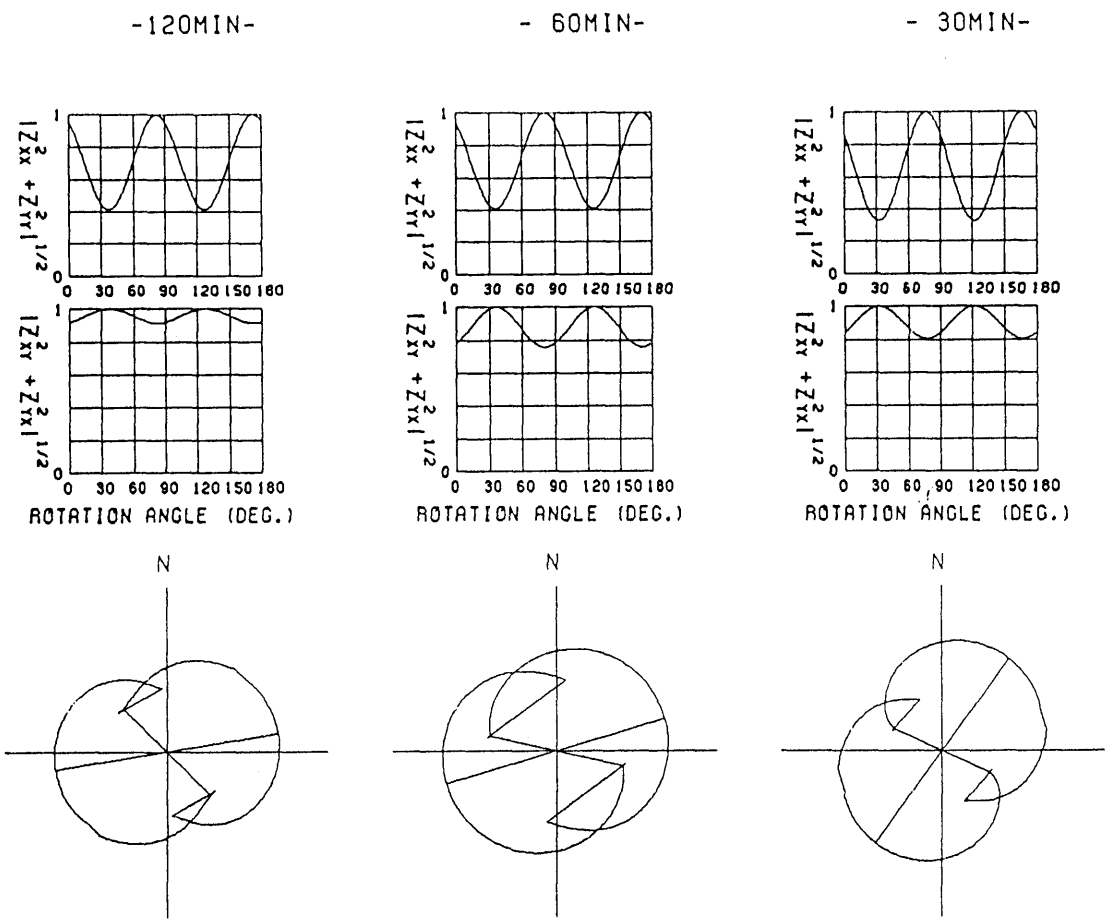

Fig.7.6(a) Polarization diagrams obtained from impedance tensor estimates at JE2.

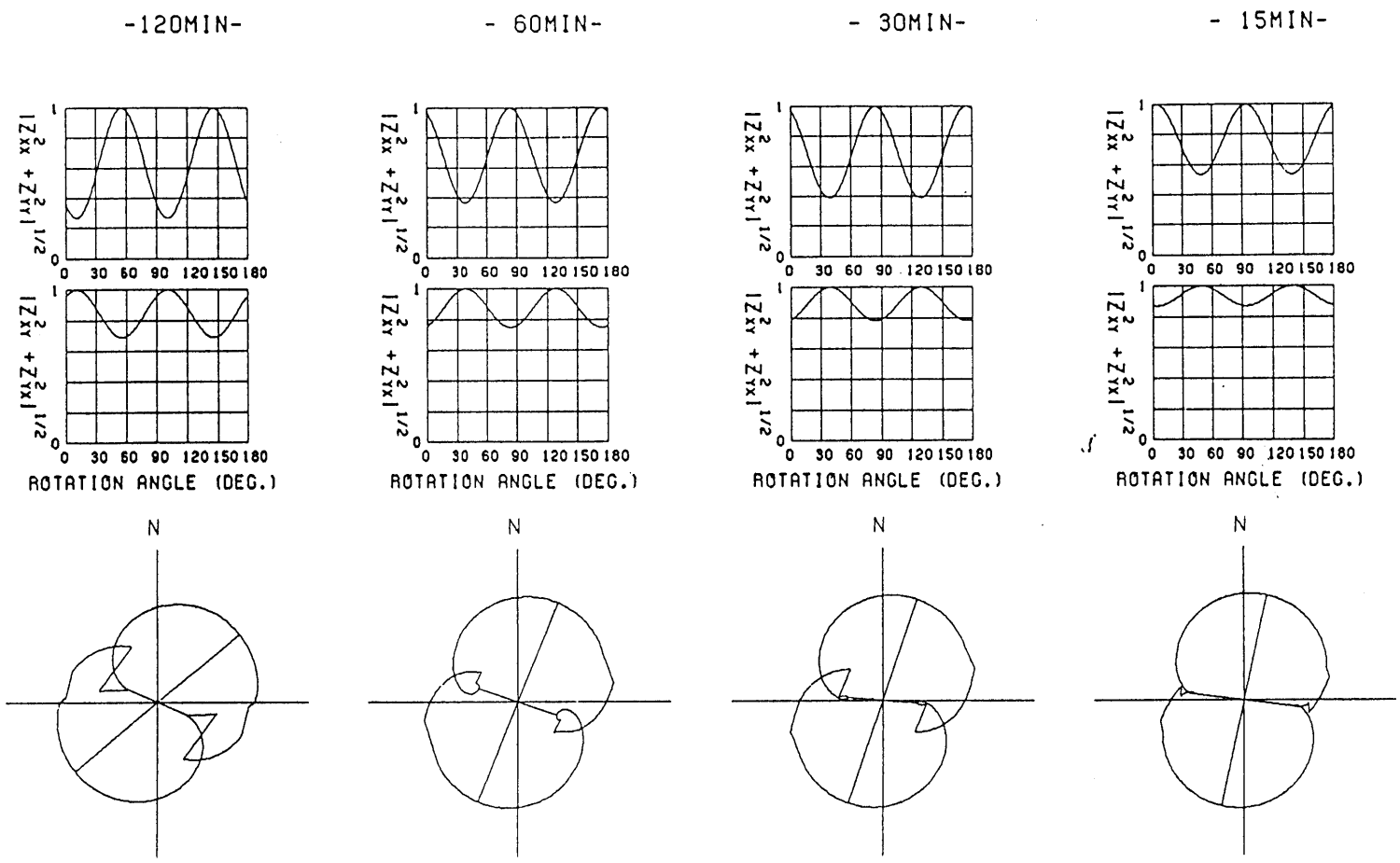

Fig.7.6(b) Polarization diagrams obtained from impedance tensor estimates at No.14.

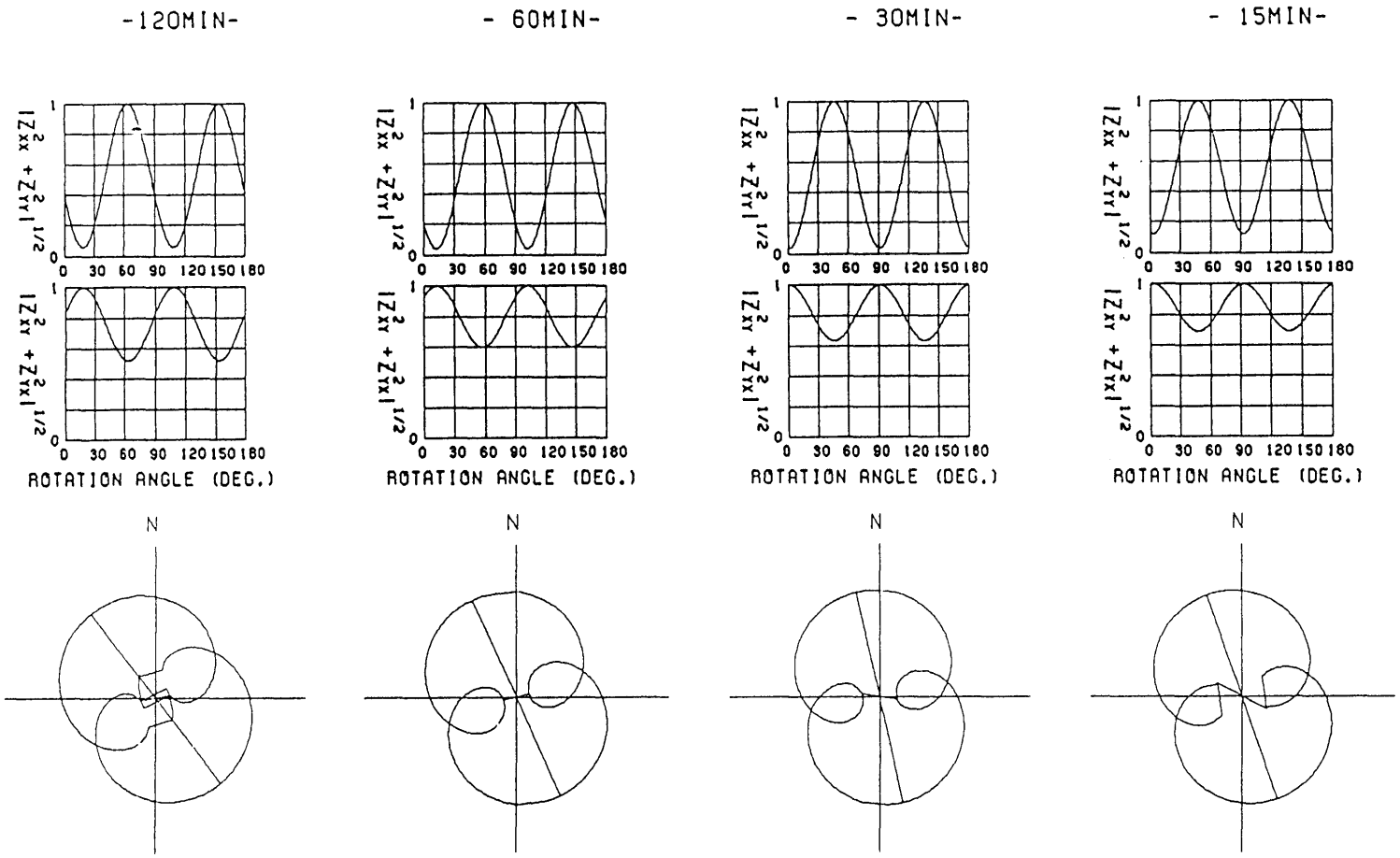

Fig.7.6(c) Polarization diagrams obtained from impedance tensor estimates at No.13.

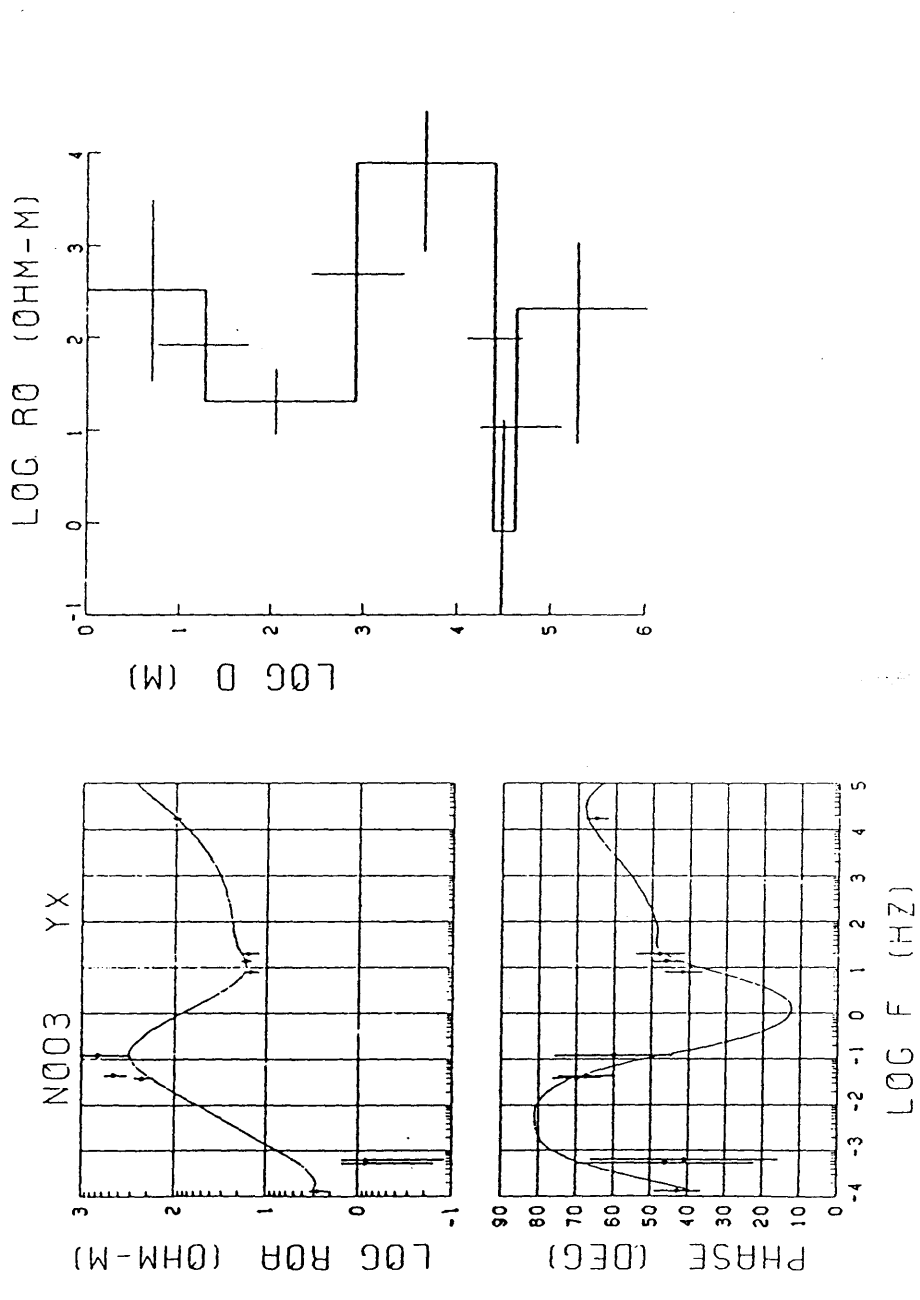

Fig.7.7 Result of one-dimensional magnetotelluric inversion at the site No.3. The left figure shows the fitness between the observations and the theoretical curve for the optimum model. The right figure gives the optimum structure with confidence intervals in estimated layer parameters (thickness and resistivity).

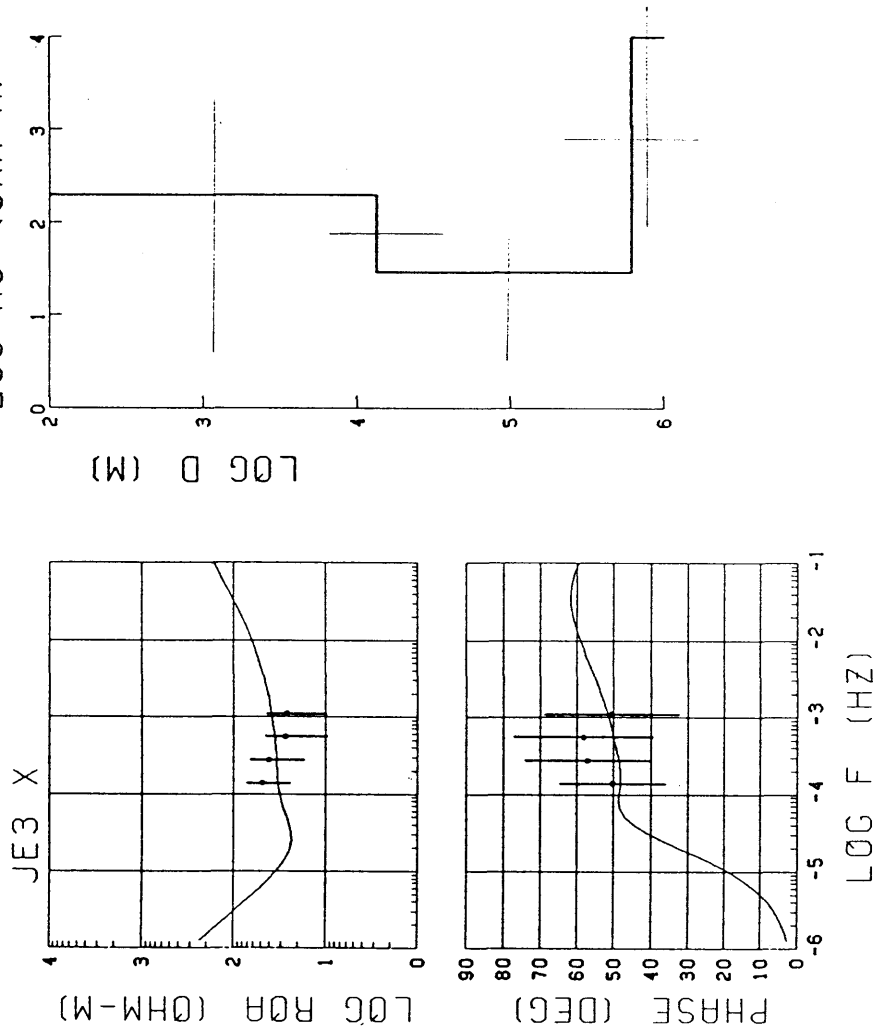

Fig.7.8 Result of one-dimensional magnetotelluric inversion at the seafloor site JE3 in the vicinity of the Nankai Trough.

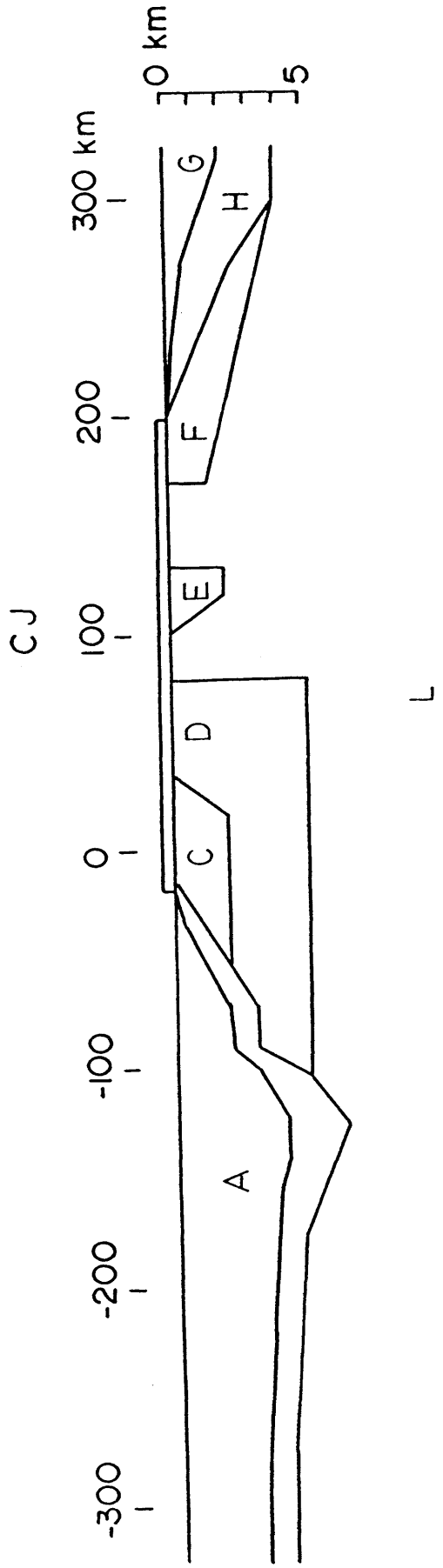

Fig.7.9 Near surface view of the block division for the inversion of central Japan data. See text for detail.

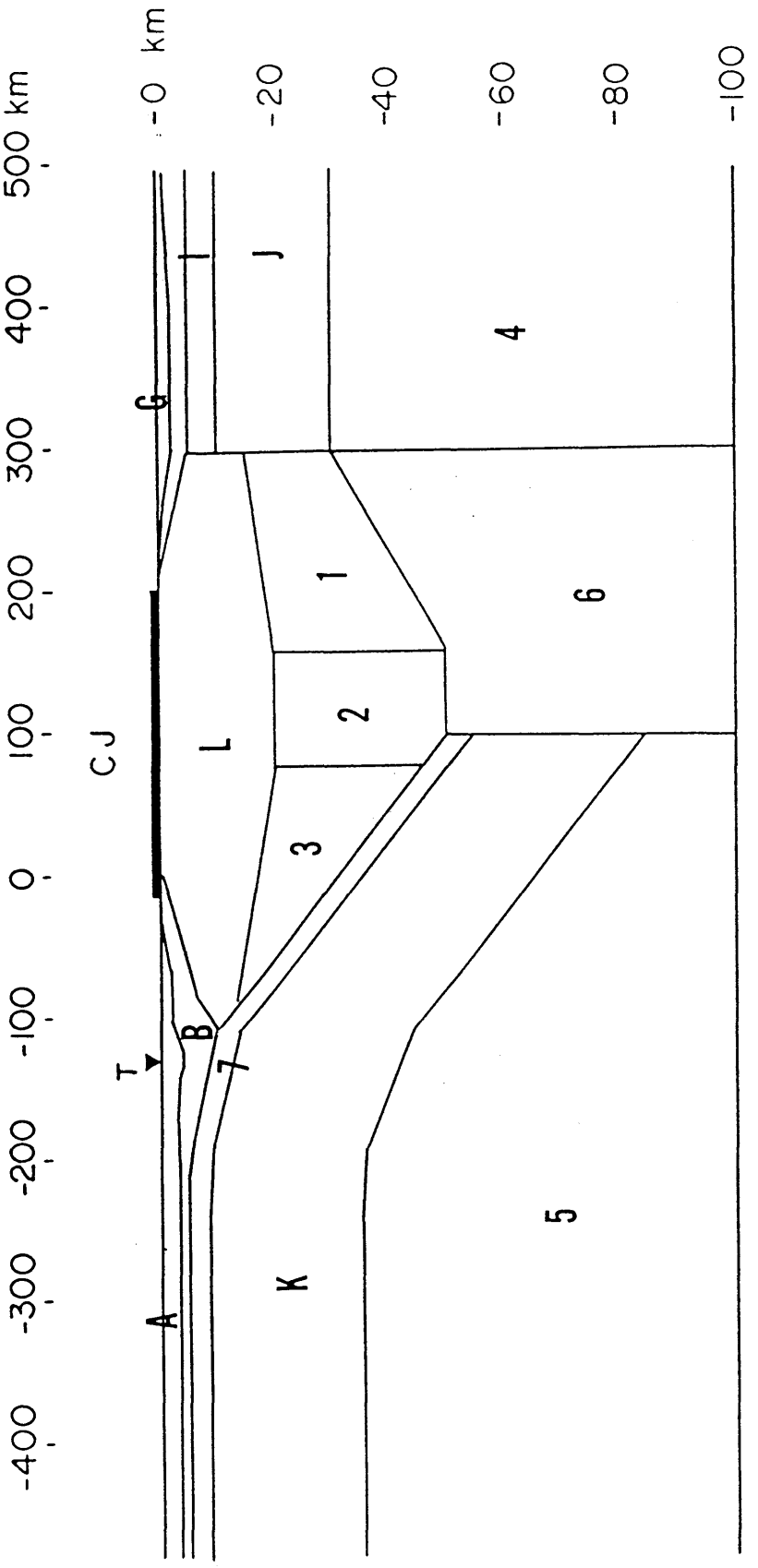

Fig.7.10 Deeper block division for the inversion of central Japan data.

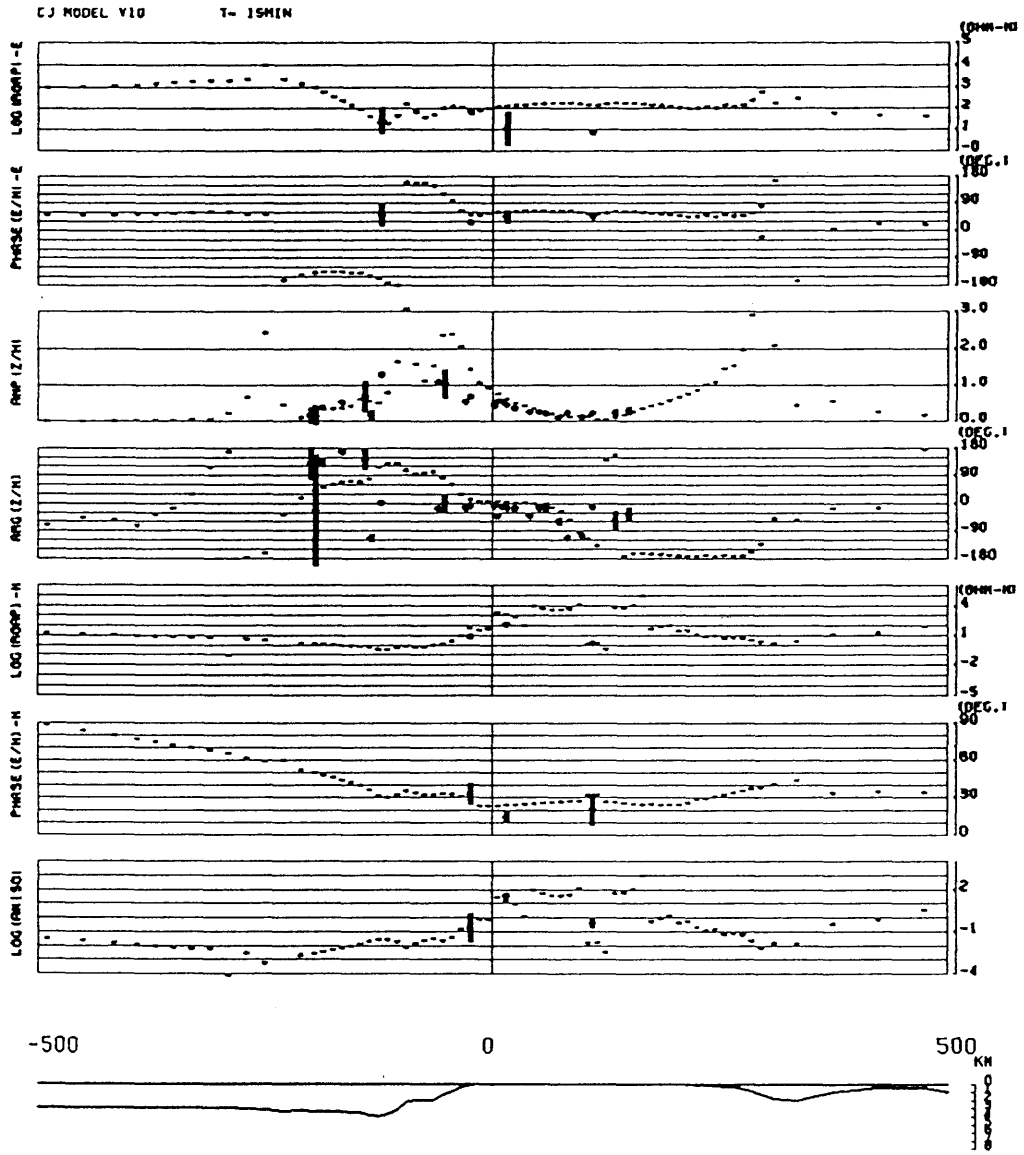

Fig.7.11 Calculated profiles of response functions at the period of 15 minutes for the model where uniform subsurface conductivity of 0.001 S/m is assumed except for the given surface structure illustrated in Fig.7.9. Observed responses are denoted by closed circles with error bars.

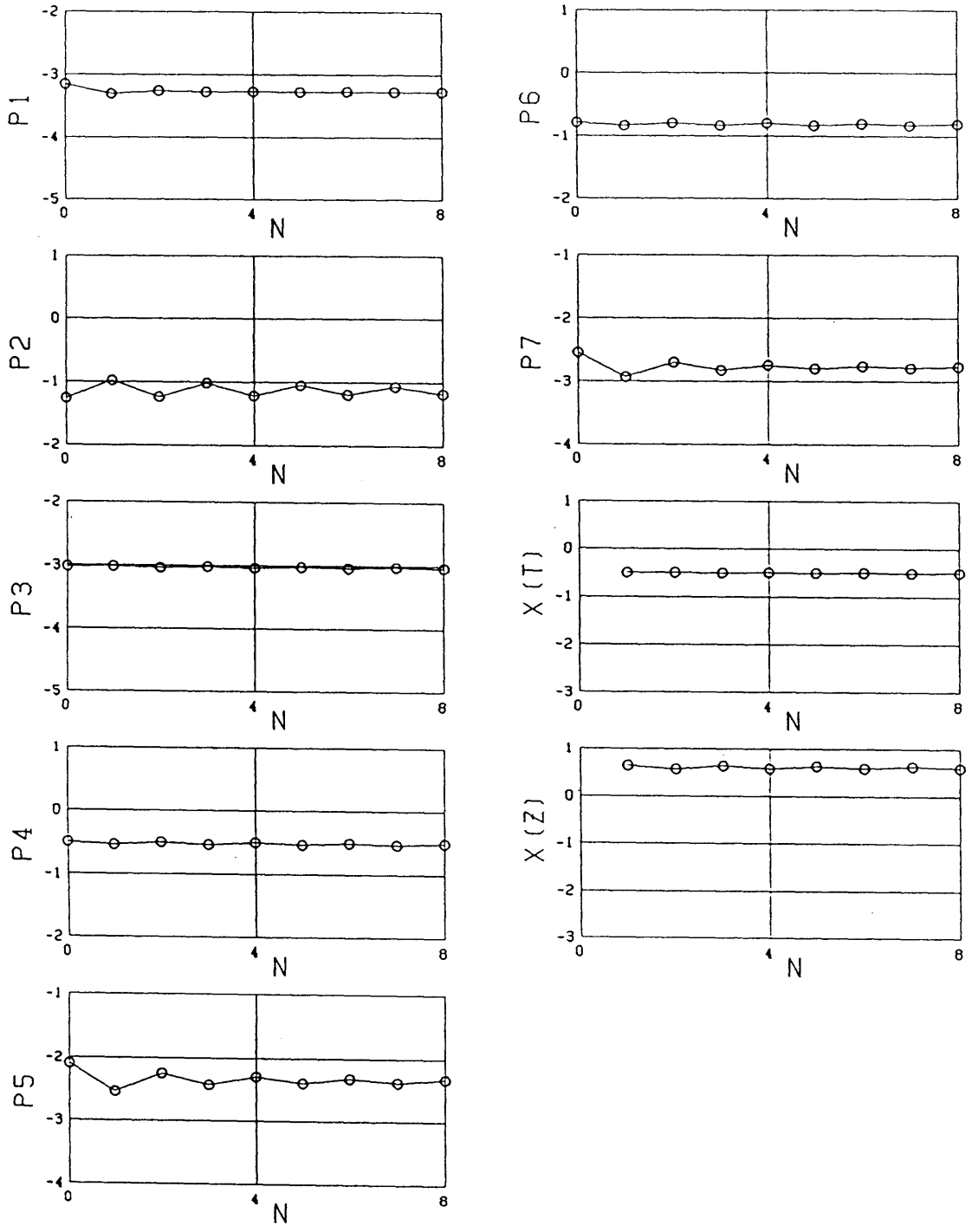

Fig.7.12 Behaviors of 7 parameters and χ^2 for the last 8 cycles of the whole iteration process.

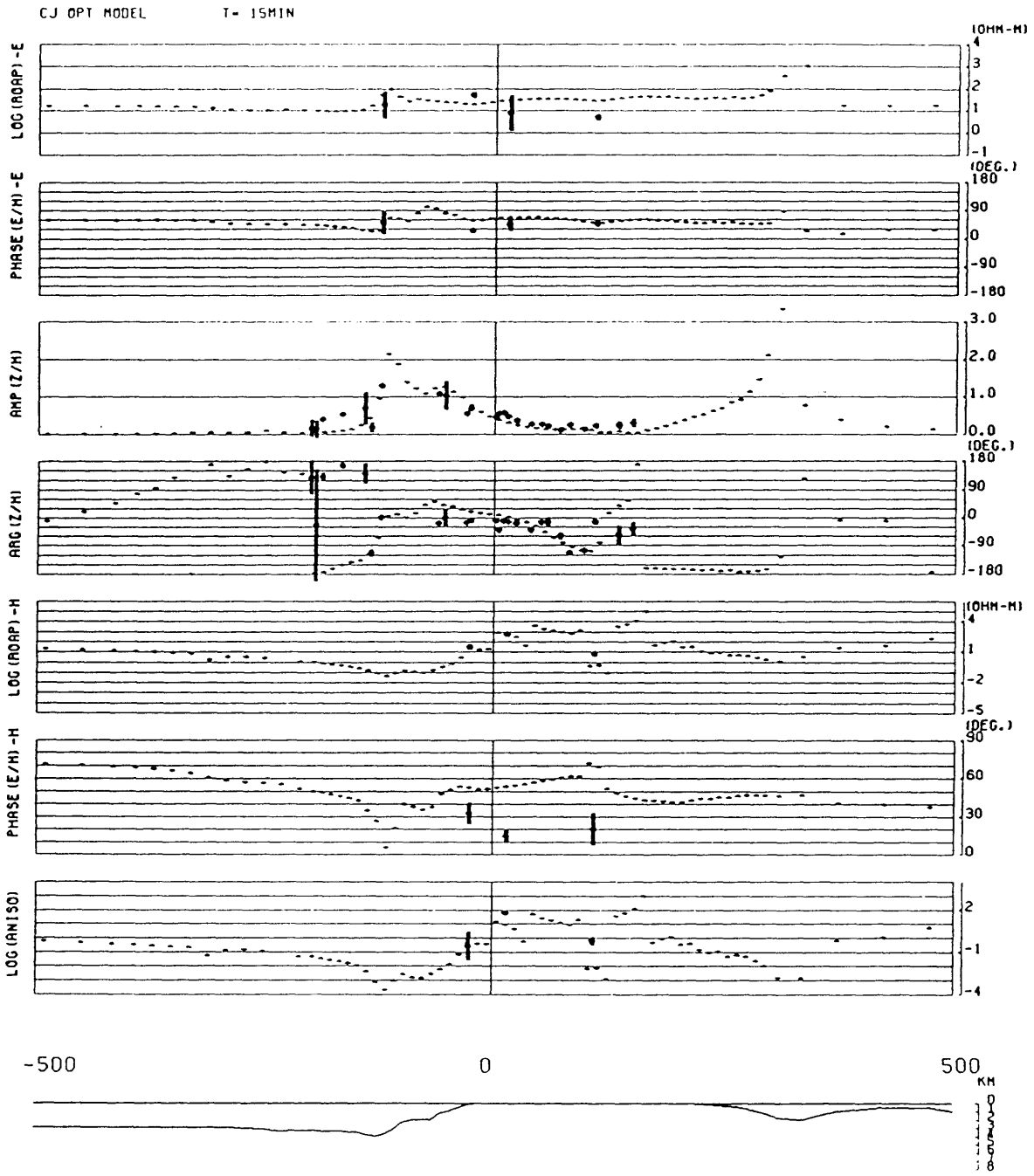

Fig.7.13(a) Calculated responses for the final model for the period of 15 minutes. Dotted lines show the calculated responses, while closed circles with error bars denote observed responses.

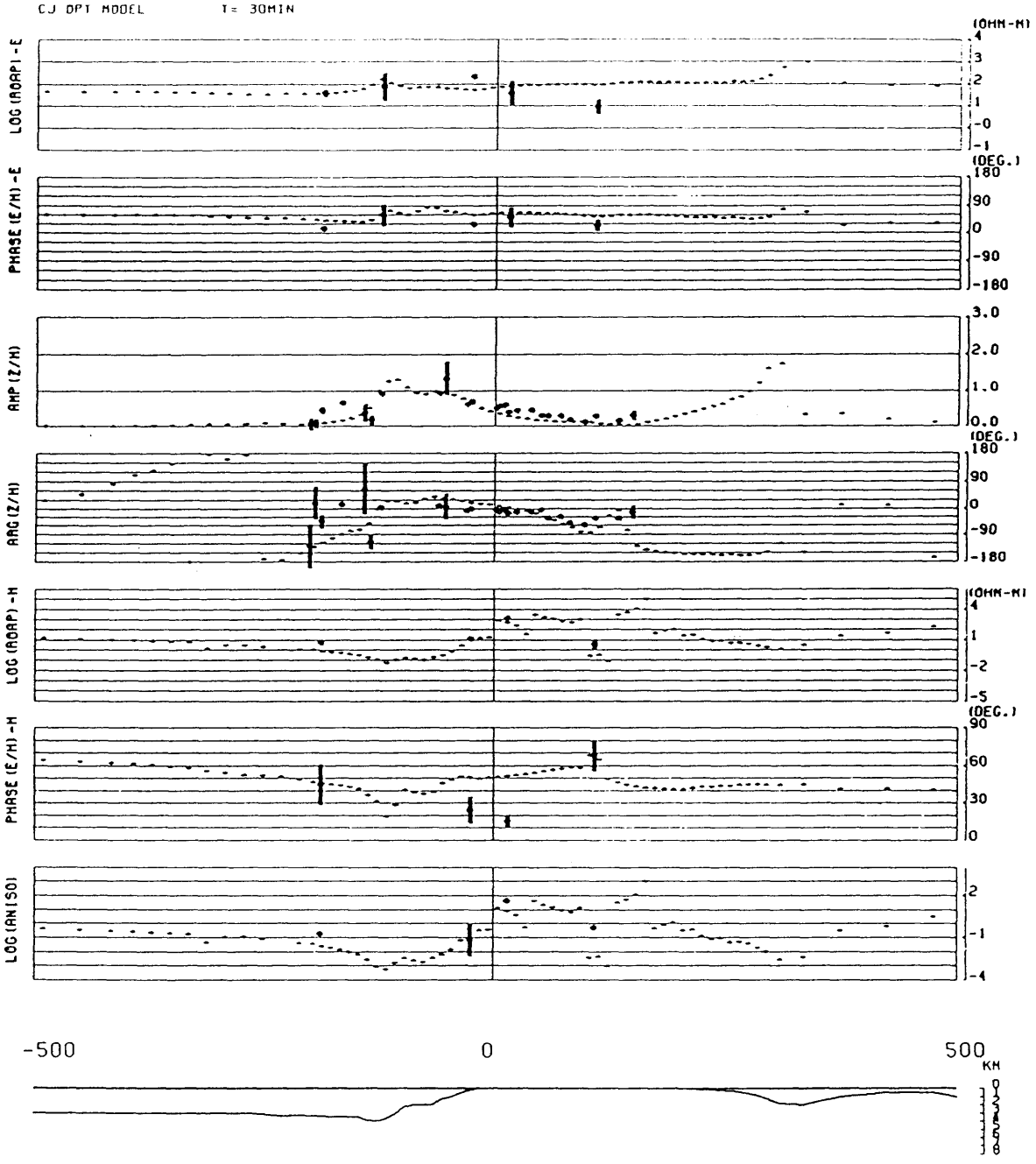

Fig.7.13(b) Calculated responses for the final model for the period of 30 minutes.

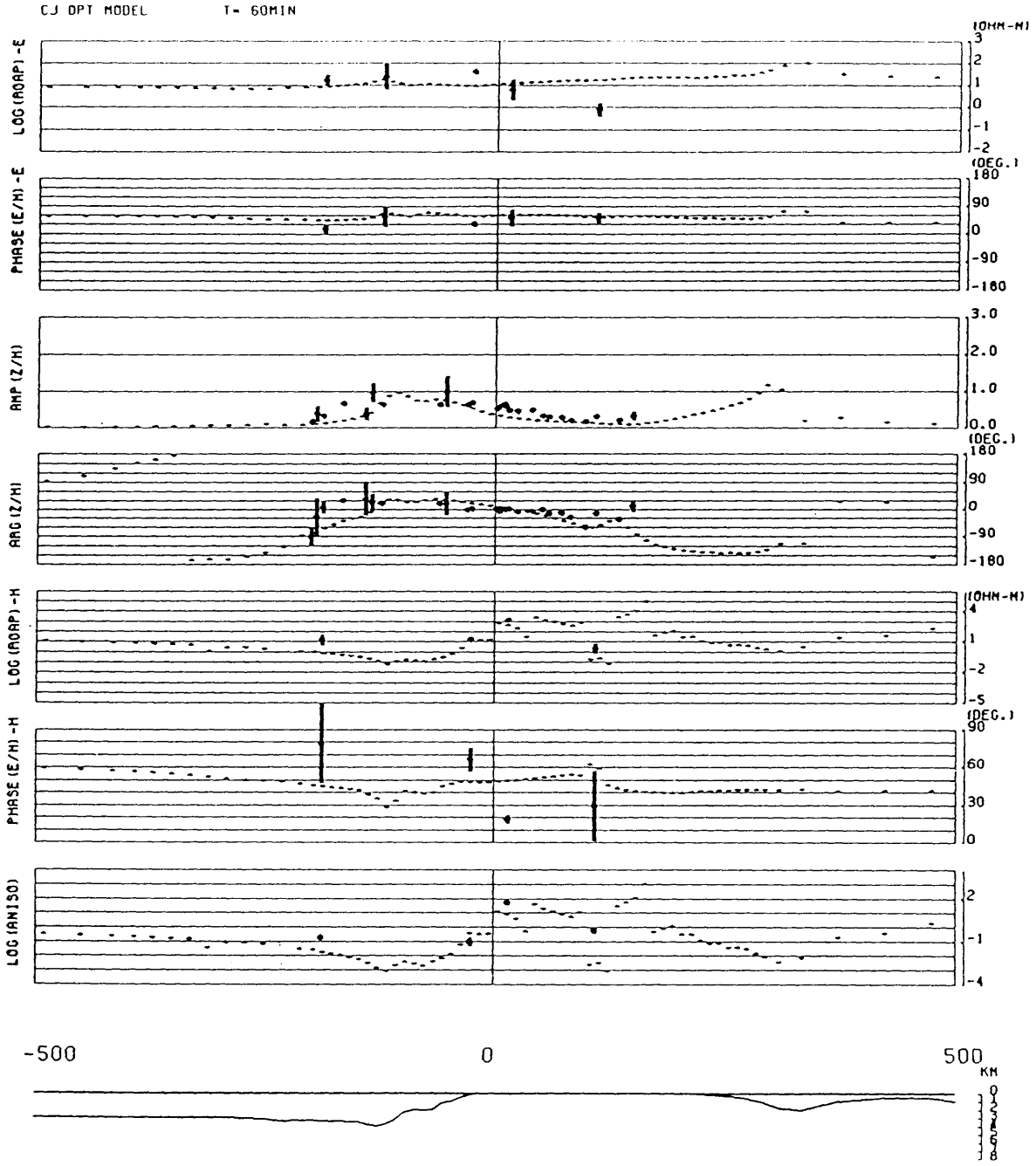

Fig.7.13(c) Calculated responses for the final model for the period of 60 minutes.

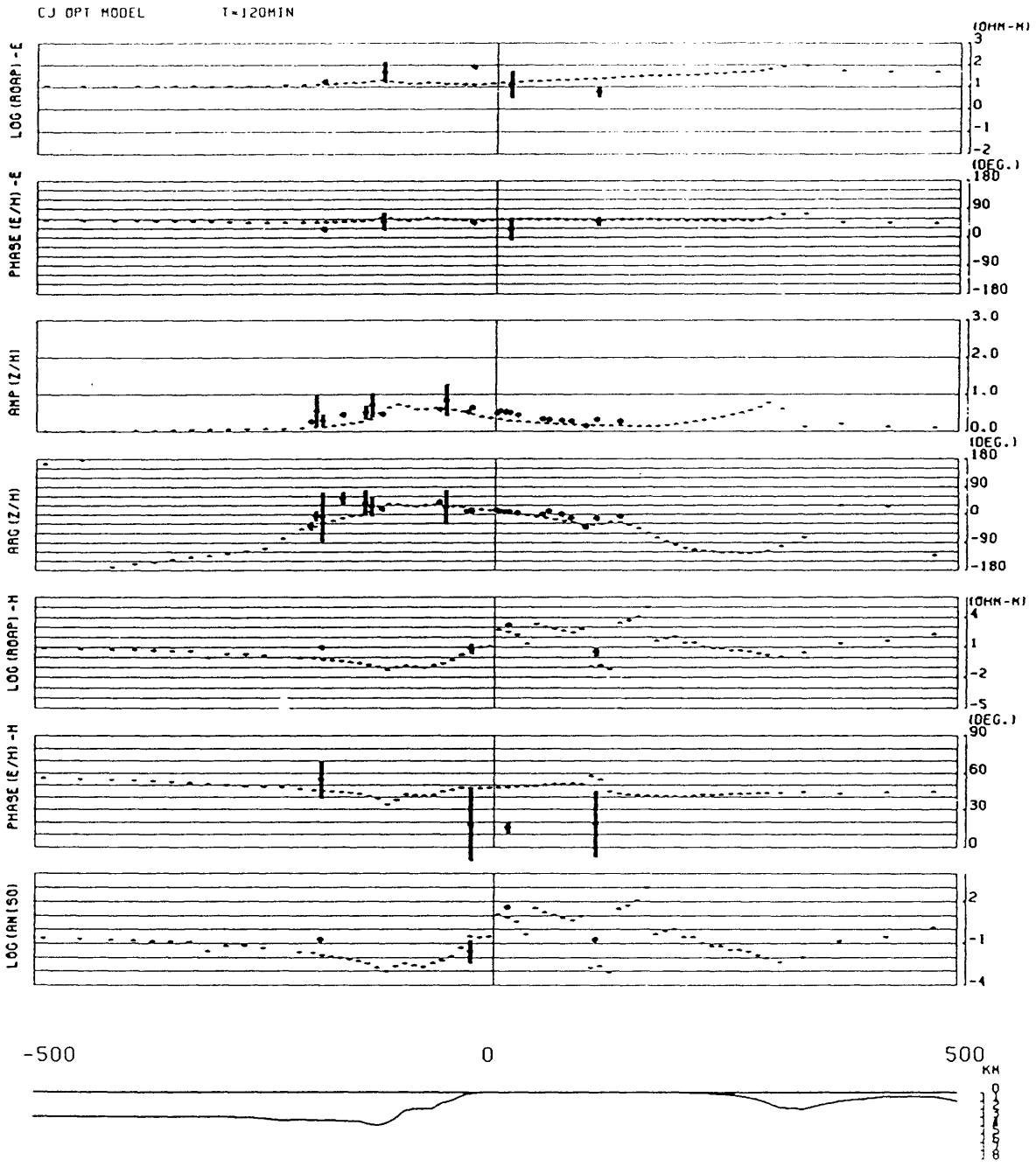

Fig.7.13(d) Calculated responses for the final model for the period of 120 minutes.

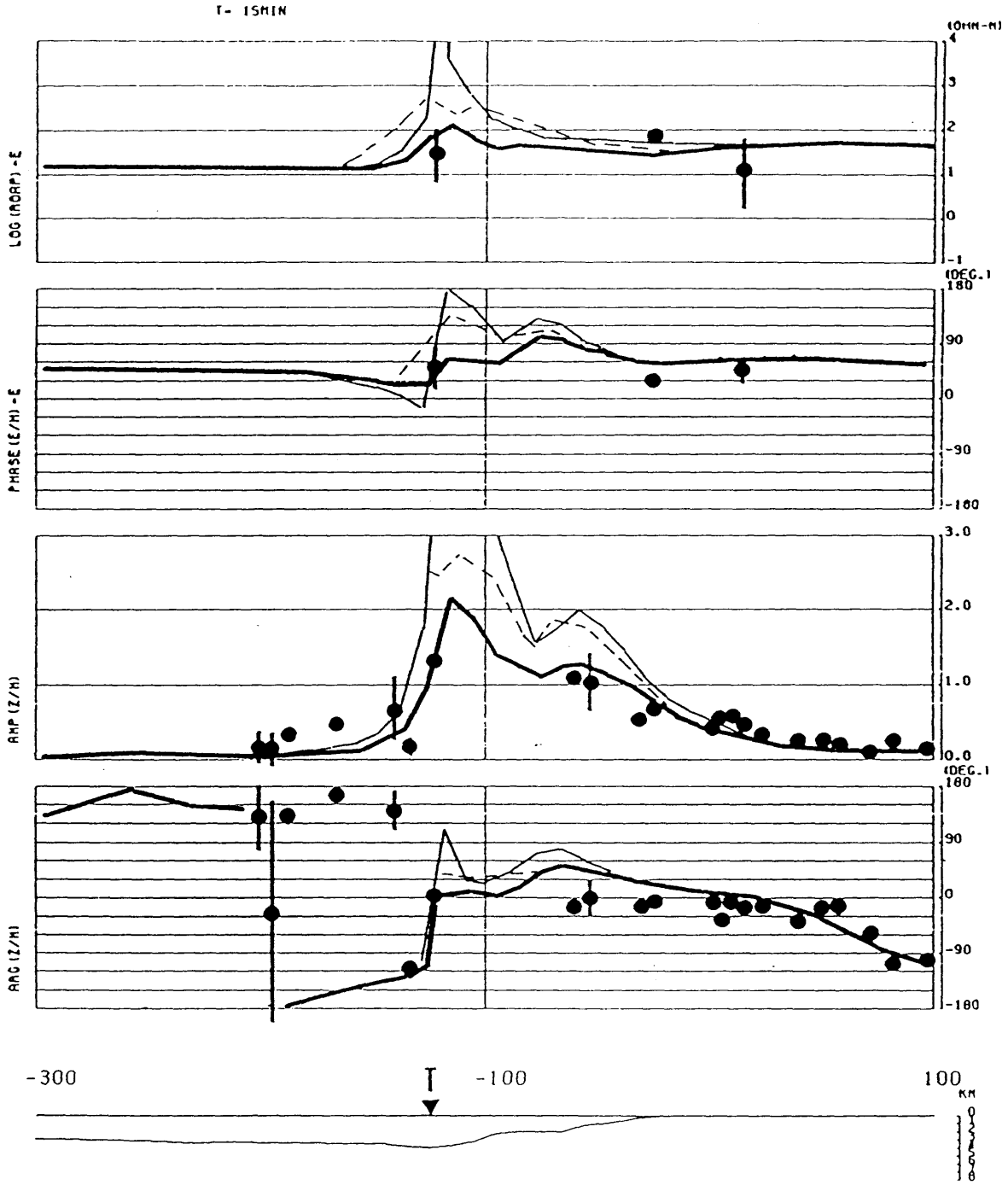

Fig.7.14 The effect of the conductive layer beneath the Philippine Sea plate for the period of 15 minutes. Thick lines denote the theoretical response functions calculated from the final model. Thin lines are those from a model without the conductor, while dashed lines correspond to those from a model with no extension of the conductor beneath central Japan. E-polarization apparent resistivity and the phase, and the amplitude of apparent resistivity and its phase are illustrated.

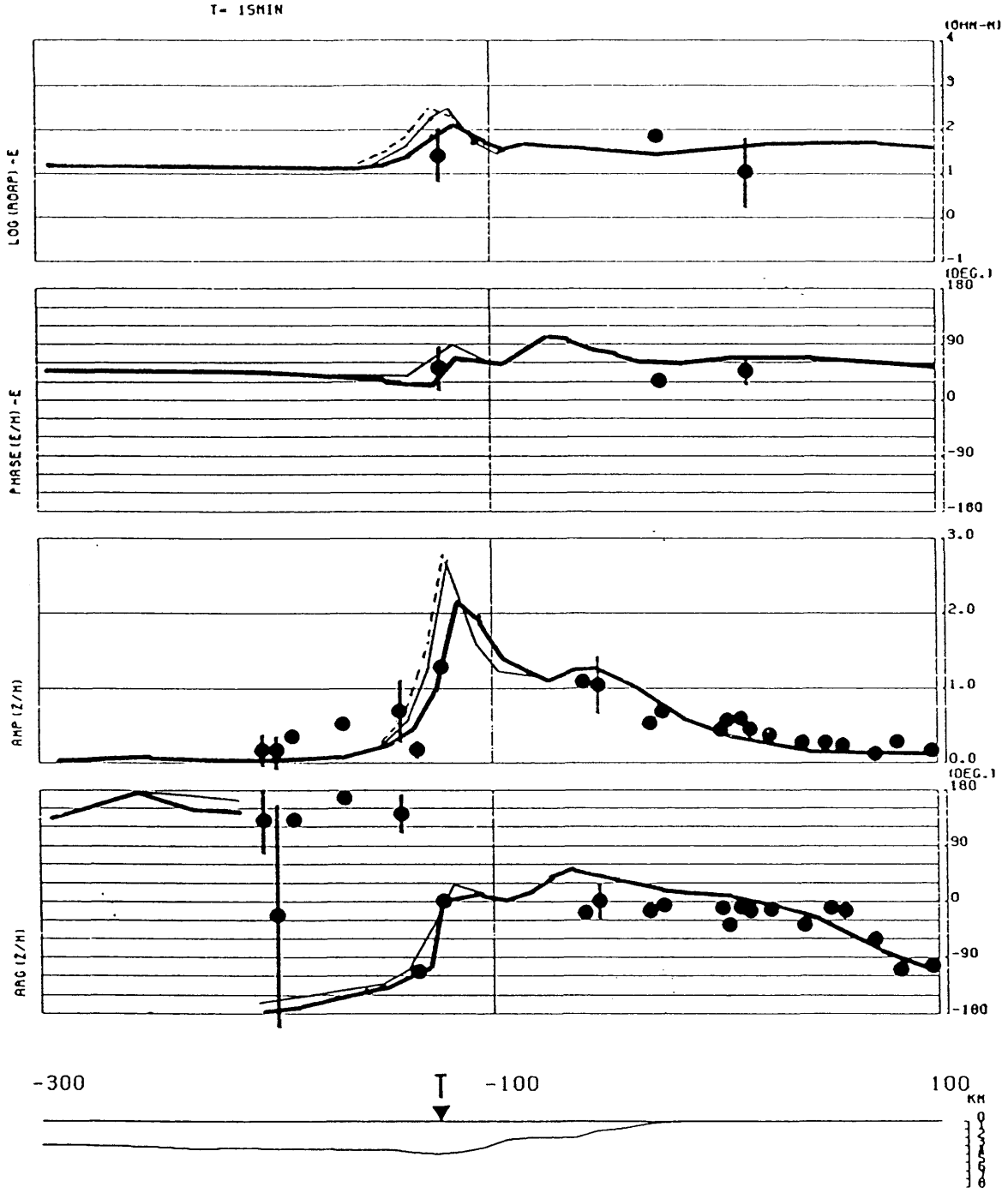

Fig.7.15 The effect of the thin conductive layer on the subducting Philippine Sea plate for the period of 15 minutes. Thick lines denote the theoretical response functions calculated from the final model with the conductor down to the depth of 60 km. Thin lines are those from a model without the conductor. The model is scarcely improved by introducing the conductor which extends down to the depth of 40 km (dashed lines).

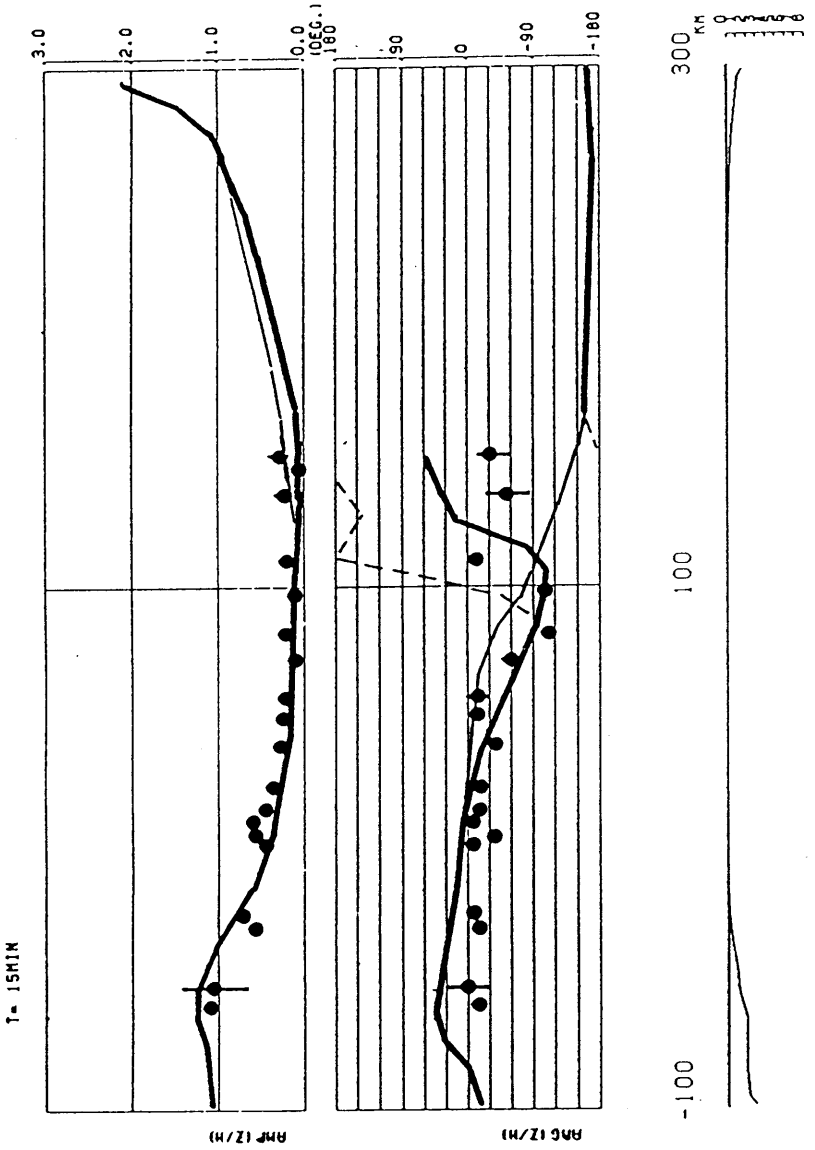

Fig.7.16 The effect of the crustal conductor beneath the central part of Japan for the period of 15 minutes. Thick lines denote the theoretical transfer functions calculated from the final model. Thin lines are those from a model without the conductor, while dashed lines correspond to those from a model with a highly conductive layer in the upper mantle beneath the Japan Sea.

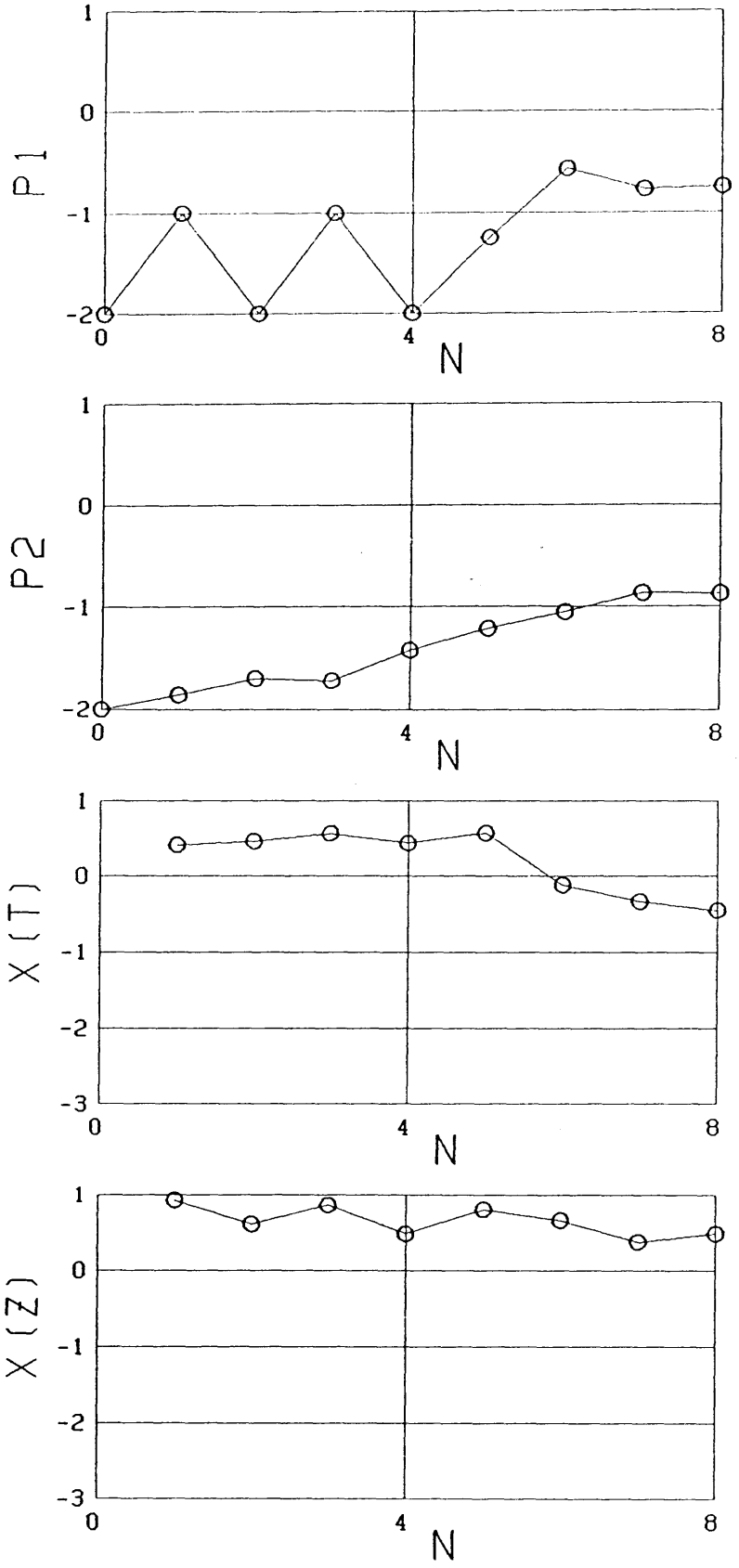

Fig.7.17 Result of the direct inversion for two unknown parameters, p_1 and p_2, corresponding to the conductivities of the upper mantle beneath the Philippine Sea and the lower crust beneath the central part of Japan, respectively. The initial value of conductivity for each is taken as one order of magnitude lower than that in the final model.

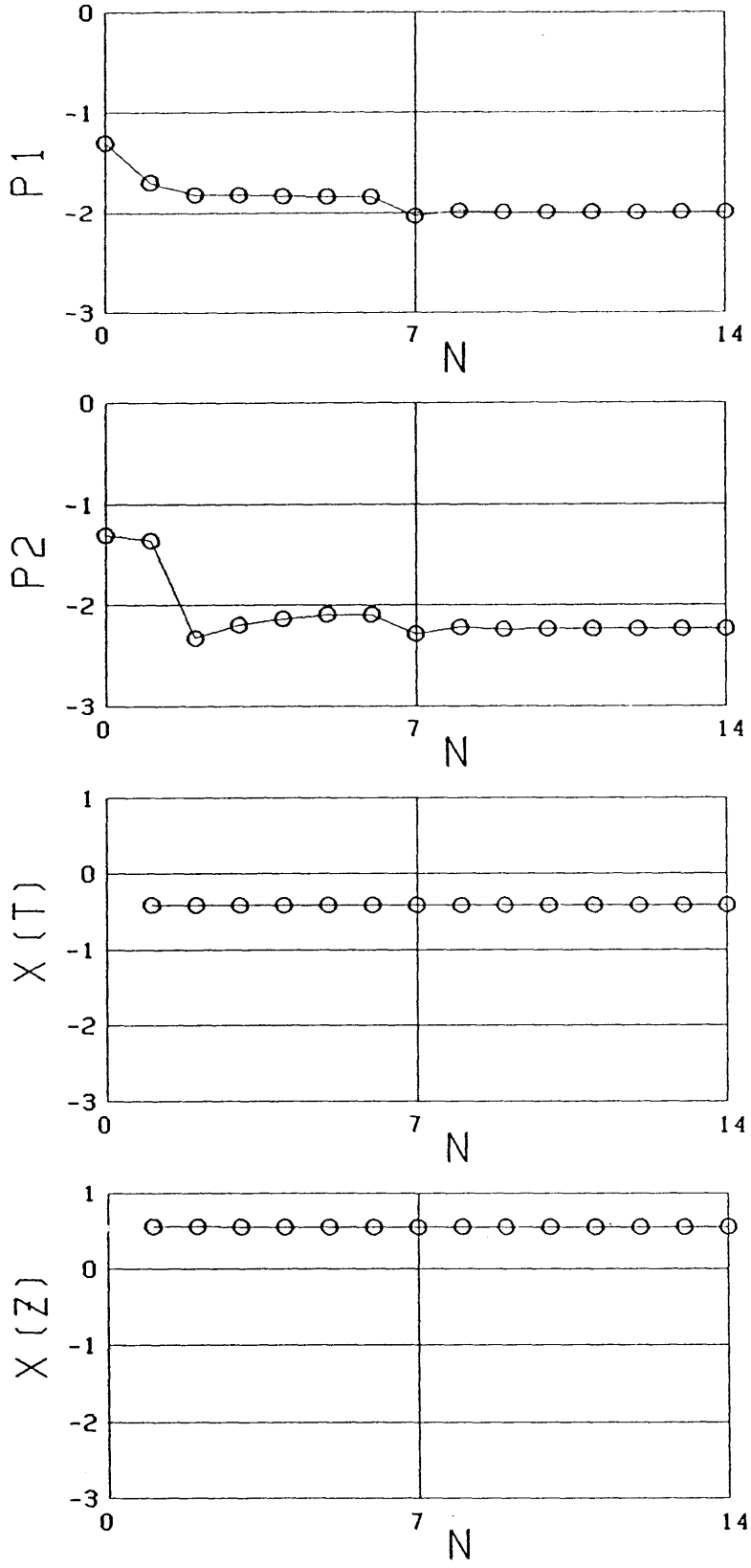

Fig.7.18 Result of the direct inversion for two unknown parameters, p_1 and p_2, corresponding to the conductivities of the upper mantle beneath Japan and beneath the Japan Sea, respectively. The initial value of conductivity for each is taken as one order of magnitude higher than that in the final model.

Table 7.1 Location of observation sites for inversion of centaral Japan data.

Site		Latitude	Longitude	Obs. year	Remark
UCU	Uchiura	37°18.0	137°16.0	1965	
No 2	Kinasa	36°41.3	137°56.9	1982	
No17	Kamitakara	36°16.7	137°26.9	1982	
No 3	Nagawa	36° 5.3	137°41.1	1982	
KMR	Komoro	36°19.0	138°27.5	1959	
YAT	Yatsugatake	36° 4.1	138°26.3		(*)
No 4	Kawakami	35°57.6	138°33.3	1982	
No 5	Ohshika	35°34.5	138° 3.8	1982	
No 6	Namiai	35°22.4	137°41.4	1982	
No 7	Minamishinano	35°21.2	137°57.4	1982	
No 9	Asagiri	35°25.3	138°35.2	1982	
No10	Yamanaka	35°24.1	138°39.3	1982	
No11	Shinosaka	35°16.3	138°38.0	1982	
No12	Tawaramine	35° 6.5	138°23.4	1984	
No13	Haruno	35° 0.1	137°55.2	1982	
No 8	Mori	34°53.6	137°57.4	1982	
No14	Hamaoka	34°38.8	138° 7.3	1982	
No15	Omaezaki	34°36.4	138°13.3	1982	
SRT	Sarutani	34°10.5	135°38.7	1967	
SIM	Shimosato	33°34.5	135°55.5	1965	(**)
J6		34° 9.0	137°30.0	1983	OBM
J8		33°14.0	137°30.0	1983	OBM
J12		32°47.0	136°34.0	1984	OBM
J9		32°19.0	137°31.0	1983	OBM
J13		32°13.0	137°20.0	1984	OBM
J14		31°38.0	136°12.0	1984	OBM
J15				1985	OBM
J16				1985	OBM
J17				1985	OBM
JE 3				1985	OBE
JE 2		32° 5.0	137° 3.0	1984	OBE

(*) Permanent geomagnetic observatory belonging to Erthquake Research-Institute, University of Tokyo. (**) Permanent observatory belonging to the Maritime Safety Agency, Japan.

Table 7.2(a) Observed transfer functions for the period of 15 minutes.

Site	Y(km)	amp(T)	arg(T)	ε_T
No 2	150.	0.292	-35.0	0.1150
No17	135.	0.247	-55.7	0.0962
No 3	110.	0.224	-12.8	0.0283
KMR	98.	0.129	-106.0	0.0233
YAT	82.	0.247	-112.0	0.0054
No 4	72.	0.113	-58.2	0.0228
No 5	58.	0.218	-13.0	0.0599
No 6	51.	0.265	-14.6	0.0111
No 7	40.	0.262	-39.9	0.0157
No 9	24.	0.366	-16.3	0.0144
No10	10.	0.574	-10.9	0.0292
No11	11.	0.562	-9.3	0.0241
No12	2.	0.447	-8.4	0.0199
No13	15.	0.460	-14.1	0.0192
No 8	5.	0.559	-39.9	0.0113
No14	- 25.	0.691	-7.9	0.0100
No15	- 30.	0.547	-15.2	0.0114
J6	- 53.	1.039	0.3	0.3889
J8	-133.	0.175	-113.6	0.1318
J12	-140.	0.696	141.0	0.4322
J9	-194.	0.138	-23.5	0.2380
J14	-200.	0.167	128.9	0.2258
J15	- 60.	1.096	-17.2	0.0175
J16	-122.	1.300	2.6	0.0322
J17	-165.	0.531	166.6	0.0277
J13	-187.	0.392	131.3	0.0467

Table 7.2(b) Observed transfer functions for the period of 30 minutes.

Site	Y(km)	amp(T)	arg(T)	ε_T
No 2	150.	0.307	-13.5	0.1348
No17	135.	0.154	-36.5	0.0202
No 3	110.	0.293	-35.0	0.0189
KMR	98.	0.119	-59.6	0.0144
YAT	82.	0.187	-51.5	0.0118
No 4	72.	0.295	-29.6	0.0183
No 5	58.	0.294	-35.4	0.0452
No 6	51.	0.305	-5.6	0.0054
No 7	40.	0.456	-12.8	0.0312
No 9	24.	0.446	-14.4	0.0053
No10	10.	0.596	-1.9	0.0152
No11	11.	0.610	-5.7	0.0233
No12	2.	0.506	-5.2	0.0140
No13	15.	0.400	-18.0	0.0124
No 8	5.	0.564	-14.4	0.0047
No14	- 25.	0.707	-1.4	0.0074
No15	- 30.	0.612	-8.3	0.0011
J6	- 53.	1.352	7.0	0.4477
J8	-133.	0.179	-115.3	0.1352
J12	-140.	0.382	64.5	0.2532
J9	-194.	0.082	18.3	0.1348
J14	-200.	0.057	-129.4	0.1700
J15	- 60.	0.940	10.3	0.0056
J16	-122.	0.919	3.5	0.0223
J17	-165.	0.665	14.3	0.0307
J13	-187.	0.452	-44.9	0.0932

Table 7.2(c) Observed transfer functions for the period of 60 minutes.

Site	Y(km)	amp(T)	arg(T)	ε_T
No 2	150.	0.321	12.2	0.1201
No17	135.	0.203	-33.3	0.0202
No 3	110.	0.308	-13.5	0.0218
KMR	98.	0.166	-58.5	0.0237
YAT	82.	0.193	-26.9	0.0049
No 4	72.	0.281	-12.3	0.0114
No 5	58.	0.304	-13.5	0.0501
No 6	51.	0.319	-0.3	0.0054
No 7	40.	0.489	-5.8	0.0369
No 9	24.	0.459	-7.1	0.0072
No10	10.	0.662	3.5	0.0252
No11	11.	0.605	-0.1	0.0174
No12	2.	0.530	2.5	0.0151
No13	15.	0.477	2.1	0.0442
No 8	5.	0.589	-7.1	0.0139
No14	- 25.	0.696	2.5	0.0118
No15	- 30.	0.636	-1.1	0.0173
J6	- 53.	1.003	19.2	0.4262
J8	-133.	0.973	24.7	0.2618
J12	-140.	0.382	35.7	0.1764
J9	-194.	0.387	-26.1	0.2222
J14	-200.	0.163	-90.0	0.1004
J15	- 60.	0.639	19.2	0.0372
J16	-122.	0.645	21.0	0.0167
J17	-165.	0.672	30.4	0.0228
J13	-187.	0.324	6.8	0.0591

Table 7.2(d) Observed transfer functions for the period of 120 minutes.

Site	Y(km)	amp(T)	arg(T)	ε_T
No17	135.	0.275	-6.1	0.0273
No 3	110.	0.321	-12.2	0.0209
KMR	98.	0.143	-40.9	0.0242
YAT	82.	0.276	-11.9	0.0124
No 4	72.	0.294	1.4	0.0150
No 5	58.	0.318	11.7	0.0438
No 6	51.	0.340	1.2	0.0053
No 9	24.	0.438	5.4	0.0142
No10	10.	0.514	10.3	0.0203
No11	11.	0.547	9.4	0.0266
No12	2.	0.487	14.4	0.0142
No13	15.	0.512	10.2	0.0423
No 8	5.	0.551	10.1	0.0119
No14	- 25.	0.646	12.1	0.0612
No15	- 30.	0.516	10.8	0.0242
J6	- 53.	0.852	25.3	0.4374
J8	-133.	0.714	27.6	0.3308
J12	-140.	0.512	38.2	0.1818
J9	-194.	0.553	-4.3	0.4222
J14	-200.	0.258	-37.1	0.0708
J15	- 60.	0.593	41.2	0.0211
J16	-122.	0.472	18.5	0.0315
J17	-165.	0.453	54.8	0.0739
J13	-187.	0.286	-6.5	0.1841

Table 7.3(a) E-polarization apparent resistivities, phases and standard errors for the period of 15minutes.

Site	Y(km)	$\rho_E(\Omega \cdot m)$	$\phi_E(deg)$	ε_E
No 3	110.	6.99	47.3	0.994
No13	15.	10.49	45.9	8.434
No14	-25.	73.02	26.2	10.81
JE 3	-122.	26.13	50.6	16.25

Table 7.3(b) E-polarization apparent resistivities, phases and standard errors for the period of 30minutes.

Site	Y(km)	$\rho_E(\Omega \cdot m)$	$\phi_E(deg)$	ε_E
No 3	110.	3.46	25.0	1.13
No13	15.	14.44	50.5	8.13
No14	-25.	82.19	27.9	3.90
JE 3	-122.	27.01	58.2	17.28
JE 2	-187.	14.96	14.5	2.72

Table 7.3(c) E-polarization apparent resistivities, phases and standard errors for the period of 60minutes.

Site	Y(km)	$\rho_E(\Omega \cdot m)$	$\phi_E(deg)$	ε_E
No 3	110.	1.35	53.1	0.40
No13	15.	10.49	51.7	4.96
No14	-25.	68.60	31.3	3.83
JE 3	-122.	40.47	57.0	23.55
JE 2	-187.	29.43	15.9	7.36

Table 7.3(d) E-polarization apparent resistivities, phases and standard errors for the period of 120minutes.

Site	Y(km)	$\rho_E(\Omega \cdot m)$	$\phi_E(deg)$	ε_E
No 3	110.	6.15	52.0	1.58
No13	15.	13.20	27.3	8.43
No14	-25.	85.48	48.6	9.01
JE 3	-122.	47.70	50.2	23.37
JE 2	-187.	17.82	26.6	2.69

Table 7.4(a) H-polarization apparent resistivities, phases and standard errors for the period of 15minutes.

Site	Y(km)	$\rho_H(\Omega \cdot m)$	$\phi_H(deg)$	ε_H
No 3	110.	2.89	20.5	0.670
No13	15.	219.7	14.4	18.42
No14	-25.	13.54	32.9	2.011

Table 7.4(b) H-polarization apparent resistivities, phases and standard errors for the period of 30minutes.

Site	Y(km)	$\rho_H(\Omega \cdot m)$	$\phi_H(deg)$	ε_H
No 3	110.	1.53	47.3	0.994
No13	15.	550.0	45.9	8.434
No14	-25.	5.25	26.2	10.81
JE 2	-187.	2.47	44.8	0.70

Table 7.4(c) H-polarization apparent resistivities, phases and standard errors for the period of 60minutes.

Site	Y(km)	$\rho_H(\Omega \cdot m)$	ϕ_H(deg)	ε_H
No 3	110.	0.893	29.3	0.436
No13	15.	624.3	18.6	38.2
No14	-25.	7.71	66.3	1.28
JE 2	-187.	6.17	79.1	3.37

Table 7.4(d) H-polarization apparent resistivities, phases and standard errors for the period of 120minutes.

Site	Y(km)	$\rho_H(\Omega \cdot m)$	ϕ_H(deg)	ε_H
No 3	110.	1.98	18.9	0.897
No13	15.	856.2	15.6	68.0
No14	-25.	3.86	17.7	1.92
JE 2	-187.	5.41	54.5	1.40

Table 7.5 Blocked conductivity structure with given conductivity for the direct inversion of central Japan data.

Block	conductivity(S/m)	comment
A	4.0×10^{0}	Philippine Sea
B	2.0×10^{-1}	sea floor sediment
C	1.0×10^{-1}	sediment on Pasific coast
D	1.2×10^{-2}	inland sediment (resistive)
E	1.0×10^{-1}	inland sediment (conductive)
F	1.0×10^{-1}	sediment on Japan Sea coast
G	4.0×10^{0}	Japan Sea
H	2.0×10^{-1}	sea floor sediment
I	3.0×10^{-2}	crust of Japan Sea (shallow)
J	2.0×10^{-3}	crust of Japan Sea floor
K	2.0×10^{-3}	Lithosphere of Philippine Sea Plate
L	5.0×10^{-4}	Upper crust of Japan
M	2.0×10^{-2}	Upper mantle (100-400km)
N	1.0×10^{0}	Mantle (>400km)

Table 7.6 Result of direct inversion of central Japan data for 7 inhomogeneities with unknown conductivity given in Figs.7.10(a) and (b).

No.	initial(S/m)	C_{popo}	final(S/m)	C_{pp}	C_{popo}/C_{pp}
1	1.0×10^{-3}	1×10^{-1}	5.9×10^{-4}	5.0×10^{-2}	2.00×10^{0}
2	1.0×10^{-1}	1×10^{-1}	7.6×10^{-2}	1.0×10^{-3}	1.00×10^{1}
3	1.0×10^{-3}	5×10^{-2}	9.6×10^{-4}	4.5×10^{-2}	1.11×10^{0}
4	5.0×10^{-3}	1×10^{-2}	4.0×10^{-3}	9.3×10^{-3}	1.08×10^{0}
5	1.0×10^{-1}	5×10^{-1}	1.4×10^{-1}	2.2×10^{-4}	2.27×10^{3}
6	5.0×10^{-3}	2×10^{-2}	5.2×10^{-3}	1.0×10^{-2}	2.00×10^{0}
7	1.0×10^{-2}	5×10^{-2}	1.6×10^{-1}	1.3×10^{-2}	3.85×10^{0}

Iteration cycles	32
Initial $\chi^2(d_Z)$	3.908×10^{0}
Final $\chi^2(d_Z)$	2.432×10^{0}
Initial $\chi^2(d_T)$	4.146×10^{-1}
Final $\chi^2(d_T)$	3.120×10^{-1}

Table 7.7 Result of direct inversion of central Japan data for 2 inhomogeneities (the lower crust of central Japan and the Philippine Sea asthenosphere).

No.	initial(S/m)	C_{PoPo}	final(S/m)	C_{PP}	C_{PoPo}/C_{PP}
1	1.0×10^{-2}	1×10^{-1}	1.4×10^{-1}	1.6×10^{-3}	6.25×10^{1}
2	1.0×10^{-2}	2×10^{0}	1.3×10^{-1}	3.4×10^{-3}	5.88×10^{2}

Iteration cycles	14
Initial $\chi^2(d_Z)$	8.452×10^{0}
Final $\chi^2(d_Z)$	2.576×10^{0}
Initial $\chi^2(d_T)$	2.580×10^{0}
Final $\chi^2(d_T)$	3.542×10^{-1}

Table 7.8 Result of direct inversion of central Japan data for 2 inhomogeneities (upper mantle beneath Japan Sea and Japanese Island).

No.	initial(S/m)	C_{PoPo}	final(S/m)	C_{PP}	C_{PoPo}/C_{PP}
1	5.0×10^{-2}	1×10^{-2}	3.5×10^{-2}	9.7×10^{-3}	1.03×10^{0}
2	5.0×10^{-2}	2×10^{-2}	5.8×10^{-3}	1.8×10^{-2}	1.11×10^{0}

Iteration cycles	14
Initial $\chi^2(d_Z)$	2.883×10^{0}
Final $\chi^2(d_Z)$	2.549×10^{0}
Initial $\chi^2(d_T)$	3.848×10^{-1}
Final $\chi^2(d_T)$	3.148×10^{-1}

8. Discussion and Conclusion

A direct inversion method has been developed for two-dimensional modeling of the electrical conductivity distribution in the earth. In the present method, an optimum model is obtained by minimizes the unfitness between the observational and calculated values in the magnetotelluric impedances and the geomagnetic transfer function at the same time. In other word, this method utilizes the combined information on the subsurface electrical conductivity distribution both from the magnetovariational and the magnetotelluric investigations. In most of the previous studies, the transfer functions and the impedances, were used separately for constructing a model. In the present study, it has been demonstrated that the transfer functions and the impedances show different responses to the conductivity structure; i.e. the transfer function is sensitive to the lateral conductivity contrast, while the impedance depends strongly on the absolute value of the conductivity under the observation site. Hence, it is obvious that the combined use of these two quantities has a distinct advantage in investigation of the subsurface conductivity structure.

The present method has been applied to the investigation of the subterranean conductivity distribution beneath the northeastern and central parts of Japan, on the basis of the spatial and temporal dependences of the geomagnetic transfers function and the magnetotelluric impedances derived from the observations of the geomagnetic and electric field variations on land and seafloor.

The electrical conductivity structures were obtained for the two regions indicated in Fig. 8.1. In order to reduce the degree of

freedom for the inversion, conductivity distribution at the shallower depth down to several kilometers was estimated from the result of the magnetotelluric surveys at the higher frequencies in ELF and VLF ranges. And, the conductivities of the deeper part were determined by the present inversion method.

The direct inversion was performed for 8 unknown parameters for NEJ and 7 parameters for CJ, respectively. The iterative process has converged after 48 cycles for NEJ, while 32 cycles of iteration has been required for convergence of the inversion of CJ data. Final conductivity models beneath the northeast and the central part of Japan are shown in Figs.8.2(a) and (b), respectively. The result can be summarized as follows:

1) Both structures show a common feature that a part of the lower crust beneath the Japanese island is conductive by more than one order of magnitude compared with other parts of the crust. For the northeastern Japan Arc, the eastern boundary of the conductor coincides with the aseismic front (Fig.8.2(a)).

2) Beneath the Philippine Sea Plate, a highly conductive layer exists at the depth between 30 and 100 km. On the other hand, the depth to the conductive layer beneath the Pacific Plate off the Japan Trench was estimated as deep as about 140 km. The conductivity of these conductive layers were evaluated as about 0.1 S/m.

3) A thin conductive layer exists at the top of the subducting slab in both models. It was found that the total conductance (product of the conductivity and the thickness) of about 10^3 S is required in both cases in order to explain the characteristics of the electromagnetic variations in the vicinities of the Japan Trench and the Nankai Trough.

4) From the NEJ result, the mantle wedge is more conductive by several factors than the underlying oceanic lithosphere. However, the contrast becomes obscurer with increasing depth.

5) The NEJ result shows the possible tendency that the conductivity of the upper mantle decreases from the Japan Trench toward the Japan sea.

In the followings, geophysical implications of the above features will be discussed.

Honkura (1974) presented a conductivity model beneath central Japan to explain the spatial and the period dependences of the observed transfer functions by introducing highly conductive layers with conductivity of 0.5 S/m at the depth of 30 km beneath the Philippine and the Japan Sea floor. As for the Philippine Sea side, the present result is consistent with his model, except for a slight difference in the conductivity value. It has been pointed out by many studies (e.g. Filloux, 1980; see Chapter 2) that such a conductor with a conductivity of about 0.1 S/m is commonly observed beneath the major oceans. The cause of the high conductivity is usually considered as partial melting in the asthenosphere (Honkura, 1975; Shankland and Waff, 1977).

The present result indicates a highly conductive layer beneath the Philippine Sea and the Pacific Ocean, whereas such a high conductive layer is not required beneath the Japan Sea (Chapter 7). This result is somewhat puzzling because the observed heat flow values are high in the Japan Sea area, implying the high temperature state and possibly the existence of partial melting (e.g. Uyeda and Rikitake, 1971; see Chapter 2).

Based on a simple theoretical model, Hamano (1985) suggested

that the bulk conductivity of the asthenosphere can be highly sensitive to the applied stress. He assumed an isolated state of partially molten regions in the asthenosphere (see Chapter 2). Under a stress free condition, the bulk conductivity of the asthenosphere shows only a slight increase even if the melt fraction is sufficiently large, when the molten regions are isolated (see Chapter 2). When a shear stress is applied to the asthenosphere by the plate motion, each molten region is elongated to enhance the interconnectivity and, as a result, to increase its bulk conductivity with a high anisotropy, in which the conductivity parallel to the direction of the plate motion becomes highly conductive compared with the perpendicular direction.

This model might solve the apparent low conductivity in the upper mantle beneath the Japan Sea. The Pacific and the Philippine Sea plates have definite plate motions relative to the asthenosphere. Therefore, highly conductive layers exist beneath these oceanic plates. On the other hand, if the spreading of the back arc basins are different from that of the open ocean, the different electrical state in the upper mantle beneath the Japan Sea can be postulated (Utada et al.,1986). Of course, there remains a possibility that a highly conductive layer exists far from the coast beneath the Japan Sea, so to say beneath the Japan Basin. Further detailed measurements will make it possible to clarify these uncertainties in the electrical structure beneath the Japan Sea.

In recent years, information on the electrical state in the ocean areas has been accumulated from results of the seafloor electromagnetic measurements in various regions (see Chapter 2). These results indicate that the existence of a highly conductive layer with a conductivity of about 0.1 S/m is a common feature in the upper

mantle beneath major oceans. Besides, a systematic relation can be recognized between the depth to the conductive layer and the age of the oceanic plate. The highly conductive zone usually coincides with the seismic low velocity zone (Oldenburg, 1981) which is considered to correspond to the asthenosphere. Thus, increasing depth to the conductive layer in various oceanic regions can be ascribed to the thickening of the lithosphere with age. The difference in the depth to the conductive layer in the northwest Pacific Ocean and the Philippine Sea is possibly reflecting the difference in the age of the lithosphere.

The present investigation revealed the existence of a thin conductive layer on the subducting slab for both the Pacific and the Philippine Sea plates. For the Pacific Ocean, the thickness and the conductivity of this layer are estimated as 10 km and 0.08 S/m, respectively, whereas they are estimated as 6 km and 0.16 S/m for the Philippine Sea Plate. The absolute values of the thickness and the conductivity are rather insignificant, considering the relatively long period range of the signals used in this study (Price, 1949). Essentially, meaningful quantity for such a thin conductive layer compared with the skin depth of the electromagnetic variation, is the product of the conductivity and the thickness, i.e. the conductance. Above result shows that the slabtop conductor has the conductance of about 10^3 S.

A similar slabtop conductor has been inferred in the subducting Juan de Fuca Plate beneath Vancouver Island on the basis of magnetotelluric results (Kurtz et al.,1986), although its conductance is estimated as about 200 S which is about one fifth of that beneath Japan. Thus, the existence of such a conductor may be regarded as a common feature for subducting oceanic plates. If so, it has a great

significance in considering the cause for the thin conductor. The conductive layer is regarded as corresponding to a sedimentary layer and/or a layer of water-bearing oceanic basalt as indicated in the model of the oceanic crust by Drury (1979). Petrological models of the island arc (Takahashi, 1978; Tatsumi et al., 1983) assumed a water rich state in the mantle wedge due to continuous supply of water from the subducting slab by squeezing of water from sediments and water bearing basalt and the dehydration of hydrated rocks in the oceanic crust. These assumptions, however, have not been clearly supported by geophysical evidences.

The present result seems to be a distinct evidence to support the prescribed petrological models. This may also account for the tendency of the conductivity distribution in the mantle wedge being less conductive toward backarc side; i.e. it can be attributed to the change in water content in the mantle wedge to the back arc direction. Moreover, the existence of the slabtop conductor as a possible water reservoir to the mantle wedge, can be related with the highly conductive part in the lower crust.

Fig.8.4 shows the actual coverage of the lower crustal conductor beneath central Japan. It should be noted that many of the Quaternary volcanoes denoted by solid triangles are included in this conductive area. The conductivity model for northeast Japan also indicated a lower crustal conductor. Ogawa, et al. (1986) suggested that the conductor exists in the lower crust of northeast Japan between the volcanic front and the Japan Sea coast. Similar result was obtained by one-dimensional modeling based on magnetotelluric sounding (Research Group for Crustal Resistivity Structure, Japan, 1983; Yukutake, 1985). The more precise modeling in the present study, however,

revealed that the eastern edge of the high conductor coincides with the aseismic front in the region. The present results for central and northeast Japan strongly suggest that there exists some relationship between the tectonic activities in both areas and the conductive lower crust. Taking into account the fact that the surface heat flow values increase sharply just at the volcanic front (Nagao, 1986), the high conductivity of the lower crust can not be fully explained by the only thermal origin. Nevertheless, the evidences shown above imply the definite correlation between the lower crustal conductor and the present volcanism in this region. Therefore, we have to search for a mechanism of the high conductivity in the lower crust, which relates the volcanism in the island arc of Japan but is of non-thermal origin.

Many petrological investigations suggest that the lower crust of active island arc including northeast Japan is generally composed of mafic rocks with hydrated minerals like hornblende gabbro or amphibolite (Takahashi,1978, Conrad and Kay,1980), and water required for the hydration is considered to be continuously supplied from the plate by means of the dehydration of the oceanic basalt. On the other hand, there also are many petrological evidences that the lower crustal rocks beneath the southwestern part of Japan are composed of the same rock-forming minerals in chemical composition but they are unhydrated (Fujii, 1984). This difference can be interpreted as follows; the southwestern part of Japan is located too far from the tip of the subducting plate for water to be supplied from, while there is continuous water supply from the oceanic plate to the lower crust in the eastern part. It should be noted here that the boundary of the lower crustal conductor facing to the Japan Trench or to the Nankai Trough, coincides with the position where the slabtop conductor is found at

the depth of about 60 km (Figs.8.2(a) and (b)). This fact suggests the relation between the water supply from the slab and the lower crustal conductor.

Some laboratory experiments show that, under some thermal condition, free water possibly exists in the crustal rocks at the depths of 20 - 25 km (e.g. Shankland and Ander, 1983; see Chapter 2). Lower crustal rocks, which are highly resistive in dry state (Kariya and Shankland, 1983), become remarkably conductive if free water exists, as was shown by Olhoeft(1981) and Shankland and Ander(1983). Consequently, this seems to be a plausible cause of the high conductivity in the lower crust beneath central and northeastern parts of Japan.

Several results of seismic observation in central Japan have demonstrated that the S waves traveling beneath the Hida mountain area are highly attenuated (Kono et al., 1985). The area is supposed to be localized at such a depth as about 10 km, which is significantly shallower than the depth to the lower crustal conductor. The cause of this high attenuation (low-Q) region was attributed to the existence of molten regions. Although the low-Q region is different from the conductive layer obtained in the present model, they seem to be connected by a common cause. Existence of free water in the lower crust increases its conductivity, while it also effectively reduces the solidus of rocks and causes a partial melting at depth (Fujii,1984). The high attenuation region possibly corresponds to the magma reservoir, to which molten magma is supplied from the deeper partial melting zone.

Another geophysical evidence concerned with difference in seismicity in the upper and lower crust of the northeastern part of Japan should be mentioned. Takagi et al.(1977) examined the occurrence of

microearthquakes in the northeastern part of Japan to reveal the distribution of seismic foci in detail. They concluded that most earthquakes in the crust occurred in its upper part and quite few in the lower part in the west of the aseismic front. Their result strongly suggests that there lies a difference in the mechanical properties between the upper and the lower parts of the crust. This can also be explained by the presence of water. Water contained in rocks plays a significant role not only in enhancing the electrical conduction, but also in changing the mechanical property from brittle to ductile nature (Carter, 1976). The present investigation, thus, strongly implied that the presence of water in the lower crust controls the physical properties as well as the tectonic activities in the crust and upper mantle in the island arc of Japan.

As an ending remark, several unrevealed problems should be pointed out for the future works. The present investigation revealed the existence of highly conductive region in the lower crust beneath the northeast and central parts of Japan. However, the conductor has been found to be spatially localized; i.e. not all the lower crust is conductive but is highly resistive at other part. If the high conductivity is caused by the presence of water, the localization of conductor means the localization of water. The first problem is to clarify the mechanism of the localization of water in the lower crust. This may be attributed to the difference in the porosity in each region.

The second problem would be to reveal the electrical state beneath the Japan Sea. In the previous discussion, the possible nonexistence of a conductive layer beneath the Japan Sea has been accounted for by introducing the stress sensitivity of the conductivity

of partially molten rocks. However, since the subterranean structure in this region has been the most weakly resolved by the present inversion method due to the lack in data, it should be determined with seafloor data in the Japan Sea. The seafloor data will promisingly lead us to reveal the effect of three-dimensionality of the Japan Sea on the regional geomagnetic induction (Honkura, 1974; Ogawa et al., 1986).

The result of the present investigation can be regarded as settling the starting point for the study of conductivity structure beneath the Japanese Islands. The final model given in Figs.8.2(a) and (b) will work as an first order approximation of the subterranean structure. The more realistic model will be obtained by accumulation of detailed observations on the basis of the present investigation.

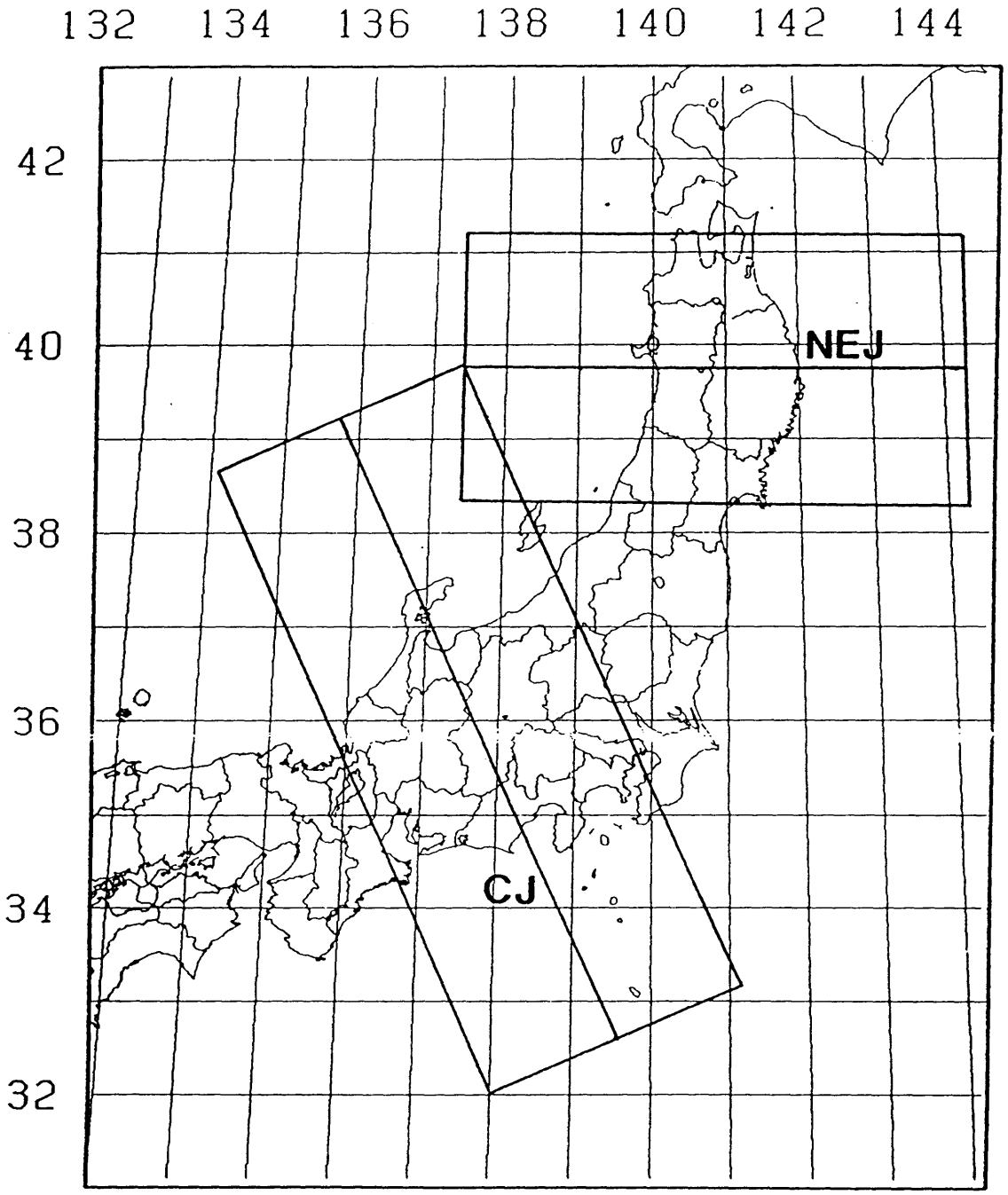

Fig.8.1 Areas of the present investigation. NEJ denotes the east-west cross section of northeast Japan, while CJ denotes the cross section of central Japan along N30°W-S30°E.

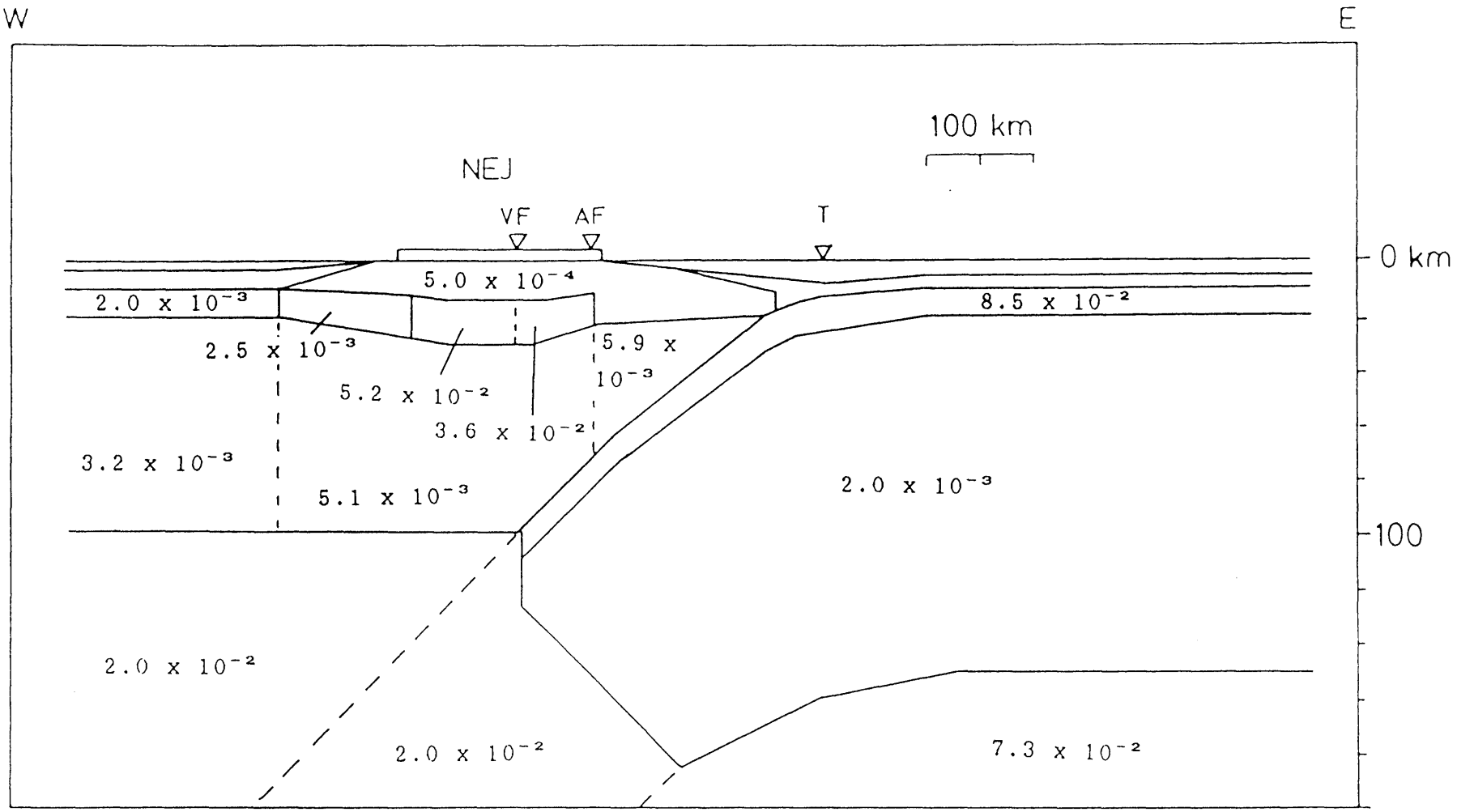

Fig.8.2(a) The east-west cross section of the final two-dimensional conductivity model across the northeastern Japan arc. Conductivity of each block is given in S/m.

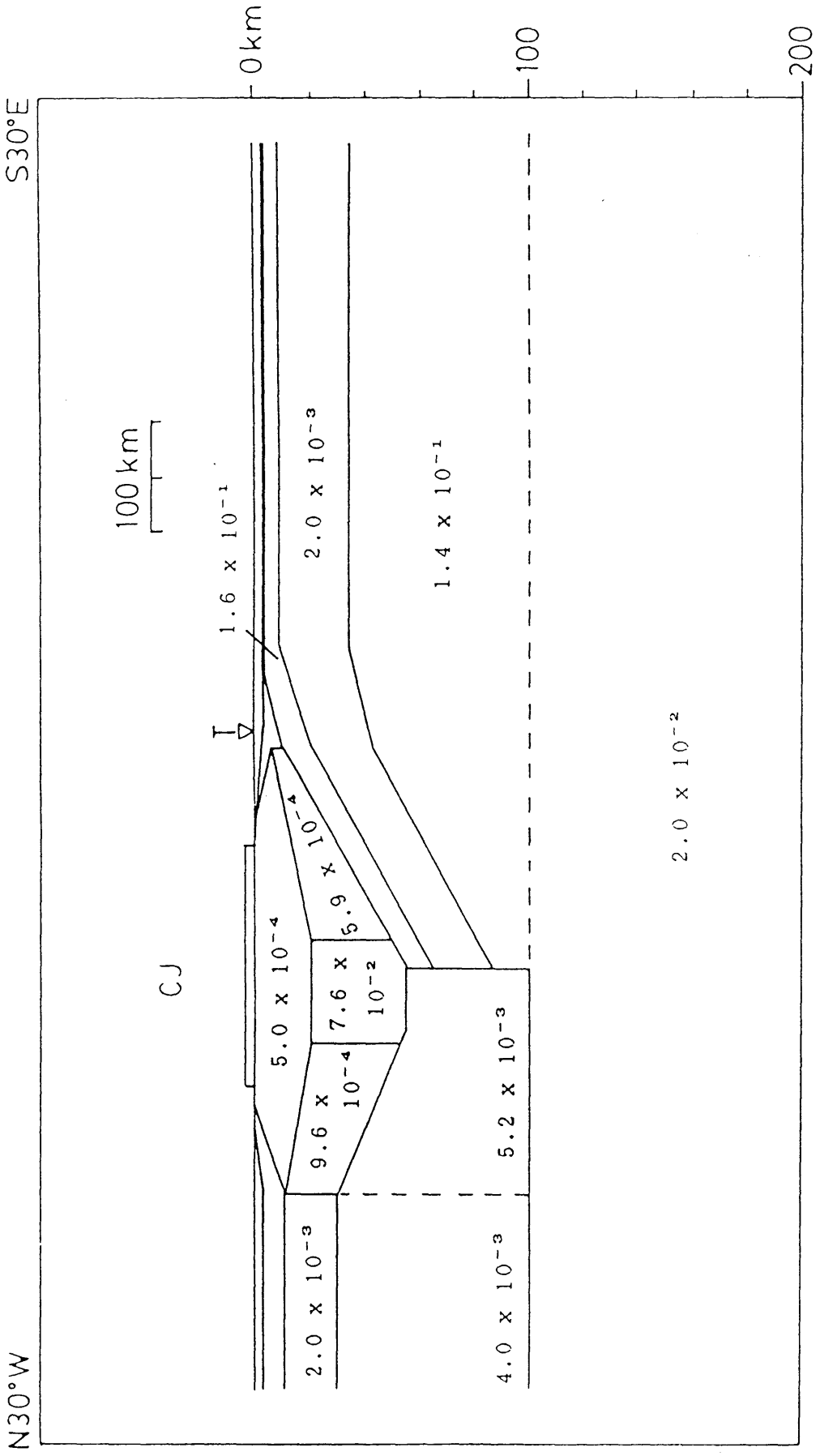

Fig.8.2(b) The N30°W-S30°E cross section of the final two-dimensional conductivity model across central Japan.

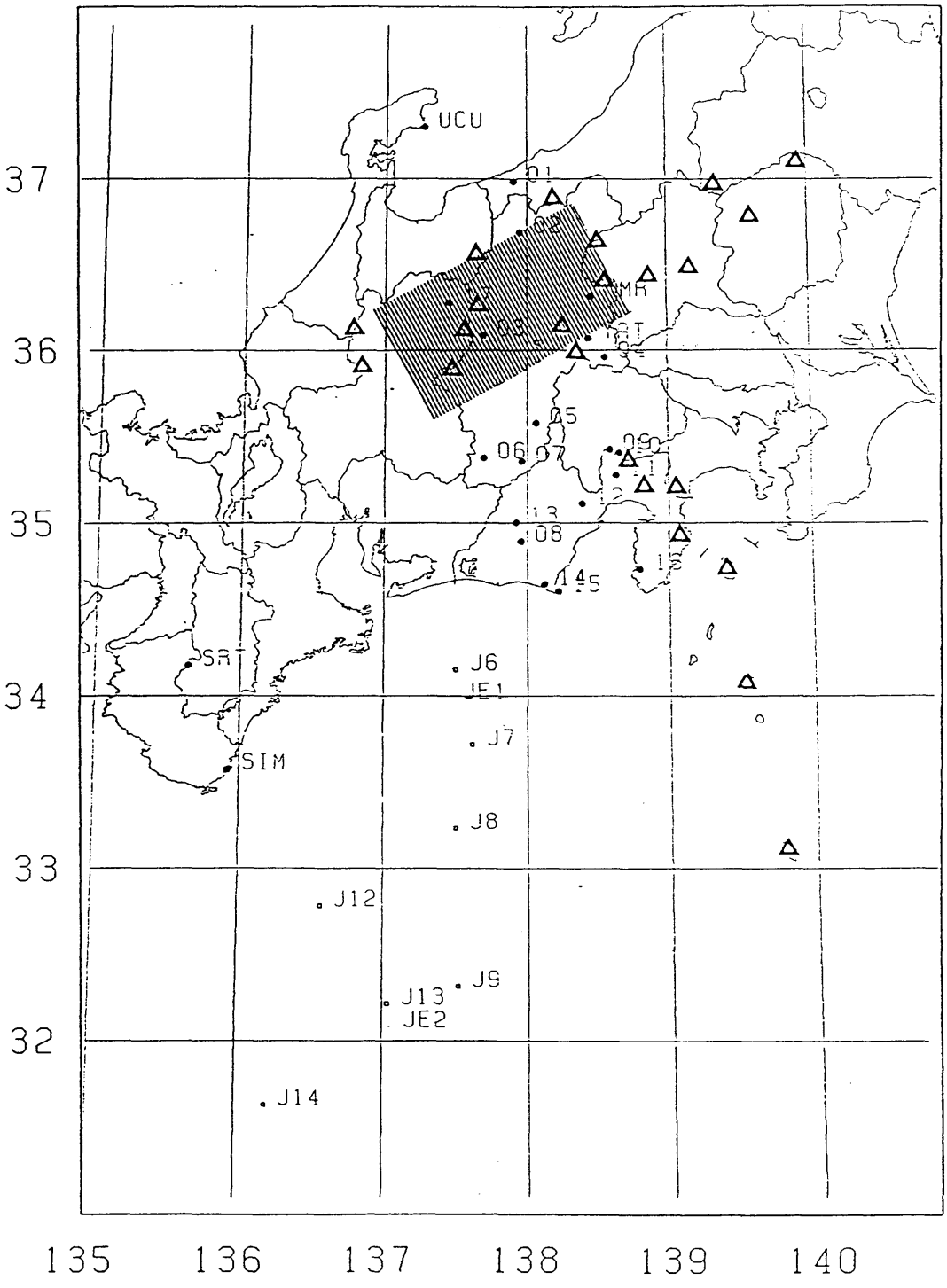

Fig.8.3 Horizontal coverage of the lower crustal conductor beneath the central part of Japan (hatched area). Triangles denote Quaternary volcanoes (after Utada et al., 1986).

References

Anderssen, R. S., On the inversion of global electromagnetic induction data, Phys. Earth Planet. Inter., 10, 292-298, 1975.

Asada, T. and S. Asano, Crustal structure of Honshu, Japan, The Crust and Upper Mantle of Japanese Area, Part I Geophysics, edited by Japanese National Committee for Upper Mantle Project, Earthq. Res. Inst. Univ. Tokyo, pp45-55, 1972.

Asakawa, E., Application of Sompi method of spectrum analysis to magnetovariational and magnetotelluric data processing, M. Sci. Thesis, Univ. Tokyo, 176pp, 1986 (in Japanese).

Bailey, R. C., Inversion of the geomagnetic induction problem, Proc. Roy. Soc. Lond. A, 315, 185-194, 1970.

Balser, M. and C. A. Wagner, Observations of earth-ionosphere cavity resonances, Nature, 188, 638-641, 1960.

Banks, R. J., Geomagnetic variations and the electrical conductivity of the upper mantle, Geophys. J. Roy. astr. Soc., 17, 457-487, 1969.

Banks, R. J., The overall conductivity distribution of the earth, J. Geomag. Geoelectr., 24, 337-351, 1972.

Banks, R. J. and P. Ottey, Geomagnetic deep sounding in and around Kenya Rift Valley, Geophys. J. Roy. astr. Soc., 36, 321-335, 1974.

Bartels, J., Erdmagnetisch erschliessbare lokale Inhomogenitaten der elektrischen Leitfahigkeit im Untergrund, Nachr. Akad. Wiss. Gottingen, II, Math. Phys. Kl., 2a, 95-100, 1954.

Belbo, M. and A. Bjornsson, Magnetotelluric investigation of the lower crust and upper mantle beneath Iceland, J. Geophys., 45, 1-16, 1978.

Bendat, J. S. and A. G. Piersol, Random data : Analysis and measurements, 407pp., Wiley-Interscience, New York, 1971.

Bentley, C. R., Error estimation in two-dimensional Magnetotelluric analyses, Phys. Earth Planet. Int., 7, 423-430, 1973.

Berdichevsky, M. N., V. I. Dmitriev, and N. A. Mershchikova, The study of gradient media by deep electromagnetic sounding, Izuvestia AN SSSR, Fizica Zemli., 6, 61-72, 1974.

Berdichevsky, M. N., E. B. Fainberg, N. M. Rotanova, J. B. Smirnov, and L. L. Vanyan, Deep electromagnetic investigations, Ann. Geophys., 32, 143-155, 1976.

Brewitt-Taylor, C. R. and J. T. Weaver, On the finite difference solution of two-dimensional induction problems, Geophys. J. Roy. astr. Soc., 47, 375-946, 1976.

Cagniard, I., Basic theory of the magneto-telluric method of geophysical prospecting, Geophysics, 18, 605-635, 1953.

Carter, N. K., Steady state flow of rocks, Rev. Geophys. Space Phys., 14, 375-396, 1976.

Chapman, S., The solar and lunar diurnal variation of the earth's magnetism, Phil. Trans. Roy. Soc. Lond. A, 218, 1-118, 1919.

Coggon, J. H., Electromagnetic and electrical modeling by the finite-element method, Geophysics, 36, 132-155, 1971.

Conrad, W. and R. W. Kay, Petrology and significance of olivine and amphibole bearing xenoliths in Aleutian andesites (abstract), EOS Trans. AGU, 61, 400, 1980.

Duba, A., Electrical conductivity of olivine, J. Geophys. Res., 77, 2483-2495, 1972.

Drury, M. J., Electrical resistivity models of the oceanic crust based on laboratory measurements on basalts and gabbros, Geophys. J. Roy. astr. Soc., 56, 242-253, 1979.

Drury, M. J. and R. D. Hyndman, The electrical resistivity of oceanic basalts, J. Geophys. Res, 84, 4537-4545, 1979.

Dvorak, Z., Electrical conductivity of several samples of olivinites, peridotites, and dunites as a function of pressure and temperature, Geophys., 38, 14-24, 1973.

Eckhardt, D., Geomagnetic inductions in a concentrically stratified earth, J. Geophys. Res., 68, 6273-6278, 1968.

Eckhardt, D., K. Larner, and T. Madden, Long period magnetic fluctuations and mantle electrical conductivity estimates, J. Geophys. Res., 68, 6279-6286, 1963.

Edwards, R. N. and J. P. Greenhouse, Geomagnetic variations in the eastern United States: evidence for a highly conducting lower crust?, Science, 188, 726-728, 1975.

Edwards, R. N., L. K. Law, and J. M. DeLaurier, On measuring the electrical conductivity of the oceanic crust by modified magnetometric resistivity method, J. Geophys. Res., 86, 11609-11615, 1981.

Everett, J. E. and R. D. Hyndman, Geomagnetic variations and electrical conductivity structure in south-western Australia, Phys. Earth Planet. Interiors, 1, 24-34, 1967.

Fainberg, E. B. and N. M. Rotanova, Distribution of conductivity and temperature inside the Earth by the data of deep electromagnetic sounding, Geomagnetism and Aeronomy, 14, 709-714, 1974.

Filloux, J.H., Oceanic currents, geomagnetic variations and deep electrical conductivity structure of ocean-continent transition of central California, Ph.D. Thesis, Univ. California, San Diego, La Jolla, 166pp., 1967.

Filloux, J. H., Ocean-floor magnetotelluric sounding over North Central Pacific, Nature, 269, 297-301, 1977.

Filloux, J. H., North Pacific magnetotelluric experiments, J. Geomag. Geoelectr., 32, SI33-SI43, 1980a.

Filloux, J. H., Magnetotelluric sounding over the north-east Pacific may reveal spatial dependence of depth and conductance of the asthenosphere, Earth Planet. Sci. Lett., 46, 244-252, 1980b.

Filloux, J. H., Magnetotelluric exploration of the North Pacific: progress report and preliminary soundings near a spreading ridge, Phys. Earth Planet. Interiors, 25, 187-195, 1981.

Fischer, G. and J. T. Weaver, Theoretical investigation of the ocean-coast effect at a passive continental margin, Phys. Earth Planet. Int., 42, 246-254, 1986.

Fujii, T., Petrological models of lower crust, Proc. Conductivity Anomaly Symposium, Earthq. Res. Inst., Univ. Tokyo, 25-34, 1984 (in Japanese).

Fyfe, W. S., N. J. Price, and A. B. Thompson, Fluids in the earth's crust, Elsevier, New York, 1978.

Gamble, T. D., W. M. Goubau, and J. Clarke, Magnetotellurics with a remote reference, Geophys., 44, 53-68, 1979.

Goubau, W. N., T. D. Gamble, and J. Clarke, Jr., Magnetotelluric data analysis: removal of bias, Geophys., 43, 1157-1169, 1978.

Gregory, P. T. and H. P. Taylor, Jr, An oxygen isotope profile in a section of Cretaceous oceanic crust, Samail ophiorite, Oman: Evidence for $\delta\ ^{18}O$ buffering of the oceans by deep (>5km) seawater-hydrothermal circulation at midocean ridges, J. Geophys. Res., 86, 2737-2755, 1981.

Hamano, Y., Seafloor measurement of natural electric field by use of newly developed instrument, Proc. Conductivity Anomaly Sym., Earthq. Res. Inst., 259-266, 1984.

Handa, S., T. Ogawa, and M. Yasuhara, Damping coefficients of Q-type bursts in the Schumann resonance frequency range, Cont. Geophys. Inst. Kyoto Univ., 11, 1971.

Handa, S. and N. Sumitomo, The geoelectric structure of the Yamasaki and the Hanaori Faults, Southwest Japan, J. Geomag. Geoelectr., 37, 93-106, 1985.

Hasemi, A. H., H. Ishii, and A. Takagi, Fine structure beneath the Tohoku district, northeastern Japan Arc, as derived by an inversion of P-wave arrival times from local earthquakes, Tectonophysics, 101, 245-265, 1984.

Hermance, J. F., Processing magnetotelluric data, Phys. Earth Planet. Int., 7, 349-364, 1973.

Hino, M., Spectrum Analysis, Asakura Publ. Co., 300pp., 1978 (in Jpanese).

Hohmann, G. W., Three-dimensional induced polarization and electromagnetic modeling, Geophys., 40, 309-324, 1975.

Honda, S., Thermal structure beneath Tohoku, northeast Japan - a case study for understanding the detailed thermal structure of the subduction zone, Tectonophysics, 112, 69- 102, 1985.

Honkura, Y, Electrical conductivity anomalies beneath the Japan arc, J. Geomag. Geoelectr., 26, 147-171, 1974.

Honkura, Y, Partial melting and electrical conductivity anomalies beneath the Japan and Philippine Seas, Phys. Earth Planet. Interiors, 10, 128-134, 1975.

Honkura, Y, Peninsula effects in central Japan and their relation to electrical conductivity structure, J. Geomag. Geoelectr., 35, 39-56, 1983.

Hyndman, R.D. and D. W. Hyndman, Water saturation and high electrical conductivity in the lower crust, Phys. Earth Planet. Inter., 24, 66-87, 1981.

Ishida, M., The spatial distribution of earthquake hypocenters and the three-dimensional velocity structure in the Kanto-Tokai district, Japan, J. Phys. Earth, 32, 399-422, 1984.

Jones, A. G., On electrical crust-mantle structure in Fennoscandia: no MOHO, an the asthenosphere revealed ?, Geophys. J. Roy. astr. Soc., 68, 371-388, 1982.

Jones, A. G. and V. R. S. Hutton, A multi-station magnetotelluric study in southern Scotland, II, Monte-Calro inversion of the data and its geophysical and tectonic implications, Geophys. J. Roy. astr. Soc., 56, 351-368, 1979.

Jones, F. W. and L. J. Pascoe, A general computer program to determine the alternating electric currents in a two-dimensional model of a region of non uniform conductivity with an embedded inhomogeneity, Geophys. J. Roy. astr. Soc., 24, 3-30, 1971.

Jupp, D. L. B. and K. Vozoff, Two-dimensional magnetotelluric inversion, Geophys. J. Roy astr. Soc., 50, 333-352, 1977.

Kariya, K. A. and T. J. Shankland, Electrical conductivity of dry lower crustal rocks, Geophysics, 48, 52-61, 1983.

Kato, Y., M. Daguchi, M.Seto, and T. Aruga, Northeastern Japan Anomaly of the upper mantle, Sci. Rep. Tohoku Univ., Ser. 5, 21, 19-35, 1971.

Klein, D. P., Magnetic variations (2-30cpd) on Hawaii Island and mantle electrical conductivity, Ph. D. Thesis, Univ. Hawaii, 82pp., 1976.

Klein, D. P. and J. C. Larsen, Magnetic induction fields (2-30cpd) on Hawaii Island and their implications regarding electrical conductivity in the oceanic mantle, Geophys. J. Roy. astr. Soc., 53, 61-77, 1978.

Kono, Y., S. Kanai, H. Wada, M. Mizoue, and I Fujii, Anomalous attenuation of seismic waves under the Hida mountain range and its cause (abstract), Bull. Volcanol. Soc. Japan, 30, 114, 1985 (in Japanese).

Ku, C. C., Numerical inverse magnetotelluric problems, Geophys., 41, 276-286, 1976.

Kurtz, R. D., J. M. DeLaurier, and J. C. Gupta, A magnetotelluric sounding across Vancouver Island detects the subducting Juan de Fuca plate, Nature, 321, 596-599, 1986.

Kushiro, I., Y. Shono, and S. Akimoto, Melting of a peridotite nodule at high pressures and high water pressures, J. Geophys. Res., 73, 6023-6029, 1968.

Lahiri, B. N. and A. T. Price, Electromagnetic induction in non-uniform conductors, and the determination of the conductivity of the earth from terrestrial magnetic variations, Phil. Trans. Roy. Soc. Lond. A, 237, 509-540, 1939.

Larsen, J. C., Low frequency (0.1-6.0 cpd) electromagnetic study of deep mantle electrical conductivity beneath the Hawaiian Islands, Geophys. J. R. astr. Soc., 43, 17-46, 1975.

Lee, K. H., D. F. Pridmore, and H. F. Morrison, A hybrid three-dimensional electromagnetic modeling scheme, Geophys., 46, 796, 805, 1981.

Madden, T. and C. M. Swift, Magnetotelluric studies of the electrical conductivity structure of the crust and upper mantle, AGU Monogr. 13, The Earth's Crust and Upper Mantle, 469-479, 1969.

Maritime Safety Agency, The result of magnetic observations for the year 1979, Data Rep. Hydrogr. Obs., ser. Geomagnetism, 15, 1981.

McDonald, K. L., Penetration of the geomagnetic secular field through a mantle with variable conductivity, J. Geophys. Res., 62, 117-141, 1957.

Nagao, T., Heat flow measurements in the Tohoku-Hokkaido regions by some new techniques and their geotectonic interpretation, Ph.D thesis, Univ. Tokyo, 219pp., 1986.

Nekut, A., J. E. P. Connerney, and A. K. Kuckes, Deep crustal electrical conductivity; evidence for water in the lower crust, Geophys. Res. Lett., 4, 239-242, 1977.

Neumann, G. A. and J. F. Hermance, The geomagnetic coast effect in the Pacific Northwest of north America, Geophys. Res. Lett., 12, 502-505, 1985.

Nishida, Y., Conductivity structure in and around Hokkaido, Japan as revealed by the period dependence of the CA transfer functions, J. Geomag. Geoelectr., 34, 453-465, 1982.

Nobes, D. C., L. K. Law, and R. N. Edwards, The determination of resistivity and porosity of the sediment and fractured basalt layers near the Juan de Fuca Ridge, Geophys. J. Roy. astr. Soc., 86, 289-317, 1986.

Norton, D. and H. P. Taylor, Jr., Quantitative simulation of the hydrothermal systems of crystallizing magmas on the basis of transport theory and oxygen data: An analysis of the Skaergaard intrusion, J. Petrol., 20, 421-486, 1979.

Ogawa, T. and Y. Tanaka, Q factors of the Schumann resonances and solar activity, Cont. Geophys. Inst. Kyoto Univ., 10, 21-28, 1970.

Ogawa, Y., T. Yukutake, and H. Utada, Two dimensional modelling of resistivity structure beneath the Tohoku district, northern Honshu of Japan, by a finite element method, J. Geomag. Geoelectr.,38, 45-79, 1986.

Oldenburg, D. W., One-dimensional inversion of natural source magnetotelluric observations, Geophysics, 44, 1218-1244, 1979.

Oldenburg, D. W., Conductivity structure of oceanic upper mantle beneath the Pacific plate, Geophys. J. Roy. astr. Soc., 65, 359-394, 1981.

Olhoeft, G. R., Electrical properties of granite with implications for the lower crust, J. Geophys. Res., 86, 931-936, 1981b.

Olhoeft, G. R., Electrical properties of rocks, in Physical Properties of Rocks and Minerals, edited by Y. S. Touloukian, W. R. Judd, and R. F. Roy, McGraw-Hill, New York, 1981b.

Parkhomenko, E. I., Electrical resistivity of minerals and rocks at high temperature and pressure, Rev. Geophys. Space Phys., 20, 193-218, 1982.

Parkinson, W. D., Directions of rapid geomagnetic fluctuations, Geophys. J. R. astr. Soc., 2, 1-14, 1959.

Parkinson, W. D., Conductivity anomalies in Australia and the ocean-effect, J. Geomag. Geoelectr., 15, 222-226, 1964.

Poehls A. J. and R. P. Von Herzen, Electrical resistivity structure beneath the North-west Atlantic Ocean, Geophys. J. Roy. astr. Soc., 47, 331-346, 1976.

Porath, H. and A. Dziewonski, Crustal electrical conductivity anomalies in the Great Plains Province of the United States, Geophysics, 36, 382-395, 1971.

Presnall, D. C., C. L. Simmons, and H. Porath, Changes in electrical conductivity of synthetic basalt during melting, J. Geophys. Res. 77, 5665-5672, 1972.

Price, A. T., The induction of electric current in non-uniform thin sheets and shells, Q. J. Mech. appl. Math., 2, 283-310.

Quist, A. S. and W. L. Marshall, Electrical conductances of aqueous sodium chloride solution from 0 to 800° and pressures to 4000 bars, J. Phys. Chem., 72, 684-703, 1968.

Rai, C. S. and M. H. Manghnani, Electrical conductivity of ultramafic rocks to 1820 Kelvin, Phys. Earth Planet. Inter., 17, 6-13, 1978.

Reddy, I. K. and D. Rankin, Magnetotelluric response of laterally inhomogeneous and anisotropic media, Geophysics, 40, 1035-1045, 1975.

Research Group for Crustal Resistivity Structure, Japan, Preliminary report on a study of resistivity structure beneath the northern Honshu of Japan, J. Geomag. Geoelectr., 35, 589-608, 1983.

Rikitake, T., Electromagnetic induction within the earth and its relation to the electrical state of the earth's interior. 1(1), Bull. Earthq. Res. Inst., Univ. Tokyo, 28, 45-100, 1950a.

Rikitake, T., Electromagnetic induction within the earth and its relation to the electrical state of the earth's interior. 1(2), Bull. Earthq. Res. Inst., Univ. Tokyo, 28, 219-262, 1950b.

Rikitake, T., Electromagnetic induction within the earth and its relation to the electrical state of the earth's interior. 2, Bull. Earthq. Res. Inst., Univ. Tokyo, 28, 263-283, 1950c.

Rikitake, T., Electromagnetic induction within the earth and its relation to the electrical state of the earth's interior. 3, Bull. Earthq. Res. Inst., Univ. Tokyo, 29, 61-69, 1951.

Rikitake, T., Electromagnetism and the Earth's Interior, 308pp., Elsevier, Amsterdam, 1966.

Rikitake, T., The undulation of an electrical conductive layer beneath the island of Japan, Techtonophys., 7, 257-264, 1969.

Rikitake, T., Global electrical conductivity of the earth, Phys. Earth Planet. Inter., 6, 340-345, 1973.

Rikitake, T., A model of geoelectric structure beneath Japan, J. Geomag. Geoelectr., 27, 233-244, 1975.

Rikitake, T. and Y. Honkura, Recent Japanese studies on conductivity anomalies, Phys. Earth Planet. Interiors, 7, 203-212, 1973.

Rikitake, T. and Y. Honkura, Solid earth electromagnetism, 384pp., Terra Sci. Publ. Co., Tokyo, 1985.

Rikitake, T. and I. Yokoyama, Anomalous relations between H and Z components of transient geomagnetic variations, J. Geomag. Geoelectr., 5, 59-65, 1953.

Rodi, W. L., A technique for improving The accuracy of finite element solution for magnetotelluric data, Geophys. J. Roy. astr. Soc., 44, 483-506, 1976.

Saito, M., Automatic design of recursive digital filters, Geoexploration, 31, 240-263, 1978.

Sasai, Y., Spatial dependence of short-period geomagnetic fluctuation on Oshima Island(1), Bull. Earthq. Res. Inst., Univ. Tokyo, 45, 137-157, 1967a.

Sasai, Y., Spatial dependence of short-period geomagnetic fluctuation on Oshima Island(2), Bull. Earthq. Res. Inst., Univ. Tokyo, 46, 907-926, 1967b.

Sasai, Y., Observations of the geomagnetic variation in Kii Peninsula, Proc. Conductivity Anomaly Symposium, 2, Earthq. Res. Inst., Univ. Tokyo, 43-48, 1969(in Japanese).

Schumann, W. O., Uber die strahlungslosen Eigenshchwingungen einer leitenden Kugel, die von einer Luftschicht und einer Ionospharenhulle umgeben ist, Z. Naturforsch., 7, 149-154.

Schmucker, U., Anomalies of geomagnetic variations in the southern United States, Bull. Scripps Inst. Oceanogr., 13, 165pp, Univ. California Press, Berkeley and Los Angeles, 1970.

Segawa, J., T. Yukutake, Y. Hamano, T. Kasuga, and H. Utada, Sea floor measurement of geomagnetic field using newly developed ocean bottom magnetometers, J. Geomag. Geoelectr., 34, 571-585, 1982.

Shankland, T. J., and M. E. Ander, Electrical conductivity temperature, and fluid in the lower crust, J. Geophys. Res., 88, 9475-9484, 1983.

Shankland, T. J. and H. S. Waff, Partial melting and electrical conductivity anomalies in the upper mantle, J. Geophys. Res., 82, 5409-5417, 1977.

Shankland, T. J., R. J. O'Connell, and H. S. Waff, Geophysical constraints on partial melt in the upper mantle, Rev. Geophys. Space Phys., 19, 394-406, 1981.

Swift, C. M., Theoretical magnetotelluric and Turam response from two-dimensional inhomogeneities, Geophysics, 36, 38-52, 1971.

Takagi, A, A. Hasegawa, and N. Umino, Seismic activity in the northeastern Japan arc, J. Phys. Earth, 25, Suppl., S95-S104, 1977.

Takahashi, E., Petrologic model of the crust and upper mantle of the Japanese Island arcs, Bull. Volcanol., 41, 529-547, 1978.

Takeuchi H. and M. Saito, Electromagnetic induction within the earth, J. Geophys. Res., 68, 6287-6291, 1963.

Talantola, A. and B. Valette, Generalized nonlinear inverse problems solved using the least squares criterion, Rev. Geophys. Space Phys., 20, 219-232, 1982.

Tatsumi, Y., M. Sakuyama, M. Fukuyama, and I. Kushiro, Generation of arc basalt magmas and thermal structure of the mantle wedge in subduction zones, J. Geophys. Res., 88, 5815-5825, 1983.

Untiedt, J., Conductivity anomalies in central and southern Europe, J. Geomag. Geoelectr., 24, 131-149, 1970.

Utada, H., S. Koyama, and Y. Sasai, Resistivity structure of the crust in Tohoku district by ELF·VLF magnetotelluric measurements, Proc. Conductivity Anomaly Symposium 1982, Earthq. Res. Inst., Univ. Tokyo, 167-182, 1968 (in Japanese).

Utada, H., Y. Sasai, I. Nakagawa, S. Koyama, Y. Ishikawa, and Y. Hamano, Changes in electrical resistivity associated with the 1983 eruption of Miyake-jima Volcano, Bull. Volcanol. Soc., Japan, Ser. 2, 29, Suppl., S113-S124, 1984 (in Japanese).

Utada, H., Y Hamano, and T. Yukutake, A two-dimensional conductivity model across central Japan, J. Geomag. Geoelectr., 38, 447-473, 1986.

Uyeda, S. and T. Rikitake, Electrical conductivity anomaly and terrestrial heat flow, J. Geomag. Geoelectr., 22, 75-90, 1970.

Vozoff, K., The magnetotelluric method in the exploration of sedimentary basins, Geophys., 37, 98-141, 1972.

Waff, H. S., Theoretical consideration of electrical conductivity in a partially molten mantle and implications for geothermometory, J. Geophys. Res., 79, 4003-4010, 1974.

Watanabe, T., Temperature profiles at continental margin, Proc. Conductivity Anomaly Symposium, Earthq. Res. Inst., Univ. Tokyo, 167-182, 1968.

Weidelt, P., Inversion of two-dimensional conductivity structure, Phys. Earth Planet. Int., 10, 282,291, 1975.

Weidelt, P., Electromagnetic induction in three-dimensional structures, J. Geophys., 41, 85-109, 1975.

Wiese, H., Geomagnetische Tiefentellurik. I. Die elektrische Leftfahigkeit der Erdkruste und des oberen Erdmantels, Geophis. Pura Appl., 51, 59-78, 1962.

Yamashita, H. and I. Yokoyama, Interpretation of the "Northeastern Japan Anomaly" in electrical conductivity of the upper mantle, J. Geomag. Geoelectr., 28, 329-332, 1976.

Yoshii, T., A detailed cross section of the deep seismic zone beneath Northeastern Honshu, Japan, Tectonophysics, 55, 349-360, 1979.

Yukutake, T., Electromagnetic observations in Tokai-Koushin'etsu District, Proc. Conductivity Anomaly Symposium, Earthq. Res. Inst., Univ. Tokyo, 35-44, 1984 (in Japanese).

Yukutake, T., A review of studies on the electrical resistivity structure of the crust in Japan, Earthq. Predict. Res. 3, 345-364, 1985.

Yukutake, T., J. H. Filloux, J. Segawa, Y. Hamano, and H. Utada, Preliminary report on a magnetotelluric array study in the northwest Pacific, J. Geomag. Geoelectr., 35, 575-587, 1983.

Zablocki, C. J., Application of the VLF induction method for studying some volcanic processes of Kilauea Volcanoes, Hawaii, J. Volcanol. Geotherm. Res., 3, 155-195, 1978.

Appendix A. Derivation of iteration formula Eq.(3-5-5)

We will follow the notation mainly used by Tarantola and Valette (1982). Let Γ be a physical system, which can be described by a set of parameters $X = \{ X_1, X_2, \cdots, X_m \}$. We write any particular value of the parameter set by $x = \{ x_1, x_2, \cdots x_m \}$. We assume here that physical theories, which impose constraints between the possible values of the parameters, can be expressed by a functional form:

$$f(x) = 0 \qquad \text{(A1-1)}$$

In most usual cases one can naturally expect a partitioned form of the parameter set as:

$$X = \begin{bmatrix} X_1 \\ X_2 \\ \cdot \\ \cdot \\ \cdot \\ X_m \end{bmatrix} = \begin{bmatrix} D_1 \\ \cdot \\ \cdot \\ D_r \\ P_1 \\ \cdot \\ \cdot \\ P_s \end{bmatrix} = \begin{bmatrix} D \\ P \end{bmatrix} \qquad \text{(A1-2)}$$

We denote the set of the directly measurable parameters as D and that of the unmeasurable parameters as P. In the induction studies, D consists of geomagnetic transfer function, impedance and other inductive response functions., while P of the subsurface conductivity. The physical constraints Eq(A1-1) is replaced by theoretical equation:

$$\begin{aligned} d_1 &= g_1(p_1, \cdots p_s) \\ &\cdot \\ d_r &= g_r(p_1, \cdots p_s) \end{aligned} \qquad \text{(A1-3)}$$

or, for short

$$d = g(p) \qquad \text{(A1-4)}$$

Eq.(A1-4) shows simply that the inductive responses can be calculated if the parameters are given. Since the inductive responses are generally given by ratios of electromagnetic fields, the theoretical equation g is a non-linear function of p. We should also note that g is a complex function derived from complex induction equation.

Next we set up two assumptions as follows:

1) If we have a set of measurements D, we assume that the measurement has the stochastic characteristics with Gaussian error distribution; i.e. it can be described by expectation, the variance, and the covariance with other measurements.

2) In order to solve undetermined problem, we assume that we have some a priori knowledge about the set of unmeasurable parameters P, and that this knowledge may also be expressed in a Gaussian form.

The a priori information, a vector of the expected values, x_o, and a covariance matrix, C_o, can be written as:

$$x_o = \begin{bmatrix} d_o \\ p_o \end{bmatrix}, \qquad C_o = \begin{bmatrix} C_{dodo} & C_{dopo} \\ C_{podo} & C_{popo} \end{bmatrix} \qquad \text{(A1-5)}$$

The uncertainties in measurements are considered to be uncorrelated with uncertainties in estimation of parameters, then we can naturally assume:

$$C_{dopo} = {}^{T}C_{podo} = 0 \qquad \text{(A1-6)}$$

where ${}^{T}A$ denotes a transpose matrix if A is a real matrix, and a Hermite conjugate matrix if A is a complex matrix.

Since we have assumed that the a priori information has a Gaussian error, the probability density function may be written by $\mathbf{x}_o$ and C_o as:

$$\rho(\mathbf{x}) = \rho_o \cdot \exp[\, -{}^{T}(\mathbf{x}-\mathbf{x}_o)\cdot C_o^{-1}\cdot(\mathbf{x}-\mathbf{x}_o)/2 \,] \qquad \text{(A1-7)}$$

where ρ_o is an arbitrary constant. The least squares problem can be generally stated as the search of the point x of the theoretical manifold for which the induced probability density is maximum. In order to find the maximum, we should minimize the argument of exponential in Eq.(A1-7). Then the problem is equivalent to searching for the point **x** which satisfies the set of equations:

$$\begin{aligned} f(\mathbf{x}) &= 0 \\ s(\mathbf{x}) &= {}^{T}(\mathbf{x}-\mathbf{x}_o)\cdot C_o^{-1}\cdot(\mathbf{x}-\mathbf{x}_o) = \text{minimum over } \Gamma \end{aligned} \qquad \text{(A1-8)}$$

When a point x verifies Eqs.(A1-8), it is required to verify the following set of equations:

$$\begin{aligned} f(\mathbf{x}) &= 0 \\ s(\mathbf{x}) &= \text{stationary over } \Gamma \end{aligned} \qquad \text{(A1-9)}$$

We assume that both f and s are differentiable. The matrix and vector of respective partial derivatives,

$$F_{ij} = \partial f_i / \partial x_j \qquad \text{(A1-10)}$$

$$S_j = \partial s / \partial x_j \qquad \text{(A1-11)}$$

define the so-called tangent linear application. If **x** is a solution of Eq.(A1-8), s is stationary at **x**; i.e. the tangent linear application S is null over the tangent linear manifold to Γ at **x**. We can write as:

$$S = 2 \cdot {}^T(\mathbf{x}-\mathbf{x}_o)\cdot C_o^{-1} \qquad \text{(A1-12)}$$

Let a vector **V** belong to the tangent linear manifold to Γ at **x**. This holds only if V satisfies $F \cdot V = 0$. Therefore, following expressions are possible which equivalent to Eqs.(A1-9):

$$\begin{aligned} f(\mathbf{x}) &= 0 \\ F\cdot\mathbf{v} = 0 \rightarrow {}^T(\mathbf{x}-\mathbf{x}_o)\cdot C_o^{-1}\cdot\mathbf{v} &= 0 \end{aligned} \qquad \text{(A1-13)}$$

The lower equation of (A1-13) can be solved for (x-x0) by introducing a vector of Lagrange's undetermined parameters as:

$$(\mathbf{x}-\mathbf{x}_o) = C_o\cdot{}^TF\cdot(F\cdot C_o\cdot{}^TF)^{-1}\cdot F\cdot(\mathbf{x}-\mathbf{x}_o) \qquad \text{(A1-14)}$$

With the upper equation of Eq.(A1-13), Eq.(A1-14) can be rewritten as

$$(\mathbf{x}-\mathbf{x}_o) = C_o\cdot{}^TF\cdot(F\cdot C_o\cdot{}^TF)^{-1}\cdot\{\ F\cdot(\mathbf{x}-\mathbf{x}_o)-f(\mathbf{x})\ \} \qquad \text{(A1-15)}$$

Here we assume that Eq.(A1-15) gives the iterative process to search for the next parameter by using a fixed point method. Then x of left hand side can be replaced by x_{K+1} and x of right hand side by x_K,

where x_{k+1} and x_k denote the next and current points, respectively. We obtain following iterative formula:

$$(x_{k+1}-x_o) = C_o \cdot {}^T F \cdot (F \cdot C_o \cdot {}^T F)^{-1} \cdot \{ F \cdot (x_k - x_o) - f(x_k) \} \quad \text{(A1-16)}$$

This gives a generalized expression of total inversion, which can be stated a kind of generalization of Newton's algorithm for search for the zeros of a non-linear function f(x).

Let us now consider the case where the parameter X takes partitioned form given by Eq.(A1-2) and the theoretical equation f(x)=0 can be simplified by Eq.(A1-3). In this case, the matrix of partial derivatives, F, also takes a partitioned form

$$F = [\ I\ -\ G\ ] \quad \text{(A1-17)}$$

where I is the identity matrix and G is the matrix of partial derivatives, or the Jacobian matrix of the theoretical function g; that is:

$$G_{ij} = \partial g_i / \partial p_j \quad \text{(A1-18)}$$

Using Eqs.(A1-4), (A1-5) and (A1-17), we can obtain successively,

$$F_k \cdot (x_k - x_o) - f(x_k) = [\ I\ -\ G\ ] \cdot \begin{bmatrix} d_k - d_o \\ p_k - p_o \end{bmatrix} - [\ d_k - g(p_k)\ ]$$

$$= -\{\ d_o - g(p_k) + G_k \cdot (p_k - p_o)\ \} \quad \text{(A1-19)}$$

$$C_o \cdot {}^T F_k = \begin{bmatrix} C_{dodo} & C_{dopo} \\ C_{podo} & C_{popo} \end{bmatrix} \cdot \begin{bmatrix} I \\ -{}^T G_k \end{bmatrix}$$

$$= \begin{bmatrix} C_{dodo} - C_{dopo} \cdot {}^T G_k \\ C_{podo} - C_{popo} \cdot {}^T G_k \end{bmatrix} \qquad \text{(A1-20)}$$

$$F_k \cdot C_o \cdot {}^T F_k = C_{dodo} - C_{dopo} \cdot {}^T G_k - G_k \cdot C_{podo} + G_k \cdot C_{popo} \cdot {}^T G_k \qquad \text{(A1-21)}$$

Thus, Eq.(A1-16) can be written as:

$$\begin{bmatrix} d_{k+1} \\ p_{k+1} \end{bmatrix} = \begin{bmatrix} d_o \\ p_o \end{bmatrix} + \begin{bmatrix} C_{dopo} \cdot {}^T G_k - C_{dodo} \\ C_{popo} \cdot {}^T G_k - C_{podo} \end{bmatrix}$$

$$\cdot [\, C_{dodo} - C_{dopo} \cdot {}^T G_k - G_k \cdot C_{podo} + G_k \cdot C_{popo} \cdot {}^T G_k \,]^{-1}$$

$$\cdot [\, d_o - g(p_k) + G_k \cdot (p_k - p_o) \,] \qquad \text{(A1-22)}$$

This gives a corresponding algorithm to search for sets of data and parameter describing the physical system. Using the condition of Eq.(A1-6), we derive the iterative process to predict the next point of the parameter p_{k+1} as:

$$p_{k+1} = p_k + ({}^T G_k \cdot C_{dodo}{}^{-1} \cdot G_k + C_{popo}{}^{-1})^{-1}$$

$$\cdot \{ {}^T G_k \cdot C_{dodo}{}^{-1} \cdot [d_o - g(p_k)] - C_{popo}{}^{-1} \cdot (p_k - p_o) \} \qquad \text{(A1-22)}$$

Appendix B. Distribution of the partial derivatives of the response functions for inversion of the northeast Japan data.

In the actual execution of the non-linear least squares given by Eq.(3-5-5), we have to evaluate the partial derivatives of the response functions (geomagnetic transfer functions and impedances) with respect to conductivity of each inhomogeneity. As has shown in the present investigation, the partial derivative works as a good indicator of the sensitivity to the underlying structure (See Chapter 3). Therefore, it is quite useful to refer to the spatial distribution of the partial derivatives in order to examine the reliability of the solution (final model parameters).

Figures given here are the complete list of the partial derivatives calculated for the initial values of the eight unknown model parameters in the inversion of the northeast Japan data described in Chapter 6. Distribution of the partial derivatives for each parameter is presented by two figures; the one for the transfer functions (a) and the other for the impedances (b), denoted by $\partial d_T/\partial p_i$'s and $\partial d_Z/\partial p_i$'s, respectively. In each figure, amplitude and argument (phase) of the derivatives are given at the periods of 15, 30, 60, and 120 minutes, from top to bottom, respectively. At the bottom of each figure, a cross section of two-dimensional model is illustrated. The partial derivatives are evaluated for the conductivity of the shaded block in each cross section

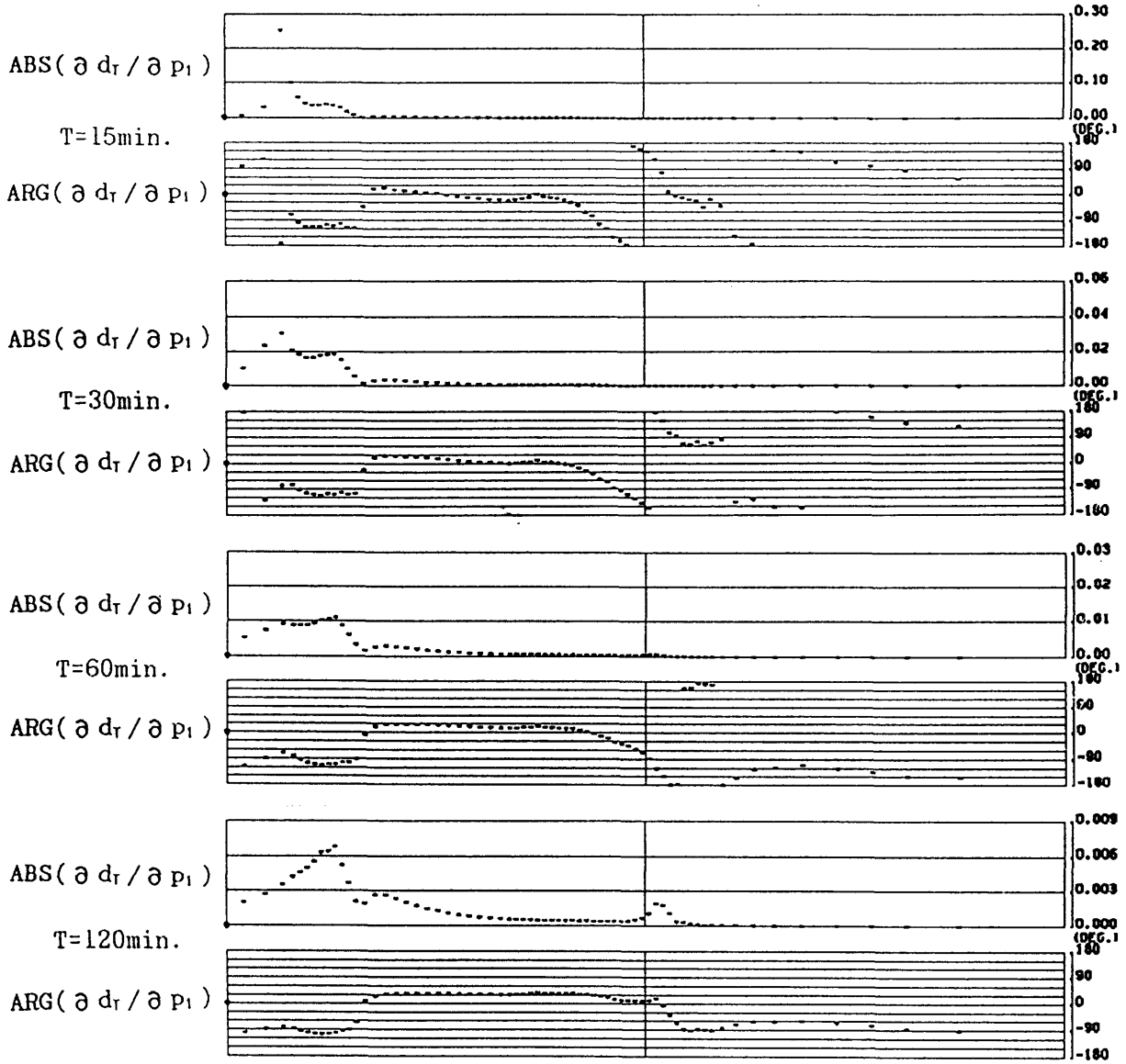
ABS(∂ dT / ∂ pI)
T=15min.
ARG(∂ dT / ∂ pI)
ABS(∂ dT / ∂ pI)
T=30min.
ARG(∂ dT / ∂ pI)
ABS(∂ dT / ∂ pI)
T=60min.
ARG(∂ dT / ∂ pI)
ABS(∂ dT / ∂ pI)
T=120min.
ARG(∂ dT / ∂ pI)
(DEG.)

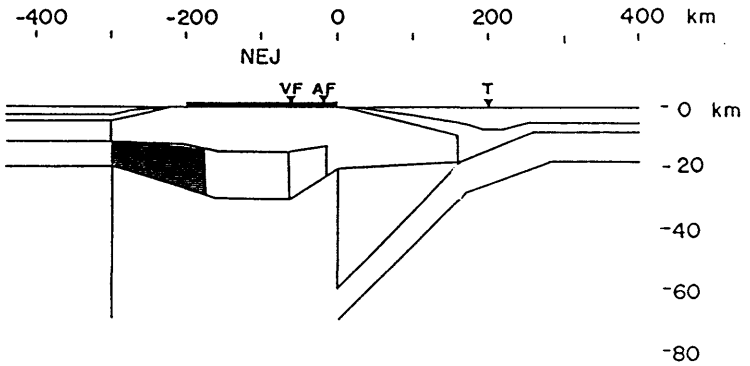
-400
-200
0
200
400 km
NEJ
VF AF
T
0 km
-20
-40
-60
-80

B-1(a)

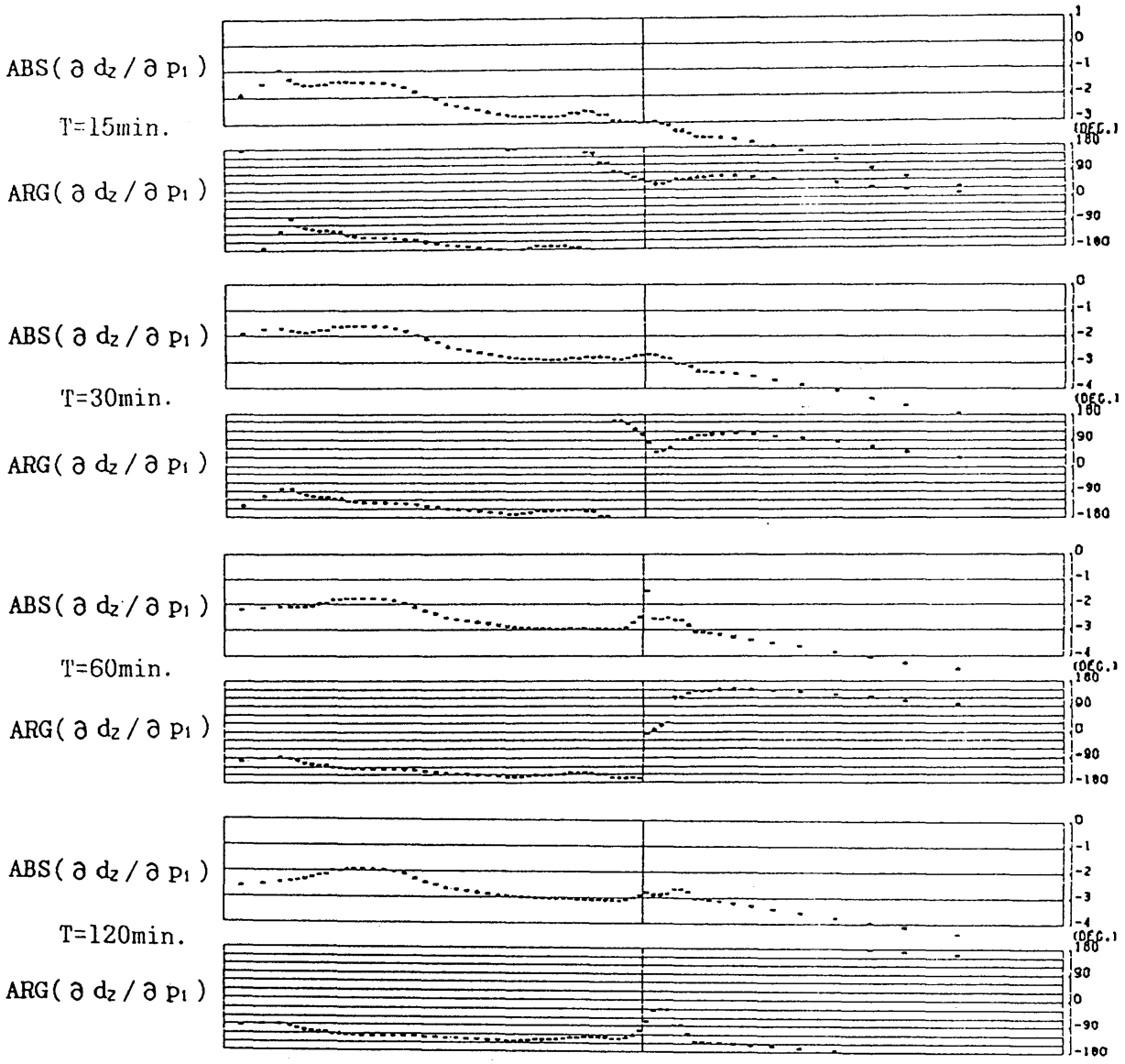
ABS(∂ dz / ∂ p1)
T=15min.
ARG(∂ dz / ∂ p1)
ABS(∂ dz / ∂ p1)
T=30min.
ARG(∂ dz / ∂ p1)
ABS(∂ dz / ∂ p1)
T=60min.
ARG(∂ dz / ∂ p1)
ABS(∂ dz / ∂ p1)
T=120min.
ARG(∂ dz / ∂ p1)
(DEG.)

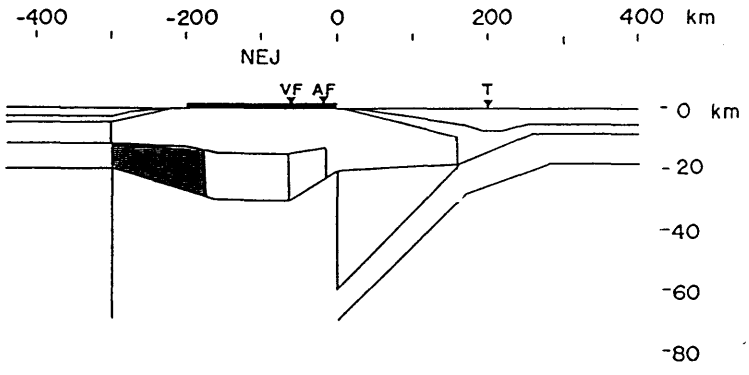
-400
-200
0
200
400 km
NEJ
VF AF
T
0 km
-20
-40
-60
-80

B-1(b)

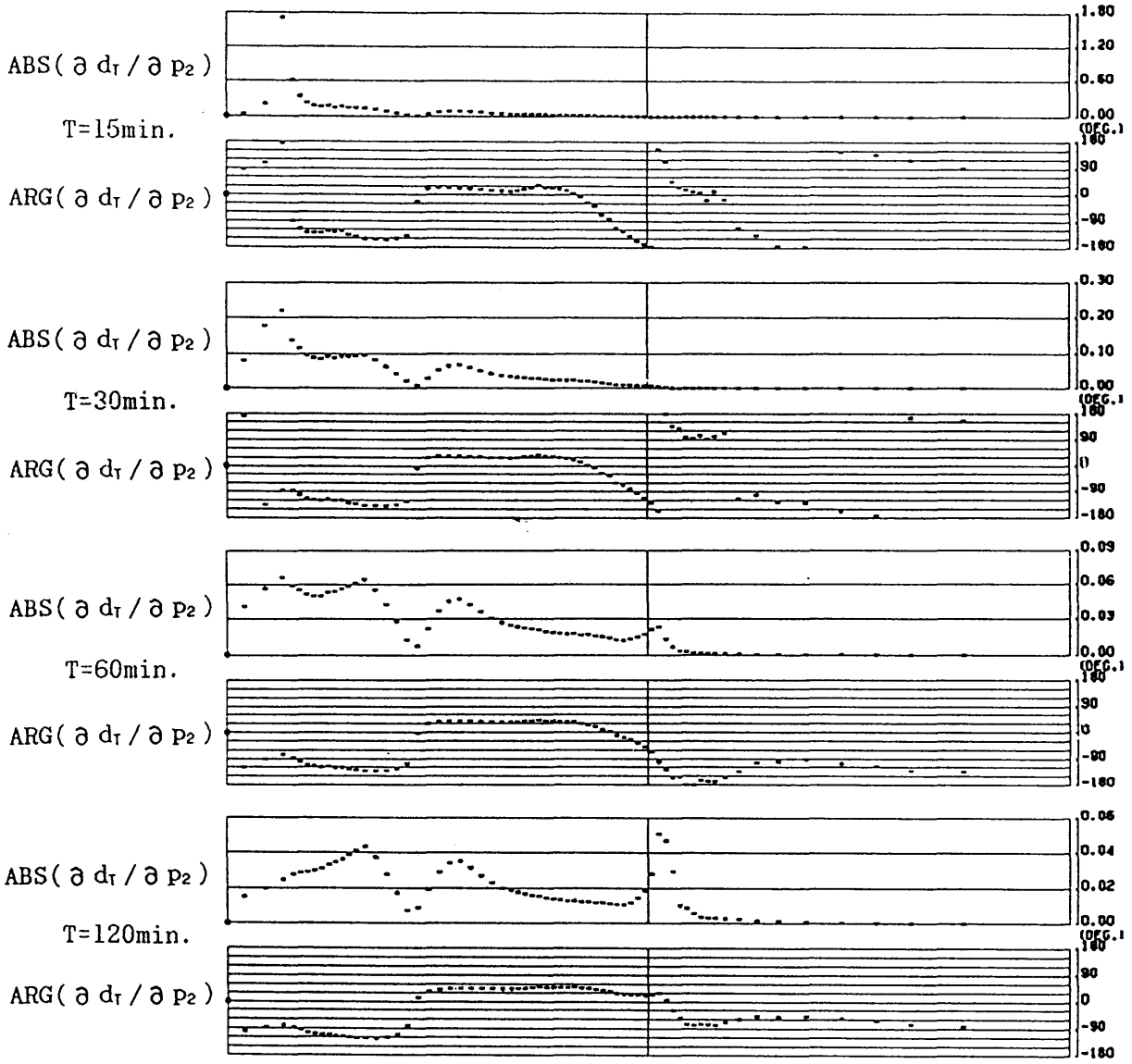
ABS(∂ dT / ∂ p2)
T=15min.
ARG(∂ dT / ∂ p2)
ABS(∂ dT / ∂ p2)
T=30min.
ARG(∂ dT / ∂ p2)
ABS(∂ dT / ∂ p2)
T=60min.
ARG(∂ dT / ∂ p2)
ABS(∂ dT / ∂ p2)
T=120min.
ARG(∂ dT / ∂ p2)
(DEG.)

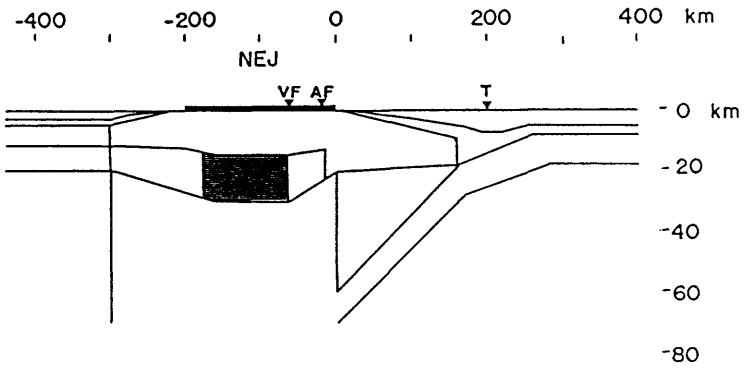
-400
-200
0
200
400 km
NEJ
VF AF
T
0 km
-20
-40
-60
-80

B-2(a)

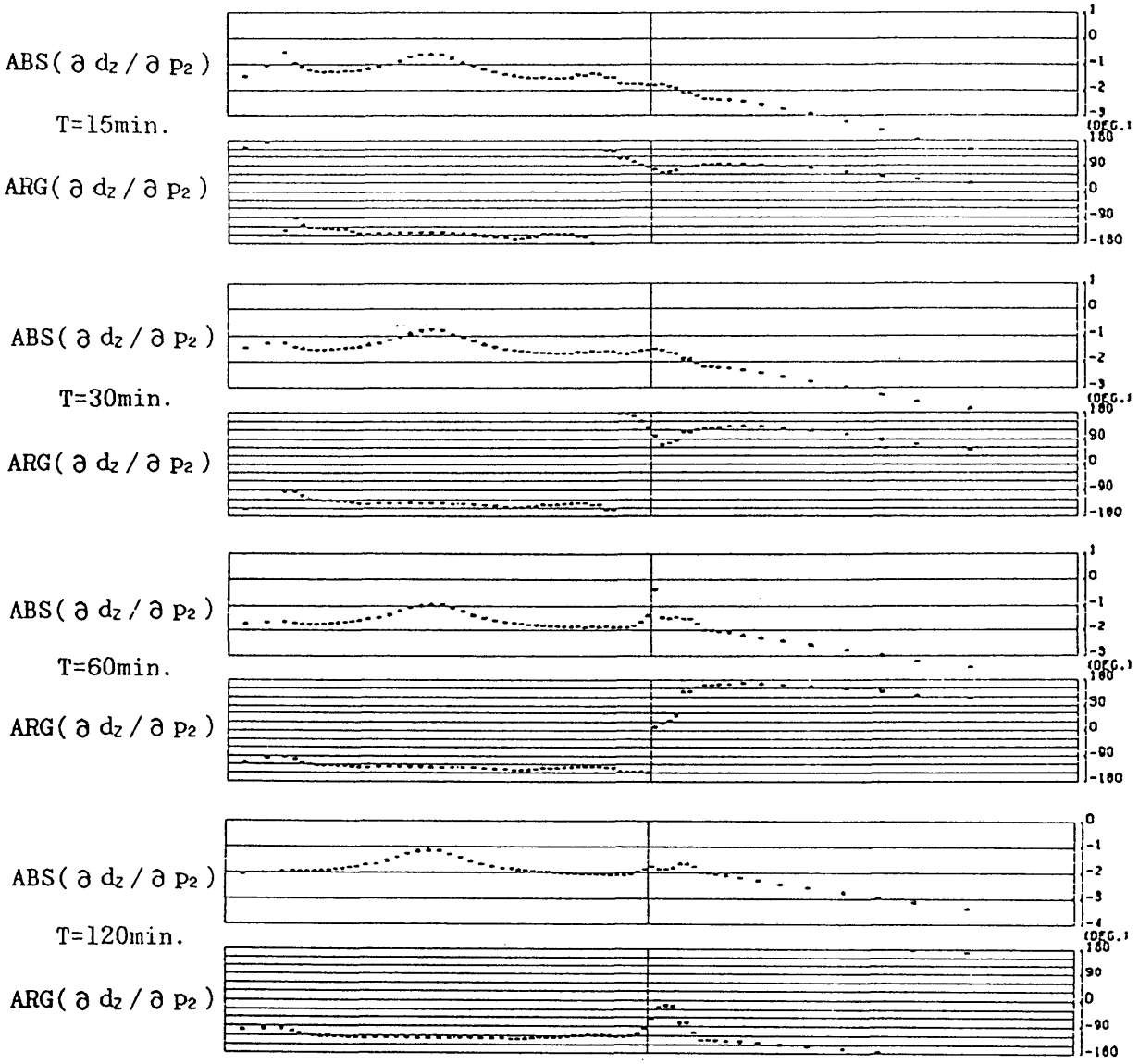
ABS(∂ dz / ∂ p2)
T=15min.
ARG(∂ dz / ∂ p2)
ABS(∂ dz / ∂ p2)
T=30min.
ARG(∂ dz / ∂ p2)
ABS(∂ dz / ∂ p2)
T=60min.
ARG(∂ dz / ∂ p2)
ABS(∂ dz / ∂ p2)
T=120min.
ARG(∂ dz / ∂ p2)
(DEG.)

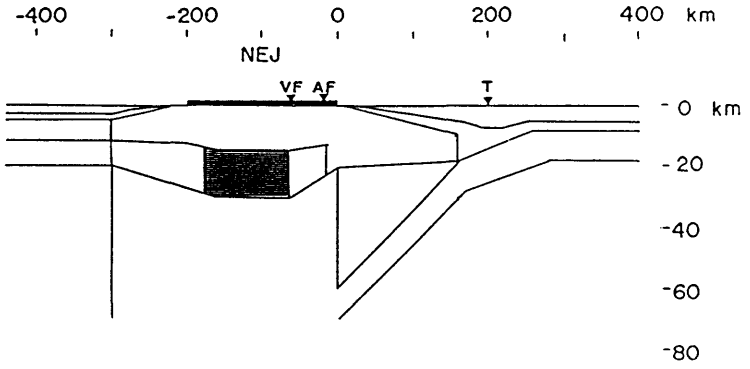
-400
-200
0
200
400 km
NEJ
VF AF
T
0 km
-20
-40
-60
-80

B-2(b)

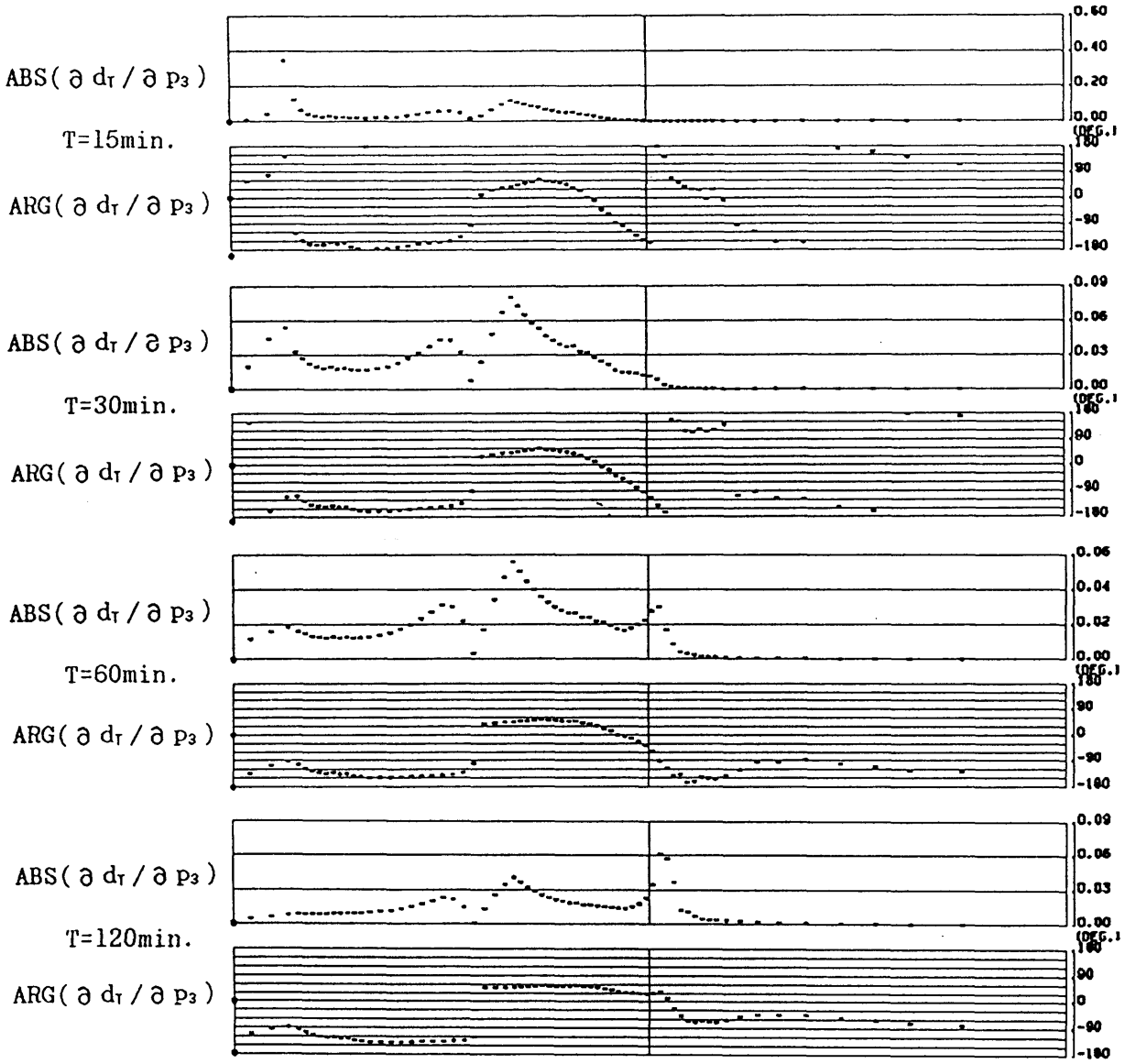
ABS(∂ dT / ∂ p3)
T=15min.
ARG(∂ dT / ∂ p3)
ABS(∂ dT / ∂ p3)
T=30min.
ARG(∂ dT / ∂ p3)
ABS(∂ dT / ∂ p3)
T=60min.
ARG(∂ dT / ∂ p3)
ABS(∂ dT / ∂ p3)
T=120min.
ARG(∂ dT / ∂ p3)
0.60
0.40
0.20
0.00
(DEG.)
180
90
0
-90
-180
0.09
0.06
0.03
0.00
0.06
0.04
0.02
0.00

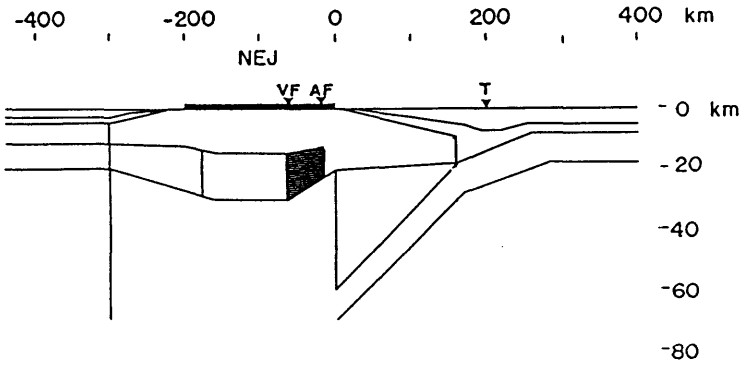
-400
-200
0
200
400 km
NEJ
VF AF
T
- 0 km
- 20
-40
-60
-80

B-3(a)

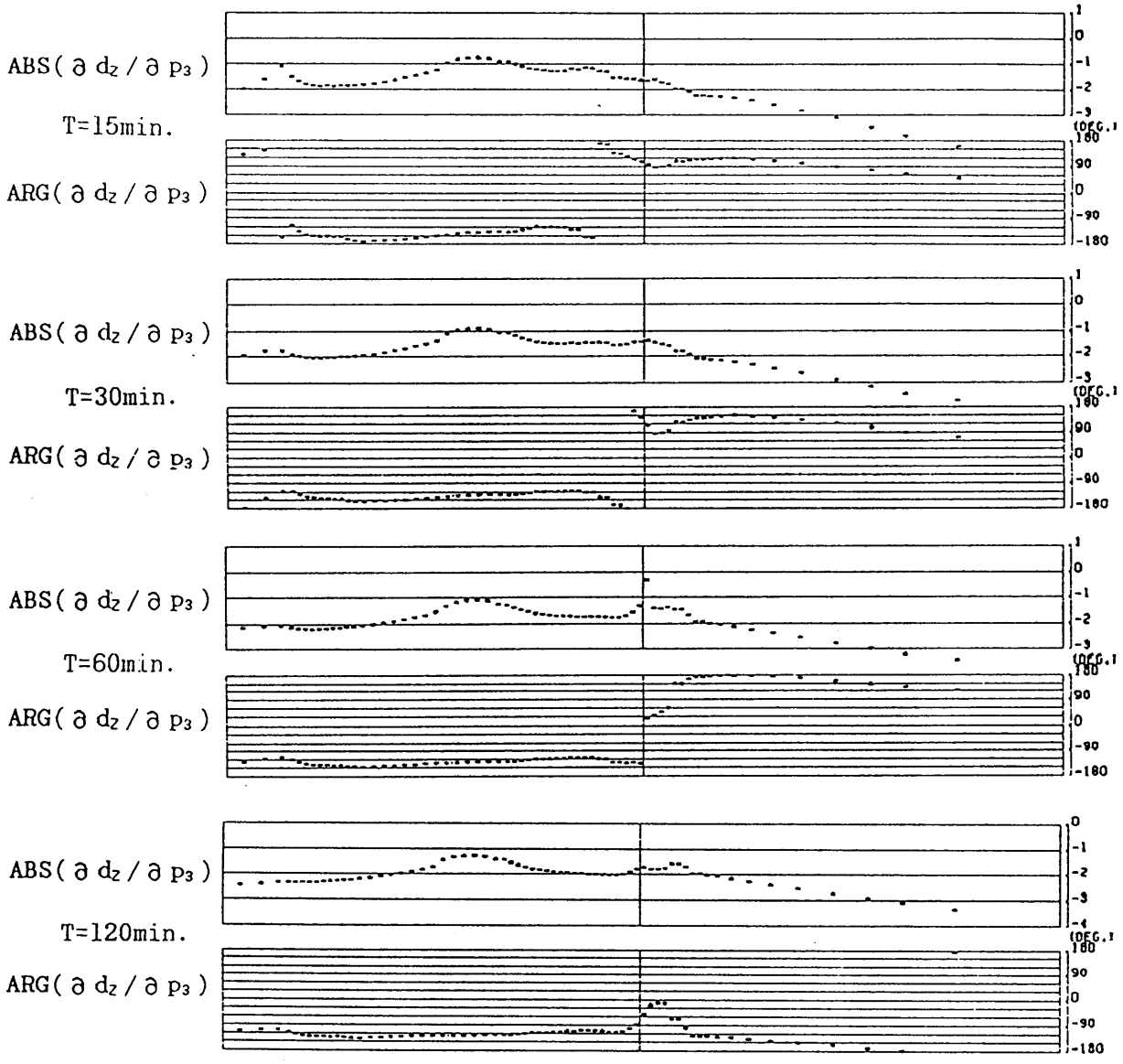
ABS(∂ dz / ∂ p3)
T=15min.
ARG(∂ dz / ∂ p3)
ABS(∂ dz / ∂ p3)
T=30min.
ARG(∂ dz / ∂ p3)
ABS(∂ dz / ∂ p3)
T=60min.
ARG(∂ dz / ∂ p3)
ABS(∂ dz / ∂ p3)
T=120min.
ARG(∂ dz / ∂ p3)
(DEG.)
180
90
0
-90
-180

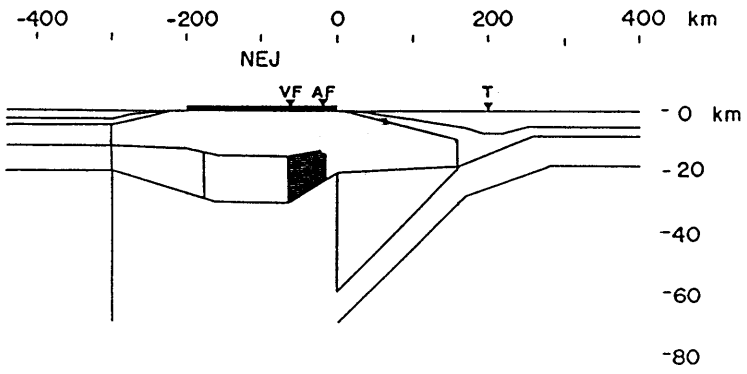
-400
-200
0
200
400 km
NEJ
VF AF
T
0 km
-20
-40
-60
-80

B-3(b)

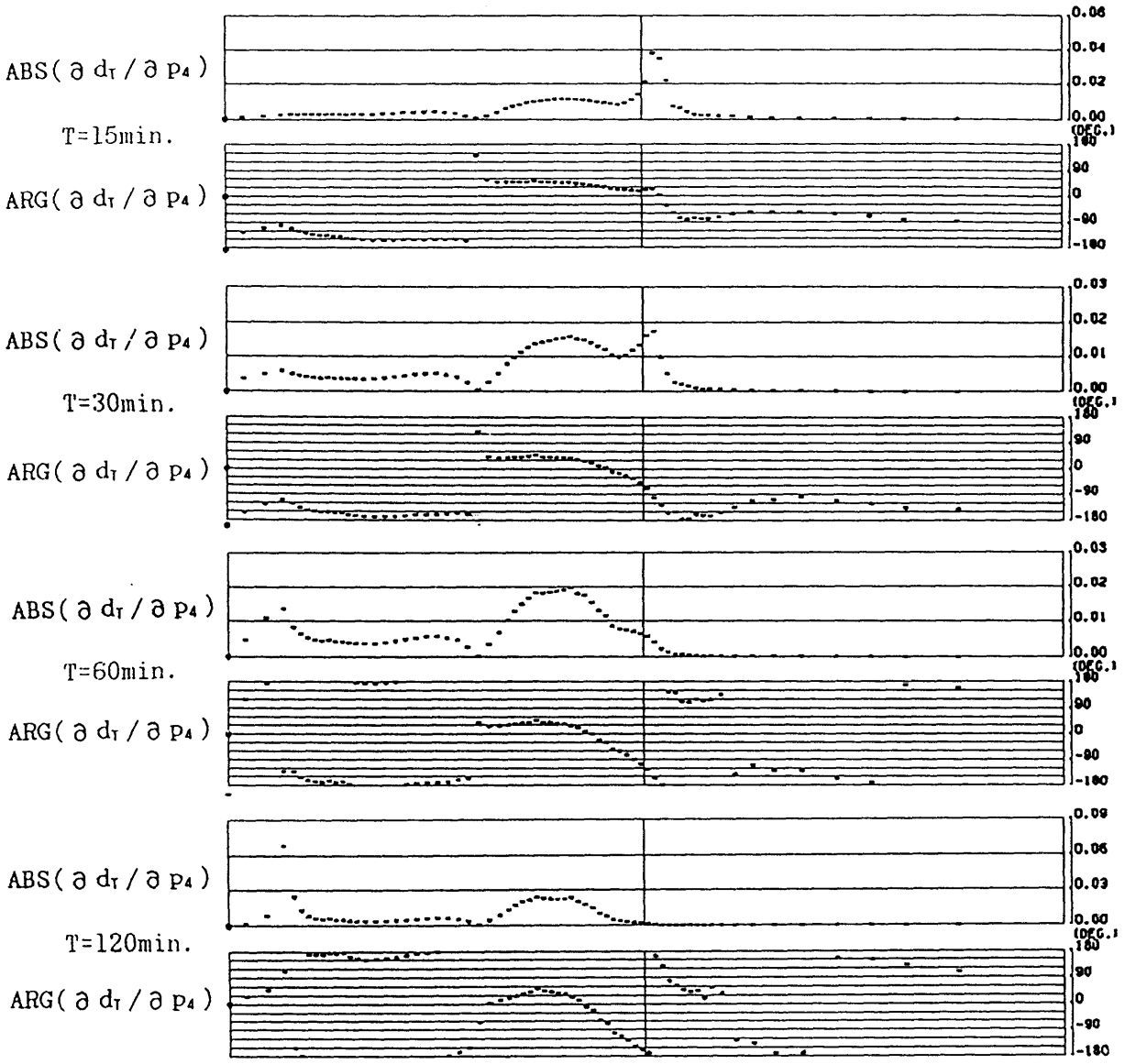
ABS(∂ dT / ∂ p4)
T=15min.
ARG(∂ dT / ∂ p4)
ABS(∂ dT / ∂ p4)
T=30min.
ARG(∂ dT / ∂ p4)
ABS(∂ dT / ∂ p4)
T=60min.
ARG(∂ dT / ∂ p4)
ABS(∂ dT / ∂ p4)
T=120min.
ARG(∂ dT / ∂ p4)
0.06
0.04
0.02
0.00
(DEG.)
180
90
0
-90
-180
0.03
0.02
0.01
0.00
0.09
0.06
0.03

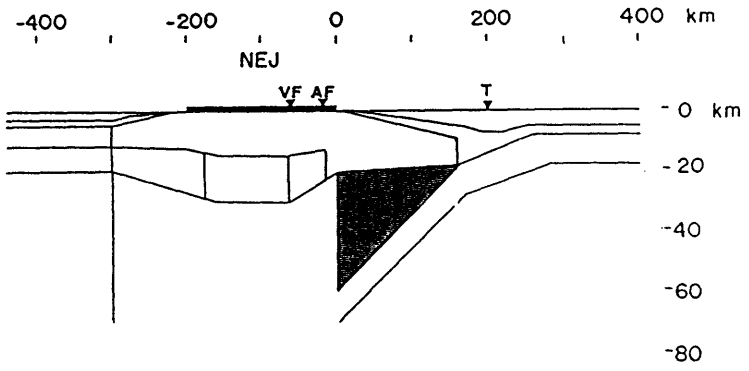
-400
-200
0
200
400 km
NEJ
VF AF
T
0 km
-20
-40
-60
-80

B-4(a)

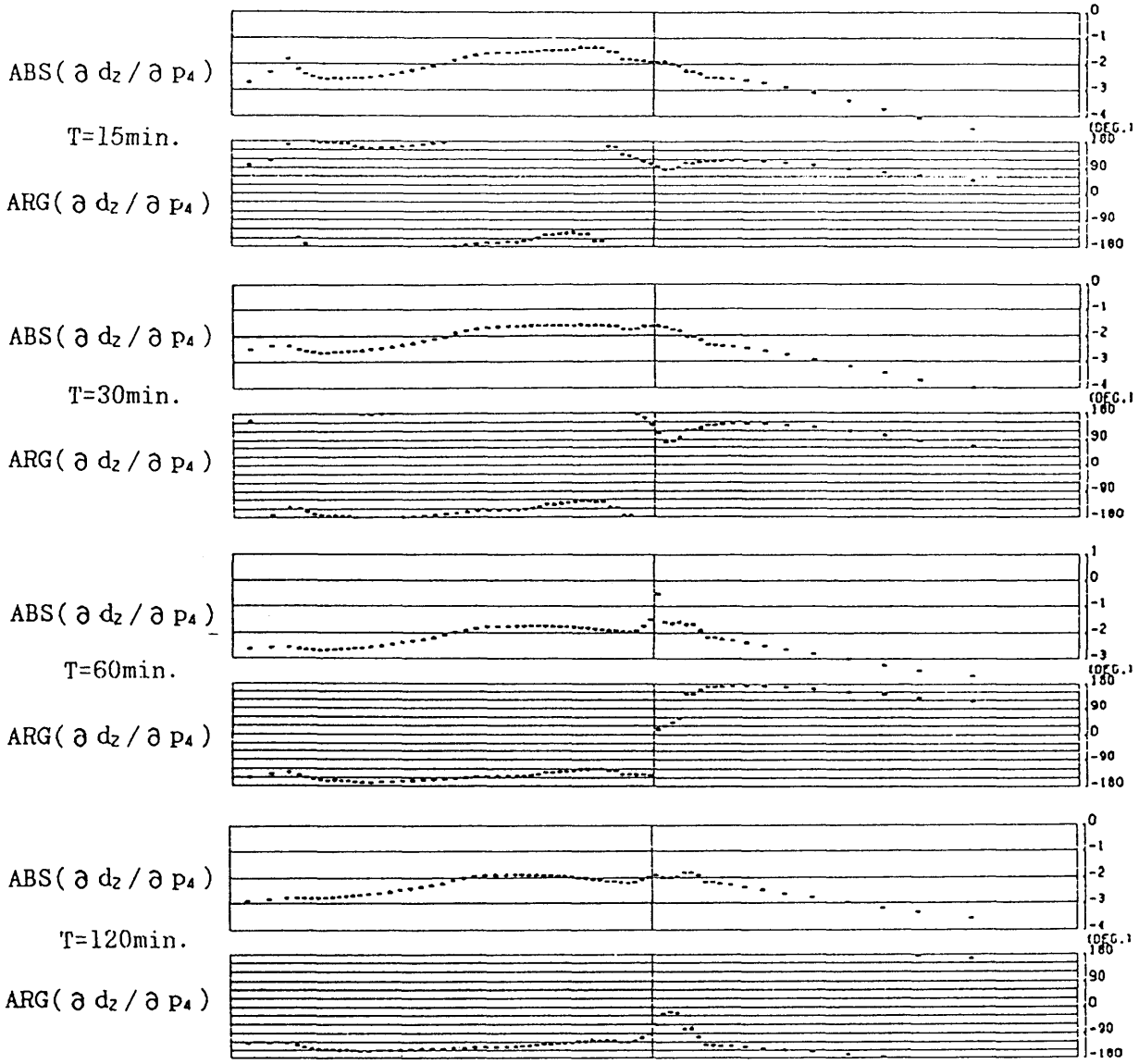
ABS(∂ dz / ∂ p4)
T=15min.
ARG(∂ dz / ∂ p4)
ABS(∂ dz / ∂ p4)
T=30min.
ARG(∂ dz / ∂ p4)
ABS(∂ dz / ∂ p4)
T=60min.
ARG(∂ dz / ∂ p4)
ABS(∂ dz / ∂ p4)
T=120min.
ARG(∂ dz / ∂ p4)
(DEG.)

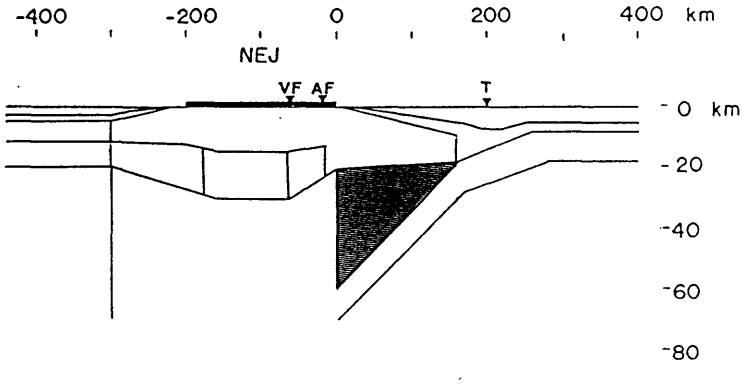
-400
-200
0
200
400 km
NEJ
VF AF
T
0 km
-20
-40
-60
-80

B-4(b)

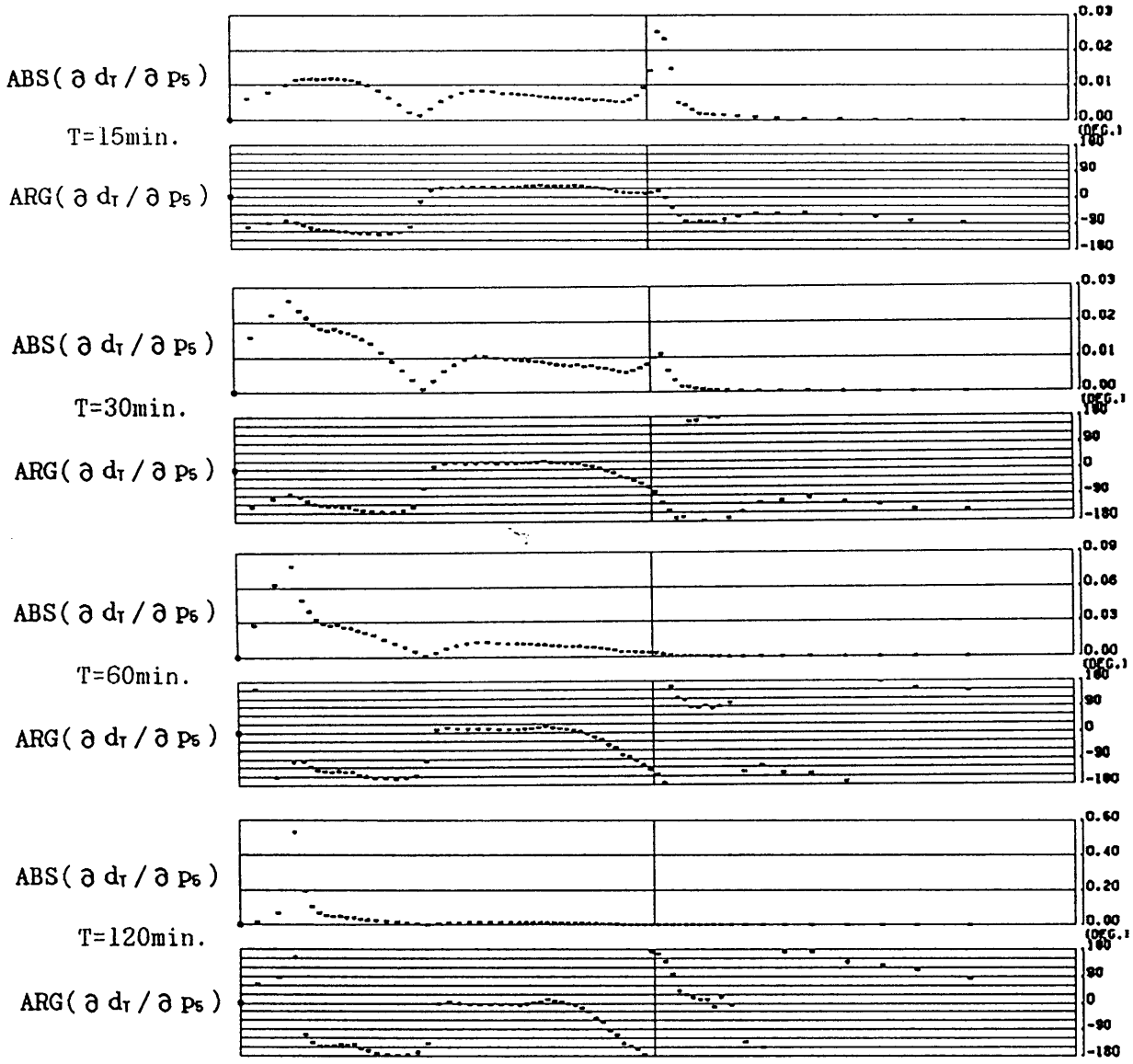
ABS(∂ dT / ∂ p5)
T=15min.
ARG(∂ dT / ∂ p5)
ABS(∂ dT / ∂ p5)
T=30min.
ARG(∂ dT / ∂ p5)
ABS(∂ dT / ∂ p6)
T=60min.
ARG(∂ dT / ∂ p6)
ABS(∂ dT / ∂ p6)
T=120min.
ARG(∂ dT / ∂ p6)
0.03
0.02
0.01
0.00
0.09
0.06
0.03
0.60
0.40
0.20
(DEG.)
180
90
0
-90
-180

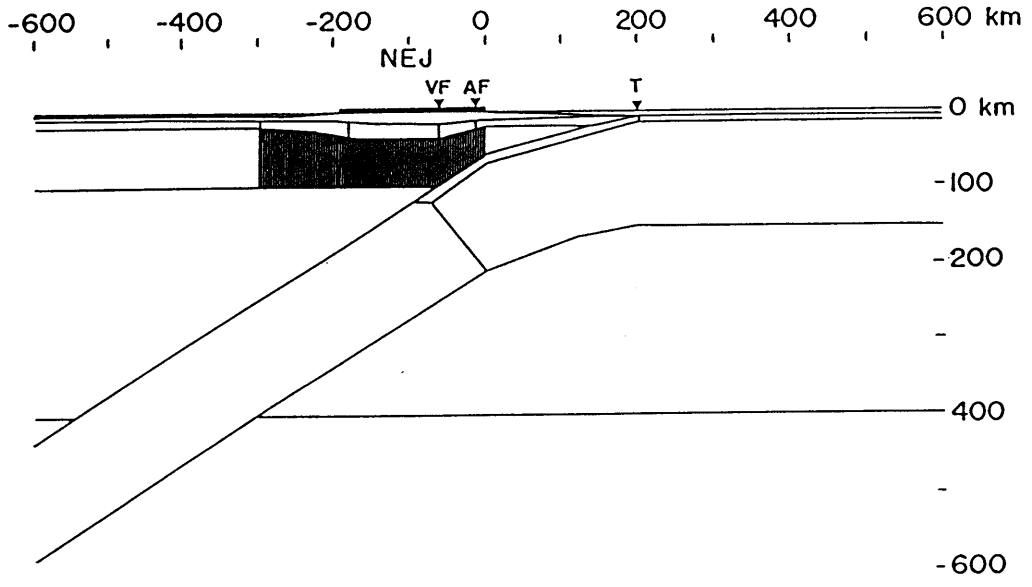
-600
-400
-200
0
200
400
600 km
NEJ
VF
AF
T
0 km
-100
-200
-400
-600

B-5(a)

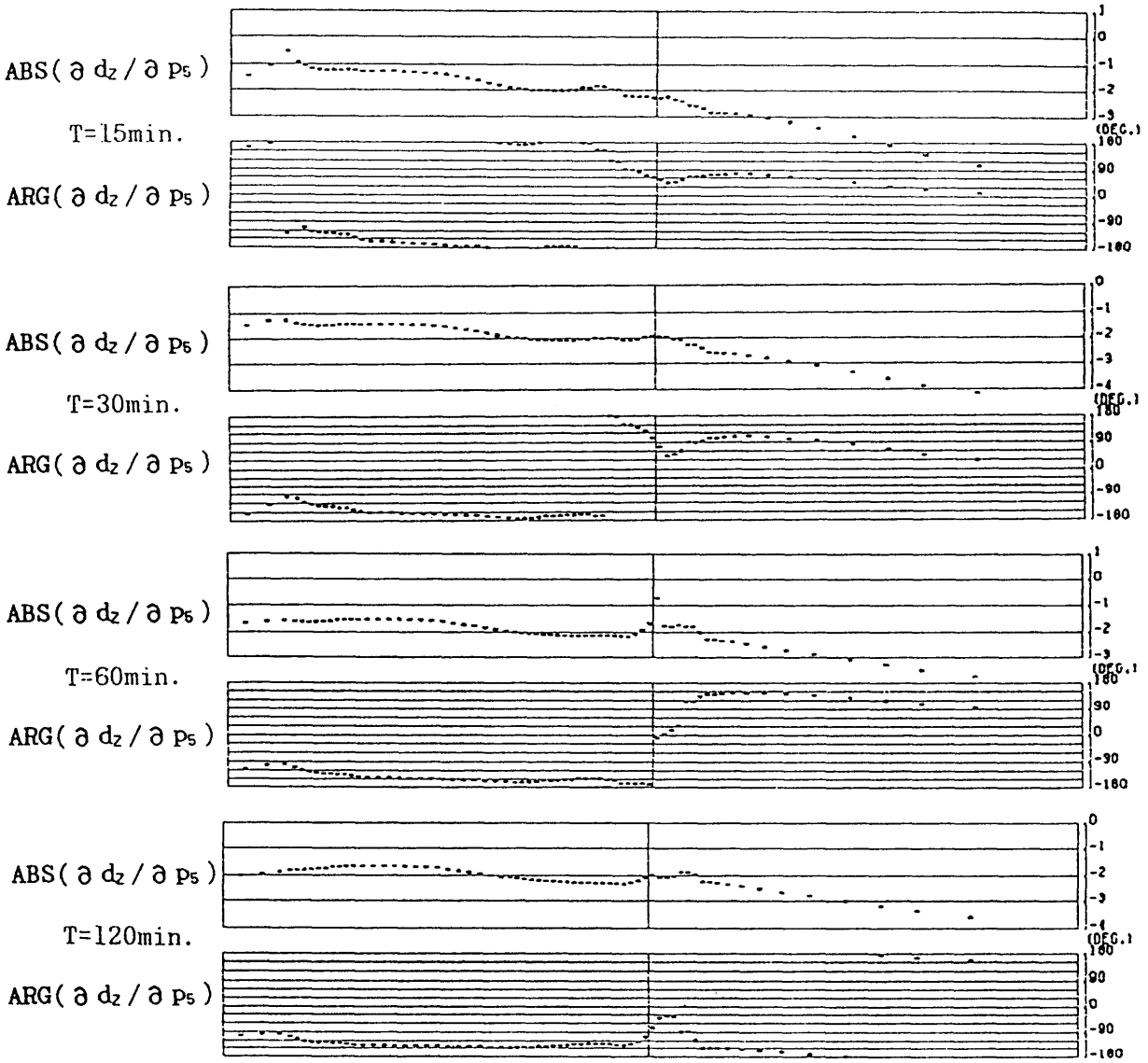
ABS(∂ dz / ∂ ps)
T=15min.
ARG(∂ dz / ∂ ps)
ABS(∂ dz / ∂ ps)
T=30min.
ARG(∂ dz / ∂ ps)
ABS(∂ dz / ∂ ps)
T=60min.
ARG(∂ dz / ∂ ps)
ABS(∂ dz / ∂ ps)
T=120min.
ARG(∂ dz / ∂ ps)
(DEG.)

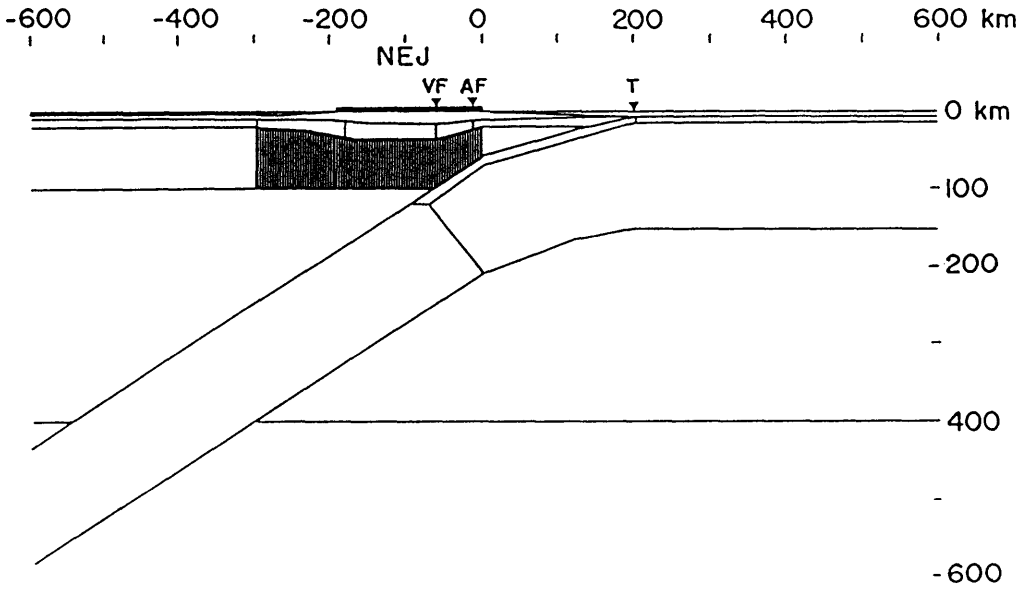
-600
-400
-200
0
200
400
600 km
NEJ
VF
AF
T
0 km
-100
-200
-400
-600

B-5(b)

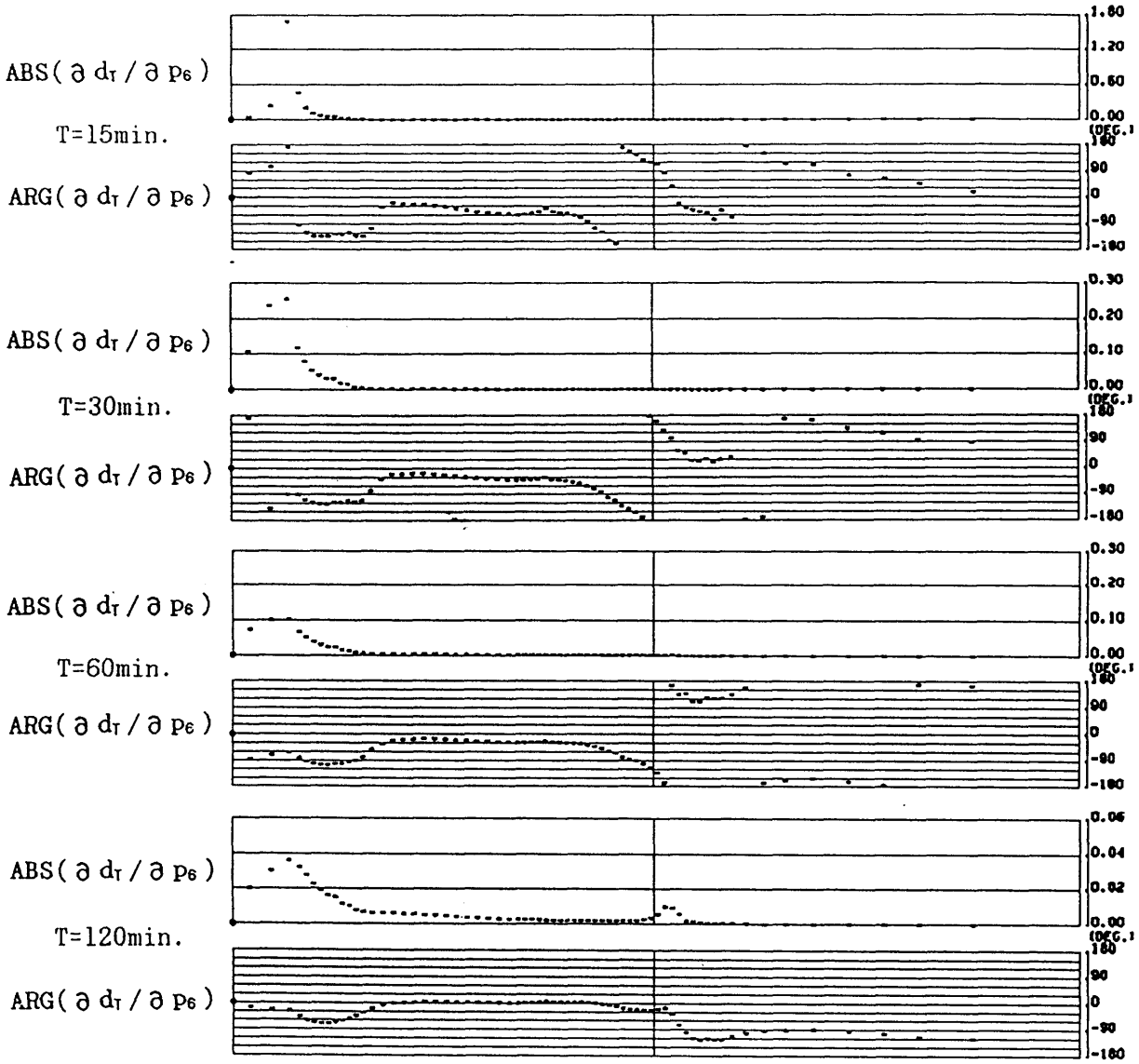
ABS(∂ dT / ∂ pe)
T=15min.
ARG(∂ dT / ∂ pe)
ABS(∂ dT / ∂ pe)
T=30min.
ARG(∂ dT / ∂ pe)
ABS(∂ dT / ∂ pe)
T=60min.
ARG(∂ dT / ∂ pe)
ABS(∂ dT / ∂ pe)
T=120min.
ARG(∂ dT / ∂ pe)
1.60
1.20
0.60
0.00
(DEG.)
180
90
0
-90
-180
0.30
0.20
0.10
0.00
0.06
0.04
0.02

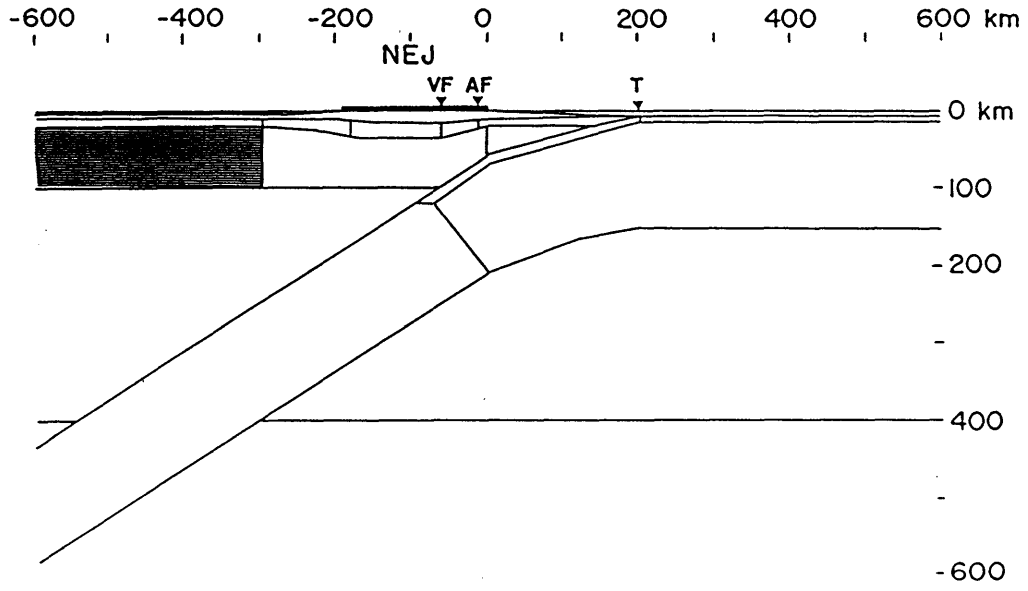
-600
-400
-200
0
200
400
600 km
NEJ
VF
AF
T
0 km
-100
-200
-400
-600

B-6(a)

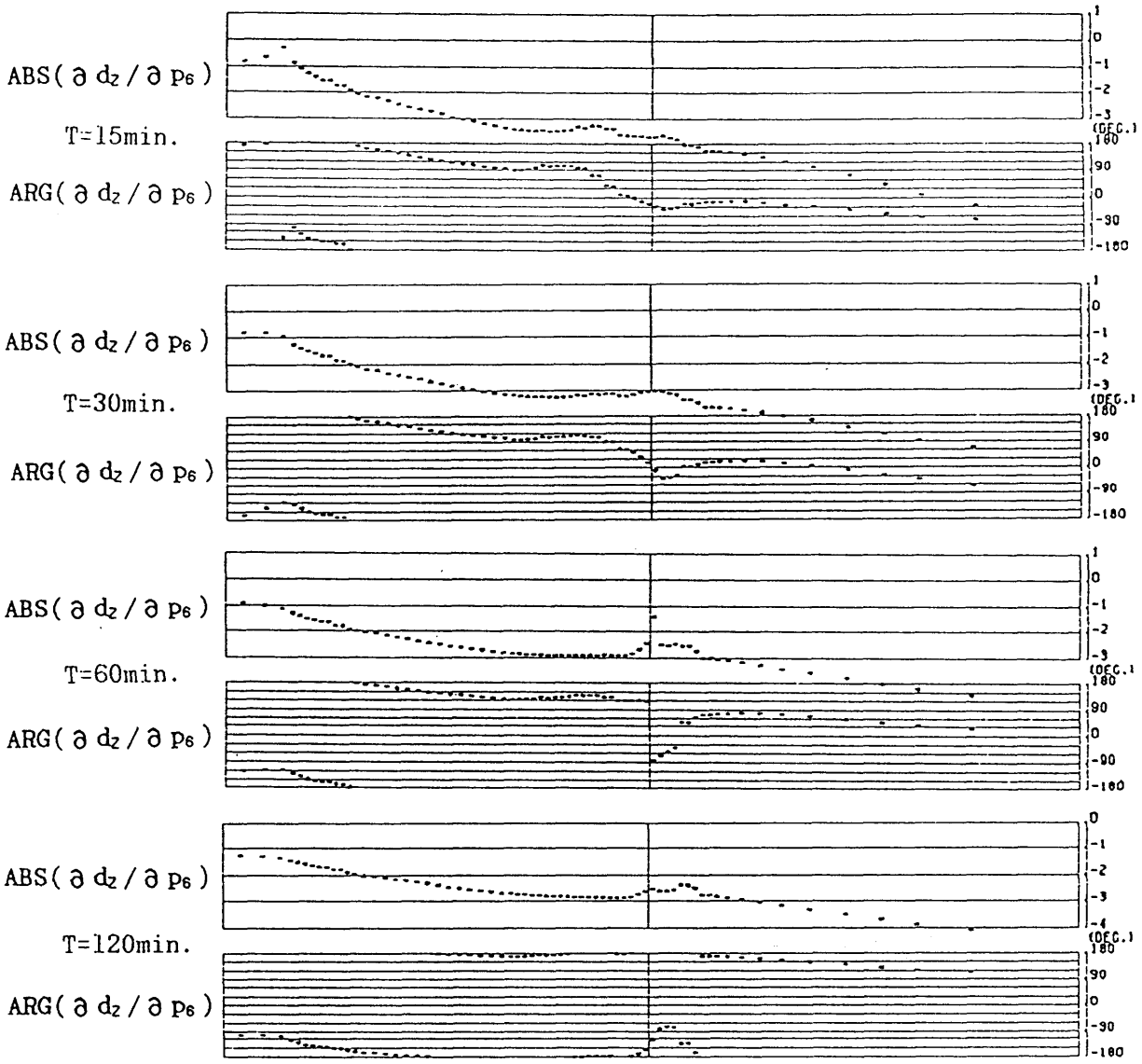
ABS(∂ dz / ∂ p6)
T=15min.
ARG(∂ dz / ∂ p6)
ABS(∂ dz / ∂ p6)
T=30min.
ARG(∂ dz / ∂ p6)
ABS(∂ dz / ∂ p6)
T=60min.
ARG(∂ dz / ∂ p6)
ABS(∂ dz / ∂ p6)
T=120min.
ARG(∂ dz / ∂ p6)
(DEG.)

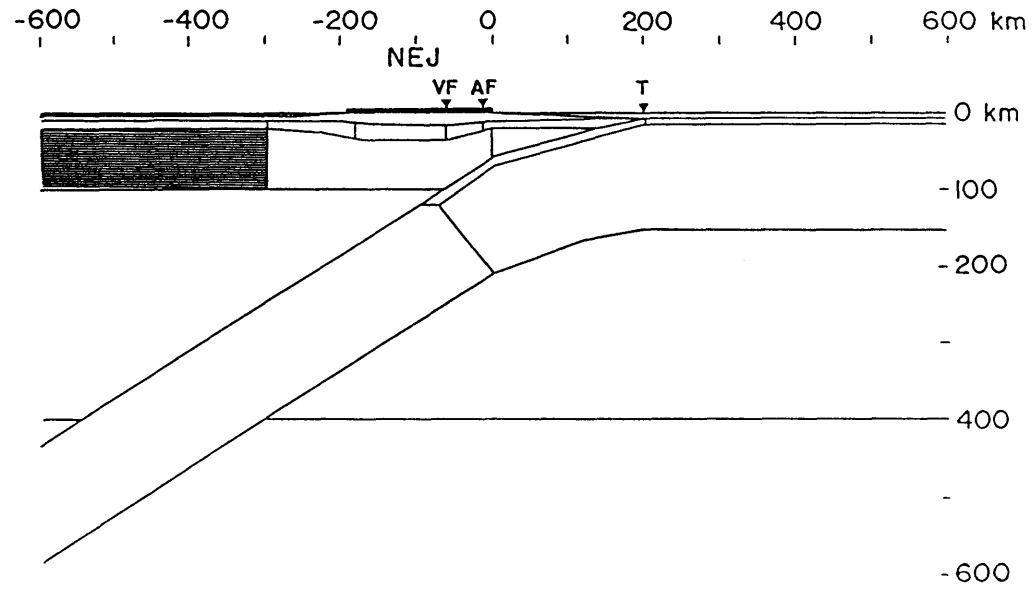
-600
-400
-200
0
200
400
600 km
NEJ
VF
AF
T
0 km
-100
-200
-400
-600

B-6(b)

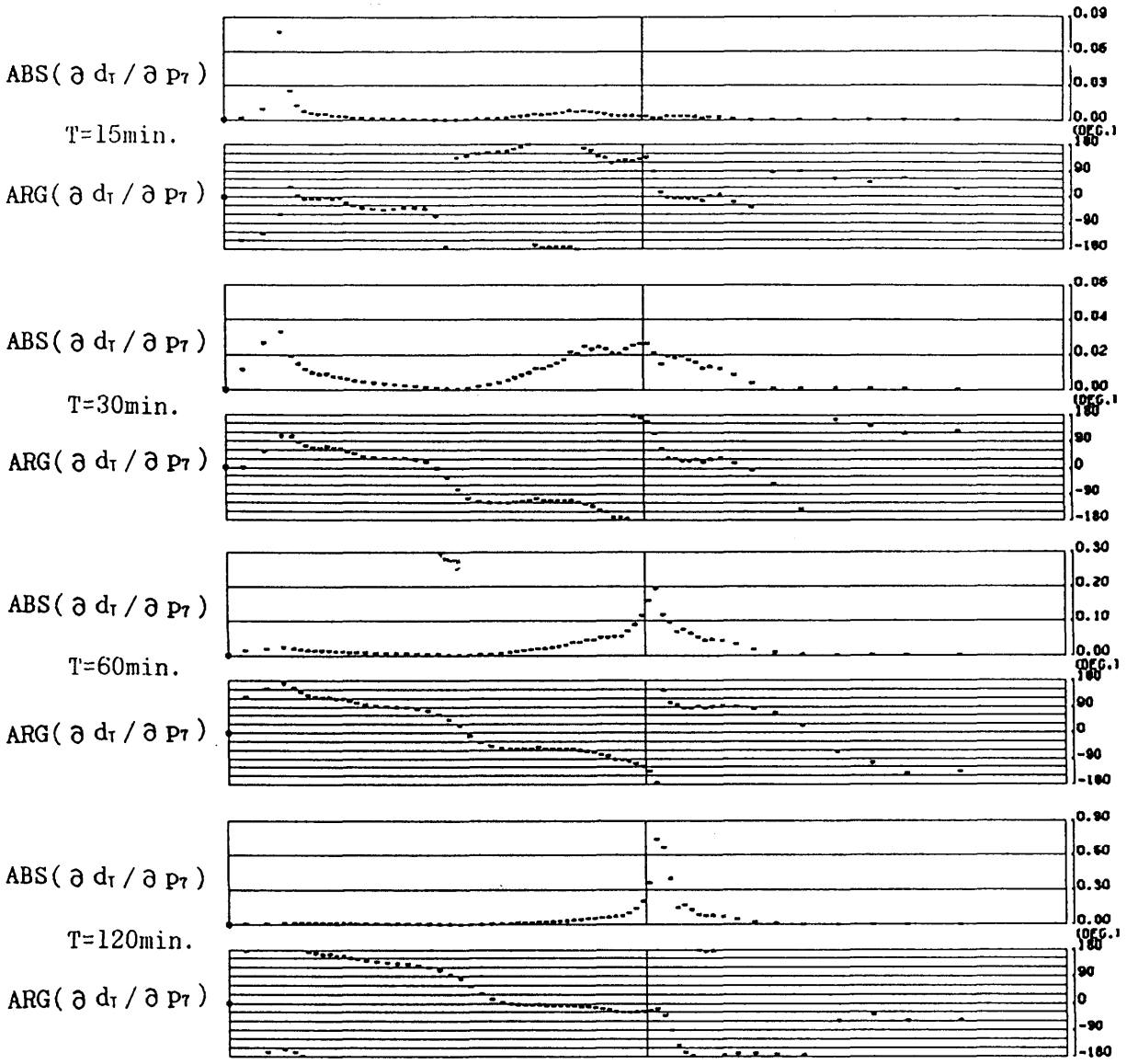
ABS(∂ dT / ∂ pT)
T=15min.
ARG(∂ dT / ∂ pT)
ABS(∂ dT / ∂ pT)
T=30min.
ARG(∂ dT / ∂ pT)
ABS(∂ dT / ∂ pT)
T=60min.
ARG(∂ dT / ∂ pT)
ABS(∂ dT / ∂ pT)
T=120min.
ARG(∂ dT / ∂ pT)
(DEG.)

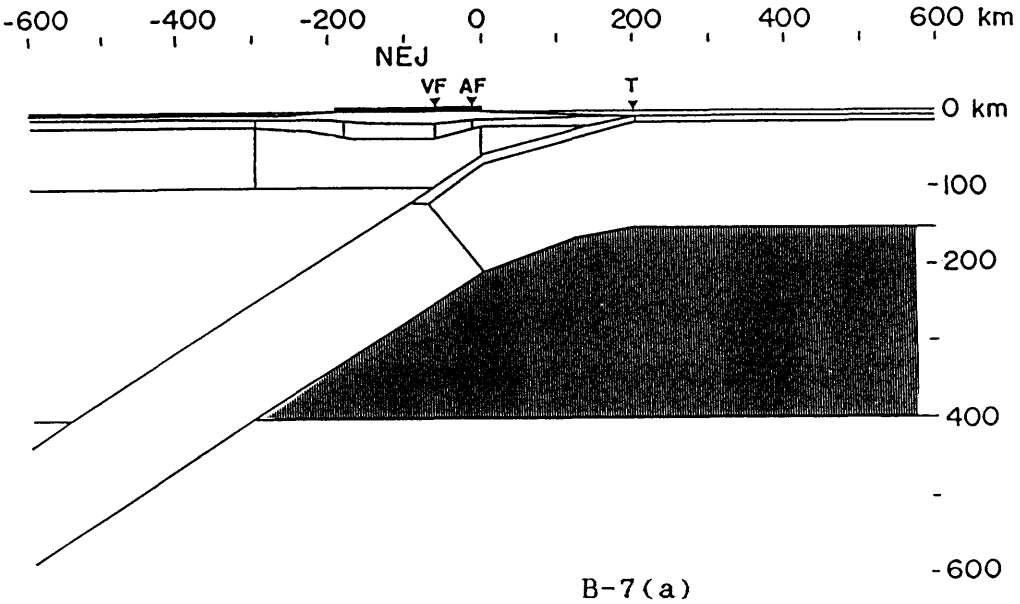
-600
-400
-200
0
200
400
600 km
NEJ
VF
AF
T
0 km
-100
-200
-400
-600

B-7(a)

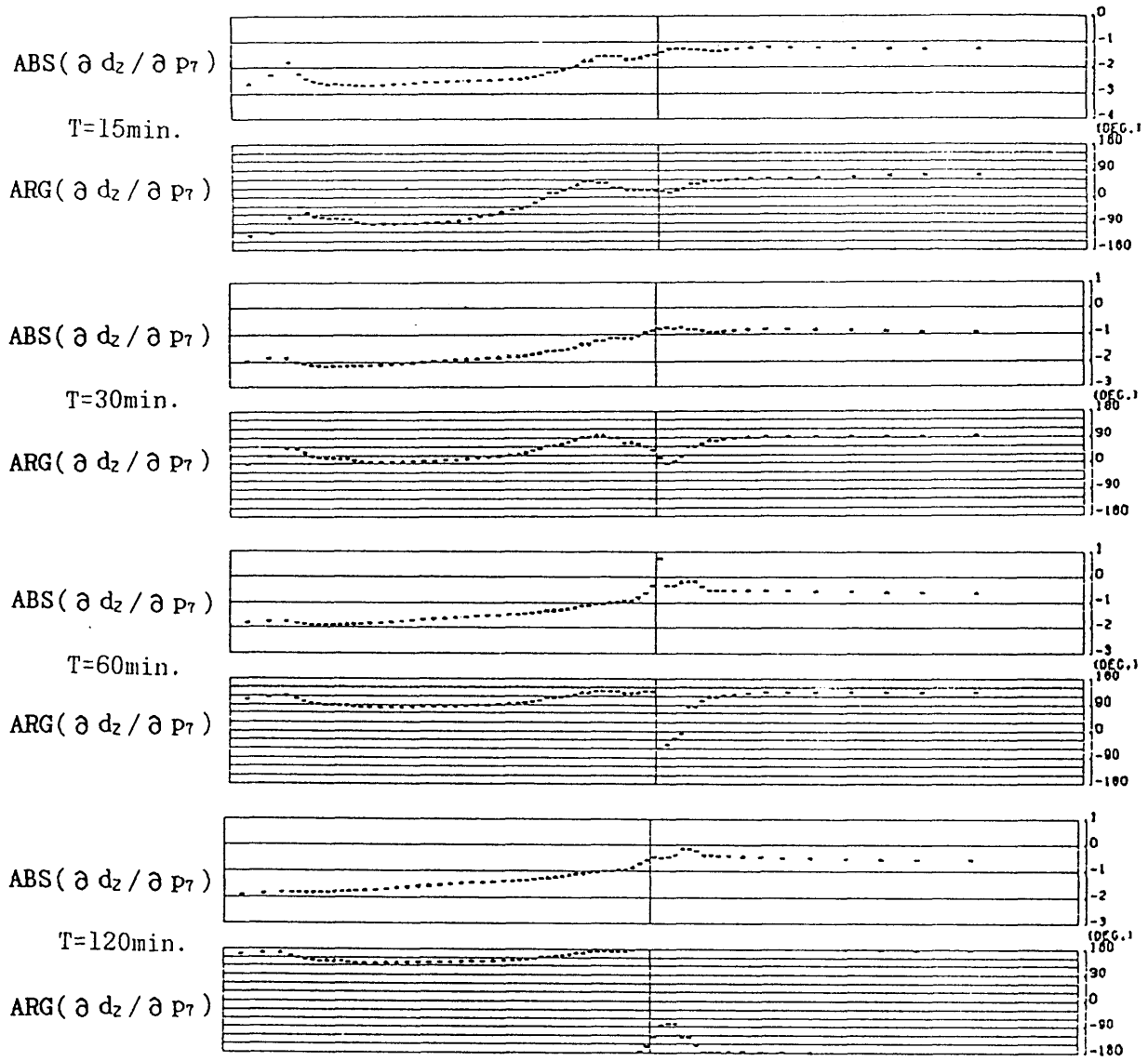
ABS(∂ dz / ∂ p7)
T=15min.
ARG(∂ dz / ∂ p7)
ABS(∂ dz / ∂ p7)
T=30min.
ARG(∂ dz / ∂ p7)
ABS(∂ dz / ∂ p7)
T=60min.
ARG(∂ dz / ∂ p7)
ABS(∂ dz / ∂ p7)
T=120min.
ARG(∂ dz / ∂ p7)
(DEG.)

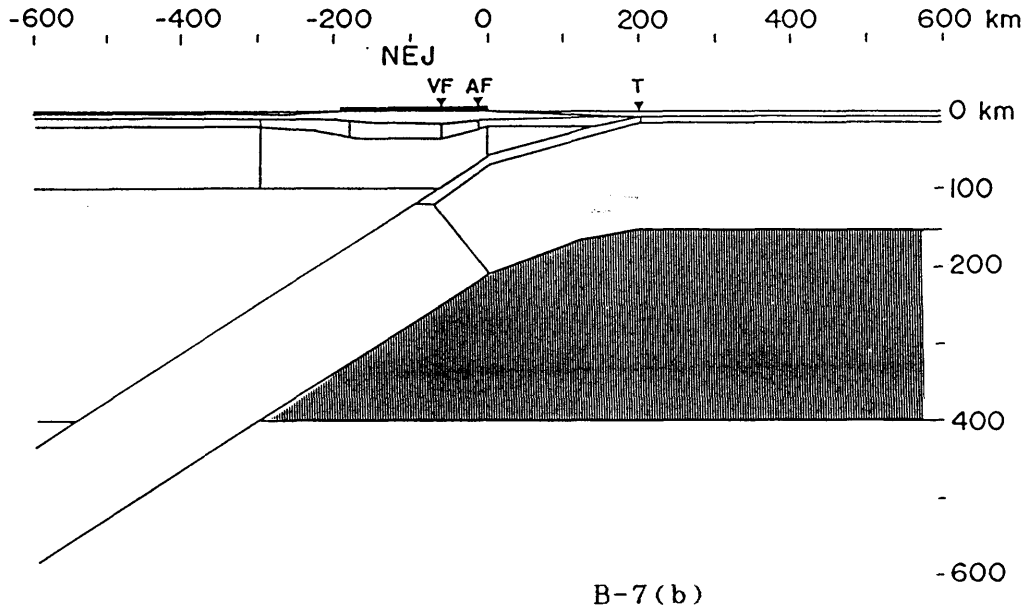
-600
-400
-200
0
200
400
600 km
NEJ
VF
AF
T
0 km
-100
-200
-400
-600

B-7(b)

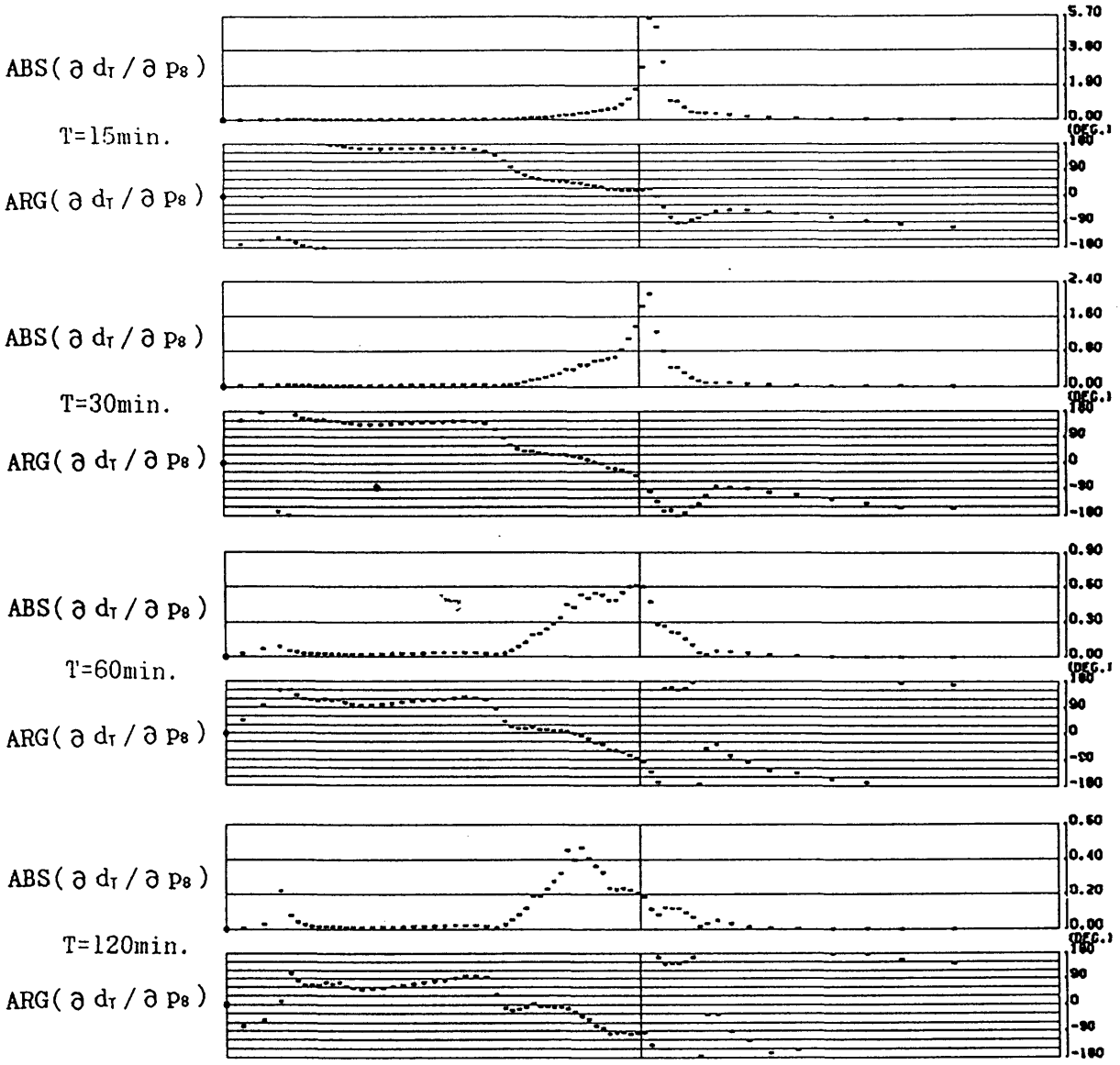
ABS(∂ dT / ∂ p8)
T=15min.
ARG(∂ dT / ∂ p8)
ABS(∂ dT / ∂ p8)
T=30min.
ARG(∂ dT / ∂ p8)
ABS(∂ dT / ∂ p8)
T=60min.
ARG(∂ dT / ∂ p8)
ABS(∂ dT / ∂ p8)
T=120min.
ARG(∂ dT / ∂ p8)

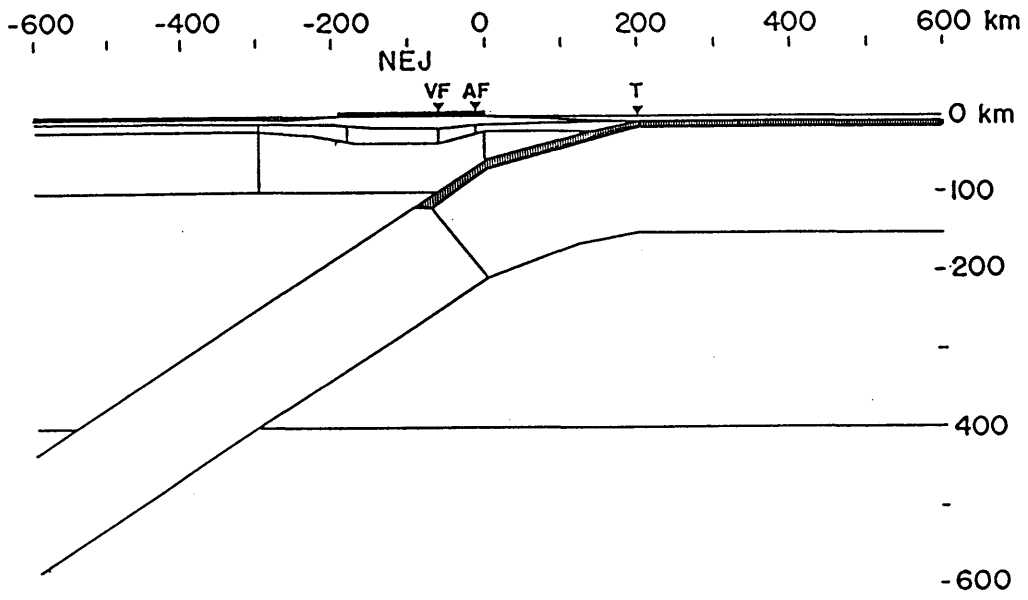
-600
-400
-200
0
200
400
600 km
NEJ
VF
AF
T
0 km
-100
-200
-400
-600

B-8(a)

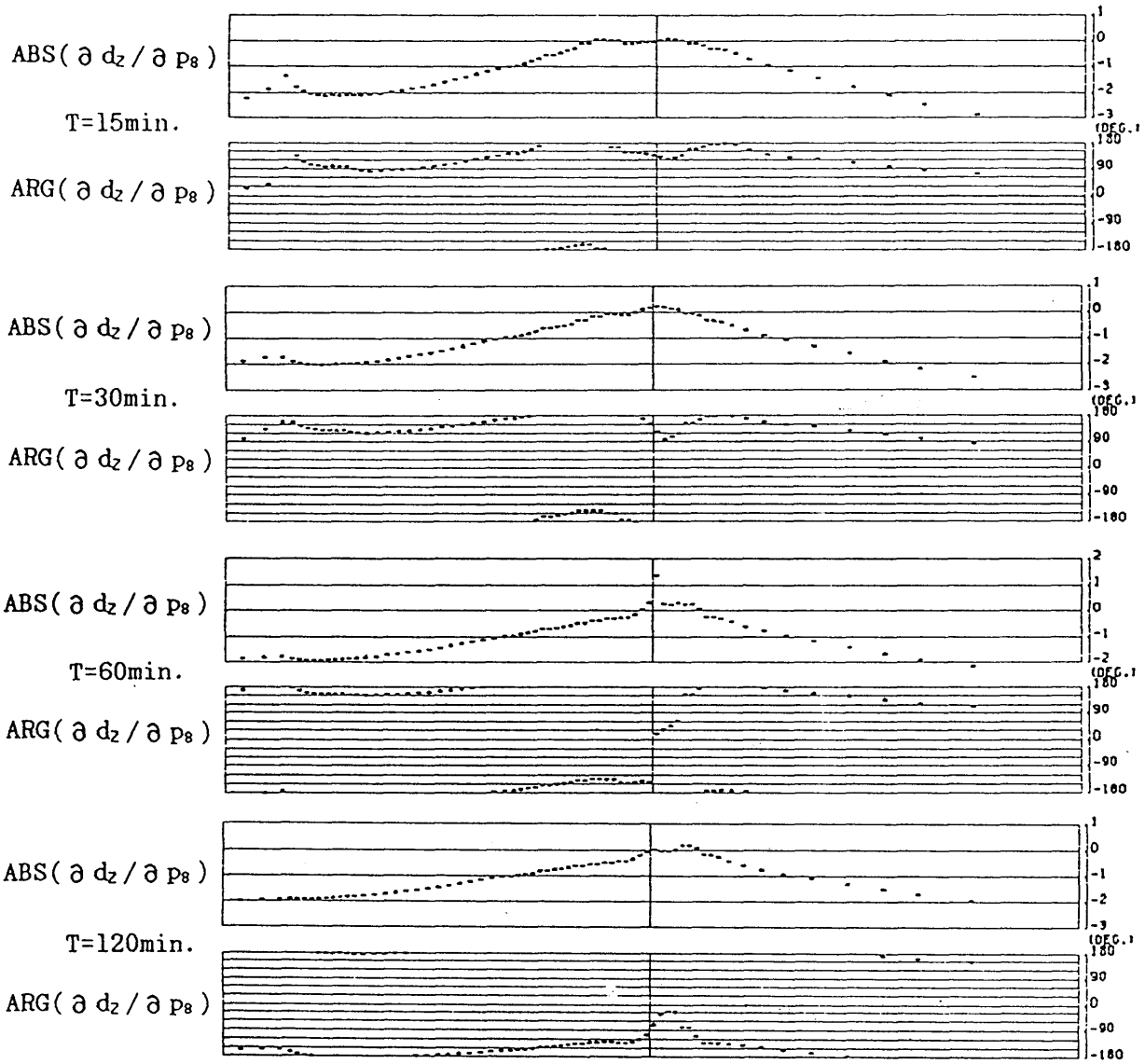
ABS(∂ dz / ∂ ps)
T=15min.
ARG(∂ dz / ∂ ps)
ABS(∂ dz / ∂ ps)
T=30min.
ARG(∂ dz / ∂ ps)
ABS(∂ dz / ∂ ps)
T=60min.
ARG(∂ dz / ∂ ps)
ABS(∂ dz / ∂ ps)
T=120min.
ARG(∂ dz / ∂ ps)
(DEG.)

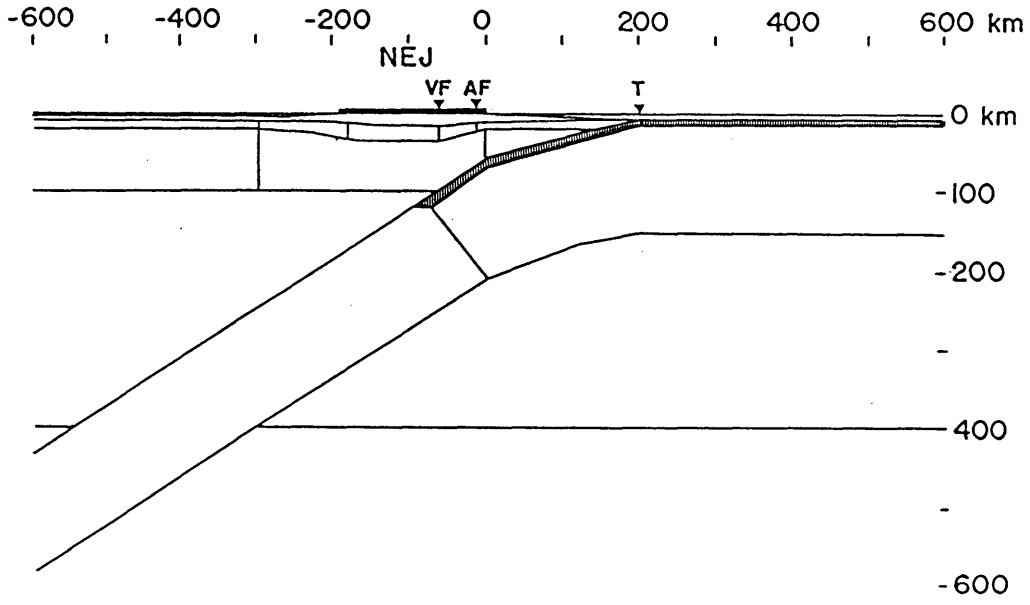
-600
-400
-200
0
200
400
600 km
NEJ
VF
AF
T
0 km
-100
-200
-400
-600

B-8(b)

Appendix C. Distribution of the partial derivatives of the response functions for inversion of the central Japan data.

Figures given here are the complete list of the partial derivatives calculated for the initial values of the seven unknown model parameters in the inversion of the central Japan data. Presentation is the same as that in Appendix B.

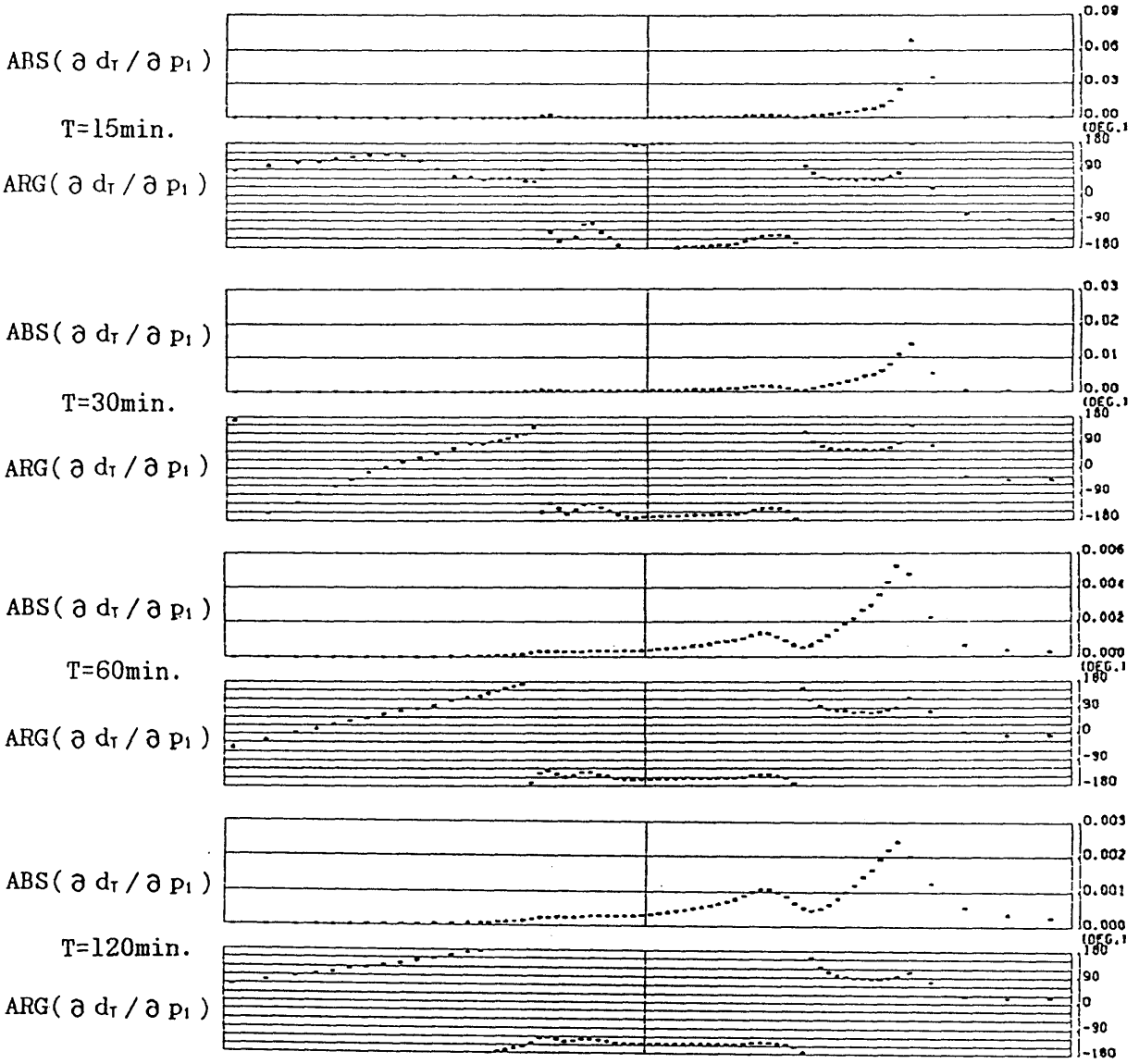
ABS(∂ dT / ∂ p1)
T=15min.
ARG(∂ dT / ∂ p1)
ABS(∂ dT / ∂ p1)
T=30min.
ARG(∂ dT / ∂ p1)
ABS(∂ dT / ∂ p1)
T=60min.
ARG(∂ dT / ∂ p1)
ABS(∂ dT / ∂ p1)
T=120min.
ARG(∂ dT / ∂ p1)
(DEG.)
180
90
0
-90
-180

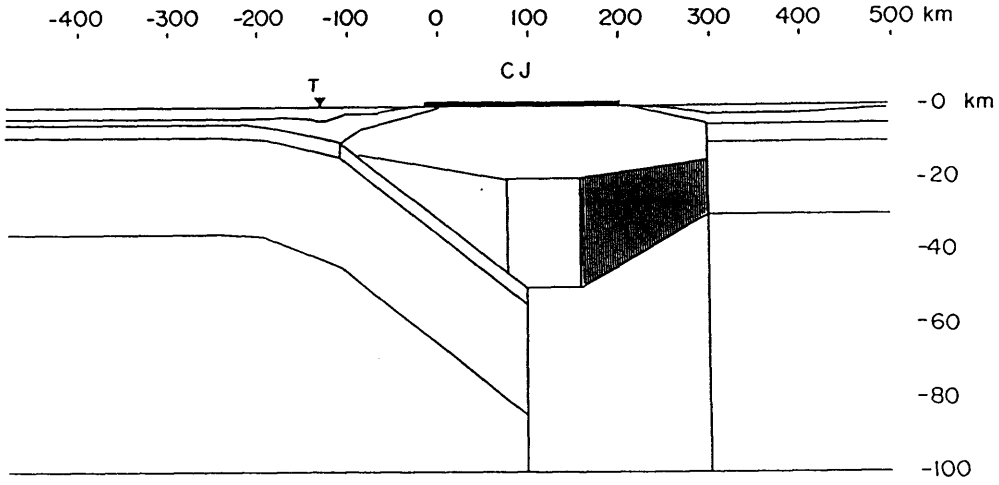
-400
-300
-200
-100
0
100
200
300
400
500 km
CJ
T
-0 km
-20
-40
-60
-80
-100

C-1(a)

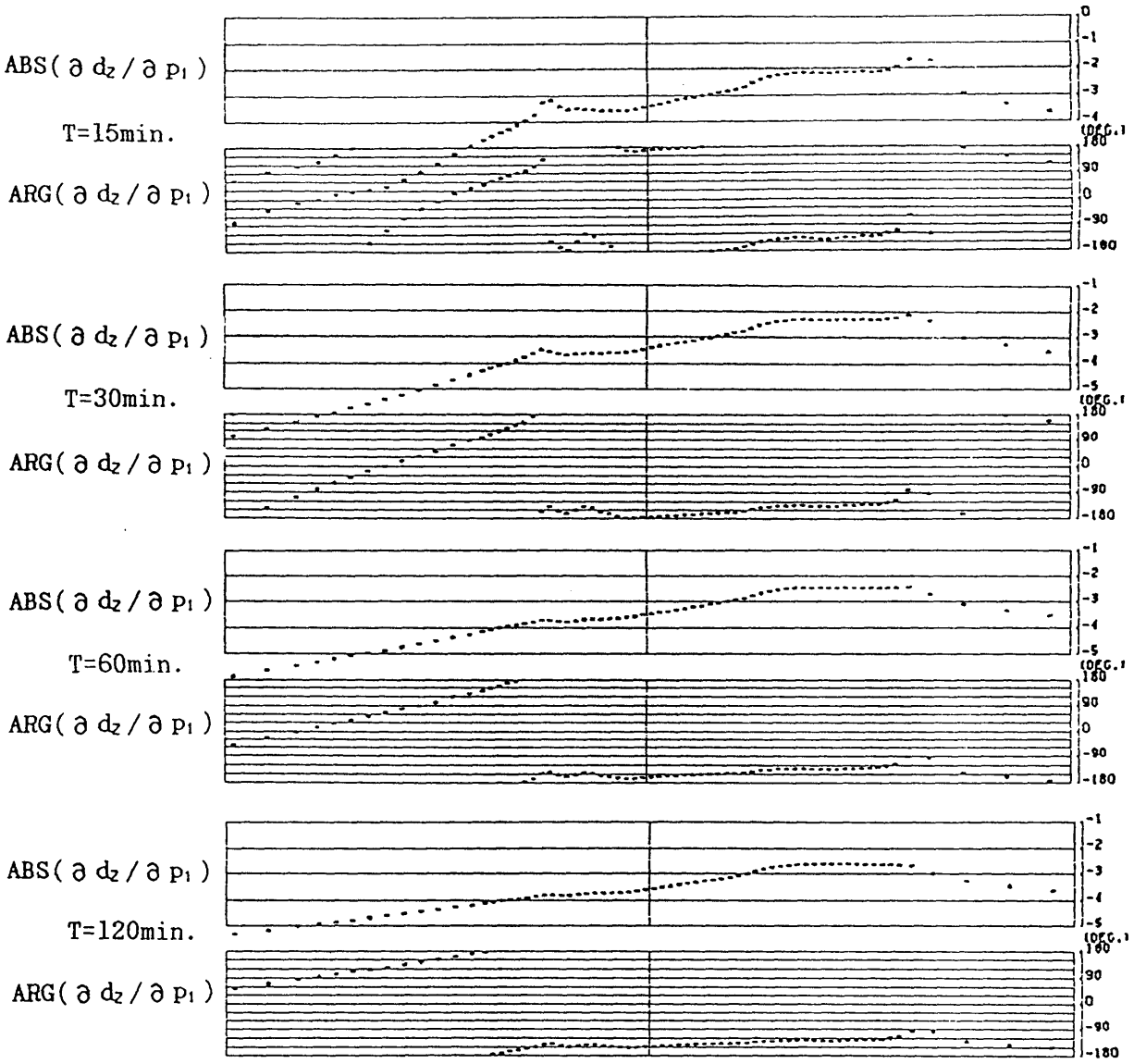
ABS(∂ dz / ∂ p1)
T=15min.
ARG(∂ dz / ∂ p1)
ABS(∂ dz / ∂ p1)
T=30min.
ARG(∂ dz / ∂ p1)
ABS(∂ dz / ∂ p1)
T=60min.
ARG(∂ dz / ∂ p1)
ABS(∂ dz / ∂ p1)
T=120min.
ARG(∂ dz / ∂ p1)

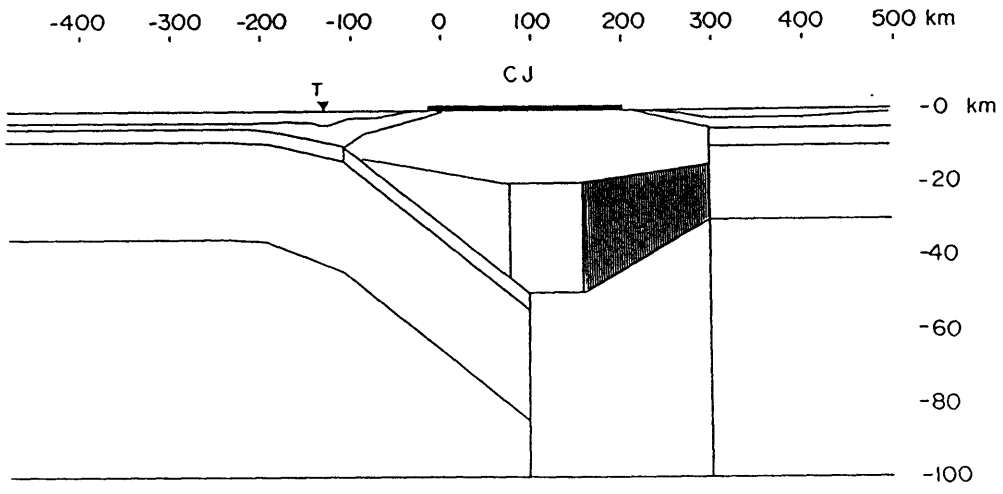
-400
-300
-200
-100
0
100
200
300
400
500 km
T
CJ
-0 km
-20
-40
-60
-80
-100

C-1(b)

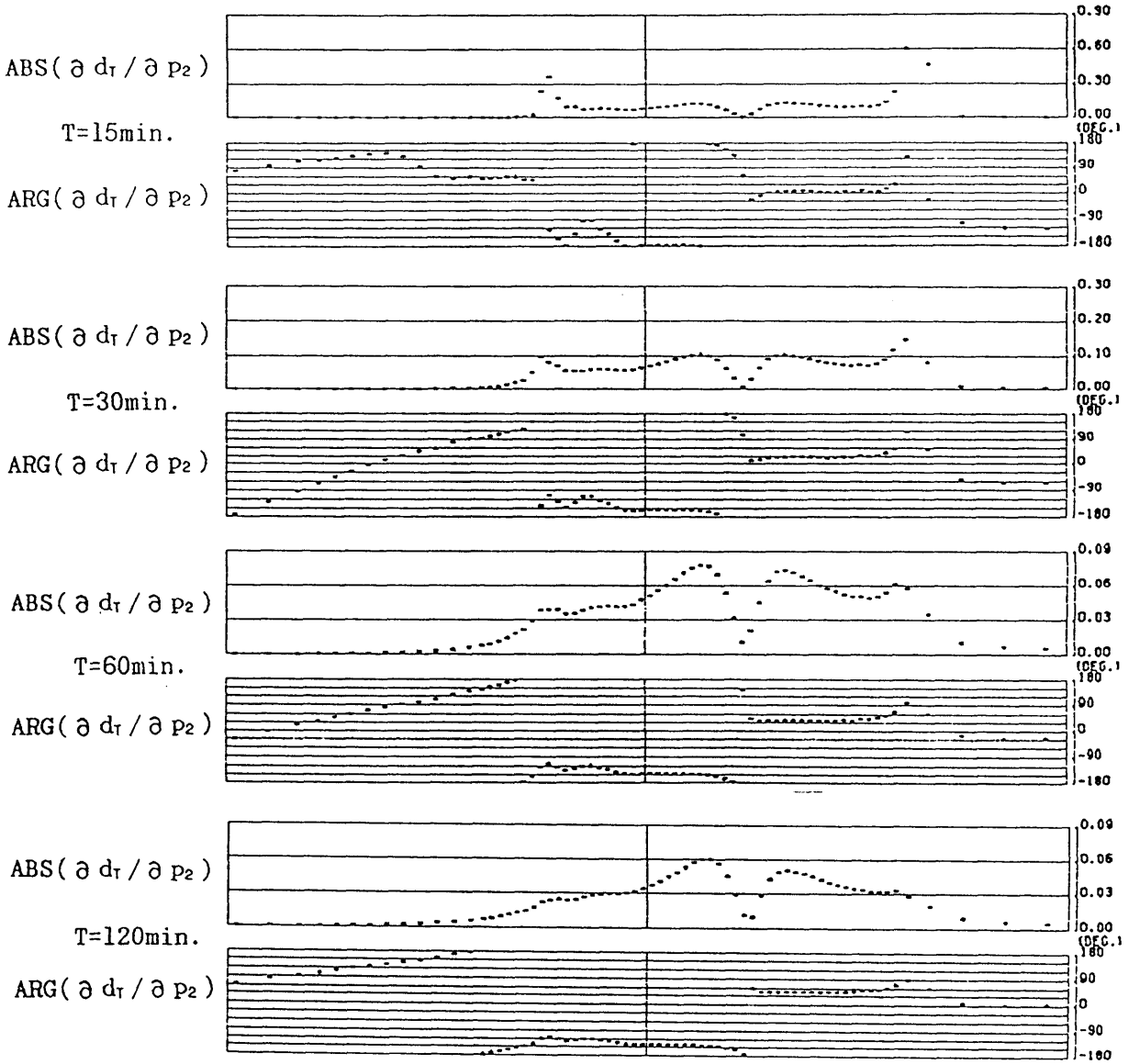
ABS(∂ dT / ∂ p2)
T=15min.
ARG(∂ dT / ∂ p2)
ABS(∂ dT / ∂ p2)
T=30min.
ARG(∂ dT / ∂ p2)
ABS(∂ dT / ∂ p2)
T=60min.
ARG(∂ dT / ∂ p2)
ABS(∂ dT / ∂ p2)
T=120min.
ARG(∂ dT / ∂ p2)
0.90
0.60
0.30
0.00
0.20
0.10
0.09
0.06
0.03
(DEG.)
180
90
0
-90
-180

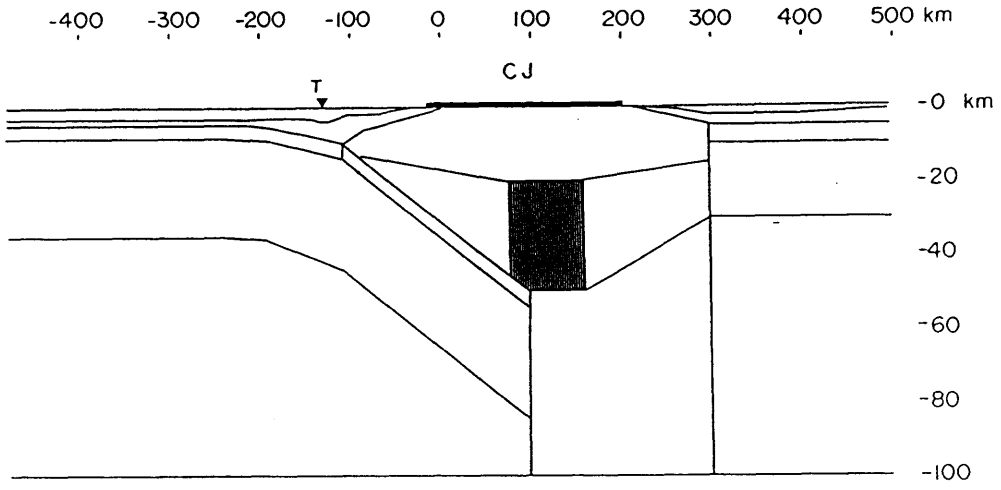
-400
-300
-200
-100
0
100
200
300
400
500 km
CJ
T
-0 km
-20
-40
-60
-80
-100

C-2(a)

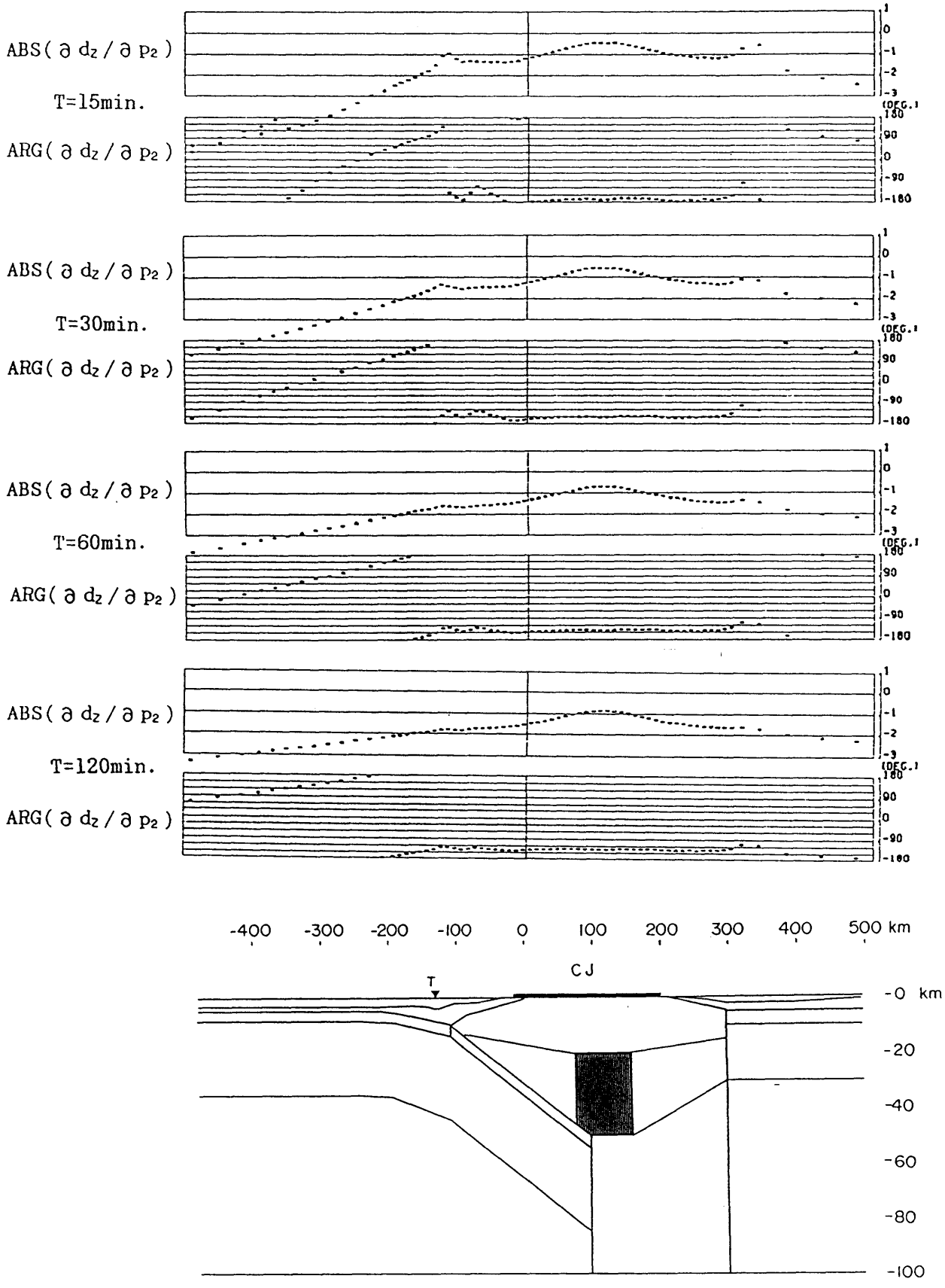
ABS(∂ dz / ∂ p2)
T=15min.
ARG(∂ dz / ∂ p2)
ABS(∂ dz / ∂ p2)
T=30min.
ARG(∂ dz / ∂ p2)
ABS(∂ dz / ∂ p2)
T=60min.
ARG(∂ dz / ∂ p2)
ABS(∂ dz / ∂ p2)
T=120min.
ARG(∂ dz / ∂ p2)
1
0
-1
-2
-3
(DEG.)
180
90
0
-90
-180

-400
-300
-200
-100
0
100
200
300
400
500 km
CJ
T
-0 km
-20
-40
-60
-80
-100

C-2(b)

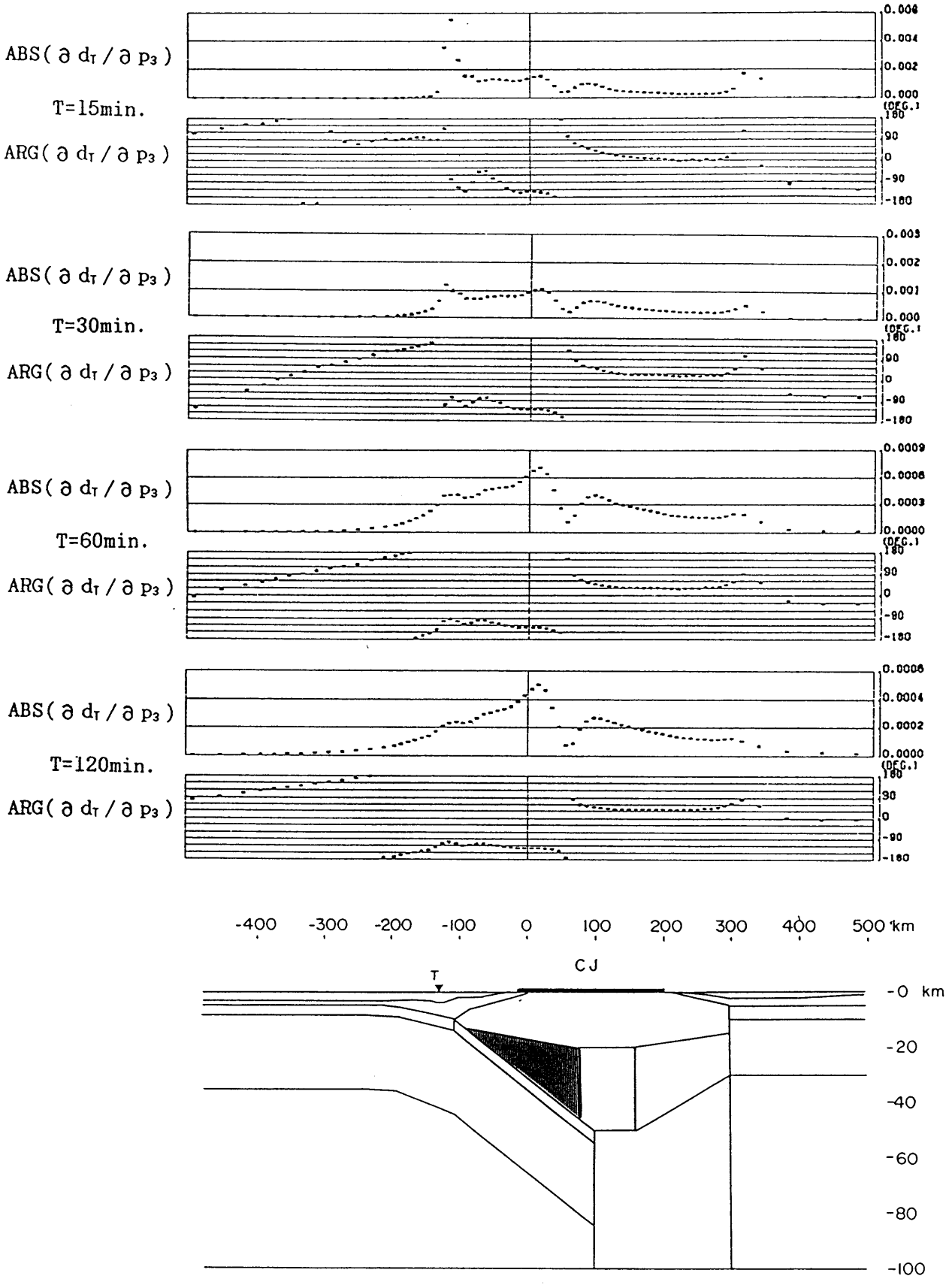
ABS(∂ dT / ∂ p3)
T=15min.
ARG(∂ dT / ∂ p3)
0.006
0.004
0.002
0.000
(DEG.)
180
90
0
-90
-180
ABS(∂ dT / ∂ p3)
T=30min.
ARG(∂ dT / ∂ p3)
0.003
0.002
0.001
0.000
(DEG.)
180
90
0
-90
-180
ABS(∂ dT / ∂ p3)
T=60min.
ARG(∂ dT / ∂ p3)
0.0009
0.0006
0.0003
0.0000
(DEG.)
180
90
0
-90
-180
ABS(∂ dT / ∂ p3)
T=120min.
ARG(∂ dT / ∂ p3)
0.0006
0.0004
0.0002
0.0000
(DEG.)
180
90
0
-90
-180
-400
-300
-200
-100
0
100
200
300
400
500 km
CJ
T
-0 km
-20
-40
-60
-80
-100

C-3(a)

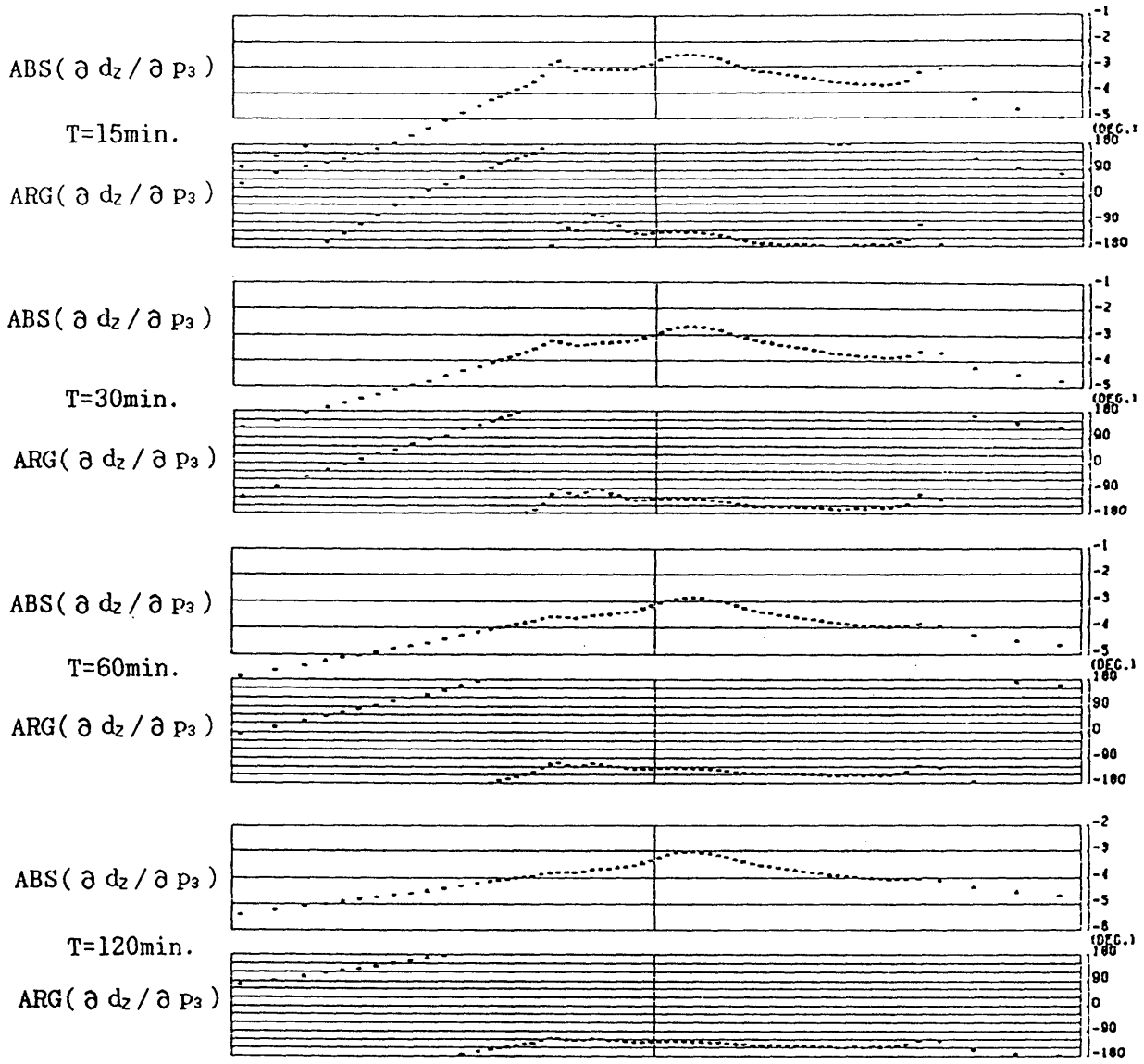
ABS(∂ dz / ∂ p3)
T=15min.
ARG(∂ dz / ∂ p3)
ABS(∂ dz / ∂ p3)
T=30min.
ARG(∂ dz / ∂ p3)
ABS(∂ dz / ∂ p3)
T=60min.
ARG(∂ dz / ∂ p3)
ABS(∂ dz / ∂ p3)
T=120min.
ARG(∂ dz / ∂ p3)
(DEG.)
180
90
0
-90
-180

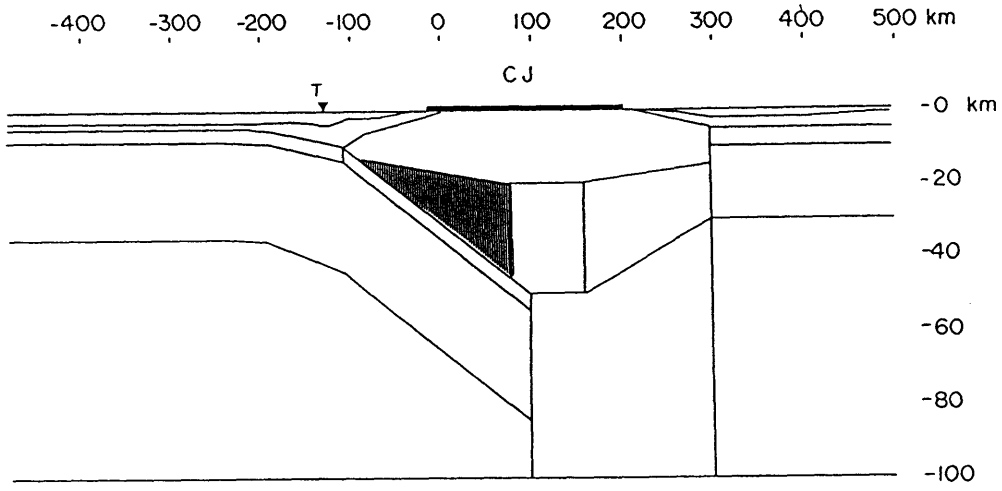
-400
-300
-200
-100
0
100
200
300
400
500 km
CJ
T
-0 km
-20
-40
-60
-80
-100

C-3(b)

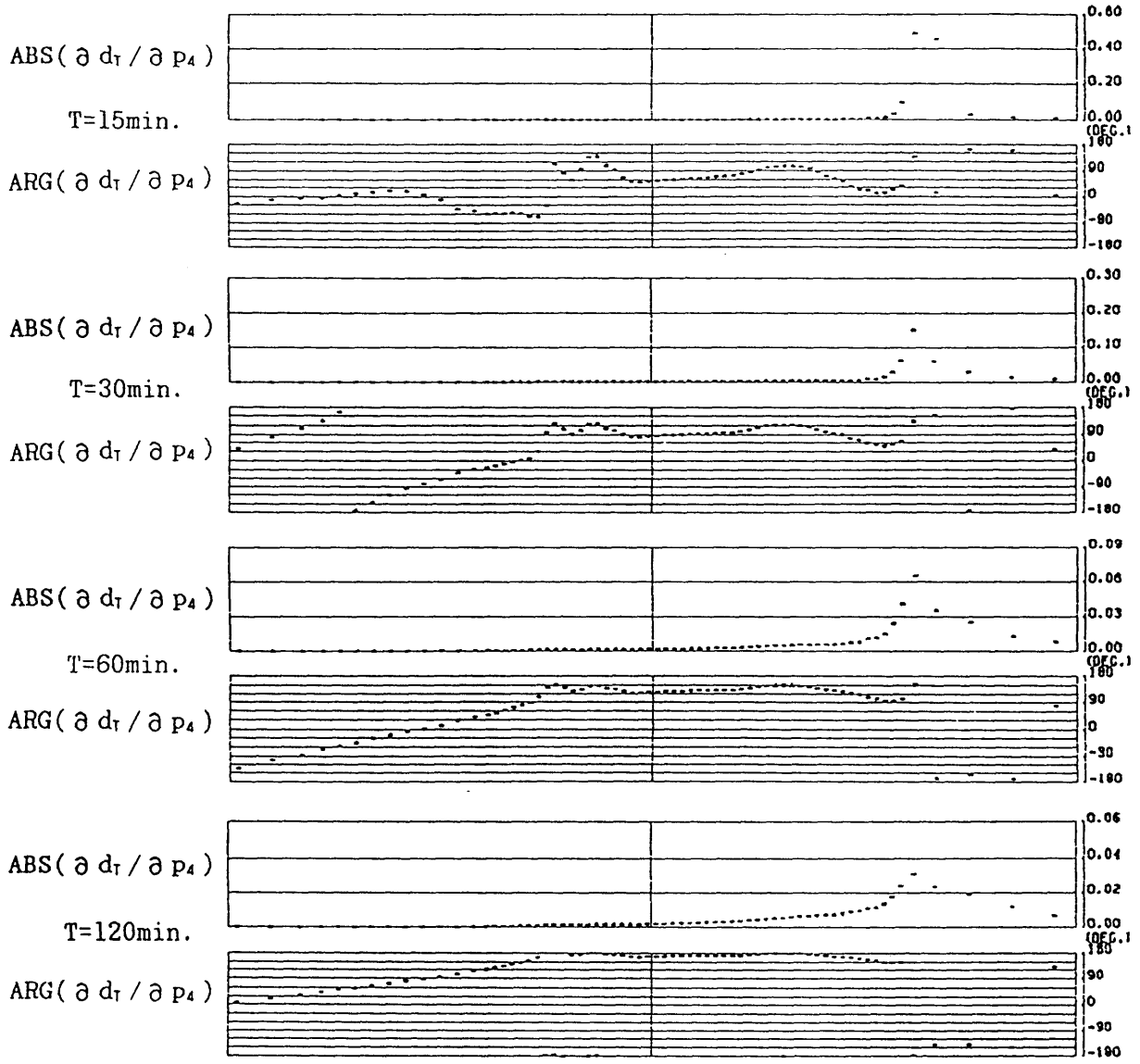
ABS(∂ dT / ∂ p4)
T=15min.
ARG(∂ dT / ∂ p4)
ABS(∂ dT / ∂ p4)
T=30min.
ARG(∂ dT / ∂ p4)
ABS(∂ dT / ∂ p4)
T=60min.
ARG(∂ dT / ∂ p4)
ABS(∂ dT / ∂ p4)
T=120min.
ARG(∂ dT / ∂ p4)
(DEG.)

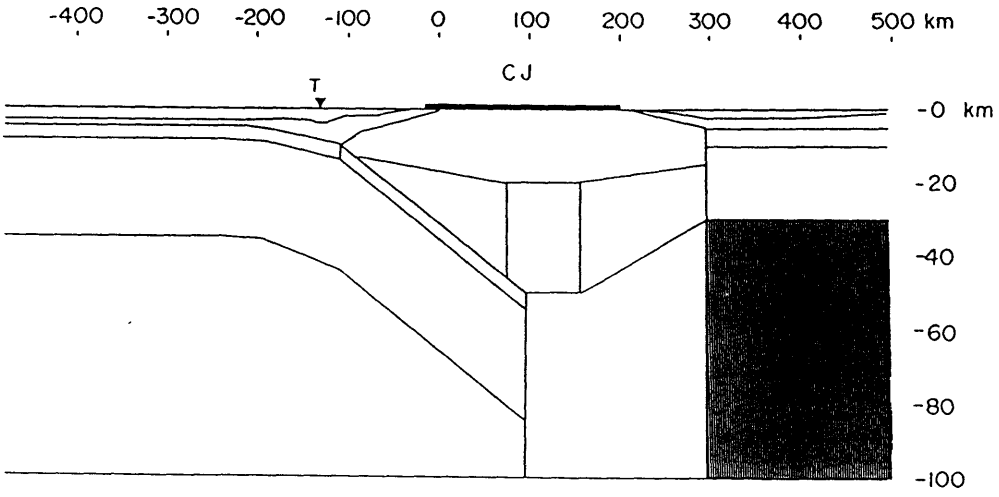
-400
-300
-200
-100
0
100
200
300
400
500 km
T
CJ
-0 km
-20
-40
-60
-80
-100

C-4(a)

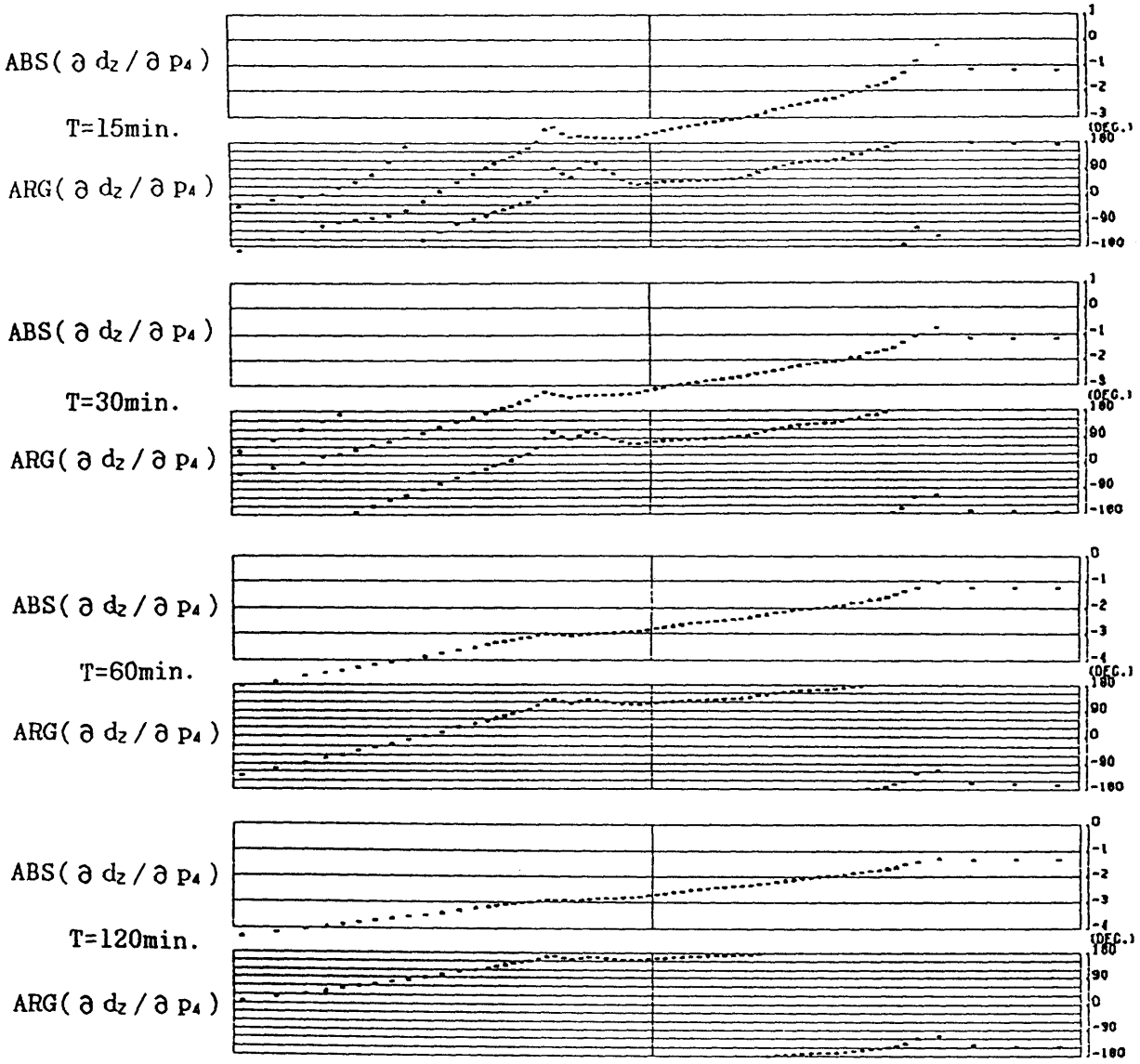
ABS(∂ dz / ∂ p4)
T=15min.
ARG(∂ dz / ∂ p4)
ABS(∂ dz / ∂ p4)
T=30min.
ARG(∂ dz / ∂ p4)
ABS(∂ dz / ∂ p4)
T=60min.
ARG(∂ dz / ∂ p4)
ABS(∂ dz / ∂ p4)
T=120min.
ARG(∂ dz / ∂ p4)
(DEG.)

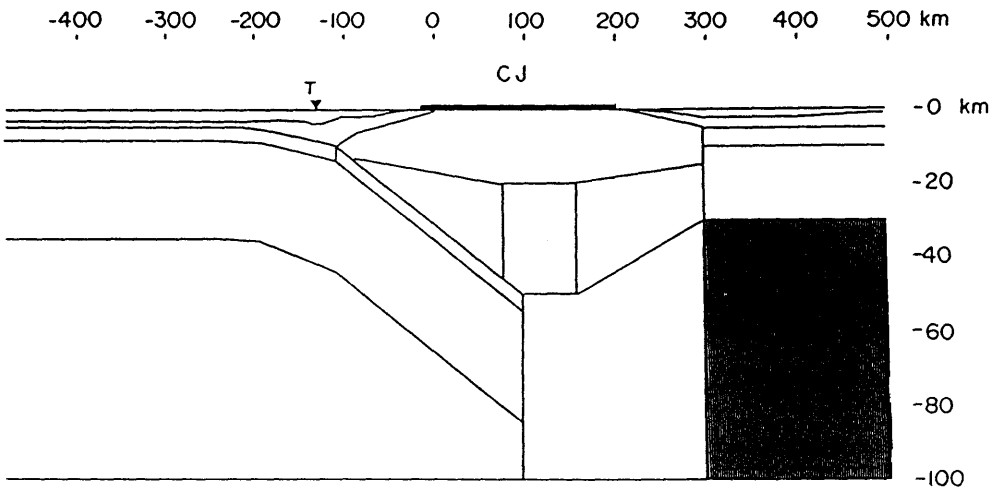
-400
-300
-200
-100
0
100
200
300
400
500 km
T
CJ
-0 km
-20
-40
-60
-80
-100

C-4(b)

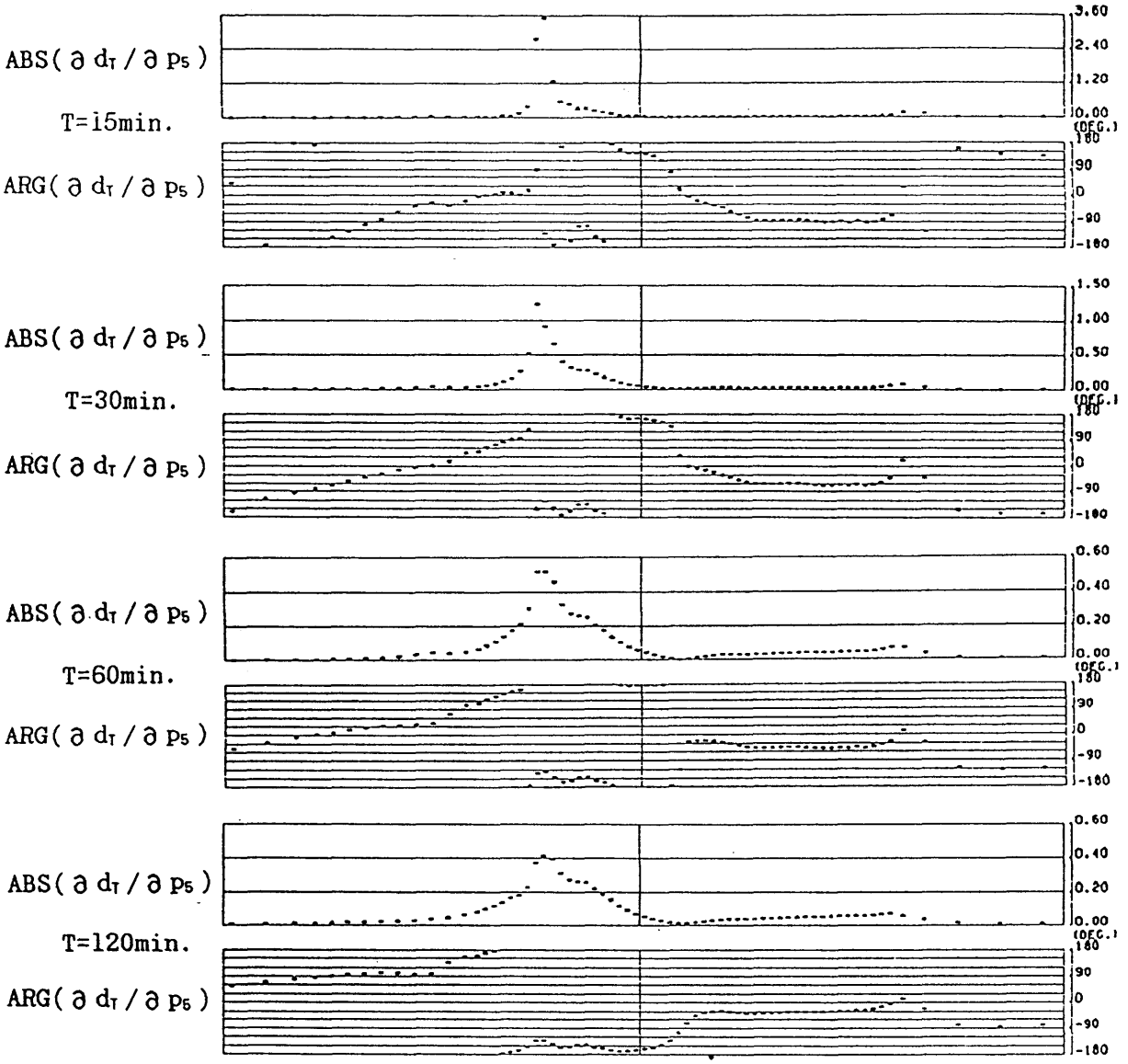
ABS(∂ dT / ∂ p5)
T=15min.
ARG(∂ dT / ∂ p5)
3.60
2.40
1.20
0.00
(DEG.)
180
90
0
-90
-180
ABS(∂ dT / ∂ p5)
T=30min.
ARG(∂ dT / ∂ p5)
1.50
1.00
0.50
0.00
(DEG.)
180
90
0
-90
-180
ABS(∂ dT / ∂ p5)
T=60min.
ARG(∂ dT / ∂ p5)
0.60
0.40
0.20
0.00
(DEG.)
180
90
0
-90
-180
ABS(∂ dT / ∂ p5)
T=120min.
ARG(∂ dT / ∂ p5)
0.60
0.40
0.20
0.00
(DEG.)
180
90
0
-90
-180

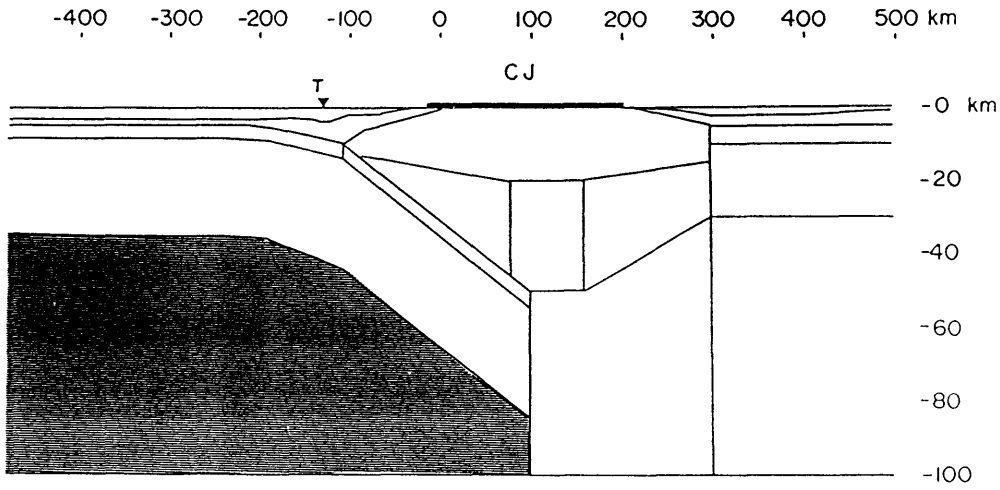
-400
-300
-200
-100
0
100
200
300
400
500 km
CJ
T
-0 km
-20
-40
-60
-80
-100

C-5(a)

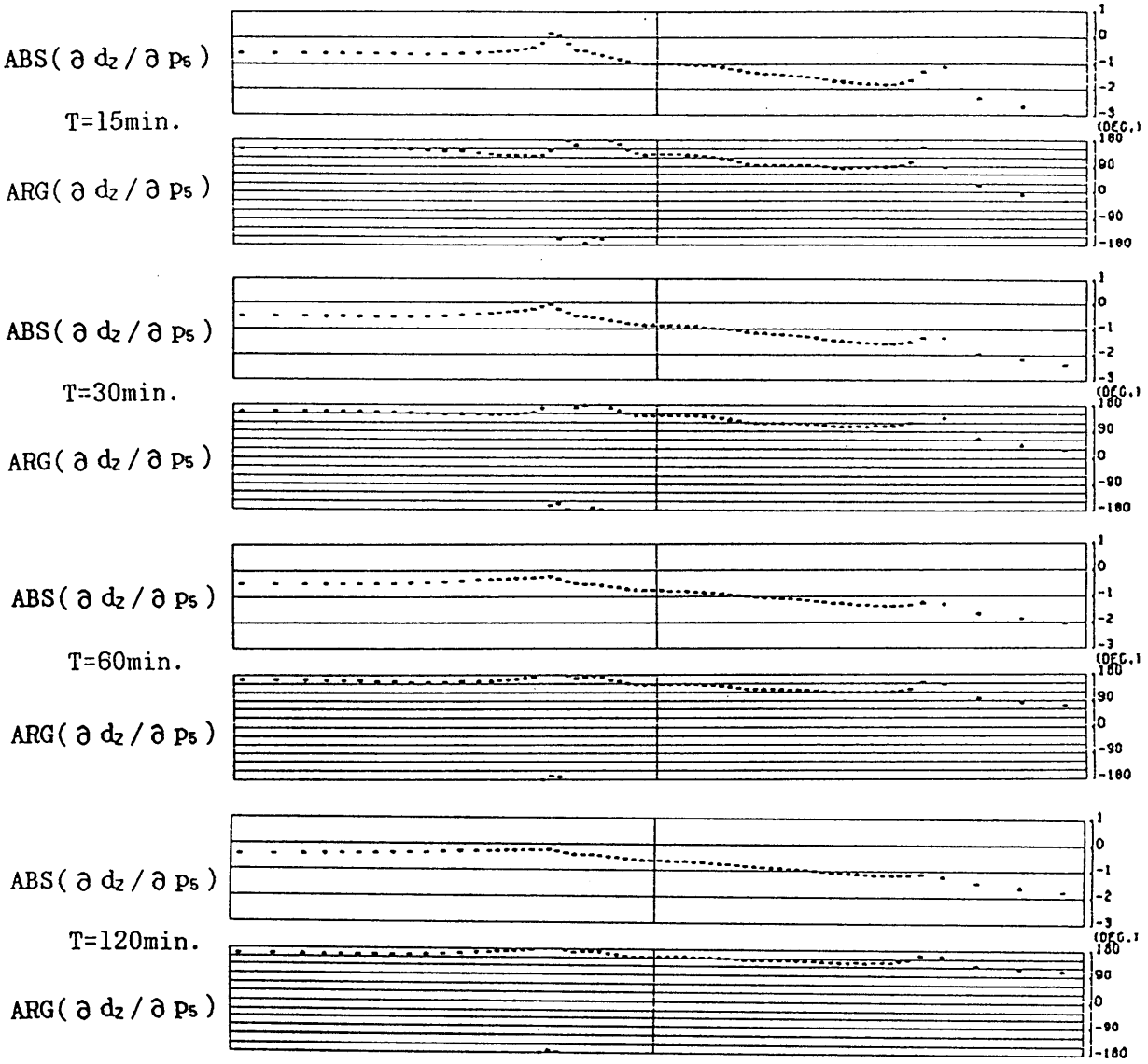
ABS(∂ dz / ∂ ps)
T=15min.
ARG(∂ dz / ∂ ps)
ABS(∂ dz / ∂ ps)
T=30min.
ARG(∂ dz / ∂ ps)
ABS(∂ dz / ∂ ps)
T=60min.
ARG(∂ dz / ∂ ps)
ABS(∂ dz / ∂ ps)
T=120min.
ARG(∂ dz / ∂ ps)
1
0
-1
-2
-3
(DEG.)
180
90
0
-90
-180

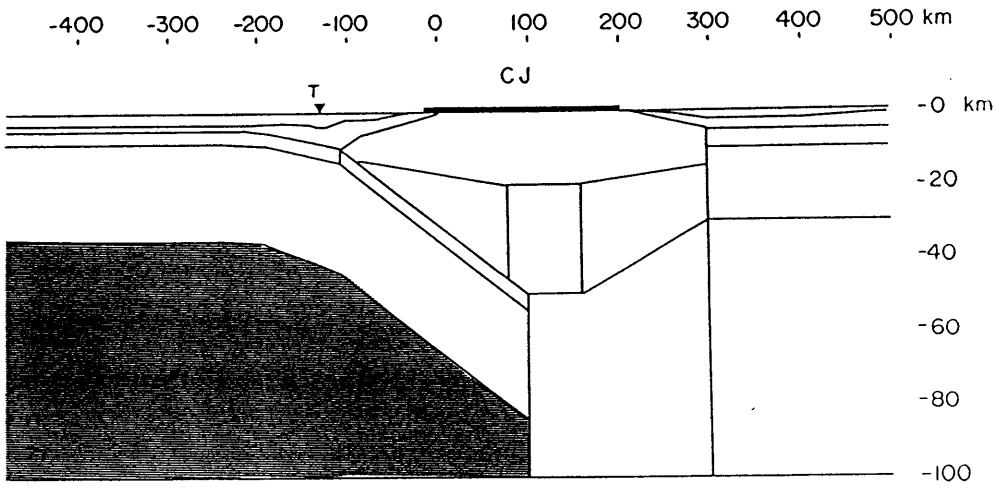
-400
-300
-200
-100
0
100
200
300
400
500 km
CJ
T
-0 km
-20
-40
-60
-80
-100

C-5(b)

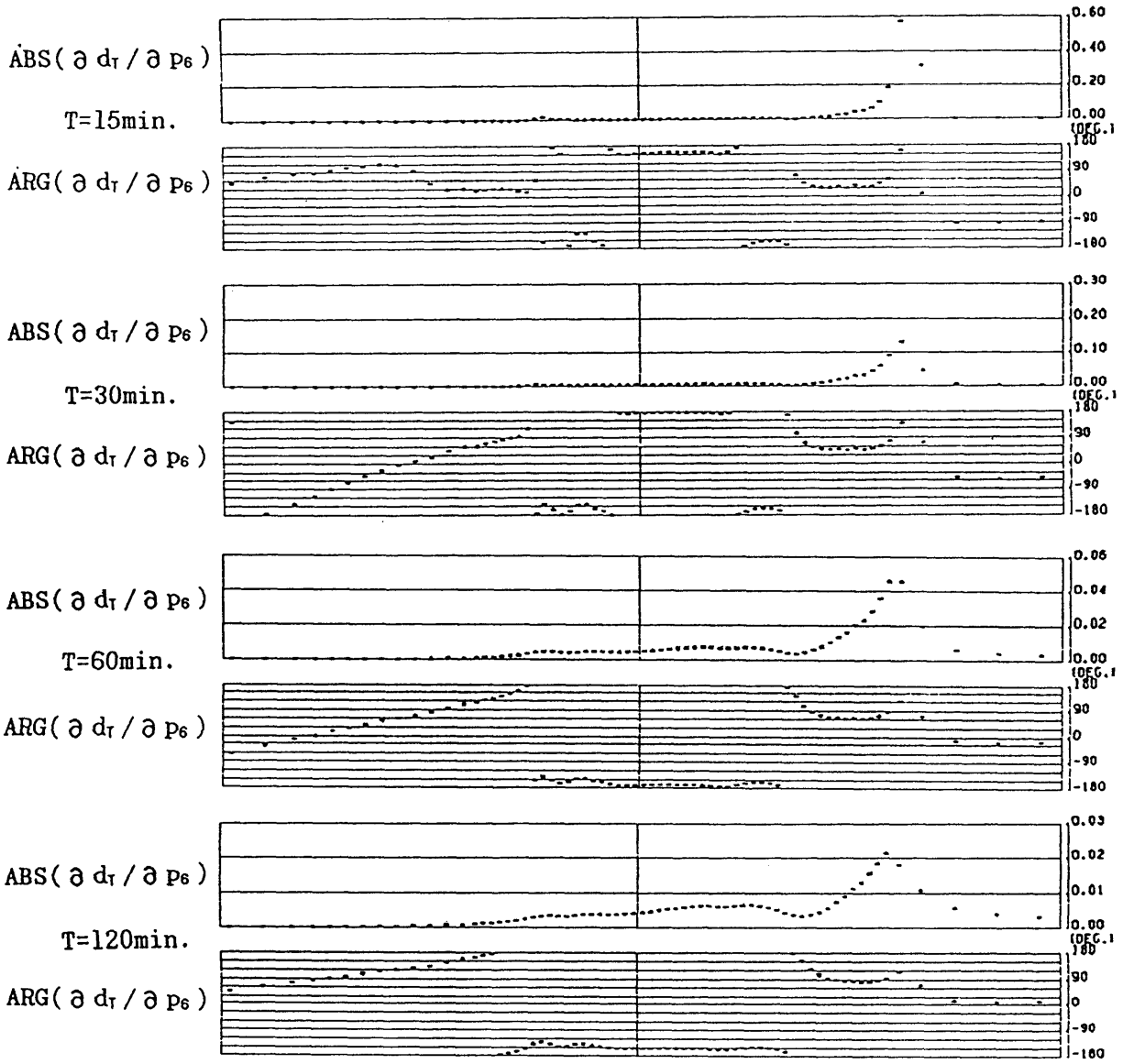
ABS(∂ dT / ∂ p6)
T=15min.
ARG(∂ dT / ∂ p6)
0.60
0.40
0.20
0.00
(DEG.)
180
90
0
-90
-180
ABS(∂ dT / ∂ p6)
T=30min.
ARG(∂ dT / ∂ p6)
0.30
0.20
0.10
0.00
ABS(∂ dT / ∂ p6)
T=60min.
ARG(∂ dT / ∂ p6)
0.06
0.04
0.02
0.00
ABS(∂ dT / ∂ p6)
T=120min.
ARG(∂ dT / ∂ p6)
0.03
0.02
0.01
0.00

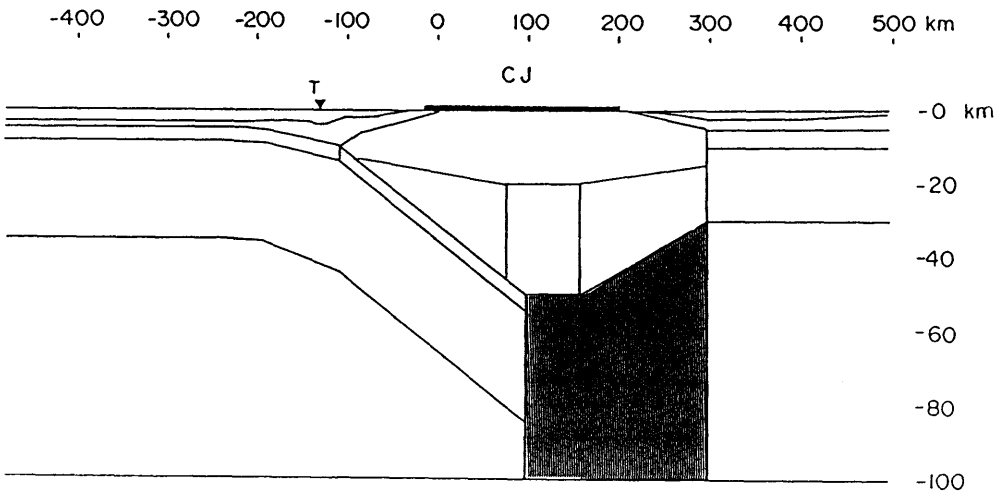
-400
-300
-200
-100
0
100
200
300
400
500 km
T
CJ
-0 km
-20
-40
-60
-80
-100

C-6(a)

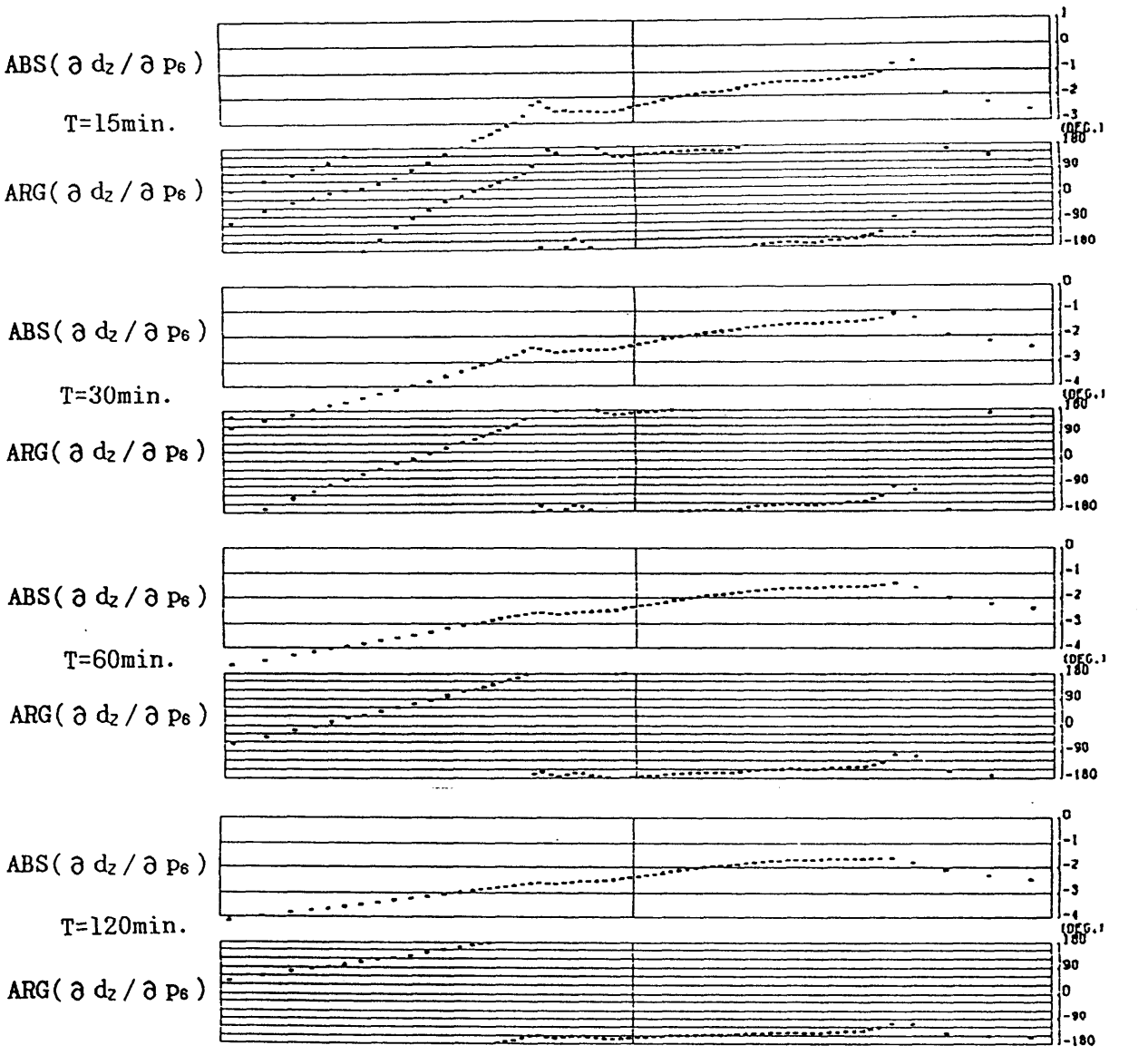
ABS(∂ dz / ∂ p6)
T=15min.
ARG(∂ dz / ∂ p6)
ABS(∂ dz / ∂ p6)
T=30min.
ARG(∂ dz / ∂ p6)
ABS(∂ dz / ∂ p6)
T=60min.
ARG(∂ dz / ∂ p6)
ABS(∂ dz / ∂ p6)
T=120min.
ARG(∂ dz / ∂ p6)
(DEG.)

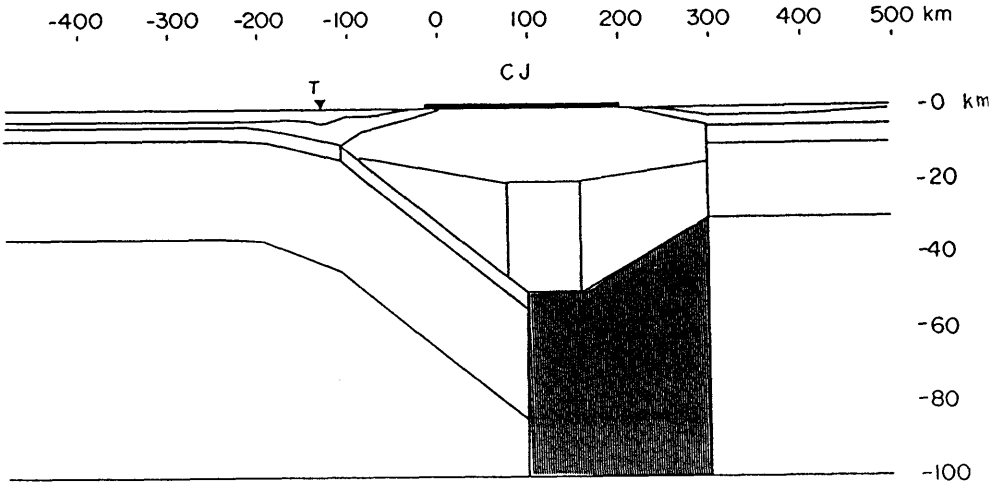
-400
-300
-200
-100
0
100
200
300
400
500 km
CJ
T
-0 km
-20
-40
-60
-80
-100

C-6(b)

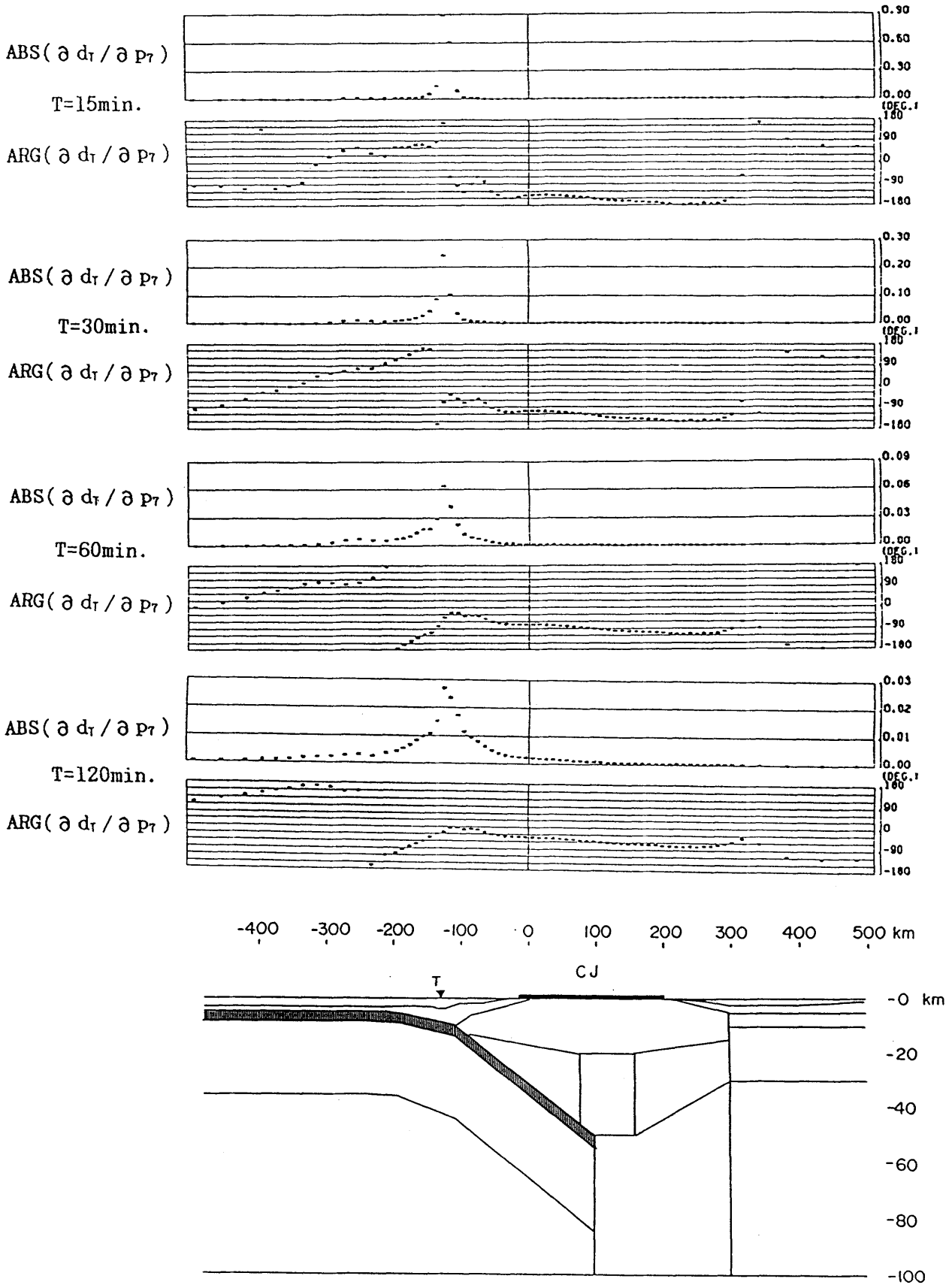
ABS(∂ dT / ∂ p7)
T=15min.
ARG(∂ dT / ∂ p7)
0.90
0.60
0.30
0.00
(DEG.)
180
90
0
-90
-180
ABS(∂ dT / ∂ p7)
T=30min.
ARG(∂ dT / ∂ p7)
0.30
0.20
0.10
0.00
ABS(∂ dT / ∂ p7)
T=60min.
ARG(∂ dT / ∂ p7)
0.09
0.06
0.03
0.00
ABS(∂ dT / ∂ p7)
T=120min.
ARG(∂ dT / ∂ p7)
0.03
0.02
0.01
0.00
-400
-300
-200
-100
0
100
200
300
400
500 km
T
CJ
-0 km
-20
-40
-60
-80
-100

C-7(a)

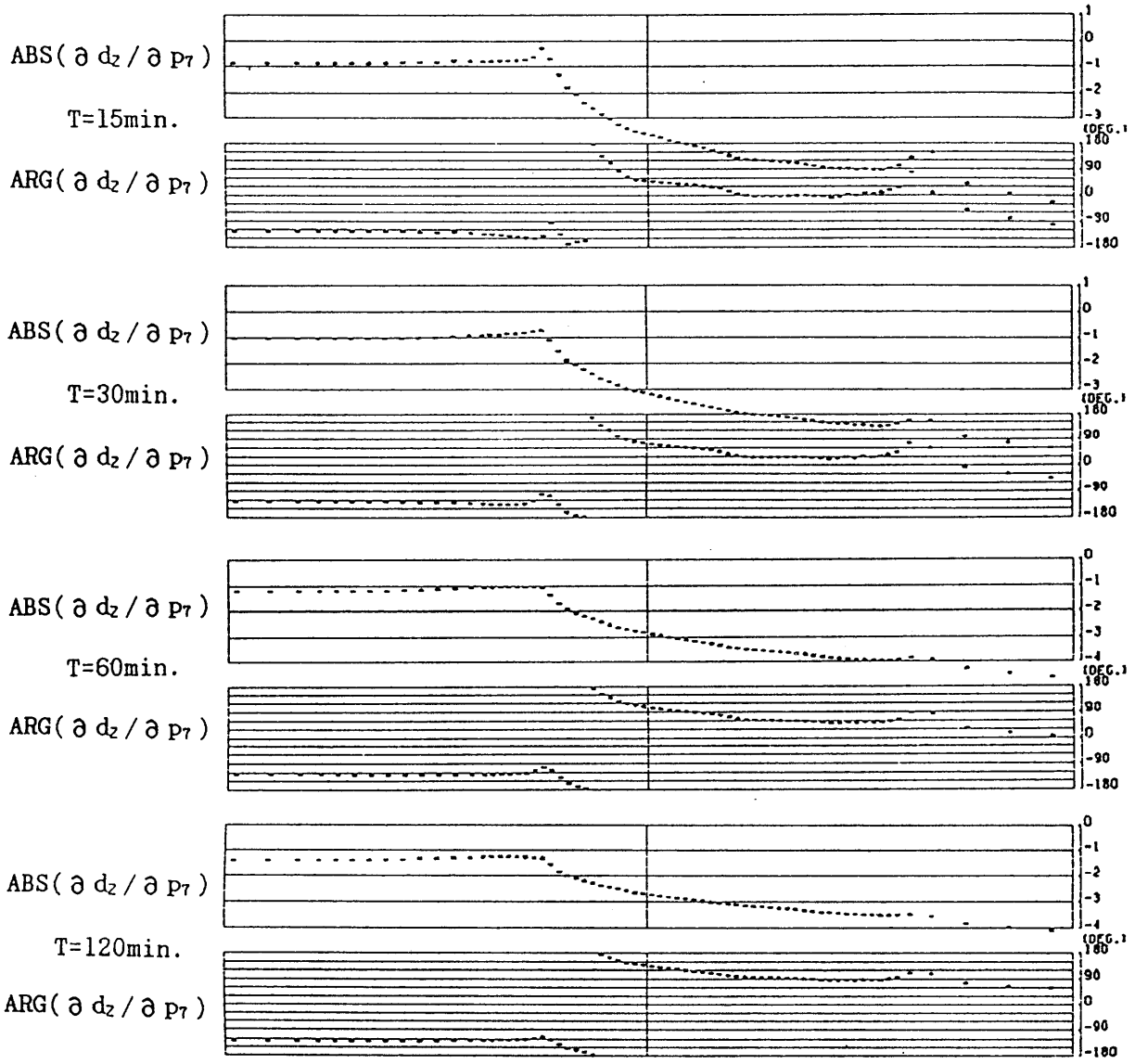
ABS(∂ dz / ∂ p7)
T=15min.
ARG(∂ dz / ∂ p7)
ABS(∂ dz / ∂ p7)
T=30min.
ARG(∂ dz / ∂ p7)
ABS(∂ dz / ∂ p7)
T=60min.
ARG(∂ dz / ∂ p7)
ABS(∂ dz / ∂ p7)
T=120min.
ARG(∂ dz / ∂ p7)
(DEG.)

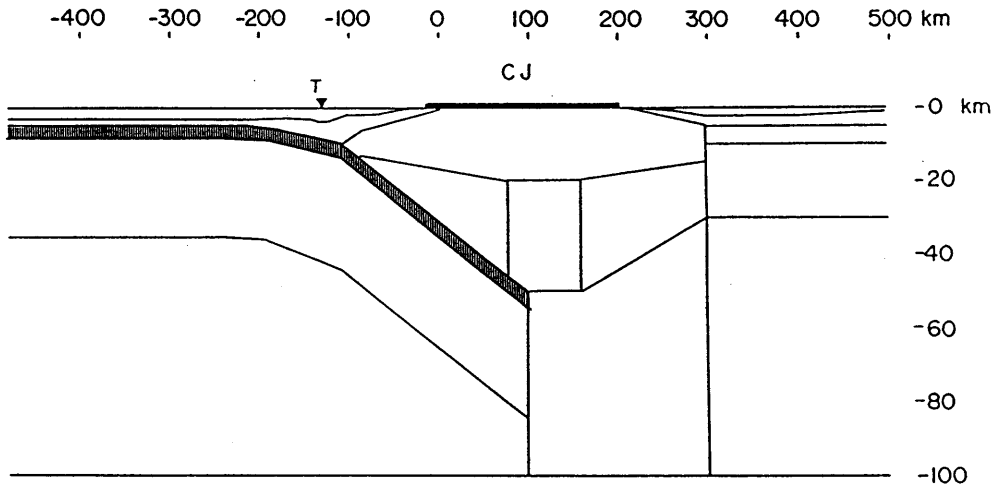
-400
-300
-200
-100
0
100
200
300
400
500 km
CJ
T
-0 km
-20
-40
-60
-80
-100

C-7(b)